2023

Ru(II) Polypyridyl Photosensitizers for Phototherapy

Houston Cole

Recommended Citation

Cole, Houston, "Ru(II) Polypyridyl Photosensitizers for Phototherapy" (2023). *Chemistry & Biochemistry Dissertations*. 276.
https://mavmatrix.uta.edu/chemistry_dissertations/276

RU(II) POLYPYRIDYL PHOTOSENSITIZERS FOR PHOTOTHERAPY

by

Houston Cole

DISSERTATION

Submitted to the Faculty of The Graduate School at The University of Texas at Arlington in
Partial Fulfillment of the Requirements for the Degree Doctor of Philosophy

December 2023

Arlington, TX

Supervising Committee:

Dr. Sherri A. McFarland, Supervising Professor
Dr. Frederick MacDonnell
Dr. Frank Foss
Dr. He Dong

TABLE OF CONTENTS

ABSTRACT

Certain metal complexes, notably those containing the IP-4T ligand, demonstrate remarkable efficiency in sensitizing singlet oxygen (>99%) and exhibit unprecedented photocytotoxicity in normoxic conditions, with notable activity under hypoxic conditions as well. This pronounced efficacy is potentially attributed to the involvement of ^{3}ILCT states in photoredox reactions, a characteristic influenced by the inherent ability of certain oligothiophenes to generate polarons and bipolarons. This dissertation details the conceptualization, creation, and photobiological evaluation of principal molecules, focusing on modifying three critical aspects: 1) the length of the IP-*n*T 'PDT' ligand, 2) the electronic attributes of ancillary ligands like bipyridine or phenanthroline, and 3) the chirality of the coordination complex. The primary goal of this study is to investigate the hypothesis that molecules possessing low-lying and enduring ^{3}ILCT states contribute to this remarkable photocytotoxic potency. Moreover, this research aims to deepen the understanding of which structural elements, beyond the IP-*n*T ligand, contribute to enhanced photobiological properties.

CHAPTER 1. INTRODUCTION

As of 2022, cancer is the second leading cause of death in the United States.[1] Alternate and adjuvant strategies are urgently needed. One such strategy is photodynamic therapy (PDT). PDT is a light-based form of cancer therapy that uses a photosensitizer (PS), light, and oxygen to destroy tumors, and has been shown to induce an immune response that can protect against recurrence.[2–13]

Scheme 1. Jablonski diagram for Photofrin.

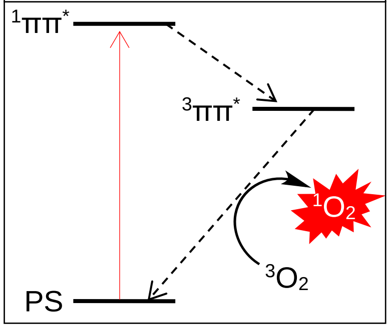

Activation of the PS by certain wavelengths of light produces triplet excited states that interact with oxygen to generate reactive oxygen species (ROS) such as singlet oxygen, which is is thought to be the most important ROS for mediating the PDT effect. The only FDA-approved PS for cancer therapy is Photofrin, a mixture of oligomeric porphyrins that is activated with 630-nm light to produce triplet excited states that interact with oxygen to generate reactive oxygen species (ROS) such as singlet oxygen ($^1O_2$) (Scheme 1). There is ongoing interest in developing non tetrapyrrole-based PSs that could exert their photocytotoxic effects through alternate mechanisms to treat hypoxic tumors, which are some of the most aggressive and drug-resistant neoplasms.[14–19]

Photocytotoxicity in hypoxia has proven extremely difficult to achieve,[20,21] necessitating entirely new approaches for manipulating the reactivity of excited states.[22,23] Traditional PSs generate ROS from triplet ππ* excited states that exploit oxygen-dependent mechanistic pathways. In contrast, metal complexes possess a variety of excited state configurations that can be accessed through different ligand and metal combinations. These excited states may be localized to the metal (MC) or the ligands (LC), may involve charge transfer between the metal and a ligand(s) (MLCT/LMCT) or even two different ligands (LLCT).[24–26] As such, each of these excited states has its own characteristic reactivity, which can include singlet oxygen sensitization or oxygen-independent photochemical reactions as well as redox chemistry.

Our lab has shown that it is possible to achieve potent photocytotoxic effects with Ru(II) and Os(II) metal-organic dyads, where the metal center is chelated to an imidazo[4,5-*f*][1,10]phenanthroline ligand that is appended to an oligothiophene chain (*n*T).[27–34] In these scaffolds, the role of the metal is to facilitate the formation of triplet states through intersystem system crossing, and the role of the ligand is to establish an "organic" triplet state that is lower in energy than the metal-to-ligand charge transfer (MLCT) states that usually dominate Ru(II) and Os(II) polypyridyl photophysics.[24,25] The organic chromophore is also responsible for prolonging the triplet excited state lifetime to allow enough time for bimolecular quenching reactions (such as singlet oxygen sensitization) to take place, which results in a greater photocytotoxic effect. While we have used a variety of organic chromophores in the past, the *n*T moiety is especially important because it introduces charge transfer character to otherwise nonpolar intraligand (IL) excited states. The resulting intraligand charge transfer (ILCT) excited states are capable of sensitizing singlet oxygen even in hypoxia[20,21] but may also facilitate oxygen-independent photoredox reactions that may contribute to the overall photocytotoxicity. This scaffold is exemplified by TLD1433, the first Ru(II)-based PS to advance to human clinical trials.[27,35] Since TLD1433, we have rationally designed and developed PSs that are even more potent in normoxia and hypoxia by installing an additional thiophene ring and by combining the organic chromophore with various other coligands on Ru(II) or Os(II).[20,21,27,36]

Certain metal complexes incorporating the IP-4T ligand sensitize $^1O_2$ in very high yield (>99%) and exert unprecedented photocytotoxic effects in normoxia, and are also active in hypoxia.[27,28] The unusually potent activity may stem, in part, from ^{3}ILCT states that participate in photoredox reactions due to the known capacities of certain oligothiophenes to form polarons and bipolarons.[27] This dissertation describes the design, synthesis, and photobiological characterization of key target molecules that modify the 1) length of the IP-nT “PDT” ligand, 2) electronic nature of the bipyridine or phenanthroline type ancillary ligands, and 3) chirality of the coordination complex. The targets and subsequent studies will test the hypothesis that molecules with low-lying and long-lived ^{3}ILCT states are responsible for this unusually high photocytotoxic potency and seeks to further understand what structural features (aside from the IP-nT ligand) lead to more favorable photobiological properties.

1.1 REFERENCES

(1) *Cancer Facts & Figures 2020*; American Cancer Society Inc.: Altanta, GA, 2021. https://www.cancer.org/research/cancer-facts-statistics/all-cancer-facts-figures/cancer-facts-figures-2020.html.

(2) Gollnick, S. O.; Vaughan, L.; Henderson, B. W. Generation of Effective Antitumor Vaccines Using Photodynamic Therapy. *Cancer Res.* **2002**, *62* (6), 1604–1608.

(3) Castano, A. P.; Mroz, P.; Hamblin, M. R. Photodynamic Therapy and Anti-Tumour Immunity. *Nat. Rev. Cancer* **2006**, *6* (7), 535–545. https://doi.org/10.1038/nrc1894.

(4) Mroz, P.; Hashmi, J. T.; Huang, Y.-Y.; Lange, N.; Hamblin, M. R. Stimulation of Anti-Tumor Immunity by Photodynamic Therapy. *Expert Rev. Clin. Immunol.* **2011**, *7* (1), 75–91. https://doi.org/10.1586/eci.10.81.

(5) Gollnick, S. O. Photodynamic Therapy and Antitumor Immunity. *J. Natl. Compr. Cancer Netw. JNCCN* **2012**, *10 Suppl 2*, S40-43. https://doi.org/10.6004/jnccn.2012.0173.

(6) Anzengruber, F.; Avci, P.; de Freitas, L. F.; Hamblin, M. R. T-Cell Mediated Anti-Tumor Immunity after Photodynamic Therapy: Why Does It Not Always Work and How Can We Improve It? *Photochem. Photobiol. Sci.* **2015**, *14* (8), 1492–1509. https://doi.org/10.1039/C4PP00455H.

(7) Shams, M.; Owczarczak, B.; Manderscheid-Kern, P.; Bellnier, D. A.; Gollnick, S. O. Development of Photodynamic Therapy Regimens That Control Primary Tumor Growth and Inhibit Secondary Disease. *Cancer Immunol. Immunother. CII* **2015**, *64* (3), 287–297. https://doi.org/10.1007/s00262-014-1633-9.

(8) Vatansever, F.; Hamblin, M. R. Photodynamic Therapy and Antitumor Immune Response. In *Cancer Immunology*; Rezaei, N., Ed.; Springer Berlin Heidelberg: Berlin, Heidelberg, 2015; pp 383–399. https://doi.org/10.1007/978-3-662-44946-2_21.

(9) Yang, Y.; Hu, Y.; Wang, H. Targeting Antitumor Immune Response for Enhancing the Efficacy of Photodynamic Therapy of Cancer: Recent Advances and Future Perspectives. *Oxid. Med. Cell. Longev.* **2016**, *2016*, 1–11. https://doi.org/10.1155/2016/5274084.

(10) Hwang, H. S.; Shin, H.; Han, J.; Na, K. Combination of Photodynamic Therapy (PDT) and Anti-Tumor Immunity in Cancer Therapy. *J. Pharm. Investig.* **2018**, *48* (2), 143–151. https://doi.org/10.1007/s40005-017-0377-x.

(11) Korbelik, M. Role of Cell Stress Signaling Networks in Cancer Cell Death and Antitumor Immune Response Following Proteotoxic Injury Inflicted by Photodynamic Therapy: TUMOR AND HOST RESPONSE TO PDT AND BCG. *Lasers Surg. Med.* **2018**, *50* (5), 491–498. https://doi.org/10.1002/lsm.22810.

(12) Nath, S.; Obaid, G.; Hasan, T. The Course of Immune Stimulation by Photodynamic Therapy: Bridging Fundamentals of Photochemically Induced Immunogenic Cell Death to

the Enrichment of T-Cell Repertoire. *Photochem. Photobiol.* **2019**, *95* (6), 1288–1305. https://doi.org/10.1111/php.13173.

(13) Falk-Mahapatra, R.; Gollnick, S. O. Photodynamic Therapy and Immunity: An Update. *Photochem. Photobiol.* **2020**, *96*, 550–559. https://doi.org/10.1111/php.13253.

(14) Muz, B.; de la Puente, P.; Azab, F.; Azab, A. K. The Role of Hypoxia in Cancer Progression, Angiogenesis, Metastasis, and Resistance to Therapy. *Hypoxia Auckl. NZ* **2015**, *3*, 83–92. https://doi.org/10.2147/HP.S93413.

(15) Lameijer, L. N.; Ernst, D.; Hopkins, S. L.; Meijer, M. S.; Askes, S. H. C.; Le Dévédec, S. E.; Bonnet, S. A Red-Light-Activated Ruthenium-Caged NAMPT Inhibitor Remains Phototoxic in Hypoxic Cancer Cells. *Angew. Chem. Int. Ed.* **2017**, *56* (38), 11549–11553. https://doi.org/10.1002/anie.201703890.

(16) van Rixel, V. H. S.; Ramu, V.; Auyeung, A. B.; Beztsinna, N.; Leger, D. Y.; Lameijer, L. N.; Hilt, S. T.; Le Dévédec, S. E.; Yildiz, T.; Betancourt, T.; Gildner, M. B.; Hudnall, T. W.; Sol, V.; Liagre, B.; Kornienko, A.; Bonnet, S. Photo-Uncaging of a Microtubule-Targeted Rigidin Analogue in Hypoxic Cancer Cells and in a Xenograft Mouse Model. *J. Am. Chem. Soc.* **2019**, *141* (46), 18444–18454. https://doi.org/10.1021/jacs.9b07225.

(17) Yu, Q.; Huang, T.; Liu, C.; Zhao, M.; Xie, M.; Li, G.; Liu, S.; Huang, W.; Zhao, Q. Oxygen Self-Sufficient NIR-Activatable Liposomes for Tumor Hypoxia Regulation and Photodynamic Therapy. *Chem. Sci.* **2019**, *10* (39), 9091–9098. https://doi.org/10.1039/C9SC03161H.

(18) Bevernaegie, R.; Doix, B.; Bastien, E.; Diman, A.; Decottignies, A.; Feron, O.; Elias, B. Exploring the Phototoxicity of Hypoxic Active Iridium(III)-Based Sensitizers in 3D Tumor Spheroids. *J. Am. Chem. Soc.* **2019**, *141* (46), 18486–18491. https://doi.org/10.1021/jacs.9b07723.

(19) Roque, J.; Havrylyuk, D.; Barrett, P. C.; Sainuddin, T.; McCain, J.; Colón, K.; Sparks, W. T.; Bradner, E.; Monro, S.; Heidary, D.; Cameron, C. G.; Glazer, E. C.; McFarland, S. A. Strained, Photoejecting Ru(II) Complexes That Are Cytotoxic Under Hypoxic Conditions. *Photochem. Photobiol.* **2020**, *96* (2), 327–339. https://doi.org/10.1111/php.13174.

(20) Roque III, J. A.; Barrett, P. C.; Cole, H. D.; Lifshits, L. M.; Shi, G.; Monro, S.; von Dohlen, D.; Kim, S.; Russo, N.; Deep, G.; Cameron, C. G.; Alberto, M. E.; McFarland, S. A.

Breaking the Barrier: An Osmium Photosensitizer with Unprecedented Hypoxic Phototoxicity for Real World Photodynamic Therapy. *Chem. Sci.* **2020**, *11*, 9784–9806. https://doi.org/10.1039/D0SC03008B.

(21) Roque, J. A.; Barrett, P. C.; Cole, H. D.; Lifshits, L. M.; Bradner, E.; Shi, G.; von Dohlen, D.; Kim, S.; Russo, N.; Deep, G.; Cameron, C. G.; Alberto, M. E.; McFarland, S. A. Os(II) Oligothienyl Complexes as a Hypoxia-Active Photosensitizer Class for Photodynamic Therapy. *Inorg. Chem.* **2020**, *59* (22), 16341–16360. https://doi.org/10.1021/acs.inorgchem.0c02137.

(22) Xu, S.; Zhu, X.; Zhang, C.; Huang, W.; Zhou, Y.; Yan, D. Oxygen and Pt(II) Self-Generating Conjugate for Synergistic Photo-Chemo Therapy of Hypoxic Tumor. *Nat. Commun.* **2018**, *9* (1), 2053. https://doi.org/10.1038/s41467-018-04318-1.

(23) Raza, A.; Archer, S. A.; Fairbanks, S. D.; Smitten, K. L.; Botchway, S. W.; Thomas, J. A.; MacNeil, S.; Haycock, J. W. A Dinuclear Ruthenium(II) Complex Excited by Near-Infrared Light through Two-Photon Absorption Induces Phototoxicity Deep within Hypoxic Regions of Melanoma Cancer Spheroids. *J. Am. Chem. Soc.* **2020**, *142* (10), 4639–4647. https://doi.org/10.1021/jacs.9b11313.

(24) Juris, A.; Balzani, V.; Barigelletti, F.; Campagna, S.; Belser, P.; von Zelewsky, A. Ru(II) Polypyridine Complexes: Photophysics, Photochemistry, Eletrochemistry, and Chemiluminescence. *Coord. Chem. Rev.* **1988**, *84*, 85–277. https://doi.org/10.1016/0010-8545(88)80032-8.

(25) McClenaghan, N. D.; Leydet, Y.; Maubert, B.; Indelli, M. T.; Campagna, S. Excited-State Equilibration: A Process Leading to Long-Lived Metal-to-Ligand Charge Transfer Luminescence in Supramolecular Systems. *Coord. Chem. Rev.* **2005**, *249* (13–14), 1336–1350. https://doi.org/10.1016/j.ccr.2004.12.017.

(26) Balzani, V.; Juris, A.; Venturi, M.; Campagna, S.; Serroni, S. Luminescent and Redox-Active Polynuclear Transition Metal Complexes. *Chem Rev* **1996**, *96* (2), 759–834. https://doi.org/10.1021/cr941154y.

(27) Monro, S.; Colón, K. L.; Yin, H.; Roque, J.; Konda, P.; Gujar, S.; Thummel, R. P.; Lilge, L.; Cameron, C. G.; McFarland, S. A. Transition Metal Complexes and Photodynamic Therapy from a Tumor-Centered Approach: Challenges, Opportunities, and Highlights

from the Development of TLD1433. *Chem. Rev.* **2019**, *119* (2), 797–828. https://doi.org/10.1021/acs.chemrev.8b00211.

(28) Shi, G.; Monro, S.; Hennigar, R.; Colpitts, J.; Fong, J.; Kasimova, K.; Yin, H.; DeCoste, R.; Spencer, C.; Chamberlain, L.; Mandel, A.; Lilge, L.; McFarland, S. A. Ru(II) Dyads Derived from α-Oligothiophenes: A New Class of Potent and Versatile Photosensitizers for PDT. *Coord. Chem. Rev.* **2015**, *282–283*, 127–138. https://doi.org/10.1016/j.ccr.2014.04.012.

(29) Ghosh, G.; Colón, K. L.; Fuller, A.; Sainuddin, T.; Bradner, E.; McCain, J.; Monro, S. M. A.; Yin, H.; Hetu, M. W.; Cameron, C. G.; McFarland, S. A. Cyclometalated Ruthenium(II) Complexes Derived from α-Oligothiophenes as Highly Selective Cytotoxic or Photocytotoxic Agents. *Inorg. Chem.* **2018**, *57* (13), 7694–7712. https://doi.org/10.1021/acs.inorgchem.8b00689.

(30) McCain, J.; Colón, K. L.; Barrett, P. C.; Monro, S. M. A.; Sainuddin, T.; Roque III, J.; Pinto, M.; Yin, H.; Cameron, C. G.; McFarland, S. A. Photophysical Properties and Photobiological Activities of Ruthenium(II) Complexes Bearing π-Expansive Cyclometalating Ligands with Thienyl Groups. *Inorg. Chem.* **2019**, *58* (16), 10778–10790. https://doi.org/10.1021/acs.inorgchem.9b01044.

(31) Monro, S.; Cameron, C. G.; Zhu, X.; Colón, K. L.; Yin, H.; Sainuddin, T.; Hetu, M.; Pinto, M.; Fuller, A.; Bennett, L.; Roque, J.; Sun, W.; McFarland, S. A. Synthesis, Characterization and Photobiological Studies of Ru(II) Dyads Derived from α-Oligothiophene Derivatives of 1,10-Phenanthroline. *Photochem. Photobiol.* **2019**, *95* (1), 267–279. https://doi.org/10.1111/php.13012.

(32) Arenas, Y.; Monro, S.; Shi, G.; Mandel, A.; McFarland, S.; Lilge, L. Photodynamic Inactivation of Staphylococcus Aureus and Methicillin-Resistant Staphylococcus Aureus with Ru(II)-Based Type I/Type II Photosensitizers. *Photodiagnosis Photodyn. Ther.* **2013**, *10* (4), 615–625. https://doi.org/10.1016/j.pdpdt.2013.07.001.

(33) Chen, Q.; Ramu, V.; Aydar, Y.; Groenewoud, A.; Zhou, X.-Q.; Jager, M. J.; Cole, H.; Cameron, C. G.; McFarland, S. A.; Bonnet, S.; Snaar-Jagalska, B. E. TLD1433 Photosensitizer Inhibits Conjunctival Melanoma Cells in Zebrafish Ectopic and Orthotopic Tumour Models. *Cancers* **2020**, *12* (3), 587. https://doi.org/10.3390/cancers12030587.

(34) Chamberlain, S.; Cole, H. D.; Roque, J.; Bellnier, D.; McFarland, S. A.; Shafirstein, G. TLD1433-Mediated Photodynamic Therapy with an Optical Surface Applicator in the Treatment of Lung Cancer Cells In Vitro. *Pharmaceuticals* **2020**, *13* (7), 137. https://doi.org/10.3390/ph13070137.

(35) McFarland, S. A.; Mandel, A.; Dumoulin-White, R.; Gasser, G. Metal-Based Photosensitizers for Photodynamic Therapy: The Future of Multimodal Oncology? *Curr. Opin. Chem. Biol.* **2020**, *56*, 23–27. https://doi.org/10.1016/j.cbpa.2019.10.004.

(36) Lifshits, L. M.; Roque, J. A.; Cole, H. D.; Thummel, R. P.; Cameron, C. G.; McFarland, S. A. NIR-Absorbing Ru II Complexes Containing α-Oligothiophenes for Applications in Photodynamic Therapy. *ChemBioChem* **2020**, *21*, 3594–3607. https://doi.org/10.1002/cbic.202000419.

(37) Hall, J. P.; Keane, P. M.; Beer, H.; Buchner, K.; Winter, G.; Sorensen, T. L.; Cardin, D. J.; Brazier, J. A.; Cardin, C. J. Delta Chirality Ruthenium 'Light-Switch' Complexes Can Bind in the Minor Groove of DNA with Five Different Binding Modes. *Nucleic Acids Res.* **2016**, *44* (19), 9472–9482. https://doi.org/10.1093/nar/gkw753.

(38) Keane, P. M.; Poynton, F. E.; Hall, J. P.; Clark, I. P.; Sazanovich, I. V.; Towrie, M.; Gunnlaugsson, T.; Quinn, S. J.; Cardin, C. J.; Kelly, J. M. Enantiomeric Conformation Controls Rate and Yield of Photoinduced Electron Transfer in DNA Sensitized by Ru(II) Dipyridophenazine Complexes. *J. Phys. Chem. Lett.* **2015**, *6* (4), 734–738. https://doi.org/10.1021/jz502743q.

(39) Zhang, X.; Huang, Z.; Wu, S.; Lin, R.; Liu, J.; Su, N. Investigation of Antitumor Mechanism of the Chiral Ruthenium Complex Λ-[Ru(Phen) 2 p-MOPIP] 2+ in Human Gastric Cancer MGC-803 Cells. *Inorg. Chem. Commun.* **2016**, *72*, 1–6. https://doi.org/10.1016/j.inoche.2016.07.018.

(40) Sun, B.; Wang, Y.-C.; Qian, C.; Chu, J.; Liang, S.-M.; Chao, H.; Ji, L.-N. Synthesis, Characterization and DNA-Binding Studies of Chiral Ruthenium(II) Complexes with 2-(5-Nitrofuran-2-Yl)-1H-Imidazo[4,5-f][1,10]Phenanthroline. *J. Mol. Struct.* **2010**, *963* (2–3), 153–159. https://doi.org/10.1016/j.molstruc.2009.10.028.

(41) Shi, S.; Xu, J.-H.; Gao, X.; Huang, H.-L.; Yao, T.-M. Binding Behaviors for Different Types of DNA G-Quadruplexes: Enantiomers of [Ru(Bpy)$_2$(L)]$^{2+}$ (L=dppz, Dppz-Idzo). *Chem. - Eur. J.* **2015**, *21* (32), 11435–11445. https://doi.org/10.1002/chem.201501093.

(42) Shi, S.; Yao, T.-M.; Geng, X.-T.; Jiang, L.-F.; Liu, J.; Yang, Q.-Y.; Ji, L.-N. Synthesis, Characterization, and DNA-Binding of Chiral Complexes Δ- and Λ-[Ru(Bpy)$_2$(Pyip)]$^{2+}$. *Chirality* **2009**, *21* (2), 276–283. https://doi.org/10.1002/chir.20573.

(43) Peng, M.-N.; Zhu, Z.-Y.; Tan, L.-F. Binding Differences of Two Homochiral [Ru(Bpy)$_2$Dppz]$^{2+}$ Complexes with Poly(U)·poly(A)*poly(U) Triplex RNA. *Inorg. Chem.* **2017**, *56* (13), 7312–7315. https://doi.org/10.1021/acs.inorgchem.7b00670.

(44) Hall, J. P.; Cook, D.; Morte, S. R.; McIntyre, P.; Buchner, K.; Beer, H.; Cardin, D. J.; Brazier, J. A.; Winter, G.; Kelly, J. M.; Cardin, C. J. X-Ray Crystal Structure of *Rac*-[Ru(Phen)$_2$Dppz]$^{2+}$ with d(ATGCAT)$_2$ Shows Enantiomer Orientations and Water Ordering. *J. Am. Chem. Soc.* **2013**, *135* (34), 12652–12659. https://doi.org/10.1021/ja403590e.

(45) Hu, X.; Yang, D.; Yao, T.; Gao, R.; Wumaier, M.; Shi, S. Regulation of Multi-Factors (Tail/Loop/Link/Ions) for G-Quadruplex Enantioselectivity of Δ- and Λ- [Ru(Bpy)$_2$(Dppz-Idzo)]$^{2+}$. *Dalton Trans.* **2018**, *47* (15), 5422–5430. https://doi.org/10.1039/C8DT00501J.

CHAPTER 2. RU(II) PHENANTHROLINE-BASED OLIGOTHIENYL COMPLEXES AS PHOTOTHERAPY AGENTS

Houston D. Cole,[a] Abbas Vali,[a] John A. Roque III,[a,b] Ge Shi,[a] Gurleen Kaur,[a] Rachel O. Hodges,[b] Antonio Francés-Monerris,[c] Marta E. Alberto,[d*] Colin G. Cameron,[a*] Sherri A. McFarland[a*]

[a] *Department of Chemistry and Biochemistry, The University of Texas at Arlington, Arlington, Texas, 76019-0065 USA*

[b] *Department of Chemistry and Biochemistry, The University of North Carolina at Greensboro, Greensboro, North Carolina 27402 USA*

[c] *Institut de Ciència Molecular, Universitat de València, 46071 València, Spain*

[d] *Dipartimento di Chimica e Tecnologie Chimiche, Università della Calabria, Arcavacata di Rende, 87036 Italy*

**Corresponding authors:* C.G.C. <colin.cameron@uta.edu> ORCID 0000-0003-0978-0894, S.A.M. <sherri.mcfarland@uta.edu> ORCID 0000-0002-8028-5055

2.1 ABSTRACT

Ru(II) polypyridyl complexes have gained widespread attraction as photosensitizers for photodynamic therapy (PDT). Herein, we systematically investigate a series of the type $[Ru(phen)_2(IP\text{-}n\text{T})]^{2+}$, featuring 1,10-phenanthroline (phen) coligands and imidazo[4,5-*f*][1,10]phenanthroline ligands tethered to *n*= 0–4 thiophene rings (IP-*n*T). The complexes were characterized and investigated for their electrochemical, spectroscopic, and (photo)biological properties. The electrochemical oxidation of the *n*T unit shifted by -350 mV as *n*=1→4 (+920 mV for **Ru-1T**, +570 mV for **Ru-4T**); *n*T reductions were observed in complexes **Ru-3T** (−2530 mV) and **Ru-4T** (−2300 mV). Singlet oxygen quantum yields ranged from 0.53–0.88, with **Ru-3T** and **Ru-4T** being equally efficient (~0.88). The time-resolved absorption spectra of **Ru-0T–1T** were dominated by metal-to-ligand charge transfer (^{3}MLCT) states (τ_{TA}=0.40–0.85 μs), but long-lived intraligand charge transfer (^{3}ILCT) states were observed in **Ru-2T–4T** (τ_{TA}=25–148 μs). The 3ILCT energies of **Ru-3T** and **Ru-4T** were computed to be 1.6 eV and 1.4 eV, respectively. Phototherapeutic efficacy against melanoma cells (SK-MEL-28) under broad-band visible light (400–600 nm) increases as *n*=0→4: **Ru-0T** was inactive up to 300 μM, **Ru-1T–2T** were moderately active (EC_{50} ~600 nM, PI=200), and **Ru-3T** (EC_{50}=57 nM, PI=>1100) and **Ru-4T** (EC_{50}=740 pM, PI=114,000) were the most phototoxic. Activity diminishes with longer wavelengths of light and is completely suppressed for all complexes except **Ru-3T** and **Ru-4T** in hypoxia. **Ru-4T** is the more potent and robust PS in 1% O_2 over seven biological replicates (avg EC_{50}=1.3 μm, avg PI=985). **Ru-3T** exhibited hypoxic activity in five out of seven replicates, underscoring the need for biological replicates in compound evaluation. Singlet oxygen sensitization is likely responsible for phototoxic effects of the compounds in normoxia, but the presence of redox-active excited states may facilitate additional photoactive pathways for complexes with 3 or more thienyl groups. The ^{3}ILCT state with its extended lifetime (30–40x longer than the ^{3}MLCT state for **Ru-3T** and **Ru-4T**) implicates its predominant role in photocytotoxicity.

Keywords: Ruthenium polypyridyl complexes, photosensitizers, photobiology, photodynamic therapy, metal-to-ligand charge transfer (MLCT), intraligand charge-transfer (ILCT), ligand-to-ligand charge transfer (LLCT), melanoma, phenanthroline (phen), hypoxia

2.2 INTRODUCTION

Cancer remains the second most common cause of death globally, surpassed only by cardiovascular disease.[1] Despite significant advancements in treatment over the past few decades, particularly in the realms of immunotherapy[2–4] and targeted therapy,[5,6] there remains a pressing need for novel treatments and adjuvant therapies to complement surgery, radiation, and chemotherapy. In this regard, light-driven treatment modalities present a compelling alternative.

Photodynamic therapy (PDT) represents a unique and promising approach to targeted cancer treatment, which leverages a nontoxic photosensitizer (PS), benign light, and molecular oxygen to generate cytotoxic reactive oxygen species (ROS) for destroying tumors. PDT offers the advantage of localized intervention and minimal invasiveness, yielding fewer adverse effects and enhanced patient quality of life.[7,8]

PDT leverages two layers of precision: (1) the selective uptake and retention of PSs in malignant tissues and (2) the use of light to trigger toxicity. The result is that phototoxicity is confined to regions where the PS, light, and oxygen overlap spatiotemporally. The PDT effect can be maximized by optimization of the light regimen, including wavelength, fluence, irradiance, and dosimetry as well as the drug-to-light interval (DLI).

The intrinsic reliance of PDT on oxygen to generate ROS is problematic for treating hypoxic tumours. In addition, PDT can induce hypoxia as oxygen is consumed during irradiation.[9,10] Decreased generation of ROS limits the damage to cancerous cells. To address this, there is motivation to develop light-triggered compounds that exploit oxygen-independent mechanisms for phototoxicity.[11–59] In this context, metal complexes such as Ru(II) polypyridyl systems have attracted considerable attention.[7,11,13,60–73] Judicious choice of ligand-metal combinations provides access to access a variety of excited state configurations with characteristic photophysical properties and reactivities. Strategies have included photorelease of bulky ligands to reveal phototoxic metals and/or ligands,[11,15,21,22,63,74–77] photocaging of chemotherapeutics and enzyme inhibitors,[13,14,16,71,74,78–95] photoredox reactions,[96,97] and increasing ROS yields (to maintain $^1O_2$ generation at low oxygen tension).[23,24,63]

Our group has a longstanding interest in metal complexes as PSs, not just for alternate modes of action. Their modular architectures and straightforward assembly allow rapid tuning of physicochemical, photophysical, and biological properties, which facilitates our tumor-centered approach to PS design. Our guiding premise is that an ideal PS does not exist, and PS design and optimization should consider the specific application. Our TLD1433, a terthienyl-containing Ru(II) polypyridyl complex, is exemplary and is currently in Phase II clinical trials for treating non-muscle invasive bladder cancer (NMIBC) with PDT (Clinicaltrials.gov identifier NCT03945162).[7,98] It has a high quantum yield for $^1O_2$ generation and is phototoxic toward cancer cells with minimal dark toxicity. It is preferentially activated in the clinic with green light to avoid any damage to underlying muscle tissue.

To better understand the properties of oligothiophene-based metal complexes such as TLD1433, and to also develop additional PSs, we are exploring different metal ions, coligands, thienyl groups, counter ions, and coordination geometries.[7,15,23,24,63,76,99] The longer-term goal is to establish structure-activity relationships (SARs) for photoactive oligothiophene-containing metal complexes that consider their physicochemical, photophysical, electrochemical, and biological characteristics. We are motivated by the remarkable activities of some of these complexes containing longer thienyl chains. In this study, we describe a new family of Ru(II) PSs bearing two ancillary 1,10-phenanthroline (phen) ligands and an imidazo[4,5-*f*][1,10]phenanthroline (IP) ligand tethered to thienyl groups (*n*T) with *n*=0–4. The five members of the $[Ru(phen)_2(IP\text{-}n T)]^{2+}$ family and the reference compound $[Ru(phen)_3]^{2+}$ were investigated for their photocytotoxic effects toward melanoma cells using different wavelengths of light in normoxia and in hypoxia. Their lipophilicities, ground state absorption and emission properties, excited state configurations and lifetimes, and redox characteristics are systematically compared. The study provides a framework for understanding photophysical properties and biological activities, offering a robust platform to probe the fundamental dynamics that underpin PDT efficacy across a variety of oligothiophene-containing metal complexes with future biological studies. It also introduces two new hypoxia-active PSs that could be further developed.

2.3 MATERIALS AND METHODS

All complexes in this series were thoroughly characterized synthetically, spectroscopically, electrochemically, and (photo)biologically. Additional procedural details and characterization data may be found in the Supplementary Information.

2.3.1 Instrumentation.

Microwave reactions were performed in a CEM Discover microwave reactor. NMR spectra were collected using a JEOL ECA 500 NMR spectrometer (^{1}H) at UNCG's NMR facility or Agilent 700 MHz NMR spectrometer (^{1}H, ^{1}H–^{1}H COSY, ^{13}C–^{1}H HSQC, ^{13}C–^{1}H HMBC) at the Joint School of Nanoscience and Nanoengineering (JSNN). ESI mass spectra were obtained using a Thermo Fisher LTQ Orbitrap XL coupled to a Water's Acquity Ultra-high Performance Liquid Chromatography (UPLC) stack using a BEH

C18 column at UNCG's Triad Mass Spectrometry facility. HPLC analyses were carried out on an Agilent/Hewlett Packard 1100 series instrument (ChemStation Rev. A. 10.02 software) using a Hypersil GOLD C18 column (Thermo 25005-254630, guard 25003-014001) with an A–B gradient (40 min run; 2% → 95% B; A=0.1% formic acid in H_2O, B=0.1% formic acid in MeCN). Reported retention times are accurate to within ±0.1 min. Flash chromatography relied on the Teledyne Isco CombiFlash EZ Prep system with Silicycle SiliaSep silica flash cartridges (FLH-R10030B-ISO25).

2.3.2 Synthesis and Characterization

To the best of our knowledge, **Ru-0T**–**Ru-4T** have not been previously published. $[Ru(phen)_3](Cl)_2$ was synthesized using a modified literature procedure[100] that is described in detail below. Unless otherwise specified, all reagents and solvents were purchased from commercial sources and used without further purification. Water used for all biological experiments was deionized to a resistivity ≥ 18.2 MΩ using either a Barnstead or Milli-Q® filtration system. $Ru(phen)_2Cl_2 \cdot 2H_2O$[101] and IP-based ligands[102] were prepared according to adapted literature procedures. The synthesis of IP-based ligands follows that described below for IP-4T. [2,2′:5′,2″:5″,2‴-quaterthiophene]-5-carbaldehyde (4T-CHO) was prepared as previously described.[103,104] Final products are synthetically characterized in Figure S1–Figure S22 via ^1H NMR, ^1H–^1H COSY NMR, HPLC, and ESI$^+$–MS. **Ru-4T** required additional ^{13}C, ^{13}C–^1H HSQC, and ^{13}C–^1H HMBC NMR experiments for full assignment of the quaterthiophene-containing complex (Figure S9–Figure S10). The Cl^- salts of final complex products were obtained *via* anion metathesis on HCl-treated Amberlite IRA-410 resin with methanol as eluent and isolated in vacuo. Final complexes are a mixture of Δ/Λ isomers.

[Ru(phen)₃](Cl)₂. $Ru(Cl)_3 \cdot {\sim}3H_2O$ (58 mg, 0.20 mmol) and 1,10-phenanthroline (115 mg, 0.64 mmol) was added to a microwave vessel containing argon-purged ethylene glycol (3 mL), then the mixture was subjected to microwave irradiation at 180°C for 15 min with stirring. The resulting dark red solution was then transferred to a separatory funnel with deionized water (25 mL) and CH_2Cl_2 (25 mL). After gentle agitation, the CH_2Cl_2 was drained, and the remaining aqueous layer was washed with CH_2Cl_2 until the CH_2Cl_2 layer was colorless (3x 25 mL portions). Then, CH_2Cl_2 (25 mL) and saturated aqueous KPF_6 (5 mL) was added, and the mixture was shaken gently. The CH_2Cl_2 layer was drained, and the product was further extracted from the aqueous layer using CH_2Cl_2 until the aqueous layer was colorless (4x25 mL portions). The CH_2Cl_2 extracts were then combined and concentrated under reduced pressure. The product was then eluted from a silica gel flash column chromatography cartridge with a gradient of MeCN to 10% water in MeCN, followed by 7.5% water in MeCN with 0.5% KNO_3. The dark red, product-containing fractions, which eluted only in the presence of KNO_3, were then combined and concentrated

under vacuum, then transferred to a separatory funnel with CH_2Cl_2 (25 mL), deionized water (25 mL), and saturated aqueous KPF_6 (1 mL). The resulting mixture was gently agitated and the CH_2Cl_2 layer was drained. Additional CH_2Cl_2 (2x25 mL portions) was used to extract the remaining product until the aqueous layer was colorless. The CH_2Cl_2 layers were then combined and dried under vacuum to yield $[Ru(phen)_3](PF_6)_2$, which was then converted to the corresponding Cl^- salt in quantitative yield using Amberlite IRA-410 with MeOH as the eluent, then purified further using Sephadex LH-20 with MeOH as the eluent, affording product $[Ru(phen)_3](Cl)_2$ as a dark red solid (107 mg, 58%). ^{1}H NMR (700 MHz, MeOD-d_3, ppm): δ 8.67 (d, J = 8.1 Hz, 6H, *4*,*7*), 8.30 (s, 6H, *5*,*6*), 8.10 (d, J = 5.2 Hz, 6H, *2*,*9*), 7.70 (dd, J = 8.3, 5.2 Hz, 6H, *3*,*8*). HRMS (ESI+) *m*/*z* for $[M\text{-}2Cl^-]^{2+}$ calcd: 321.0547; Found: 321.0547. HPLC retention time 9.27 min (99.5% purity by peak area).

[Ru(phen)₂(IP)](Cl)₂ (**Ru-0T**). $Ru(phen)_2Cl_2{\cdot}2H_2O$ (57 mg, 0.1 mmol) and IP (22 mg, 0.1 mmol) were added to a microwave vessel containing argon-purged ethylene glycol (4 mL) and subjected to microwave irradiation at 180°C for 15 min. The resulting dark red mixture was then isolated and purified in the same manner as $[Ru(phen)_3](Cl)_2$, yielding the desired product **Ru-0T** as a dark red solid (48 mg, 64%). ^{1}H NMR (700 MHz, MeOD-d_3, ppm): δ 9.00 (broad s, 2H, *c*), 8.70 (d, J = 8.3 Hz, 4H. *4*,*7*), 8.67 (s, 1H, *d*), 8.33 (s, 4H, *5*,*6*), 8.16 (dd, J = 5.3, 1.3 Hz, 2H, *2*), 8.11 (dd, J = 5.2, 1.3 Hz, 2H, *9*), 8.07 (dd, J = 5.3, 1.3 Hz, 2H, *a*), 7.77 (dd, J = 8.3, 5.3 Hz, 2H, *b*), 7.72 (m, 4H, *8*,*3*). HRMS (ESI+) *m*/*z* for $[M\text{-}2Cl^-]^{2+}$ calcd: 341.0578; Found: 341.0582. $[M\text{-}2Cl^-\text{-}H]^+$ calcd: 681.1084; Found: 681.1110. HPLC retention time: 9.07 min (98% purity by peak area).

[Ru(phen)₂(IP-1T)](Cl)₂ (**Ru-1T**). $Ru(phen)_2Cl_2{\cdot}2H_2O$ (57 mg, 0.1 mmol) and IP-1T (30 mg, 0.1 mmol) were added to a microwave vessel containing argon-purged ethylene glycol (4 mL) and subjected to microwave irradiation at 180°C for 15 min. The resulting dark red mixture was then isolated and purified in the same manner as compound $[Ru(phen)_3](Cl)_2$, yielding the desired product **Ru-1T** as a dark red solid (49 mg, 59%). ^{1}H NMR (700 MHz, MeOD-d_3, ppm): δ 9.09 (broad s, 2H, *c*), 8.70 (dd, J = 8.4, 1.4 Hz, 4H, *4*,*7*), 8.33 (s, 4H, *5*,*6*), 8.18 (dd, J = 5.3, 1.3 Hz, 2H, *2*), 8.12 (dd, J = 5.2, 1.3 Hz, 2H, *9*), 8.05 (dd, J = 5.2, 1.3 Hz, 2H, *a*), 8.01 (dd, J = 3.7, 1.2 Hz, 1H, *d*), 7.76 (dd, J = 8.3, 5.3 Hz, 2H, *b*), 7.75 – 7.72 (m, 5H, *f*,*3*,*8*), 7.30 (dd, J = 5.1, 3.7 Hz, 1H, *e*). HRMS (ESI+) *m*/*z* for $[M\text{-}2Cl^-]^{2+}$ calcd: 382.0517; Found: 382.0523. $[M\text{-}2Cl^-\text{-}H]^+$ calcd: 763.0961; Found: 763.0974. HPLC retention time 10.62 min (99.5% purity by peak area).

[Ru(phen)₂(IP-2T)](Cl)₂ (**Ru-2T**). $Ru(phen)_2Cl_2{\cdot}2H_2O$ (57 mg, 0.1 mmol) and IP-2T (38 mg, 0.1 mmol) were added to a microwave vessel containing argon-purged ethylene glycol (4 mL) and subjected to

microwave irradiation at 180°C for 15 min. The resulting dark red mixture was then isolated and purified in the same manner as compound [Ru(phen)$_3$](Cl)$_2$, yielding the desired product **Ru-2T** as a dark red solid (58 mg, 39%). ^{1}H NMR (700 MHz, MeOD-*d$_3$*, ppm): δ 9.03 (broad s, 2H, *c*), 8.71 (d, *J* = 8.30, 4H, *4*,*7*), 8.34 (s, 4H, *5*,*6*), 8.21 (dd, *J* = 5.4, 1.3 Hz, 2H, *2*), 8.12 (dd, *J* = 5.2, 1.3 Hz, 2H, *9*), 8.05 (dd, *J* = 5.3, 1.3 Hz, 2H, *a*), 7.92 (d, *J* = 3.9 Hz, 1H, *d*), 7.78 – 7.71 (m, 6H, *b*,*3*,*8*), 7.44 (dd, *J* = 5.1, 1.2 Hz, 1H, *f*), 7.36 (d, *J* = 3.9 Hz, 1H, *e*), 7.33 (d, *J* = 3.5 Hz, 1H, *h*), 7.09 (dd, *J* = 5.1, 3.6 Hz, 1H, *g*). HRMS (ESI+) *m*/*z* for [M-2Cl$^-$]$^{2+}$ calcd: 423.0455; Found: 423.0458. [M-2Cl$^-$-H]$^+$ calcd: 845.0838; Found: 845.0852. HPLC retention time 21.19 min (99.5% purity by peak area).

[Ru(phen)$_2$(IP-3T)](Cl)$_2$ (**Ru-3T**). Ru(phen)$_2$Cl$_2$·2H$_2$O (114 mg, 0.2 mmol) and IP-3T (76 mg, 0.164 mmol) were added to a microwave vessel containing argon-purged ethylene glycol (4 mL) and subjected to microwave irradiation at 180°C for 15 min. The resulting dark red mixture was then isolated and purified in the same manner as [Ru(phen)$_3$](Cl)$_2$, yielding the desired product **Ru-3T** as a dark red solid (59 mg, 59%). ^{1}H NMR (700 MHz, MeOD-*d$_3$*, ppm): δ 9.03 (d, *J* = 8.2 Hz, 2H, *c*), 8.70 (d, *J* = 8.9 Hz, 2H, *4*), 8.68 (d, *J* = 8.4 Hz, 2H, *7*), 8.34 (s, 4H, *5*,*6*), 8.22 (d, *J* = 5.6 Hz, 2H, *2*), 8.12 (dd, *J* = 5.2, 1.3 Hz, 2H, *9*), 8.04 (d, *J* = 5.6 Hz, 2H, *a*), 7.90 (d, *J* = 3.9 Hz, 1H, *d*), 7.77 (dd, *J* = 8.2, 5.4 Hz, 2H, *3*, 7.72 (dd, *J* = 8.53 Hz, 5.33 Hz, 2H, *8*), 7.70 (dd, *J* = 8.20 Hz, 5.38 Hz, 2H, *b*), 7.35 (d, *J* = 5.4 Hz, 1H, *h*), 7.27 (d, *J* = 3.8 Hz, 1H, *e*), 7.22 (d, *J* = 3.5 Hz, 1H, *j*), 7.19 (d, *J* = 3.8 Hz, 1H, *g*), 7.11 (d, *J* = 3.7 Hz, 1H, *f*), 7.05 (dd, *J* = 5.1, 3.6 Hz, 1H, *i*). HRMS (ESI+) *m*/*z* for [M-2Cl$^-$]$^{2+}$ calcd: 464.0394; Found: 464.0405. [M-2Cl$^-$-H]$^+$ calcd: 927.0715; Found: 927.0769. HPLC retention time 22.75 min (96% purity by peak area).

[Ru(phen)$_2$(IP-4T)](Cl)$_2$ (**Ru-4T**). Ru(phen)$_2$Cl$_2$·2H$_2$O (114 mg, 0.2 mmol) and IP-4T (90 mg, 0.164 mmol) were added to a microwave vessel containing argon-purged ethylene glycol (4 mL) and subjected to microwave irradiation at 180°C for 15 min. The resulting dark red mixture was then isolated and purified in the same manner as compound [Ru(phen)$_3$](Cl)$_2$, yielding the desired product **Ru-4T** as a dark red solid (49 mg, 28%). ^{1}H NMR (700 MHz, MeOD-*d$_3$*, ppm): δ 9.04 (s, 2H, *c*), 8.72 (d, *J* = 8.77 Hz, 2H, *4*), 8.70 (d, *J* = 8.89 Hz, 2H, *7*), 8.34 (s, 4H, *5*,*6*), 8.22 (dd, *J* = 5.4, 1.3 Hz, 2H, *2*), 8.12 (dd, *J* = 5.2, 1.3 Hz, 2H, *9*), 8.05 (dd, *J* = 5.2, 1.3 Hz, 2H, *a*), 7.89 (d, *J* = 3.9 Hz, 1zH, *d*), 7.77 (dd, *J* = 8.2, 5.4 Hz, 2H, *3*), 7.75 – 7.70 (m, 4H, *8*,*b*), 7.33 (d, *J* = 3.9 Hz, 1H, *e*), 7.29 (dd, *J* = 5.1, 1.2 Hz, 1H, *l*), 7.24 (d, *J* = 3.7 Hz, 1H, *f*), 7.17 (dd, *J* = 3.6, 1.3 Hz, 1H, *j*), 7.12 (d, *J* = 3.8 Hz, 1H, *h*), 7.09 (d, *J* = 3.7 Hz, 1H, *g*), 7.04 (d, *J* = 3.7 Hz, 1H, *i*), 7.00 (dd, *J* = 5.1, 3.5 Hz, 1H, *k*). ^{13}C NMR (700 MHz, MeOD-*d$_3$*, ppm): δ 153.96 (2), 153.77 (9), 151.57 (a), 150.08 (10), 149.29 (21), 149.19 (20), 147.36 (22), 141.46 (12), 138.31 (4,7,14), 138.14 (16), 137.78 (17), 136.36 (15), 136.24 (13), 132.57 (18), 132.54 (19), 131.89 (c, 11), 129.65 (d), 129.49 (6), 129.48 (5), 129.11 (k), 127.40 (8), 127.37 (3), 127.13 (b), 126.82 (f), 126.05 (l), 126.01 (h),

125.85 (e), 125.71 (g), 125.51 (i), 125.08 (j). HRMS (ESI+) *m*/*z* for $[M\text{-}2Cl^-]^{2+}$ calcd: 505.0333; Found: 505.0312. $[M\text{-}2Cl^-\text{-}H]^+$ calcd: 1009.0593; Found: 1009.0663. HPLC retention time 23.92 min (99.5% purity by peak area).

2.3.3 Computational Details

The computational protocol used to investigate the Ru(II)-complexes herein presented is based on a combination of DFT and TDDFT[105] as methods as implemented in the Gaussian16[106] code and widely tested in previous studies involving metallic photosensitizers for PDT[107–114] and successfully adopted for our related Os(II)- and Ru-compounds.[23,24,63]

The PBE0 exchange-correlation functional (XC)[115] in conjunction with the 6-31+G(d,p) basis set was chosen for the singlet ground and lowest triplet excited states optimizations in water adopting the quasi-relativistic Stuttgart-Dresden pseudopotential to treat the Ru(II) center.[116] The integral equation formalism polarizable continuum model[117,118] (IEFPCM) was used to simulate the water solvent environment by using a dielectric constant equal to $\varepsilon=80$ by means of the polarizable conductor model (PCM).[119]

The M06 exchange-correlation (XC)-functional and the Tamm-Dancoff approximation (TDA)[120] were used to compute the UV-Vis absorption spectra in water on top of the corresponding S_0 equilibrium geometries. We recently adopted this method for optimizing the lowest triplet metal-to-ligand charge transfer (^{3}MLCT) and ligand-based mixed triplet intraligand charge transfer (^{3}ILCT) / ligand-to-ligand charge transfer (^{3}LLCT) excited states and computing the emission energies.[63] The TDA circumvents the general underestimation of the triplet state energies from the conventional TDDFT approach,[121] as was also observed in our earlier investigations on other oligothiophene-based Ru(II) and Os(II) complexes for which the vertical lowest triplet excited states were underestimated.[23,24,110] The nature of the excited states was determined in all cases by computing the corresponding natural transition orbitals (NTOs) with the Chemissian 4.67 software,[122] and through Gaussian output post-processing conducted with the TheoDORE 3.1.1 program.[123]

2.3.4 Electrochemistry

Voltammetry was performed in dimethylformamide (DMF, Fisher HPLC grade) that had been dried and deoxygenated with an Inert PureSolv MD7 solvent purification system, with 100 mM tetrabutylammonium hexafluorophosphate ($TBAPF_6$) (Fisher) as the supporting electrolyte, in a two-compartment low volume cell with the three-electrode configuration under argon. A 3 mm glassy carbon disc was used as the working electrode with a platinum wire counter electrode and a Ag/AgCl/4M KCl reference electrode.

Ferrocene (Fc) was used as an internal standard. The complex solutions were approximately 4 mM for oxidation sweeps and 0.25 mM for reduction sweeps.

Measurements were conducted at room temperature using a WaveNow potentiostat (Pine Research Company) with Aftermath software. Cyclic differential-pulse voltammetry (CDPV) measurements used a sweep rate of 2 $mV \cdot s^{-1}$ with a modulation amplitude varying from 12.5 to 100 mV. For reversible processes, the formal redox potential $E°'$ was taken as the average of E_{pa} (anodic peak potential) and E_{pc} (cathodic peak potential). For quasi-reversible processes, only E_{pa} or E_{pc} is reported.

2.4 RESULTS AND DISCUSSION

2.4.1 Synthesis and Characterization

$[Ru(phen)_3](Cl)_2$ and **Ru-*n*T** were synthesized using our previously published method for related Ru(II) phenanthroline-based complexes.[63] The complexes were isolated as PF_6^- salts and purified using flash chromatography on silica. The PF_6^- salts were then converted to their corresponding Cl^- salts in quantitative yields via anion metathesis with Amberlite IRA-410 and further purified using size-exclusion chromatography on Sephadex LH-20. The final yields were ~60% for $[Ru(phen)_3](Cl)_2$, **Ru-0T**, **Ru-1T**, and **Ru-3T**, ~40% for **Ru-2T**, and ~30% for **Ru-4T**. The complexes were characterized by 1D and 2D ^1H NMR spectroscopy (Figure 1, Figure S1–Figure S10), with assignment of signals for $[Ru(phen)_3](Cl)_2$ and **Ru-0T–Ru-3T** made using ^1H–^1H COSY NMR. **Ru-4T** was additionally analysed by ^1H–^{13}C HSQC and

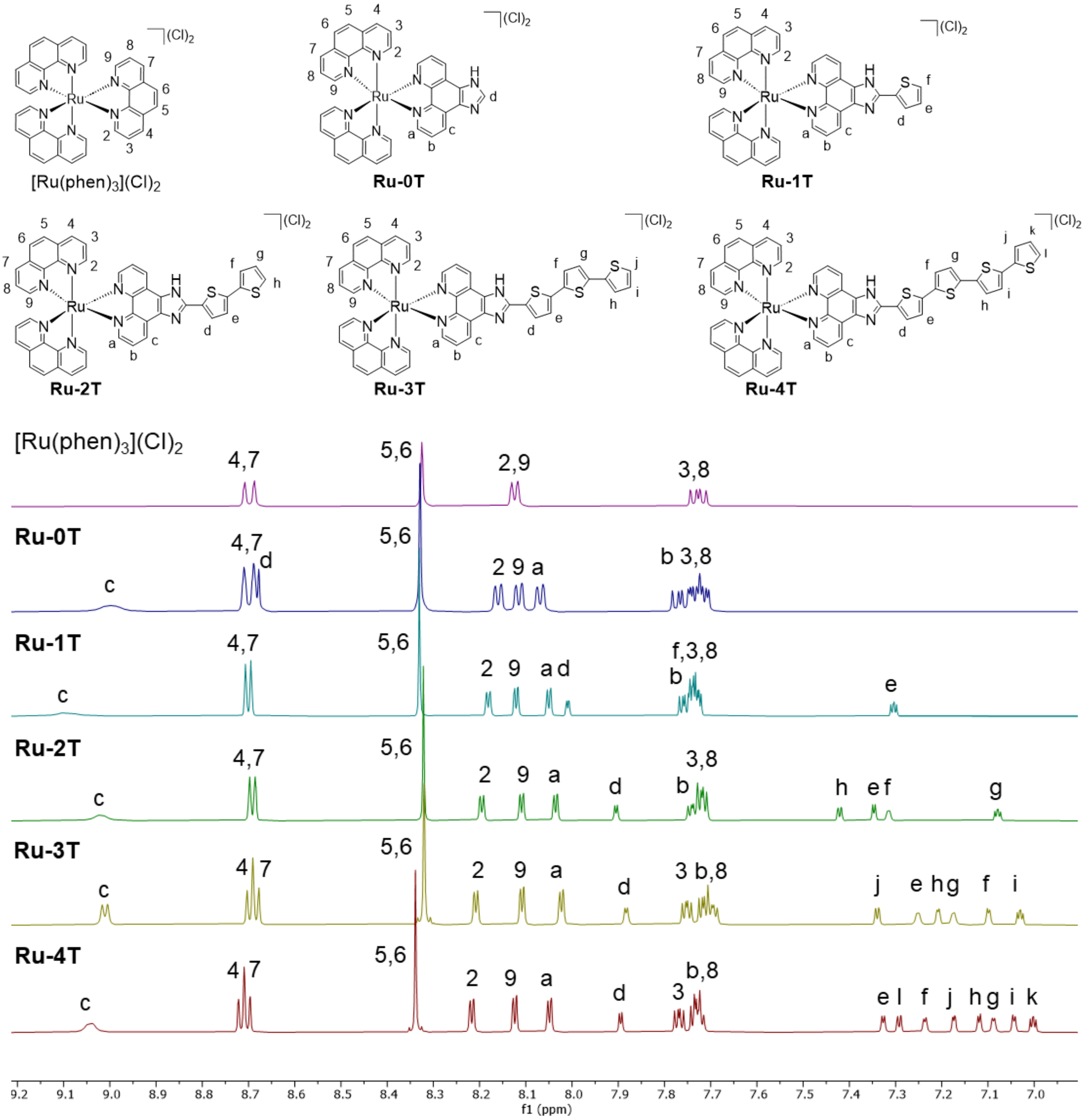

Figure 1. Aromatic region of the ^1H NMR spectra for [Ru(phen)$_3$](Cl)$_2$ and **Ru-nT** (*n*=0−4) in MeOD-d$_3$ (Cl$^−$ salts; 298 K). All spectra were collected at 500 MHz, except for **Ru-4T**, which was collected at 700 MHz.

^1H–^{13}C HMBC NMR to assign the hydrogens of the quaterthiophene unit. The assignments were consistent with our related, previously reported compounds.[23,63,76] The complexes were also characterized by high-resolution ESI+ mass spectrometry (Figure S11–Figure S16). HPLC analyses indicated that the complexes were ≥95% pure by integration (Figure S17–Figure S22).

The lipophilicities of $[Ru(phen)_3](Cl)_2$ and **Ru-*n*T** as their chloride salts were evaluated experimentally by calculating their log $D_{o/w}$ values from partitioning between 10 mM phosphate buffer solution (pH 7.4) and 1-octanol (99.9%) (Figure 2 and Table S1). A negative log $D_{o/w}$ value indicates hydrophilicity whereas a positive log $D_{o/w}$ value indicates higher lipophilicity.[124] $[Ru(phen)_3](Cl)_2$ and **Ru-*n*T** up to *n*=2 were relatively hydrophilic overall, with log $D_{o/w}$ values becoming increasingly more positive with additional thiophene rings. An abrupt change in aqueous solubility occurred at *n*=3, with **Ru-3T** showing a clear preference for 1-octanol. **Ru-4T** also preferred 1-octanol, but its log $D_{o/w}$ could not be determined due to precipitation between the two layers that left no measurable amount of compound in the aqueous phase. Precipitation at the octanol-buffer interface was also observed for the analogous Os(II) complex that self-associates in PBS to form particles of up to 1–2 µm in diameter.[23] This is not uncommon for Ru(II) and Os(II) complexes containing the IP-4T ligand.

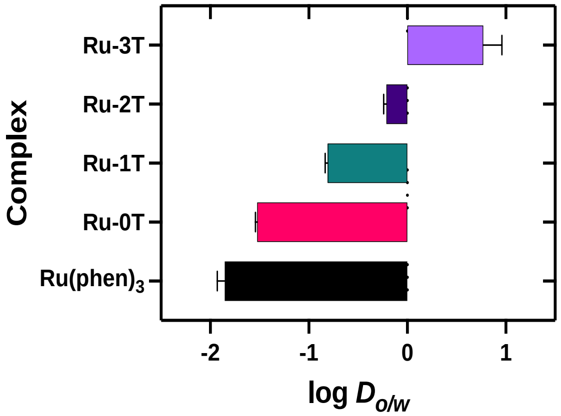

Figure 2. Lipophilicities of $[Ru(phen)_3](Cl)_2$ and **Ru-*n*T** (*n*=0–3) in 1-octanol and phosphate buffer using the shake-flask method. The log $D_{o/w}$ value for **Ru-4T** was undefined due to precipitation at the octanol:phosphate buffer interface that left no measurable amount of **Ru-4T** in the phosphate buffer phase.

2.4.2 Computation

<u>*Singlet states.*</u> Figure 3 shows the optimized singlet ground state structures of $[Ru(phen)_3]^{2+}$ and **Ru-*n*T** (n=0–4) in water at the DFT/PBE0 level of theory, and the main geometric parameters are reported in Table S2 The central Ru(II) ion adopts an octahedral geometry with similar Ru-N bond distances across the series, with the first thiophene ring being coplanar with the coordinated IP ligand. Each subsequent ring introduces more conformational flexibility, with the fourth thienyl ring of **Ru-4T** being twisted out of

plane by approximately 18°. The *n*T chain length has a major impact on the frontier orbitals. Similar to structurally related families we have reported,[23,24,63] complexes with *n*≥2 have progressively higher-energy HOMOs that give rise to a systematic reduction of the H-L gaps as the % *n*T contribution increases (Figure 4 and Figure S23, Table S3. The HOMO for **Ru-2T** extends over both the IP and *n*T unit, whereas the HOMOs are localized primarily to the *n*T chain for **Ru-3T** and **Ru-4T**, where the *n*T contribution to the HOMO is about 46% and 61%, respectively. In contrast, the LUMOs across the series are primarily phen-based (>95% for all complexes) and not affected significantly by *n*T.

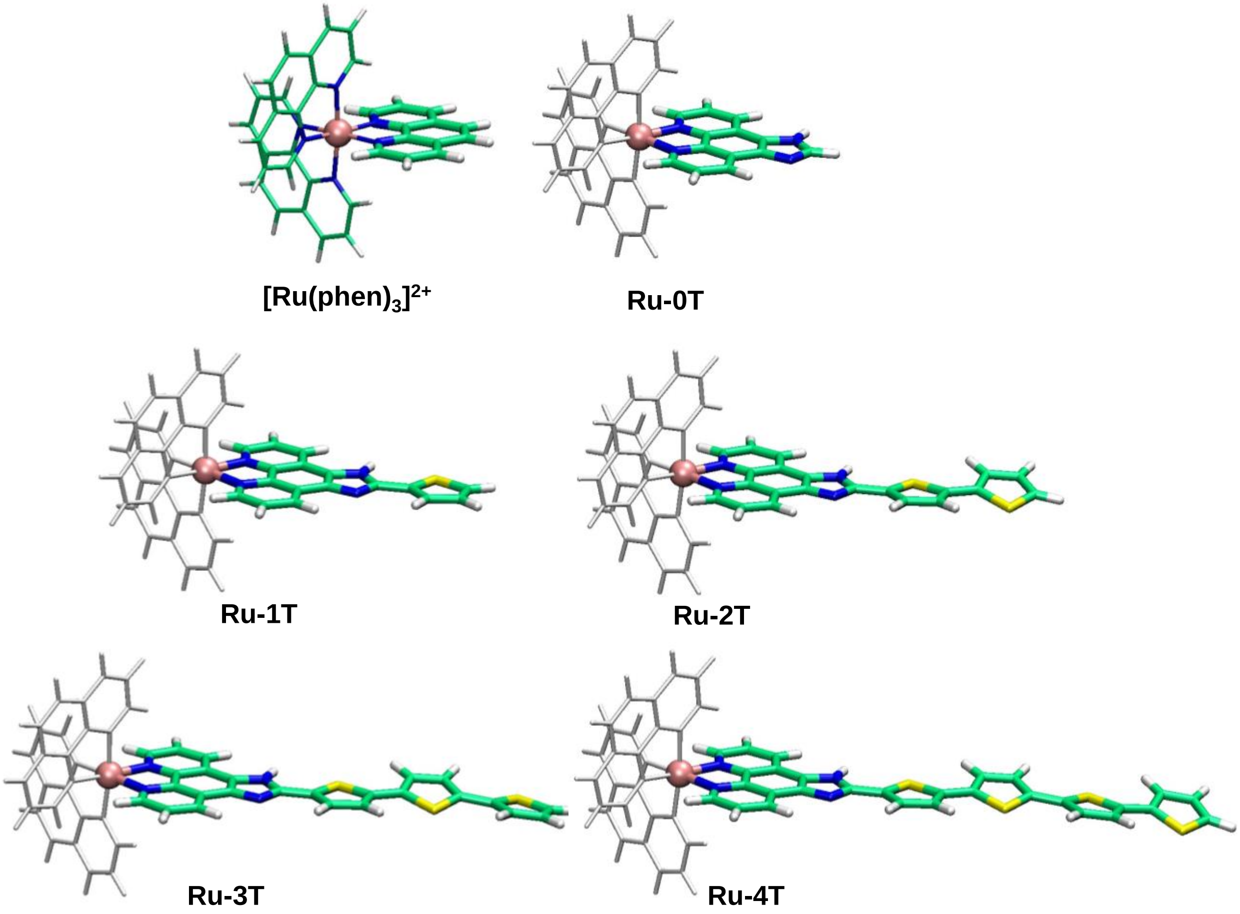

$[Ru(phen)_3]^{2+}$
Ru-0T
Ru-1T
Ru-2T
Ru-3T
Ru-4T

Figure 3. Optimized geometries of $[Ru(phen)_3]^{2+}$ and **Ru-*n*T** (***n***=0-4) in a water environment at the PBE0/6-31+G(d,p)/SDD/ level of theory. The two phen ligands are shown in grey for the Ru IP-*n*T complexes for clarity.

The computed lowest-energy, spin-allowed singlet-singlet absorption transitions shift to longer wavelengths with increasing *n* (Figure 5). The NTOs are predominantly ^{1}MLCT (Ru phen/IP) for

$[Ru(phen)_3]^{2+}$, **Ru-0T** and **Ru-1T**. Their computed transitions are similar near 432–438 nm and slightly higher in energy than the experimental bands (vide infra). The lowest energy transitions for **Ru-2T**, **Ru-3T**, and **Ru-4T** are red-shifted with *n*, in agreement with experimental spectra. The lowest energy absorption was computed at 455 nm and was mixed ^{1}MLCT/^{1}LLCT character for **Ru-2T**. In the case of **Ru-3T** and **Ru-4T**, the lowest energy transitions were ^{1}ILCT/^{1}IL/^{1}LLCT character (mostly localized to the IP-*n*T ligand) and computed at 466 nm and 488 nm, respectively. **Ru-4T** has twice as much ^{1}ILCT/^{1}IL character compared to **Ru-3T**. Here, LLCT mainly refers to CT between *n*T and IP (but does include very minor involvement of the phen coligands); ILCT involves CT within *n*T; IL is ππ* localized to *n*T or IP. Further details are summarized in Table S4 and Figure S24.

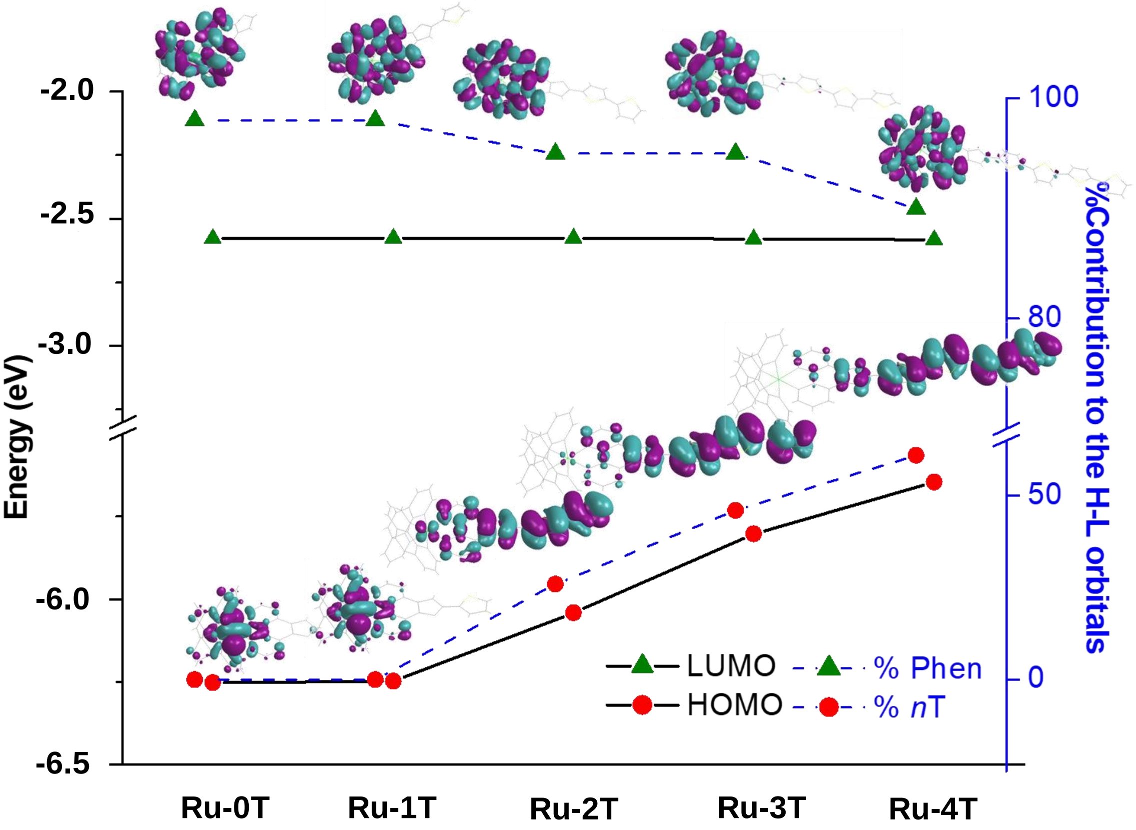

Figure 4. Computed HOMO and LUMO orbital energies (solid black lines) and percent contribution of the *n*T chain to the HOMO (dashed line, red filled circles) and of the phen coligands to the LUMO (dashed line, green filled triangles), for **Ru-*n*T** (*n*=0-4) in the singlet ground state, at the M06/6-31+G(d,p)/SDD level of theory, in water. Images of Ru(II)-based HOMOs for **Ru-0T** and **Ru-1T**, the *n*T-based HOMOs for *n*=2-4, and the phen-based LUMOs for all compounds, obtained at the same level of theory. Additional details can be found in Figure S23.

__Triplet states.__ The optimized structures of the lowest excited triplet states (T_1) for the **Ru-*n*T** family involve a fully planar arrangement of the *n*T chain that maximizes the π-conjugation, with successive *n*T groups antiplanar to one another. The geometrical parameters of the T_1 states for $[Ru(phen)_3]^{2+}$ and **Ru-*n*T** (*n*=0–4) are listed in Table S2 alongside the data for S_0, and the optimized T_1 state structures are shown in Figure S25. The lowest-energy triplet excited state configurations of this series are either ^{3}MLCT for complexes without thiophenes (or only one thiophene as in the case of **Ru-1T**) or mixed ^{3}ILCT/^{3}LLCT states for complexes with two or more thiophenes. The lowest-energy ^{3}MLCT states lie near 2.2 eV for all complexes in the series regardless of the thiophene chain length and whether the ^{3}MLCT state is T_1. The energies of the mixed ^{3}ILCT/^{3}LLCT states depend on *n* and decrease systematically in energy from 1.82 eV for **Ru-2T** to 1.44 eV for **Ru-4T**. The triplet metal-centered (^{3}MC) and intraligand (^{3}IL) excited states localized to the phen/IP coligands are much higher in energy and contribute very little to the computed NTOs for T_1. The energies and configurations of the computed triplet states are presented in Figure 6 and complied in Table 1 and Table S5. The occupied and virtual NTOs are plotted in Figure S26.

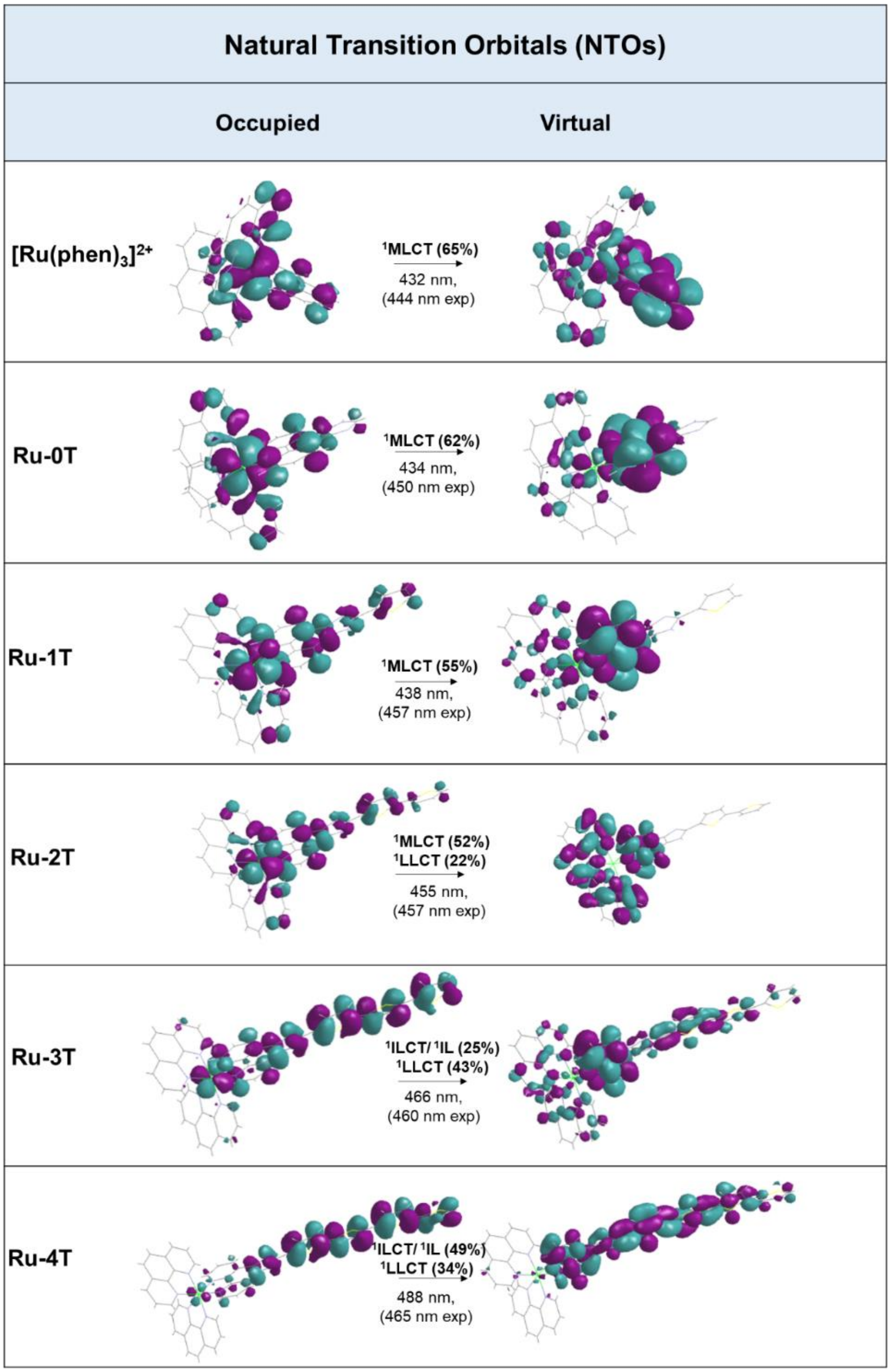

Figure 5. Occupied and Virtual NTOs of the computed lowest-energy singlet-singlet transitions in water (λ) with the predominant character indicated. The experimental longest wavelength absorption maxima (λ_{exp}) are reported in parentheses. Additional NTOs are reported in Figure S24.

Although the T_1 triplet state undergoes a significant drop in energy with increasing *n*, all are still sufficiently energetic to sensitize $^1O_2$.[125,126] Mulliken spin densities (MSD) close to 1 on the Ru(II) center further support that T_1 is predominantly ^{3}MLCT for $[Ru(phen)_3]^{2+}$, **Ru-0T**, and **Ru-1T**. The MSD values of 0 on the Ru(II) center for complexes with $n \geq 2$ indicate that the metal is not involved in T_1. The predominant character of T_1 for **Ru-2T** is mixed ^{3}ILCT/^{3}LLCT, where ^{3}ILCT involves CT within the *n*T unit (*n*T˳ *n*T) and ^{3}LLCT involves CT between *n*T and IP (*n*T˳ IP), and each contributes equally (å40%) to the transition according to the topology analysis (Figure 6b). For **Ru-3T** and **Ru-4T,** T_1 is >50% ^{3}ILCT. The drop in T_1 energy on going from *n*=2 to 4 is accompanied by diminishing ^{3}LLCT character (from ~40% down to ~20%). Such behavior is in agreement with the related Ru(II) and Os(II) families we reported previously,[23,24,63] where T_1 involves the IP-*n*T ligand for *n*=2–4 and is increasingly more localized to the *n*T portion with increasing *n*. The higher-lying ^{3}MLCT state (T_2) for these complexes is similar in energy (~2.2 eV) to those with *n*<2 having ^{3}MLCT states as T_1.

Table 1. Computed T_1 adiabatic energies, configurations, and Mulliken spin densities (MSD) on the Ru(II) metal center for $[Ru(phen)_3]^{2+}$ and **Ru-*n*T** (*n* = 0–4). A single configuration is listed if that character was >50%.

	T_1 energy (eV)	Configuration	MSD
$[Ru(phen)_3]^{2+}$	2.21	^{3}MLCT	0.86
Ru-0T	2.18	^{3}MLCT	0.86
Ru-1T	2.18	^{3}MLCT	0.91
Ru-2T	1.82	^{3}ILCT/^{3}LLCT	0
Ru-3T	1.57	^{3}ILCT	0
Ru-4T	1.44	^{3}ILCT	0

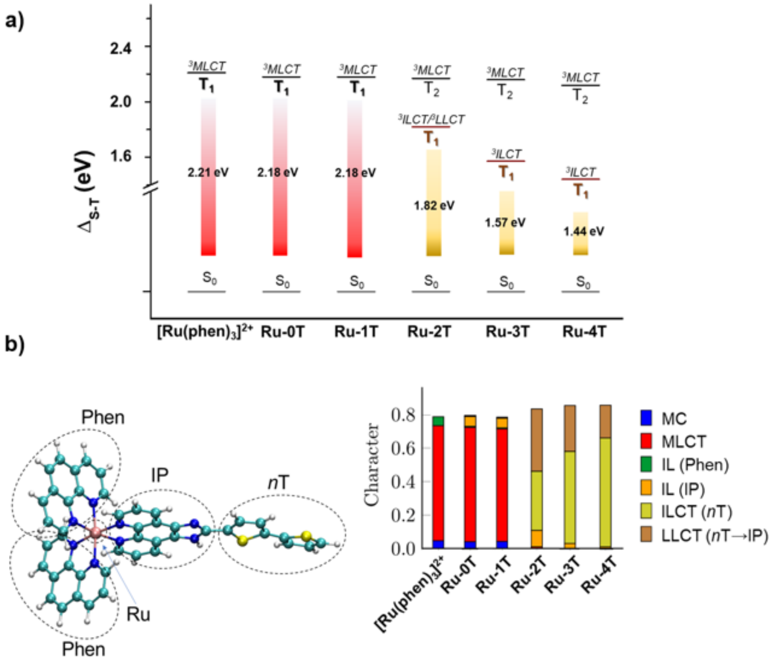

Figure 6. (a) Computed T_1 adiabatic energies for $[Ru(phen)_3]^{2+}$ and **Ru-*n*T**. (b) Molecular fragments (left) defined to quantify the molecular topology of the T_1 excited states and their configurations (right). The NTOs are reported in Figure S26 and triplet excited state energies in Table S5.

2.4.3 Spectroscopy

UV-Vis absorption and emission spectroscopy

The electronic absorption spectra of the series collected on the hexafluorophosphate salts in MeCN are shown in Figure 7, and the corresponding molar extinction coefficients are listed in Table 2. $[Ru(phen)_3]^{2+}$ has been previously reported, and our data are in agreement with published values.[127] The spectra can be generalized by two distinct regions. The sharper peaks below 300 nm, with maxima around 223 and 263 nm, are similar across the series and can be ascribed to π→π* transitions involving the phen coligands and possibly the phen portion of the IP/IP-*n*T ligands that are proximal to the metal center. These peaks occur at the same energy in related complexes[23] and are not significantly affected by the length of the pendant *n*T chain.

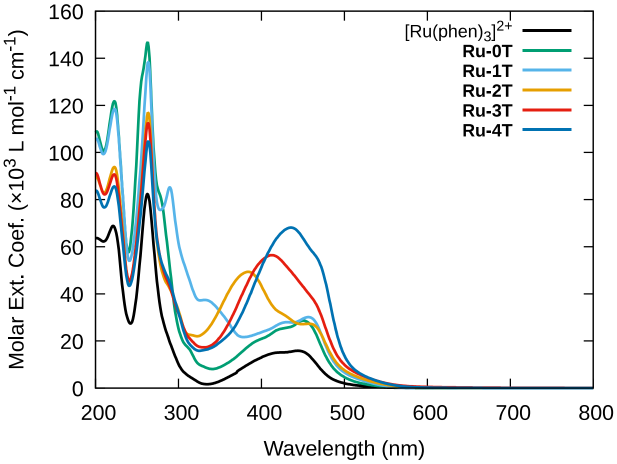

Figure 7: UV-vis spectra of [Ru(phen)$_3$]$^{2+}$ and the **Ru-*n*T** series as PF_6^- salts in MeCN.

At wavelengths between 300 to 500 nm, the absorption spectra for [Ru(phen)$_3$]$^{2+}$ and **Ru-0T** are similar and typical of Ru(II) polypyridyl type complexes with Ru^{2+}(dπ)→LL(π*) MLCT transitions involving phen or phen/IP, respectively, as the π* acceptor orbitals. The complexes with IP-*n*T ligands have additional contributions from ^{1}LLCT (*n*TŸ IP) transitions as well as ^{1}ILCT (*n*TŸ *n*T) for **Ru-2T** to **Ru-4T**. These isolated transitions can be seen in the absorption spectra of the analogous uncomplexed IP-*n*T ligands and free oligothiophenes[128] but do experience some shifting when incorporated into the metal complexes. Our computational studies considering the occupied and virtual NTOs of the **Ru-*n*T** complexes highlight the predominant configurations of the computed absorption transitions occurring >400 nm and support these ligand-based contributions. The lowest energy singlet-singlet transitions were computed to be mixed ^{1}MLCT/^{1}LLCT for **Ru-2T** and ^{1}ILCT/^{1}LLCT for **Ru-3T** and **Ru-4T** (Figure 5 and Figure S24, Table S4). These computed and experimental energies were lowest for **Ru-4T,** as expected for the more extended π system, and the ^{1}ILCT character was almost two-fold higher (Figure 5).

Table 2: Molar Extinction Coefficients at Various Absorption Peak Maxima for the **Ru-*n*T** series.

Compound	λ_{abs} (nm) (log (ε / M^{-1} cm^{-1}))
[Ru(phen)$_3$]$^{2+}$	444 (4.20), 263 (4.91), 221 (4.84)
Ru-0T	450 (4.46), 263 (5.17), 223 (5.09)
Ru-1T	457 (4.49), 332 (4.56), 289 (4.95), 264 (5.15), 223 (5.08)
Ru-2T	457 (4.44), 384 (4.69), 263 (5.08), 223 (4.97)
Ru-3T	460 (4.57), 413 (4.75), 263 (5.05), 222 (4.94)
Ru-4T	465 (4.75), 436 (4.84), 264 (5.03), 223 (4.93)

All of the complexes in the series exhibited red emission near 610–620 nm as a single, broad and featureless band in argon-sparged MeCN at room temperature (Figure 8, Table 3 and S5). The number of appended thiophene rings did not affect the emission energies, suggesting that the luminescence originates from a common ^{3}MLCT state with similar ligand acceptor orbitals across the series. The computed adiabatic ^{3}MLCT energies matched the experimental room temperature ^{3}MLCT emission energies at around 2.2 eV. For complexes lacking thienyl groups and **Ru-1T**, this ^{3}MLCT state was computed as the lowest-energy triplet state (T_1). For **Ru-2T** to **Ru-4T**, the emissive ^{3}MLCT state was T_2.

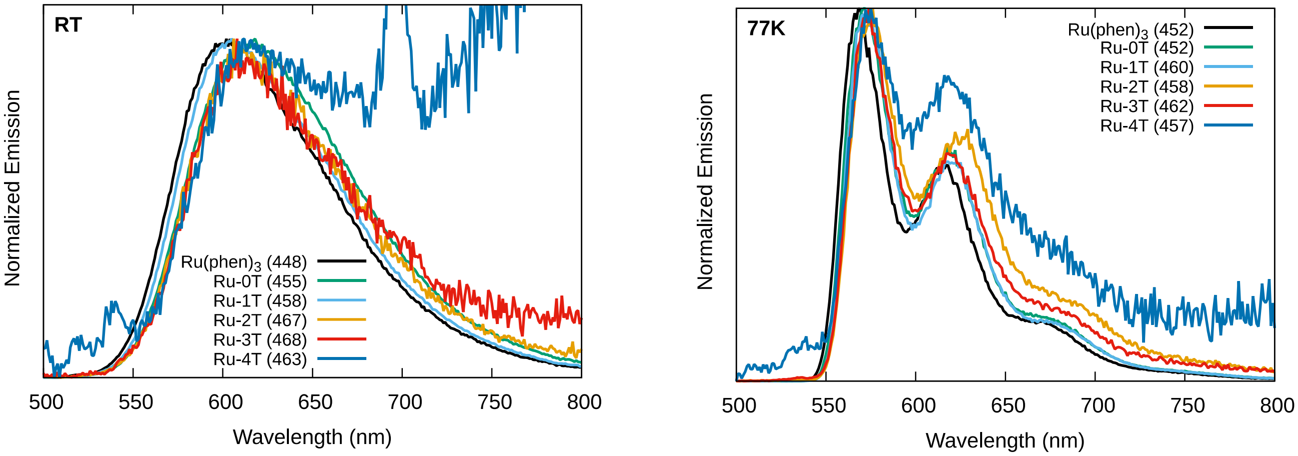

Figure 8: Normalized emission spectra of $[Ru(phen)_3]^{2+}$ and the **Ru-*n*T** series as PF_6^- salts at room temperature (left) and at 77 K (right) in MeCN. The room temperature spectra used argon-sparged MeCN and the 77 K spectra used a 4:1 EtOH:MeOH glass. The excitation wavelengths are noted in parentheses. Emission from **Ru-4T** was weak and superimposed on scatter in the room temperature measurement (blue curves).

The room temperature emission for $[Ru(phen)_3]^{2+}$ was in agreement with that previously reported,[129,130] with a quantum yield near 3% and lifetime of approximately 0.5 µs at room temperature. The rest of the complexes in the series also had emission lifetimes between 0.5 and ~1 µs (Table 3 and Figure S27), but quantum yields dropped progressively on going from **Ru-0T** to **Ru-4T**. For complexes with up to two thiophene rings, quantum yields were still between 3 and 8.5%. However, emission from complexes with longer thiophene chains was considerably weaker, falling to about 0.4% for **Ru-3T** and only 0.02% for **Ru-4T**. The spectra in Figure 8 are normalized to emphasize similar ^{3}MLCT emission energies, but the much lower quantum yields for **Ru-3T** and **Ru-4T** are reflected in the poorer signal-to-noise ratios evident in the spectra. The emission from **Ru-4T** is extremely weak and should be regarded as almost non-emissive with an extremely high error on the quantum yield as a result.

Assignment of the emission to ^{3}MLCT states was corroborated by measurements at 77 K, where the emission shifted to shorter wavelengths with increased quantum yields and exhibited vibronic character typical of ^{3}MLCT states (Figure 8). The vibronic intervals of around 1350 cm^{-1} are consistent with diimine involvement in the emissive state,[131] and did not vary significantly throughout the series. The thermally induced Stokes shifts (ΔE_S) of around 1100 cm^{-1} compare well to the related model complex $[\mathrm{Ru(bpy)_3}]^{2+}$ (ΔE_S= 1127 cm^{-1}).[132] These ^{3}MLCT emission energies were computed at around 2.0 eV, in agreement with the experimental 77 K energies (Table 3 and Table S5).

Singlet oxygen sensitization

All of the complexes have triplet excited states of sufficient energy to sensitize $^1O_2$ with an energy of approximately 0.97 eV.[133] The quantum yields for $^1O_2$ formation (Φ_Δ) were calculated for the PF_6^- salts in air-saturated MeCN calculated using the integrated $^1O_2$ emission centered near 1276 nm with $[\mathrm{Ru(bpy)_3}](\mathrm{PF_6})_2$ as the standard ($\Phi_{\Delta,s}$=0.56) according to Equation 1.[133] The results are compiled in Table 3. The $^1O_2$ quantum yields for $\mathrm{Ru(phen)_3}^{2+}$ and **Ru-0T**, the compounds lacking any thiophene rings, were very similar to the reference at 53 and 56%, respectively. Generation of $^1O_2$ increased with thienyl chain length, plateauing around 88% at *n*=3. For comparison, the related complexes $[\mathrm{Ru(bpy)_2(IP\text{-}}n\mathrm{T)}]^{2+}$ and $[\mathrm{Ru(4,4'\text{-}dmb)_2(IP\text{-}}n\mathrm{T)}]^{2+}$ exhibit near unity quantum yields for *n*=3,4 and around 75% for *n*=2.[98]

Table 3: Photophysical properties of the series, measured as $(\mathrm{PF_6})^-$ salts in MeCN. Excitation wavelengths are noted in parentheses. *Too weak to accurately quantify.

Compound	RT emission			77 K emission		Φ_Δ (λ_{ex} / nm)	τ_{TA} / μs
	$\lambda_{em.}$ (λ_{ex}) / nm	Φ_{em}	τ_{em} / μs	$\lambda_{em.}$ (λ_{ex}) / nm	$\Phi_{em,77\,K}$		
$[\mathrm{Ru(phen)_3}]^{2+}$	602 (448)	3.1×10^{-2}	0.47	568, 616, 672 (452)	5.5×10^{-1}	0.53 (450)	0.40
Ru-0T	617 (455)	8.4×10^{-2}	0.70	571, 620, 679 (452)	5.6×10^{-1}	0.56 (456)	0.85
Ru-1T	606 (458)	5.7×10^{-2}	0.73	573, 621, 678 (460)	4.4×10^{-1}	0.62 (461)	0.18, 0.79 (410, 460) 0.16 (610)
Ru-2T	612 (467)	3.0×10^{-2}	1.1	576, 625, 692 (458)	3.2×10^{-2}	0.73 (462)	148
Ru-3T	614 (468)	3.5×10^{-3}	0.97	573, 620, 685 (462)	1.7×10^{-2}	0.88 (457)	34–36
Ru-4T	614 (463)	*1.6×10^{-4}	0.85	574, 619 (457)	8.6×10^{-4}	0.87 (462)	25

Transient Absorption

Nanosecond transient absorption (TA) spectroscopy was used to examine the triplet excited states. Differential excited state absorption (ESA) spectra were measured in degassed MeCN following excitation with a 355 nm laser with a 5-ns pulse width, with correction for luminescence. Selected time slices are shown in Figure 9 and the full set of TA spectra are compiled in Figure S28. Transient lifetimes were measured at ESA maxima or bleach minima and are compiled in Table 3. The corresponding time-resolved spectra and fits are shown in Figure S29.

The TA profiles of [Ru(phen)$_3$]$^{2+}$ and **Ru-0T** are typical of what might be expected of the ^{3}MLCT state for a Ru(II) polypyridyl complex, with a bleach in the 400 to 500 nm region arising from loss of the strong ^{1}MLCT $\leftarrow$ $^1A_1$ ground state absorption. Part of the ESA due to the ligand phen$^-$ transitions can be seen at shorter wavelengths, and the extremely weak and broad absorption at longer wavelengths due to phen$^-$ or LMCT transitions involving Ru(II) is also observed. Their TA lifetimes matched their emissive lifetimes and lacked any involvement of the higher-lying ligand-based triplet excited states.

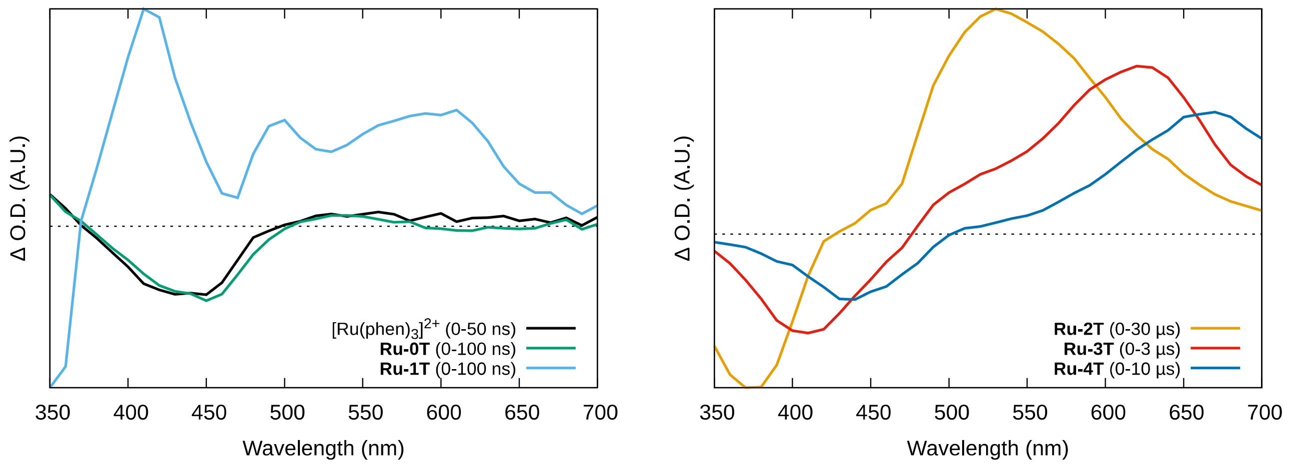

Figure 9: Transient absorption (TA) spectra of [Ru(phen)$_3$]$^{2+}$ and the **Ru-*n*T** series in deoxygenated MeCN integrated over the indicated time slice following the excitation pulse. ΔO.D.=0 is indicated by a dotted line. Data for the complexes with nanosecond lifetimes are shown on the left, and those with microsecond lifetimes are shown on the right.

The transient profile of **Ru-1T** is more complex. A strong ground state bleach appears near 350 nm alongside a strong ESA near 410 nm that overlaps the weaker ^{1}MLCT $\leftarrow$ $^1A_1$ ground state bleach in the 400 to 500 nm region and another ESA beyond 475 nm (Figure 9 and **Figure S28**). The ESA at longer wavelengths is more intense than that for [Ru(phen)$_3$]$^{2+}$ or **Ru-0T** but not nearly as strong as typical ^{3}ILCT states involving two or more thiophenes. The kinetics measured at 410 and 460 nm both exhibited a fast decay (0.2 µs) of the ESA component and a slower decay (0.8 µs) of a bleach component. The slower decay was in good agreement with the ^{3}MLCT decay from the emission experiment, and the TA spectrum collected at 0.5–1.0 µs after the laser pulse exhibits the typical ^{3}MLCT signature (Figure S30). The ESA at longer wavelengths (e.g., 610 nm) decayed with a single time constant of 0.2 µs. The strong overlap between the IP-1T ligand-localized absorption and the excitation laser pulse (355 nm) may give rise to the short decay associated with the broad ESA.

Ru-2T has the longest triplet lifetime of the family, and its TA spectrum is dominated by IP-2T ligand-localized transitions. An intense ESA, with an onset near 450 nm and characteristic signature of the oligothiophene-based ^{3}ILCT state, obscured the ^{1}MLCT ground state bleach in the 400-500 nm region. The intense bleach in the region under 400 nm, with a minimum near 380 nm, involves the loss of the ^{1}IL/^{1}ILCT ground state absorption. The decay kinetics in both the bleach and ESA regions are monoexponential with a lifetime of 148 µs.

The TA spectra of **Ru-3T** and **Ru-4T** are also dominated by the oligothiophene-based ^{3}ILCT triplets. **Ru-3T** exhibited a bleach around 410 nm and a strong ESA near 625 nm, while **Ru-4T** produced these corresponding transients at slightly longer wavelengths. The bleach for **Ru-4T** has its minimum around 440 nm, and the ESA is centered around 675 nm. Both the bleach and the ESA for both compounds decayed monoexponentially with a lifetime of 36 µs for **Ru-3T** and 25 µs for **Ru-4T**. The ^{3}ILCT state that was observed by TA and the emitting ^{3}MLCT state were decoupled as observed in the case of **Ru-2T**, suggesting that the ^{3}ILCT state is the lowest-energy triplet for n=2–4. Indeed, the computational studies estimate T_1 as predominantly ^{3}ILCT/^{3}LLCT for **Ru-2T** and ^{3}ILCT for **Ru-3T** and **Ru-4T** (Table 1). The systematic decrease in the ^{3}ILCT state lifetime on going from **Ru-2T** to **Ru-4T**, with τ_{TA} dropping from 148 to 36 to 25 µs, is consistent with the shortening of triplet lifetimes in free oligothiophenes owing to the decrease in the T_1–S_0 energy gap with increasing number of thiophenes.[128] The absence of ^{3}MLCT contributions to the decays is consistent with the extremely weak ^{3}MLCT emission quantum yields that suggest the ^{3}ILCT state dominates the relaxation dynamics on the nanosecond to microsecond timescales.

Triplet Energies and Excited State Pathways

The energies of the oligothiophene-based ^{3}ILCT states cannot be obtained directly because these states are non-emissive, nor can they be estimated from the corresponding free IP-nT ligands and nT units because they also do not emit. However, the ^{3}ILCT energies can be estimated based on the shortening of their TA lifetimes in the presence of suitable excited state quenchers, in accordance with the modified

Stern-Volmer relationship presented in Equation S2. The complexes were excited at 532 nm to avoid directly exciting the quencher. The appearance of a new long-lived signal in the ESA spectra of the mixtures confirmed that the triplet state of the quencher had indeed formed via energy transfer from the excited complex.

The rate constants (k_q) for triplet-triplet energy transfer between selected organic sensitizers of known $^3\pi\pi^*$ energies[67,134] (E_T) and the excited complexes are compiled in Table 4. Values for k_q were determined by examining the TA lifetimes of the complexes (measured at 620 nm and at 660 nm for **Ru-3T** and **Ru-4T**, respectively) as a function of quencher concentration. The values for k_q were largest when the $^3\pi\pi^*$ acceptor energy was near 1.53 eV. Therefore, the ^{3}ILCT energies were estimated to lie near 1.5 eV above the ground state. These values are in good agreement with the computed ^{3}ILCT energies of 1.57 for **Ru-3T** and 1.44 eV for **Ru-4T**.

Table 4: Stern-Volmer triplet-triplet energy transfer rate constants for **Ru-3T** and **Ru-4T** in the presence of quenchers with known $^3\pi\pi^*$ energies (E_T). n.d.=not determined.

Quencher	E_T (eV)	**Ru-3T** k_q ($M^{-1}\ s^{-1}$)	**Ru-4T** k_q ($M^{-1}\ s^{-1}$)
tetracene	1.3	9.4×10^8	n.d.
perylene	1.5	5.2×10^9	3.7×10^9
diBr-anthracene	1.7	2.9×10^9	6.2×10^8
phenazine	1.9	1.2×10^8	3.1×10^8
pyrene	2.1	2.3×10^7	n.d.
fluorene	2.9	0	n.d.

From the spectroscopic data combined with computational studies and Stern-Volmer quenching experiments, Jablonski diagrams modelling the excited state pathways for the two complexes with predominant ^{3}ILCT states are shown in Scheme 1. Excitation of **Ru-3T** and **Ru-4T** with visible light produces singlet excited states of mixed ^{1}MLCT, ^{1}LLCT, or ^{1}ILCT configurations, where the computed singlet-singlet transitions have higher ^{1}ILCT character for the longest wavelength absorption bands (Table S3). For example, **Ru-3T** has 58% ^{3}ILCT character for its 466 nm transition and **Ru-4T** has 77% for its 488 nm transition. These initially formed excited states ultimately relax to their lower-lying triplets of ^{3}MLCT (T_2) or ^{3}ILCT (T_1) configuration where T_1 has a small amount of ^{3}LLCT mixing (27% for **Ru-3T** and 19% for **Ru-4T**). The ^{3}MLCT emission is weak, and the excited state dynamics of **Ru-3T** and **Ru-4T** on the nanosecond to microsecond timescales in the TA experiments are dominated by lowest-lying

^{3}ILCT states with longer lifetimes (25–40 µs). These dynamics are similar to those we have encountered previously in other oligothienyl-containing complexes.[23,24,99,135–139] While both ^{3}MLCT and ^{3}ILCT states can generate $^{1}O_2$, it is expected that the ^{3}ILCT states with their longer lifetimes may play the larger role in ROS production. Because oligothiophenes are known to be redox active, these states may also be deactivated via electron transfer pathways in the presence of suitable electron donors or acceptors. The electrochemical properties of **Ru-3T** and **Ru-4T** along with the rest of the series were investigated to gain a better understanding of these characteristics.

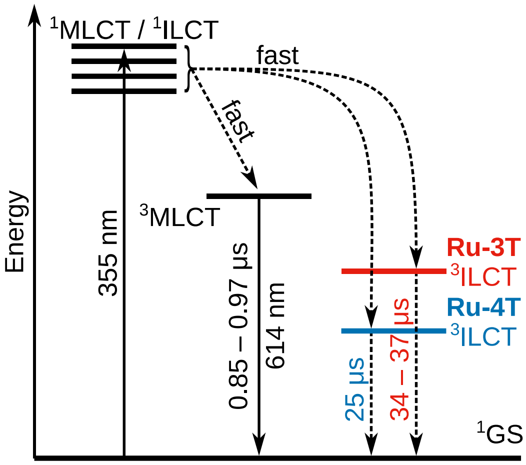

Scheme 1: Jablonksi diagram depicting the excited state pathways of **Ru-3T** and **Ru-4T**. Energies are not to scale and ^{1}LLCT contribution to initially formed excited states not shown.

2.4.4 Electrochemistry

Oxidation of [Ru(phen)$_2$(IP-nT)](PF$_6$)$_2$ complexes

Representative cyclic differential pulse voltammetry (CDPV) traces for oxidation of the complexes measured relative to Ag/AgCl (4M KCl) are presented in Figure S31, and the formal redox potentials are listed in Table 5 relative to ferrocene as the internal standard. The trends are compared in Figure 10. As is typical of Ru(II) polypyridyl complexes, a single reversible wave appears due to the Ru^{2+}/ Ru^{3+} process, occurring near +820 to +880 mV vs. ferrocene in all the complexes. The potential for the Ru^{2+}/ Ru^{3+} couple is largely unaffected by the length of the thienyl chain. For compounds **Ru-1T** through **Ru-4T**, a second, quasi-reversible wave appears, due to the oxidation of the thiophene chain. For two thienyl groups and longer, *n*T is more easily oxidized than the Ru(II) center. In contrast, the thiophene oxidation is less favorable than the metal oxidation by about 100 mV for **Ru-1T**. The change with each successive thiophene group is most pronounced on going from one to two thiophenes, with a difference of about 180 mV. Thereafter, the changes are around 80 to 90 mV. The difference in the *n*T oxidation potentials of **Ru-4T** versus **Ru-1T** is about 350 mV. This trend is consistent with the behaviour of free oligothiophenes, with oxidation occurring more readily for longer *n*T.[140]

Reduction of [Ru(phen)$_2$(IP-nT)](PF$_6$)$_2$ complexes

The electrochemistry of Ru(II) polypyridyl complexes of this type is generally typified by three reversible reduction waves as one electron is added to each ligand in succession.[129] The reduction of $[Ru(phen)_3]^{2+}$ is known to be complicated by adsorption on the electrode,[141] but we found this problem could be mitigated using DMF as the solvent and a lower concentration (0.25 mM) on the reduction sweep.

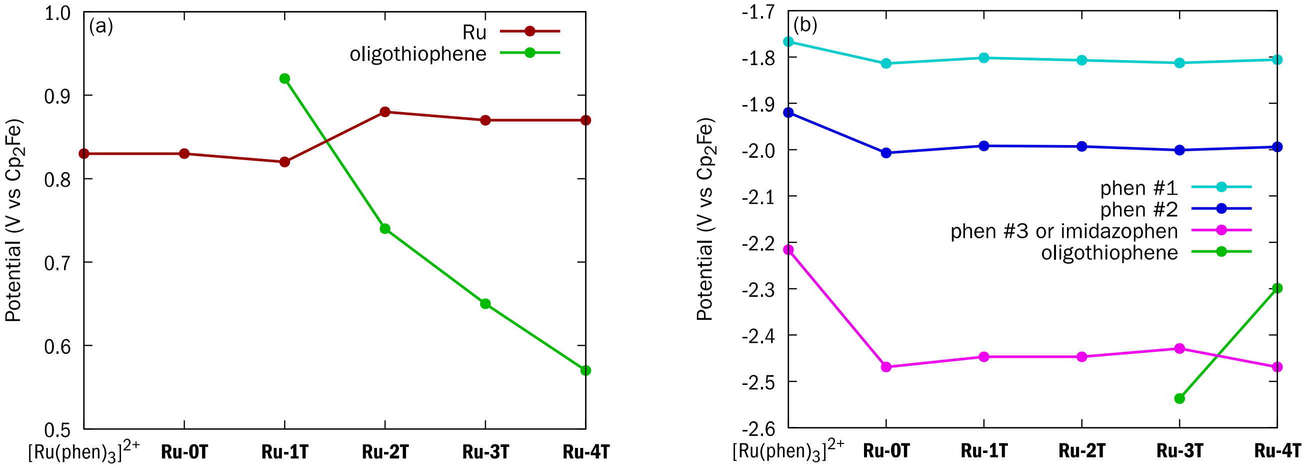

Figure 10: Formal redox potentials (vs the ferrocene internal reference) and proposed assignments of the (a) oxidation and (b) reduction processes, as measured by CDPV in DMF containing $TBAPF_6$.

The cyclic differential pulse voltammograms are shown in Figure S32 and the formal potentials are tabulated in Table 5 and compared graphically in Figure 10. The first two reduction waves for the **Ru-*n*T** series shift to slightly more negative potentials compared to the model compound $[Ru(phen)_3]^{2+}$. In contrast, the potential of third reduction changes more dramatically, shifting negative by around 250 mV, when phen is replaced by IP but is also largely unaffected by *n*. This indicates that the first two reductions involve the phen ligands, and the third reduction involves the IP-*n*T ligand.

The potential of the third reduction of the **Ru-*n*T** complexes does not change much, becoming more positive by only around 40 mV on going from **Ru-0T** to **Ru-3T**. This suggests that the reduction is localized to the IP portion of the IP-*n*T ligand and is influenced only slightly by the number of thiophenes. A fourth reduction appears only in the case of **Ru-3T** and **Ru-4T**. This fourth reduction potential shifts positive by 240 mV on going from **Ru-3T** to **Ru-4T**, in agreement with smaller HOMO-LUMO gaps associated with increasing π-conjugation in oligothiophenes.[142] Although **Ru-3T** is the first complex in the series where the oligothiophene unit can be reduced in the measurable potential window, 3T remains harder to reduce than IP. **Ru-4T** shows a marked departure and represents the first point at which the oligothiophene unit is reduced more readily than IP (Figure 10b).

Table 5. Formal redox potentials measured by CDPV in DMF containing 0.1 M TBAPF$_6$, referenced in volts against ferrocene as the internal standard. The concentration of the complexes was 4 mM for the oxidation and 0.25 mM for the reduction scans. The working and reference electrodes were glassy carbon and Ag/AgCl/4M KCl, respectively. The Pt wire was used as a counter electrode. Overlapping waves were deconvoluted mathematically. The error on these measurements is ±0.02 V.

Compound	$E^{0'}_{red}(4)$	$E^{0'}_{red}(3)$	$E^{0'}_{red}(2)$	$E^{0'}_{red}(1)$	$E^{0'}_{ox}(1)$	$E^{0'}_{ox}(2)$
$[Ru(phen)_3]^{2+}$		−2.22	−1.92	−1.78	+0.83	
Ru-0T		−2.46	−2.00	−1.81	+0.83	
Ru-1T		−2.45	−1.99	−1.81	+0.82	+0.92^{b,c}
Ru-2T		−2.45	−1.99	−1.81	+0.74^{b,c}	+0.88
Ru-3T	−2.53^{a}	−2.44	−1.99	−1.81	+0.65^{b,c}	+0.87
Ru-4T	−2.47	−2.30^{a}	−1.99	−1.81	+0.57^{b,c}	+0.87

^{a}reduction of oligothiophene unit. ^{b}quasi-reversible. ^{c}oxidation of oligothiophene unit.

Excited state redox potentials

The excited state redox potentials of Ru(II) polypyridyl complexes have been approximated from the ground state oxidation and reduction potentials and E_{00}, the energy difference between the thermally equilibrated excited state and the ground state zeroth vibrational level.[143] These earlier studies use the 77 K emission to estimate E_{00}. In the present series, the capacities of the oligothiophene units of **Ru-3T** and **Ru-4T** to also be oxidized and reduced in the ground state prompted us to estimate the redox power of the ^{3}ILCT state in addition to the ^{3}MLCT state (Table 6). Since the long-lived ^{3}ILCT state is non-emissive in this series, its computed energy from Table S5 was used. The E_{00} of the ^{3}MLCT is taken from the most intense emission peak energy as measured in a 4:1 ethanol:methanol glass at 77 K. The potentials for oxidation (Equation 1) and reduction (Equation 2) of the excited states were estimated from simple thermodynamic considerations, where ^{3}PS* denotes the ^{3}MLCT or longer-lived ^{3}ILCT state.[129,143]

$$E(^3\mathrm{PS}^* \leftarrow \mathrm{PS}^+ + e^-) = E(\mathrm{PS} \leftarrow \mathrm{PS}^+ + e^-) - E_{00} \qquad \text{Equation 1}$$

$$E(^3\mathrm{PS}^* + e^- \rightarrow \mathrm{PS}^-) = E(\mathrm{PS} + e^- \rightarrow \mathrm{PS}^-) + E_{00} \qquad \text{Equation 2}$$

The ground state redox potentials related to the ^{3}MLCT state correspond to the Ru$^{3+/2+}$ oxidation and the first phen$^{0/-}$ reduction voltametric waves and are similar throughout the series. This is consistent with an ^{3}MLCT excited state that involves ligands proximal to the Ru(II) center and thus largely unaffected by the presence and number of thiophenes. For all compounds, the Ru$^{3+/2+}$ oxidation potentials in the excited state were near –1.29 V and the first phen$^{0/-}$ reduction potentials in the excited state were around 0.35 V.

Since the ^{3}ILCT state involves the *n*T unit,[23,63] the waves corresponding to oligothiophene oxidation and reduction were used to estimate E^*_{ox} and E^*_{red}, respectively. E^*_{red} was also estimated using the IP reduction since T_1 has a small amount of ^{3}LLCT character. These values were estimated for **Ru-3T** and **Ru-4T**, the only two compounds in the series that showed both oxidations and reductions involving the IP-*n*T ligand and for which T_1 was predominantly ^{3}ILCT.

Although the *n*T unit is more easily oxidized compared to the Ru(II) center in the ground state (Figure 10), the Ru(II) center is the better reducing species in the ^{3}MLCT excited state (–1.29 V versus –0.92 for **Ru-3T** and –0.87 for **Ru-4T**). The reason for this difference is due to the higher energy stored in the ^{3}MLCT state compared to the ^{3}ILCT states (2.16 eV versus 1.57 for **Ru-3T** and 1.44 for **Ru-4T**) that offsets the differences in reducing power of the ground states. The phen ligand is the most easily reduced ligand in both the ground and the excited states, resulting in the ^{3}MLCT state being much more oxidizing than the ^{3}ILCT state (0.35 V versus –0.96 for **Ru-3T** or –0.86 for **Ru-4T**). Nevertheless, any excited state redox processes contributing to photocytotoxicity could involve the ^{3}ILCT state given that it may be formed in much higher yield and with a lifetime that is 30 to 40× longer.

Table 6: Excited state redox potentials for the ^{3}MLCT and ^{3}ILCT states of **Ru-3T** and **Ru-4T**, vs. ferrocene in DMF. E^*_{red} for the ^{3}ILCT state was estimated two ways: using $E^{0\prime}_{\mathrm{red}}$ involving *n*T or IP. The latter number is in parentheses.

	^{3}MLCT			^{3}ILCT		
Complex	E_{00} (eV)	E^*_{ox} (V vs. Cp_2Fe)	E^*_{red} (V vs. Cp_2Fe)	E_{00} (eV)	E^*_{ox} (V vs. Cp_2Fe)	E^*_{red} (V vs. Cp_2Fe)
Ru-3T	2.16	–1.29	0.35	1.57	–0.92	–0.96 (–0.87)
Ru-4T	2.16	–1.29	0.35	1.44	–0.87	–0.86 (–1.03)

2.4.5 Photobiological activity

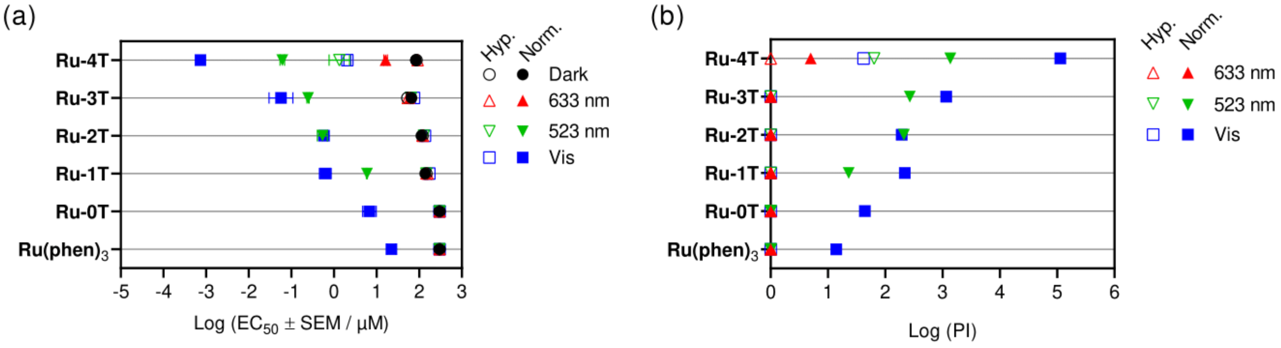

Figure 11: Summary of in vitro cytotoxicity and photocytotoxicity reported as log (EC$_{50}$ ± SEM) values (a) and PI values (b) obtained from dose−response curves in the SK-MEL-28 melanoma cell line with [Ru(phen)$_3$](Cl)$_2$ and **Ru-0T−Ru-4T**. Treatments included dark (0 J cm^{-2}; black circles) and 100 J cm^{-2} doses of 633 nm (red triangles), 523 nm (green inverted triangles), and visible light (400−700 nm, blue squares). The irradiance was approximately 20 mW cm^{-1}. Hypoxic (1% O$_2$) results are shown with open symbols, and normoxic (~18.5% O$_2$) data are shown with closed symbols.

The complexes in this series were evaluated for their dark and light-triggered cytotoxicities against human skin melanoma cells (SK-MEL-28) cultured as 2D monolayers under normoxic (~18.5% O$_2$) and hypoxic (~1% O$_2$) conditions (Figure 11). Details can be found in our previously published procedures[63] and also in the SI. Stock solutions of [Ru(phen)$_3$](Cl)$_2$ and **Ru-0T−Ru-3T** were prepared at 5 mM in water containing 10% DMSO with solubilization first in DMSO followed by addition of water. **Ru-4T** was prepared in 100% DMSO.

Normoxia.

Briefly, melanoma cells growing in log phase were seeded into two sets of 384-well plates: one set for cytotoxicity (dark plates) and one set for photocytotoxicity (light plates) evaluation. Cells were allowed to adhere to the wells at 37 °C over a period of 3−5 hours and then treated with varying concentrations of PS (1 nM to 300 µM for all compounds, 1 aM to 300 µM for **Ru-4T**) serially diluted in DPBS. Following a 13−20 h drug-to-light-interval (DLI), the light plates were irradiated while the dark plates were kept in the incubator. The light treatment used LEDs emitting broadband visible (400−700 nm, 21 mW cm^{-2}) or narrower green (523 nm, 18 mW cm^{-2}) or red (633 nm, 18 mW cm^{-2}) light with a fluence of 100 J cm^{-2}. The spectral outputs of the light sources are given in Figure S33. Both dark and light-treated plates were then incubated at 37 °C for an additional 24 h before assessing cell viability with a resazurin-based assay. The effective concentrations to reduce cell viability by 50% (EC$_{50}$ values) were calculated from sigmoidal fits of the dose-response curves for the dark and light-treated conditions based on three technical replicates. The phototherapeutic indices (PIs), representing light-triggered amplification of cytotoxic effects, were tabulated as ratios of the dark to light EC_{50} values.

The complexes of this series were relatively nontoxic to SK-MEL-28 cells in the absence of a light trigger (Figure 11a, Table S6). Only **Ru-3T** and **Ru-4T** had dark EC_{50} values <100 µM, which were still considered nontoxic (66.4 and 84.0 µM, respectively). $[Ru(phen)_3](Cl)_2$ and **Ru-0T** had dark EC_{50} values that were beyond the highest concentration tested in the assay and were tabulated as >300 µM. As a consequence, their PI values are undefined but reported as a lower limit using 300 µM as the dark cytotoxicity.

Broad-band visible light produced photocytotoxicity from all compounds in the series (Figure 11, Table S6). Systematic π-expansion from phen to IP-*n*T (*n*=1−4 thienyl groups) resulted in progressively higher potency using visible light, spanning four orders of magnitude. The visible light EC_{50} values in normoxic conditions ranged from 22 µM (PI>10) for the least active reference compound $[Ru(phen)_3](Cl)_2$ to as low as 740 pM ($PI>10^5$) for the most active compound **Ru-4T**. Replacing a phen ligand with IP (**Ru-0T**) increased the photocytotoxicity 3-fold (EC_{50}=6.8 µM, PI>40). Appending one (**Ru-1T**) or two (**Ru-2T**) thienyl groups to IP improved the potency another 10-fold, shifting the EC_{50} values into sub-micromolar regime near 0.6 µM with PIs on order of 200. Another 10-fold enhancement in photocytotoxicity was

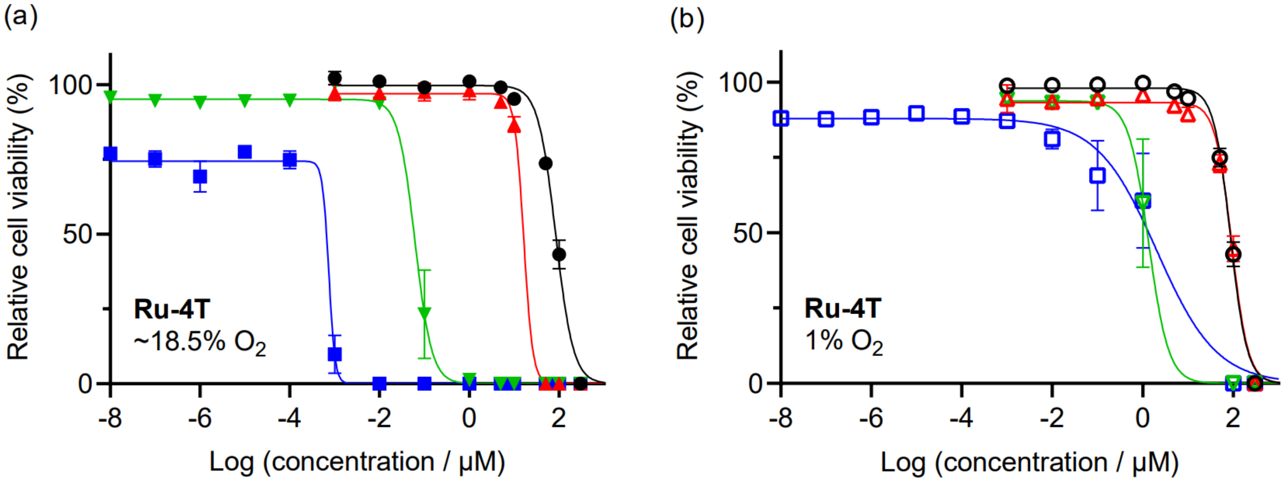

Figure 12. Dose−response (±SD) of **Ru-4T** in (a) normoxic ÿ18.5% O_2 or (b) hypoxic 1% O_2-treated SK-MEL-28 melanoma cells. Treatments included dark (0 J cm^{-2}; black circles) and 100 J cm^{-2} doses of 633 nm (red triangles), 523 nm (green inverted triangles), and visible (400−700 nm, blue squares) light.

accomplished on going to three thiophene rings (**Ru-3T**; EC_{50}=0.057 µM, PI∼10^3), but the greatest change occurred with four thiophenes (**Ru-4T**; EC_{50}=740 pM, PI>10^5).

All compounds were inactive with red light, with the exception that **Ru-3T** (EC_{50}=16.3 µM; PI=5) and **Ru-4T** (EC_{50}=16.3 µM; PI=5) exhibited marginal responses. This is in line with what would be expected for compounds having little absorption of red light.[69] $[Ru(phen)_3](Cl)_2$ and **Ru-0T** were also inactive with green light. Therefore, the observed effects with broadband visible light were likely generated preferentially by the shorter wavelengths, which is further supported by the attenuated EC_{50} values and corresponding PIs for the thienyl-containing complexes with green light. The only exception was **Ru-2T** which maintained its EC_{50} value near 0.5 µM and PI of ~200 with green light. The PIs for both **Ru-1T** and **Ru-3T** were reduced ten-fold (PI=23 and 270, respectively), while that for **Ru-4T** was reduced by several orders of magnitude (PI=~10^3). The photocytotoxic responses elicited by **Ru-4T** toward SK-MEL-28 cells under both oxygen conditions with the different light parameters are compared in Figure 12.

Hypoxia.

The hypoxia assays were carried out as described for normoxia except that the dark and light plates with adhered cells were moved to a hypoxia chamber (1% O_2) for 2–3 h before compound addition. At the end of the DLI in hypoxia, dissolved oxygen was measured using an immersive optical probe to confirm hypoxic condition before sealing the light plates with highly transparent, low gas permeable qPCR film. The light plates were illuminated outside of the hypoxia chamber alongside the normoxic plates. The films were then removed, and all plates were incubated under normoxia (37°C, 5% CO_2, ≥90% RH) for 20–23 h before cell viability determination.

As observed for the normoxic condition, the compounds were nontoxic to cells in the dark and with red light under hypoxia (Figure 11, Table S6). $[Ru(phen)_3](Cl)_2$ and **Ru-0T−Ru-3T** lost all of their photocytotoxicity with visible and green light in hypoxia, while **Ru-4T** gave modest activity with a visible EC_{50} values of approximately 1–2 µM and PIs on the order of 40–60. This marked reduction in activity for **Ru-4T** and inactivity for the rest of the series suggests that the largest contributor to the normoxic photocytotoxicity for this family likely involves oxygen-dependent photophysical pathways.

Biological replicates.

The data shown in Figure 11 and Table S6 represent our initial results and are the average of technical replicates performed in triplicate on cells of the same batch and identical passage number and have low standard deviation as a result. Biological replicates will have more variation, and thus we validated our results for **Ru-3T** and **Ru-4T** over seven biological replicates run in triplicate (Figure 13 and Table S7–Table S10). Repeat 0 is the data from Figure 11 and Table S6 that was discussed above. Repeats 1–6 represent biological replicates with variations as described previously.[63]

Both **Ru-3T** and **Ru-4T** were completely nontoxic over all biological replicates, with mean EC_{50} values just under 100 µM in both normoxia and hypoxia and standard error of the mean (SEM) being within ±25 µM for **Ru-3T** and ±10 µM **Ru-4T**. The visible EC_{50} values for **Ru-3T** in normoxia ranged from about 60 to 80 nM with a mean of 64 nM; the corresponding visible PIs ranged from 1200 to 2500 with a mean of 1600. The EC_{50} value for **Ru-4T** under the same conditions exhibited a much larger variance, ranging from 40 fM to about 8.6 nM with a mean of 2.2 nM. Nevertheless, five of the seven replicates were within an order of magnitude of each other. Three were between 0.64 and 0.80 nM and two were around 4.8 to 8.6 nM, giving rise to PIs on the order of 10^4 to 10^5. Only two of the seven biological replicates for **Ru-4T** were well outside of this range at 40 and 320 fM with unusually large PIs of 10^8–10^9. Of note, only the most potent IP-4T complexes under the most potent light condition (visible) in the normoxic condition produce more than several orders of magnitude variation in photocytotoxicity between biological replicates, with EC_{50} values extending into the ubertoxin range (fM and lower) with visible light.[63] In the case of the related analog ML19C01, $[Ru(2,9\text{-dmp})_2(IP\text{-}4T)](Cl)_2$, four of six biological replicates fell in this range and produced PIs as large as 10^{12}. To date, this behavior has only been observed for certain IP-4T complexes of Ru(II) and (to a lesser degree) of Os(II). Herein, **Ru-4T** adds one more example that may help us better understand this phenomenon in the future.

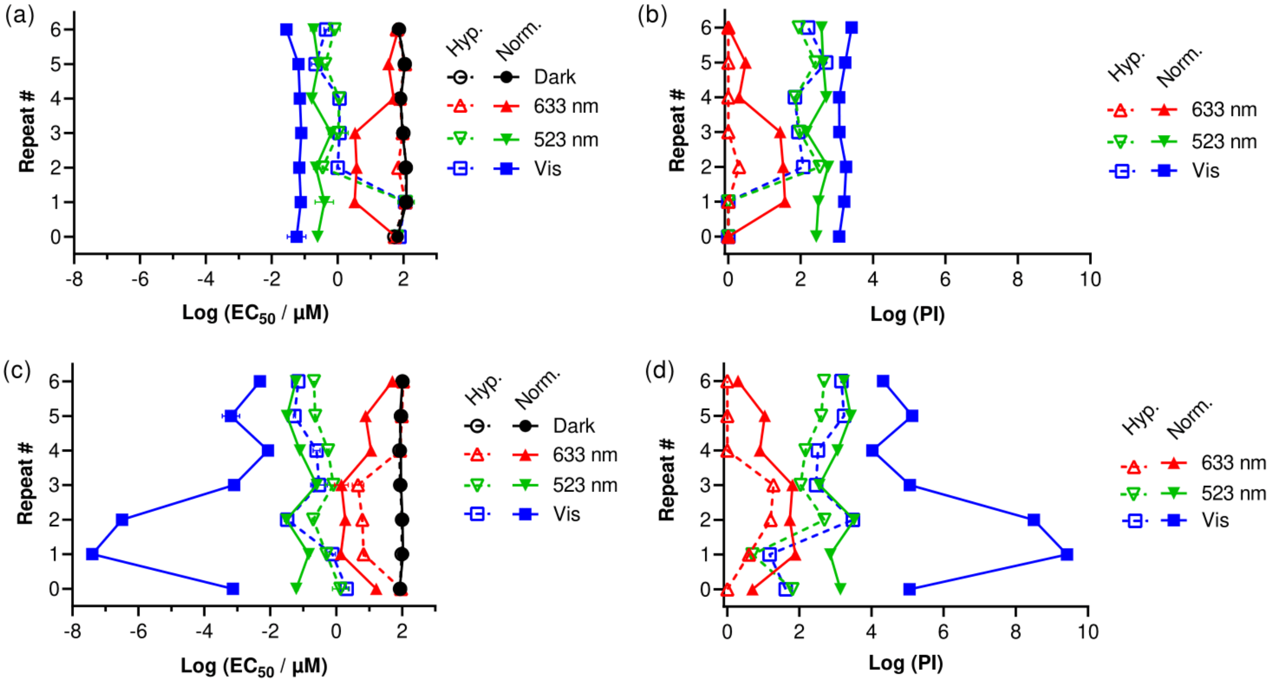

Figure 13. Interassay performance (± log(SEM)) of **Ru-3T** (top, a + b) and **Ru-4T** (bottom, c + d) in normoxic (filled symbols, solid lines, ~18.5% O_2) and hypoxic (open symbols, dashed lines, 1% O_2) SK-MEL-28 melanoma cells. Treatments included dark (no light; black circles) and 100 J cm^{-2} treatments at ~20 mW cm^{-2} of visible (400-700 nm) light (blue square), 523 nm (green inverted triangle) and 633 nm (red triangle). SEM = standard error of the mean.

With green light in normoxia, there was little variance in the activity of **Ru-3T**. The green EC$_{50}$ values varied from 0.16 to 0.64 µM and PIs from 140 to 570, with the mean being 0.30 µM and 370. For **Ru-4T**, five of seven replicates gave green EC$_{50}$ values between 30 and 80 nM (PIs ranged from 1100 to 3300). The remaining two were between 0.15 and 0.26 µM (PIs ranged from 360 to 720). On average **Ru-4T** was more active than **Ru-3T** but by only about five-fold.

With red light normoxia, **Ru-3T** was inactive in four of seven replicates and only moderately active in the remaining three with red EC$_{50}$ values around 3 to 4 µM and PIs around 30 to 40. **Ru-4T** was moderately better, with red EC$_{50}$ values of 1 to 2 µM (PIs 64 to 77) in three of the seven replicates but 10 to 50 µM (PIs 2 to 11) in the remainder.

Despite losing all activity in hypoxia in the initial evaluation, **Ru-3T** was phototoxic with visible and green light in five of the seven biological replicates under hypoxia. Three of the replicates gave EC$_{50}$ values near 1 µM and two were between 0.22 and 0.45 µM. The resulting PIs ranged from about 70 to 500.

Overall, the activity of **Ru-3T** was reduced by five to fifteen-fold in hypoxia with visible light but only about two-fold for green light (because there was a larger difference in the visible and green EC_{50} values in normoxia). There was no significant activity for **Ru-3T** with red light over seven biological replicates.

Ru-4T was also generally much more active with visible light in hypoxia than the initial evaluation showing single-digit µM photocytotoxicity. Three of the replicates produced EC_{50} values between 32 and 70 nM, while two were near 0.25–0.30 µM. The corresponding PIs were between about 290 and 3000. EC_{50} values in the two remaining replicates were 2.1 to 6.4 µM (PIs 15 and 42). The large variance in photocytotoxicity for **Ru-4T** in normoxia was reduced to only a few orders of magnitude in hypoxia, making the attenuation in activity on going from normoxia to hypoxia much more pronounced for **Ru-4T** compared to **Ru-3T**. Nevertheless, **Ru-4T** was slightly more potent on average than **Ru-3T** in hypoxia.

With green light, the difference between EC_{50} values in normoxia and hypoxia for **Ru-4T** was much less. In five of the seven hypoxic replicates, the green EC_{50} values were between 0.20 and 0.81 µM (PIs 110 to 480) compared to the mean EC_{50} value of about 0.10 µM in normoxia (mean PI 1600). With red light, **Ru-4T** was inactive in four of seven replicates and only marginally active in the rest with EC_{50} values between 4 and 20 µM (PIs between 4 and 20). Again, **Ru-4T** was only slightly more potent on average than **Ru-3T**.

To summarize, **Ru-4T** is superior to **Ru-3T** over the seven biological replicates when activated with visible light in normoxia. The light EC_{50} values and corresponding PIs for both compounds are attenuated on going from visible to green to red light, suggesting that the observed effects with broadband visible light are generated primarily by the shorter, bluer wavelengths. The light EC_{50} values and PIs are also attenuated on going from normoxia to 1% hypoxia, with the greatest differences observed with visible light as the most potent condition. For both compounds, the visible light-triggered activity in hypoxia was similar to that with green light in normoxia, and the differences between green light activity in normoxia and hypoxia were relatively small. The compounds were relatively inactive with red light, although **Ru-4T** did show modest activity in normoxia presumably due to some low probability of directly populating the lowest-lying but spin-forbidden triplet state. Of note, **Ru-4T** marks another example that follows our recently published ML19C01, with evidence of phototoxic effects at concentrations on the order of fM in several of the biological replicates.

2.5 CONCLUSIONS

The complexes of this family were designed to vary the number of thienyl groups *n*T attached to the IP ligand in a family of Ru(II) polypyridyl complexes based on 1,10-phenanthroline as the coligand. The motivation is part of a larger initiative to correlate structural variations with photobiological activities across different coordination complex families where we are considering: metal ion, coligands, thienyl-appended ligands, thienyl groups and number of thiophenes, counter ions, ionizable groups and protonation states, and coordination number and geometry. Within the phen family of IP-*n*T complexes, the extension of the thiophene chain systematically increased the lipophilicity and shifted the (oligo)thienyl-localized ππ* transitions to lower energy. The electrochemical properties of the complexes were similar and reminiscent of Ru(II) polypyridyl complexes in general with regard to metal oxidation and ligand reduction. However, complexes with at least one thiophene or more exhibited an additional oxidation, involving the thienyl group(s), that occurred more readily than metal oxidation and with increasing *n*. **Ru-3T** and **Ru-4T** could also be reduced on the thienyl chain, which was the 4th reduction for **Ru-3T** but 3rd for **Ru-4T**.

The MLCT states for the complexes were similar in energy, with ^{3}MLCT emission in agreement with typical Ru(II) polypyridyl complexes but quantum yields dropping by one to two orders of magnitude for **Ru-3T** and **Ru-4T**, respectively. The reduced phosphorescence was accompanied by an increase in the $^1O_2$ quantum yields and access to ^{3}ILCT states with prolonged lifetimes. The ^{3}ILCT state was the lowest-lying triplet for **Ru-2T** to **Ru-4T** and decoupled from the ^{3}MLCT states. T_1 was computed to be of mixed ^{3}ILCT/^{3}LLCT character for **Ru-2T**, whereas T_1 was predominantly ^{3}ILCT (>50%) for **Ru-3T** and **Ru-4T**. The % contribution of ^{3}LLCT to T_1 decreased with increasing *n*, with 65% ^{3}ILCT and <20% ^{3}LLCT character for **Ru-4T**. The triplet lifetime of **Ru-2T** was the longest at 148 μs and decreased with additional thiophenes as would be expected for a radiationless process governed by the energy gap law. The $^1O_2$ quantum yields were highest for **Ru-3T** and **Ru-4T** at about 88%.

The high ROS production for the complexes with extended thiophene chains resulted in potent phototoxicity in vitro. With visible light activation, **Ru-3T** consistently yielded EC_{50} values between 10 and 100 nM and PIs greater than 10^3. Despite having a slightly lower $^1O_2$ quantum yield and shorter ^{3}ILCT lifetime, **Ru-4T** was considerably more potent under the same conditions. On average its light EC_{50} values were sub-nanomolar with PIs in the 10^4 to 10^5 range, but the higher variability in activity led to some measurements in the femtomolar regime and PIs as large as 10^9. This activity was attenuated with longer wavelengths of light and in 1% hypoxia, but notably **Ru-4T** gave reliable sub-micromolar activity in hypoxia with PI values as high as 3,000. The trends for the most potent compounds **Ru-3T** and **Ru-4T** were verified over seven biological replicates performed in triplicate. The fact that **Ru-3T** could be generally classified as a hypoxia-active photosensitizer underscores the importance of biological replicates as this activity was missed in the initial assessment.

From these studies, a lowest-lying ^{3}ILCT state appears to be key to potent phototoxicity and activity in hypoxia. While the prolonged excited state lifetime of the *n*T-localized triplet is important, its precise magnitude and $^1O_2$ quantum yield are not sole determinants of potency since (i) **Ru-2T** has the longest lifetime but is not the most phototoxic, and (ii) **Ru-3T** and **Ru-4T** have similar $^1O_2$ yields but **Ru-4T** is superior (Figure S34). Alternate pathways could involve other ROS and oxygen-independent electron transfer processes. Although the ^{3}MLCT states were estimated to be more highly oxidizing and reducing compared to the lowest-lying ^{3}ILCT states, any excited state redox processes contributing to phototoxicity could involve the ^{3}ILCT state given that it is the lowest energy triplet with a lifetime that is 30 to 40× longer and the *n*T group is redox active. In addition, higher-lying and conformationally distinct ^{3}ILCT states cannot be excluded and have been implicated in the picosecond dynamics of similar families.[144]

Our study focused on the photophysical drivers of activity and did not consider biological factors such as cellular uptake and localization, subcellular targets, and cell death pathways that may affect cytotoxicity and potentiate phototoxicity. Future studies are aimed at reconciling both photophysical and biological characteristics to explain the unusual potency of certain oligothienyl-based PSs and building structure-activity relationship (SAR) databases for light-responsive transition metal complexes.

2.6 ASSOCIATED CONTENT

Additional method information and characterization data may be found in the Supplementary Information. This material is available free of charge via the Internet at https://pubs.acs.org.

2.6.1 Author Information

Corresponding authors

Colin G. Cameron – Department of Chemistry and Biochemistry, The University of Texas at Arlington, Arlington, Texas 76019-0065, United States; orcid.org/0000-0003-0978-0894; Email: colin.cameron@uta.edu

Sherri A. McFarland – Department of Chemistry and Biochemistry, The University of Texas at Arlington, Arlington, Texas 76019-0065, United States; orcid.org/0000-0002-8028-5055; Email: sherri.mcfarland@uta.edu

Authors

Houston D. Cole − Department of Chemistry and Biochemistry, The University of Texas at Arlington, Arlington, Texas 76019-0065, United States

Abbas Vali − Department of Chemistry and Biochemistry, The University of Texas at Arlington, Arlington, Texas 76019-0065, United States

John A. Roque III − Department of Chemistry and Biochemistry, The University of Texas at Arlington, Arlington, Texas 76019-0065, United States; Department of Chemistry and Biochemistry, The University of North Carolina at Greensboro, Greensboro, North Carolina 27402, United States; Present Address: University of North Carolina at Chapel Hill, Chapel Hill, NC, 27599

Ge Shi − Department of Chemistry and Biochemistry, The University of Texas at Arlington, Arlington, Texas 76019-0065, United States

Gurleen Kaur − Department of Chemistry and Biochemistry, The University of Texas at Arlington, Arlington, Texas 76019-0065, United States

Rachel O. Hodges − Department of Chemistry and Biochemistry, The University of North Carolina at Greensboro, Greensboro, North Carolina 27402, United States; Present Address: Wake Forest University School of Medicine, 307 Winston-Salem, NC 27109

Antonio Francés-Monerris – Institut de Ciència Molecular, Universitat de València, 46071 València, Spain

Marta E. Alberto – Dipartimento di Chimica e Tecnologie Chimiche, Università della Calabria, Arcavacata di Rende, 87036 Italy

2.6.2 Notes

S.A.M. has a potential research conflict of interest due to a financial interest with Theralase Technologies, Inc. and PhotoDynamic, Inc. A management plan has been created to preserve objectivity in research in accordance with UTA policy.

2.6.3 Acknowledgements

The authors would like to thank the National Cancer Institute (NCI) of the National Institutes of Health (NIH) (Award R01CA222227) as well as the National Science Foundation (NSF) (Award 2102459) for support. A.F.M. thanks the grant PID2021-127554NA-I00 funded by the Spanish Ministry of Science and Innovation (MCIN/AEI/10.13039/501100011033) and by “ERDF A way of making Europe”. M.E.A. acknowledges the CINECA award under the ISCRA initiative (HyPS4DAT project) for the availability of high-performance computing resources. The content in this work is solely the responsibility of the authors and does not necessarily represent the official views of the National Institutes of Health or National Science Foundation. The authors also thank Dr. Daniel Todd as UNCG’s Triad Mass Spectrometry Facility manager and his assistants Jennifer Simpson and Diane Wallace. S.A.M. likewise thanks Dr. Franklin Moy (UNCG) and Dr. Brian Edwards (UTA) for their experimental support and instrument maintenance as NMR facility managers. The authors also thank Susan Monro, Colin Spencer, Ryan DeCoste, Huimin Yin, and Lance Chamberlain for additional synthesis and characterization support for these complexes that was not reported here.

2.7 REFERENCES

(1) Sung, H.; Ferlay, J.; Siegel, R. L.; Laversanne, M.; Soerjomataram, I.; Jemal, A.; Bray, F. Global Cancer Statistics 2020: GLOBOCAN Estimates of Incidence and Mortality Worldwide for 36 Cancers in 185 Countries. *CA A Cancer J Clin* **2021**, *71* (3), 209–249. https://doi.org/10.3322/caac.21660.

(2) Mellman, I.; Coukos, G.; Dranoff, G. Cancer Immunotherapy Comes of Age. *Nature* **2011**, *480* (7378), 480–489. https://doi.org/10.1038/nature10673.

(3) Marabelle, A.; Tselikas, L.; De Baere, T.; Houot, R. Intratumoral Immunotherapy: Using the Tumor as the Remedy. *Annals of Oncology* **2017**, *28*, xii33–xii43. https://doi.org/10.1093/annonc/mdx683.

(4) Meric-Bernstam, F.; Larkin, J.; Tabernero, J.; Bonini, C. Enhancing Anti-Tumour Efficacy with Immunotherapy Combinations. *The Lancet* **2021**, *397* (10278), 1010–1022. https://doi.org/10.1016/S0140-6736(20)32598-8.

(5) Sawyers, C. Targeted Cancer Therapy. *Nature* **2004**, *432* (7015), 294–297. https://doi.org/10.1038/nature03095.

(6) Min, H.-Y.; Lee, H.-Y. Molecular Targeted Therapy for Anticancer Treatment. *Exp Mol Med* **2022**, *54* (10), 1670–1694. https://doi.org/10.1038/s12276-022-00864-3.

(7) Monro, S.; Colón, K. L.; Yin, H.; Roque, J.; Konda, P.; Gujar, S.; Thummel, R. P.; Lilge, L.; Cameron, C. G.; McFarland, S. A. Transition Metal Complexes and Photodynamic Therapy from a Tumor-Centered Approach: Challenges, Opportunities, and Highlights from the Development of TLD1433. *Chem. Rev.* **2019**, *119* (2), 797–828. https://doi.org/10.1021/acs.chemrev.8b00211.

(8) McFarland, S. A.; Mandel, A.; Dumoulin-White, R.; Gasser, G. Metal-Based Photosensitizers for Photodynamic Therapy: The Future of Multimodal Oncology? *Curr. Opin. Chem. Biol.* **2020**, *56*, 23–27. https://doi.org/10.1016/j.cbpa.2019.10.004.

(9) Busch, T. M. Local Physiological Changes during Photodynamic Therapy. *Lasers Surg. Med.* **2006**, *38* (5), 494–499. https://doi.org/10.1002/lsm.20355.

(10) Foster, T. H.; Murant, R. S.; Bryant, R. G.; Knox, R. S.; Gibson, S. L.; Hilf, R. Oxygen Consumption and Diffusion Effects in Photodynamic Therapy. *Radiat. Res.* **1991**, *126* (3), 296–303. https://doi.org/10.2307/3577919.

(11) Howerton, B. S.; Heidary, D. K.; Glazer, E. C. Strained Ruthenium Complexes Are Potent Light-Activated Anticancer Agents. *Journal of the American Chemical Society* **2012**, *134* (20), 8324–8327. https://doi.org/10.1021/ja3009677.

(12) Havrylyuk, D.; Stevens, K.; Parkin, S.; Glazer, E. C. Toward Optimal Ru(II) Photocages: Balancing Photochemistry, Stability, and Biocompatibility Through Fine Tuning of Steric, Electronic, and Physiochemical Features. *Inorganic Chemistry* **2020**, *59* (2), 1006–1013. https://doi.org/10.1021/acs.inorgchem.9b02065.

(13) Loftus, L. M.; White, J. K.; Albani, B. A.; Kohler, L.; Kodanko, J. J.; Thummel, R. P.; Dunbar, K. R.; Turro, C. New Ru^{II} Complex for Dual Activity: Photoinduced Ligand Release and $^1O_2$ Production. *Chem. Eur. J.* **2016**, *22* (11), 3704–3708. https://doi.org/10.1002/chem.201504800.

(14) Toupin, N. P.; Nadella, S.; Steinke, S. J.; Turro, C.; Kodanko, J. J. Dual-Action Ru(II) Complexes with Bulky π-Expansive Ligands: Phototoxicity without DNA Intercalation. *Inorganic Chemistry* **2020**, *59* (6), 3919–3933. https://doi.org/10.1021/acs.inorgchem.9b03585.

(15) Sainuddin, T.; Pinto, M.; Yin, H.; Hetu, M.; Colpitts, J.; McFarland, S. A. Strained Ruthenium Metal–Organic Dyads as Photocisplatin Agents with Dual Action. *J. Inorg. Biochem.* **2016**, *158*, 45–54. https://doi.org/10.1016/j.jinorgbio.2016.01.009.

(16) Lameijer, L. N.; Ernst, D.; Hopkins, S. L.; Meijer, M. S.; Askes, S. H. C.; Le Dévédec, S. E.; Bonnet, S. A Red-Light-Activated Ruthenium-Caged NAMPT Inhibitor Remains Phototoxic in Hypoxic Cancer Cells. *Angew. Chem. Int. Ed.* **2017**, *56* (38), 11549–11553. https://doi.org/10.1002/anie.201703890.

(17) Al-Afyouni, M. H.; Rohrabaugh, T. N.; Al-Afyouni, K. F.; Turro, C. New Ru(II) Photocages Operative with near-IR Light: New Platform for Drug Delivery in the PDT Window. *Chemical Science* **2018**, *9* (32), 6711–6720. https://doi.org/10.1039/C8SC02094A.

(18) Feng, W.; Gao, C.; Liu, W.; Ren, H.; Wang, C.; Ge, K.; Li, S.; Zhou, G.; Li, H.; Wang, S.; Jia, G.; Li, Z.; Zhang, J. A Novel Anticancer Theranostic Pro-Prodrug Based on Hypoxia and Photo Sequential Control. *Chem. Commun.* **2016**, *52* (60), 9434–9437. https://doi.org/10.1039/C6CC02932A.

(19) Li, M.-D.; Wong, N.-K.; Xiao, J.; Zhu, R.; Wu, L.; Dai, S.-Y.; Chen, F.; Huang, G.; Xu, L.; Bai, X.; Geraskina, M. R.; Winter, A. H.; Chen, X.; Liu, Y.; Fang, W.; Yang, D.; Phillips, D. L. Dynamics of Oxygen-Independent Photocleavage of Blebbistatin as a One-Photon Blue or Two-Photon Near-Infrared Light-Gated Hydroxyl Radical Photocage. *Journal of the American Chemical Society* **2018**, *140* (46), 15957–15968. https://doi.org/10.1021/jacs.8b10235.

(20) van Rixel, V. H. S.; Ramu, V.; Auyeung, A. B.; Beztsinna, N.; Leger, D. Y.; Lameijer, L. N.; Hilt, S. T.; Le Dévédec, S. E.; Yildiz, T.; Betancourt, T.; Gildner, M. B.; Hudnall, T. W.; Sol, V.; Liagre, B.; Kornienko, A.; Bonnet, S. Photo-Uncaging of a Microtubule-Targeted Rigidin Analogue in Hypoxic Cancer Cells and in a Xenograft Mouse Model. *J. Am. Chem. Soc.* **2019**, *141* (46), 18444–18454. https://doi.org/10.1021/jacs.9b07225.

(21) Roque, J.; Havrylyuk, D.; Barrett, P. C.; Sainuddin, T.; McCain, J.; Colón, K.; Sparks, W. T.; Bradner, E.; Monro, S.; Heidary, D.; Cameron, C. G.; Glazer, E. C.; McFarland, S. A. Strained, Photoejecting Ru(II) Complexes That Are Cytotoxic Under Hypoxic Conditions. *Photochem. Photobiol.* **2020**, *96* (2), 327–339. https://doi.org/10.1111/php.13174.

(22) Cole, H. D.; Roque, J. A.; Lifshits, L. M.; Hodges, R.; Barrett, P. C.; Havrylyuk, D.; Heidary, D.; Ramasamy, E.; Cameron, C. G.; Glazer, E. C.; McFarland, S. A. Fine-Feature Modifications to Strained Ruthenium Complexes Radically Alter Their Hypoxic Anticancer Activity. *Photochem & Photobiology* **2022**, *98* (1), 73–84. https://doi.org/10.1111/php.13395.

(23) Roque III, J. A.; Barrett, P. C.; Cole, H. D.; Lifshits, L. M.; Shi, G.; Monro, S.; von Dohlen, D.; Kim, S.; Russo, N.; Deep, G.; Cameron, C. G.; Alberto, M. E.; McFarland, S. A. Breaking the Barrier: An Osmium Photosensitizer with Unprecedented Hypoxic Phototoxicity for Real World Photodynamic Therapy. *Chem. Sci.* **2020**, *11*, 9784–9806. https://doi.org/10.1039/D0SC03008B.

(24) Roque, J. A.; Barrett, P. C.; Cole, H. D.; Lifshits, L. M.; Bradner, E.; Shi, G.; von Dohlen, D.; Kim, S.; Russo, N.; Deep, G.; Cameron, C. G.; Alberto, M. E.; McFarland, S. A Os(II) Oligothienyl

Complexes as a Hypoxia-Active Photosensitizer Class for Photodynamic Therapy. *Inorg. Chem.* **2020**, *59* (22), 16341–16360. https://doi.org/10.1021/acs.inorgchem.0c02137.

(25) Lv, Z.; Wei, H.; Li, Q.; Su, X.; Liu, S.; Zhang, K. Y.; Lv, W.; Zhao, Q.; Li, X.; Huang, W. Achieving Efficient Photodynamic Therapy under Both Normoxia and Hypoxia Using Cyclometalated Ru(II) Photosensitizer through Type I Photochemical Process. *Chemical Science* **2018**, *9* (2), 502–512. https://doi.org/10.1039/C7SC03765A.

(26) Yu, Q.; Huang, T.; Liu, C.; Zhao, M.; Xie, M.; Li, G.; Liu, S.; Huang, W.; Zhao, Q. Oxygen Self-Sufficient NIR-Activatable Liposomes for Tumor Hypoxia Regulation and Photodynamic Therapy. *Chem. Sci.* **2019**, *10* (39), 9091–9098. https://doi.org/10.1039/C9SC03161H.

(27) Evans, C. L.; Abu-Yousif, A. O.; Park, Y. J.; Klein, O. J.; Celli, J. P.; Rizvi, I.; Zheng, X.; Hasan, T. Killing Hypoxic Cell Populations in a 3D Tumor Model with EtNBS-PDT. *PLoS ONE* **2011**, *6* (8), e23434. https://doi.org/10.1371/journal.pone.0023434.

(28) Kuang, S.; Wei, F.; Karges, J.; Ke, L.; Xiong, K.; Liao, X.; Gasser, G.; Ji, L.; Chao, H. Photodecaging of a Mitochondria-Localized Iridium(III) Endoperoxide Complex for Two-Photon Photoactivated Therapy under Hypoxia. *J. Am. Chem. Soc.* **2022**, 4091–4101. https://doi.org/10.1021/jacs.1c13137.

(29) Mazuryk, O.; Janczy-Cempa, E.; Łagosz, J.; Rutkowska-Zbik, D.; Machnicka, A.; Krasowska, A.; Pietrzyk, P.; Stochel, G.; Brindell, M. Relevance of the Electron Transfer Pathway in Photodynamic Activity of Ru(II) Polypyridyl Complexes Containing 4,7-Diphenyl-1,10-Phenanthroline Ligands under Normoxic and Hypoxic Conditions. *Dalton Trans.* **2022**, *51* (5), 1888–1900. https://doi.org/10.1039/D1DT02908H.

(30) Xiao, Y.-F.; Chen, W.-C.; Chen, J.-X.; Lu, G.; Tian, S.; Cui, X.; Zhang, Z.; Chen, H.; Wan, Y.; Li, S.; Lee, C.-S. Amplifying Free Radical Generation of AIE Photosensitizer with Small Singlet–Triplet Splitting for Hypoxia-Overcoming Photodynamic Therapy. *ACS Appl. Mater. Interfaces* **2022**, *14* (4), 5112–5121. https://doi.org/10.1021/acsami.1c23797.

(31) Schneider, L.; Kalt, M.; Koch, S.; Sithamparanathan, S.; Villiger, V.; Mattiat, J.; Kradolfer, F.; Slyshkina, E.; Luber, S.; Bonmarin, M.; Maake, C.; Spingler, B. BODIPY-Based Photothermal Agents with Excellent Phototoxic Indices for Cancer Treatment. *J. Am. Chem. Soc.* **2023**, *145* (8), 4534–4544. https://doi.org/10.1021/jacs.2c11650.

(32) Deng, Z.; Li, H.; Chen, S.; Wang, N.; Liu, G.; Liu, D.; Ou, W.; Xu, F.; Wang, X.; Lei, D.; Lo, P.-C.; Li, Y. Y.; Lu, J.; Yang, M.; He, M.-L.; Zhu, G. Near-Infrared-Activated Anticancer Platinum(IV)

Complexes Directly Photooxidize Biomolecules in an Oxygen-Independent Manner. *Nat. Chem.* **2023**, *15* (7), 930–939. https://doi.org/10.1038/s41557-023-01242-w.

(33) Teng, K.-X.; Niu, L.-Y.; Yang, Q.-Z. Supramolecular Photosensitizer Enables Oxygen-Independent Generation of Hydroxyl Radicals for Photodynamic Therapy. *J. Am. Chem. Soc.* **2023**, *145* (7), 4081–4087. https://doi.org/10.1021/jacs.2c11868.

(34) Li, R.; Hu, X.; Shang, F.; Wu, W.; Zhang, H.; Wang, Y.; Pan, J.; Shi, S.; Dong, C. Treatment of Triple Negative Breast Cancer by near Infrared Light Triggered Mild-Temperature Photothermal Therapy Combined with Oxygen-Independent Cytotoxic Free Radicals. *Acta Biomaterialia* **2022**, *148*, 218–229. https://doi.org/10.1016/j.actbio.2022.06.011.

(35) Dutta, D.; Wang, J.; Li, X.; Zhou, Q.; Ge, Z. Covalent Organic Framework Nanocarriers of Singlet Oxygen for Oxygen-Independent Concurrent Photothermal/Photodynamic Therapy to Ablate Hypoxic Tumors. *Small* **2022**, *18* (37), 2202369. https://doi.org/10.1002/smll.202202369.

(36) Cao, F.; Wang, H.; Lu, N.; Zhang, P.; Huang, H. A Photoisomerizable Zinc (II) Complex Inhibits Microtubule Polymerization for Photoactive Therapy. *Angewandte Chemie* **2023**, *135* (14), e202301344. https://doi.org/10.1002/ange.202301344.

(37) Chao, X.-J.; Huang, C.-H.; Tang, M.; Yan, Z.-Y.; Huang, R.; Li, Y.; Zhu, B.-Z. Unusual Enantioselective Cytoplasm-to-Nucleus Translocation and Photosensitization of the Chiral Ru(II) Cationic Complex via Simple Ion-Pairing with Lipophilic Weak Acid Counter-Anions. *Nucleic Acids Research* **2023**, *51* (7), 3041–3054. https://doi.org/10.1093/nar/gkad155.

(38) Chen, Y.; Gu, L.; Ma, B.; Li, X.; Mei, Y.; Zhou, J.; Chong, Y.; Ma, M.; Zhang, M.; Wang, L.; Cheng, Y.; Wu, K.; Zeng, J.; Cheng, M.; Guo, P.; Zhang, P.; He, D. Photoactivatable Metal Organic Framework for Synergistic Ferroptosis and Photodynamic Therapy Using 450 Nm Laser. *Chemical Engineering Journal* **2023**, *454*, 140438. https://doi.org/10.1016/j.cej.2022.140438.

(39) Liu, M.; Luo, Y.; Yan, J.; Xiong, X.; Xing, X.; Kim, J. S.; Zou, T. Photoactivation of Boronic Acid Prodrugs via a Phenyl Radical Mechanism: Iridium(III) Anticancer Complex as an Example. *J. Am. Chem. Soc.* **2023**, *145* (18), 10082–10091. https://doi.org/10.1021/jacs.3c00254.

(40) Gandioso, A.; Izquierdo-García, E.; Mesdom, P.; Arnoux, P.; Demeubayeva, N.; Burckel, P.; Saubaméa, B.; Bosch, M.; Frochot, C.; Marchan, V.; Gasser, G. Ru(II)-Cyanine Complexes as Promising Photodynamic Photosensitizers for the Treatment of Hypoxic Tumours with Highly Penetrating 770 Nm Near-Infrared Light. *Chemistry A European J* **2023**, e202301742. https://doi.org/10.1002/chem.202301742.

(41) He, L.; Xu, F.; Li, Y.; Jin, H.; Lo, P.-C. Cupric-Ion-Promoted Fabrication of Oxygen-Replenishing Nanotherapeutics for Synergistic Chemo and Photodynamic Therapy against Tumor Hypoxia. *Acta Biomaterialia* **2023**, *162*, 57–71. https://doi.org/10.1016/j.actbio.2023.03.020.

(42) He, M.; Wang, R.; Zhang, R.; Miao, P.; Wang, P.; Wei, Z.; Leng, X.; Li, Y.; Fan, J.; Peng, X.; Sun, W. The Construction of Polyphotocage Platform for Anticancer Photochemotherapy. *Adv Funct Materials* **2023**, *33* (26), 2300780. https://doi.org/10.1002/adfm.202300780.

(43) Skelton, E.; Erasquin, U.; Sukul, A.; Zuercher, A.; White, J.; Bythell, B. J.; Cimatu, K. L. A. Visible Light-Assisted Coordination of a Rh(III)-BODIPY Complex to Guanine. *Inorg. Chem.* **2023**, *62* (8), 3368–3380. https://doi.org/10.1021/acs.inorgchem.2c03289.

(44) Luo, T.; Yang, H.; Wang, R.; Pu, Y.; Cai, Z.; Zhao, Y.; Bi, Q.; Lu, J.; Jin, R.; Nie, Y.; Shuai, X. Bifunctional Cascading Nanozymes Based on Carbon Dots Promotes Photodynamic Therapy by Regulating Hypoxia and Glycolysis. *ACS Nano* **2023**, acsnano.3c03169. https://doi.org/10.1021/acsnano.3c03169.

(45) Ma, Z.; Han, H.; Zhao, Y. Mitochondrial Dysfunction-Targeted Nanosystems for Precise Tumor Therapeutics. *Biomaterials* **2023**, *293*, 121947. https://doi.org/10.1016/j.biomaterials.2022.121947.

(46) Nwahara, N.; Abrahams, G.; Mack, J.; Prinsloo, E.; Nyokong, T. A Hypoxia Responsive Silicon Phthalocyanine Containing Naphthquinone Axial Ligands for Photodynamic Therapy Activity. *Journal of Inorganic Biochemistry* **2023**, *239*, 112078. https://doi.org/10.1016/j.jinorgbio.2022.112078.

(47) Olelewe, C.; Awuah, S. G. Mitochondria as a Target of Third Row Transition Metal-Based Anticancer Complexes. *Current Opinion in Chemical Biology* **2023**, *72*, 102235. https://doi.org/10.1016/j.cbpa.2022.102235.

(48) Peng, J.; Du, K.; Sun, J.; Yang, X.; Wang, X.; Zhang, X.; Song, G.; Feng, F. Photocatalytic Generation of Hydrogen Radical (H·) with GSH for Photodynamic Therapy. *Angew Chem Int Ed* **2023**, *62* (9), e202214991. https://doi.org/10.1002/anie.202214991.

(49) Rainho, M. D. A.; Siqueira, P. B.; De Amorim, Í. S. S.; Mencalha, A. L.; Thole, A. A. Mitochondria in Colorectal Cancer Stem Cells - a Target in Drug Resistance. *Cancer Drug Resist* **2023**, *6* (2), 273–283. https://doi.org/10.20517/cdr.2022.116.

(50) Rovira, A.; Ortega-Forte, E.; Hally, C.; Jordà-Redondo, M.; Abad-Montero, D.; Vigueras, G.; Martínez, J. I.; Bosch, M.; Nonell, S.; Ruiz, J.; Marchán, V. Exploring Structure–Activity

Relationships in Photodynamic Therapy Anticancer Agents Based on Ir(III)-COUPY Conjugates. *J. Med. Chem.* **2023**, *66* (12), 7849–7867. https://doi.org/10.1021/acs.jmedchem.3c00189.

(51) Silva, R. C.; Buzzá, H. H.; Ducas, E. S. A.; Oliveira, K. T.; Bagnato, V. S.; Souza, G. R. L.; Almeida, L. M.; Gonçalves, P. J. Synergic Vascular Photodynamic Activity by Methylene Blue-Curcumin Supramolecular Assembly. *Spectrochimica Acta Part A: Molecular and Biomolecular Spectroscopy* **2023**, *303*, 123281. https://doi.org/10.1016/j.saa.2023.123281.

(52) Yang, Y.; Zou, X.; Sun, Y.; Chen, F.; Zhao, J.; Gou, S. Naphthalene Diimide-Functionalized Half-Sandwich Ru(II) Complexes as Mitochondria-Targeted Anticancer and Antimetastatic Agents. *Inorg. Chem.* **2023**, *62* (24), 9649–9660. https://doi.org/10.1021/acs.inorgchem.3c01125.

(53) Sumit; Maravajjala, K. S.; Khanna, S.; Kachwal, V.; Swetha, K. L.; Manabala, S.; Chowdhury, R.; Roy, A.; Laskar, I. R. Rational Molecular Designing of Aggregation-Enhanced Emission (AEE) Active Red-Emitting Iridium(III) Complexes: Effect of Lipophilicity and Nanoparticle Encapsulation on Photodynamic Therapy Efficacy. *ACS Appl. Bio Mater.* **2023**, *6* (4), 1445–1459. https://doi.org/10.1021/acsabm.2c00998.

(54) Warszyńska, M.; Repetowski, P.; Dąbrowski, J. M. Photodynamic Therapy Combined with Immunotherapy: Recent Advances and Future Research Directions. *Coordination Chemistry Reviews* **2023**, *495*, 215350. https://doi.org/10.1016/j.ccr.2023.215350.

(55) Weynand, J.; Episkopou, H.; Le Berre, G.; Gillard, M.; Dejeu, J.; Decottignies, A.; Defrancq, E.; Elias, B. Photo-Induced Telomeric DNA Damage in Human Cancer Cells. *RSC Chem. Biol.* **2022**, *3* (12), 1375–1379. https://doi.org/10.1039/D2CB00192F.

(56) Zhou, J.-Y.; Shen, Q.-H.; Hong, X.-J.; Zhang, W.-Y.; Su, Q.; Li, W.-G.; Cheng, B.; Tan, C.-P.; Wu, T. Synergization of an Endoplasmic Reticulum-Targeted Iridium(III) Photosensitizer with PD-L1 Inhibitor for Oral Squamous Cell Carcinoma Immunotherapy. *Chemical Engineering Journal* **2023**, *474*, 145516. https://doi.org/10.1016/j.cej.2023.145516.

(57) Yuan, Z.; Wu, J.; Xiao, Y.; Yang, H.; Meng, S.; Dai, L.; Li, P.; Cai, K. A Photo-Therapeutic Nanocomposite with Bio-Responsive Oxygen Self-Supplying Combats Biofilm Infections and Inflammation from Drug-Resistant Bacteria. *Adv Funct Materials* **2023**, 2302908. https://doi.org/10.1002/adfm.202302908.

(58) Zhang, L.; Wang, P.; Zhou, X.-Q.; Bretin, L.; Zeng, X.; Husiev, Y.; Polanco, E. A.; Zhao, G.; Wijaya, L. S.; Biver, T.; Le Dévédec, S. E.; Sun, W.; Bonnet, S. Cyclic Ruthenium-Peptide Conjugates as Integrin-Targeting Phototherapeutic Prodrugs for the Treatment of Brain Tumors. *J. Am. Chem. Soc.* **2023**, *145* (27), 14963–14980. https://doi.org/10.1021/jacs.3c04855.

(59) Zhdankin, G. I.; Grivin, V. P.; Plyusnin, V. F.; Tkachenko, P. A.; Vasilchenko, D. B.; Glebov, E. M. Chain Photosolvation of Trans,Trans,Trans-[PtIV(Py)2(N3)2(OH)2] Complex Prospective as a Light-Activated Antitumor Agent. *Mendeleev Communications* **2023**, *33* (1), 61–63. https://doi.org/10.1016/j.mencom.2023.01.019.

(60) Knoll, J. D.; Albani, B. A.; Turro, C. Excited State Investigation of a New Ru(II) Complex for Dual Reactivity with Low Energy Light. *Chem. Commun. (Camb.)* **2015**, *51*, 8777–8780. https://doi.org/10.1039/c5cc01865j.

(61) Knoll, J. D.; Turro, C. Control and Utilization of Ruthenium and Rhodium Metal Complex Excited States for Photoactivated Cancer Therapy. *Coord. Chem. Rev.* **2015**, *282–283*, 110–126. https://doi.org/10.1016/j.ccr.2014.05.018.

(62) Bonnet, S. Why Develop Photoactivated Chemotherapy? *Dalton Transactions* **2018**, *47* (31), 10330–10343. https://doi.org/10.1039/C8DT01585F.

(63) Roque III, J. A.; Cole, H. D.; Barrett, P. C.; Lifshits, L. M.; Hodges, R. O.; Kim, S.; Deep, G.; Francés-Monerris, A.; Alberto, M. E.; Cameron, C. G.; McFarland, S. A. Intraligand Excited States Turn a Ruthenium Oligothiophene Complex into a Light-Triggered Ubertoxin with Anticancer Effects in Extreme Hypoxia. *J. Am. Chem. Soc.* **2022**, *144* (18), 8317–8336. https://doi.org/10.1021/jacs.2c02475.

(64) White, J. K.; Schmehl, R. H.; Turro, C. An Overview of Photosubstitution Reactions of Ru(II) Imine Complexes and Their Application in Photobiology and Photodynamic Therapy. *Inorg. Chim. Acta* **2017**, *454* (Supplement C), 7–20. https://doi.org/10.1016/j.ica.2016.06.007.

(65) Knoll, J. D.; Albani, B. A.; Turro, C. New Ru(II) Complexes for Dual Photoreactivity: Ligand Exchange and 1O2 Generation. *Accounts of Chemical Research* **2015**, *48* (8), 2280–2287. https://doi.org/10.1021/acs.accounts.5b00227.

(66) Sun, Y.; Joyce, L. E.; Dickson, N. M.; Turro, C. Efficient DNA Photocleavage by [Ru(Bpy)2(Dppn)]2+ with Visible Light. *Chem. Commun.* **2010**, *46* (14), 2426–2428. https://doi.org/10.1039/B925574E.

(67) Liu, Y.; Hammitt, R.; Lutterman, D. A.; Joyce, L. E.; Thummel, R. P.; Turro, C. Ru(II) Complexes of New Tridentate Ligands: Unexpected High Yield of Sensitized $^1O_2$. *Inorganic Chemistry* **2009**, *48* (1), 375–385. https://doi.org/10.1021/ic801636u.

(68) Zhao, R.; Hammitt, R.; Thummel, R. P.; Liu, Y.; Turro, C.; Snapka, R. M. Nuclear Targets of Photodynamic Tridentate Ruthenium Complexes. *Dalton Transactions* **2009**, No. 48, 10926. https://doi.org/10.1039/b913959a.

(69) Yin, H.; Stephenson, M.; Gibson, J.; Sampson, E.; Shi, G.; Sainuddin, T.; Monro, S.; McFarland, S. A. In Vitro Multiwavelength PDT with 3IL States: Teaching Old Molecules New Tricks. *Inorganic Chemistry* **2014**, *53* (9), 4548–4559. https://doi.org/10.1021/ic5002368.

(70) Albani, B. A.; Peña, B.; Leed, N. A.; de Paula, N. A. B. G.; Pavani, C.; Baptista, M. S.; Dunbar, K. R.; Turro, C. Marked Improvement in Photoinduced Cell Death by a New Tris-Heteroleptic Complex with Dual Action: Singlet Oxygen Sensitization and Ligand Dissociation. *Journal of the American Chemical Society* **2014**, *136* (49), 17095–17101. https://doi.org/10.1021/ja508272h.

(71) Wachter, E.; Heidary, D. K.; Howerton, B. S.; Parkin, S.; Glazer, E. C. Light-Activated Ruthenium Complexes Photobind DNA and Are Cytotoxic in the Photodynamic Therapy Window. *Chem. Commun.* **2012**, *48* (77), 9649. https://doi.org/10.1039/c2cc33359g.

(72) Bonnett, R. *Chemical Aspects of Photodynamic Therapy*; Advanced chemistry texts; Gordon and Breach Science Publishers: Amsterdam, The Netherlands, 2000.

(73) Bonnet, S. Shifting the Light Activation of Metallodrugs to the Red and Near-Infrared Region in Anticancer Phototherapy. *Comments on Inorganic Chemistry* **2015**, *35* (4), 179–213. https://doi.org/10.1080/02603594.2014.979286.

(74) Cuello-Garibo, J.-A.; Meijer, M. S.; Bonnet, S. To Cage or to Be Caged? The Cytotoxic Species in Ruthenium-Based Photoactivated Chemotherapy Is Not Always the Metal. *Chem. Commun.* **2017**, *53* (50), 6768–6771. https://doi.org/10.1039/C7CC03469E.

(75) Azar, D. F.; Audi, H.; Farhat, S.; El-Sibai, M.; Abi-Habib, R. J.; Khnayzer, R. S. Phototoxicity of Strained Ru(II) Complexes: Is It the Metal Complex or the Dissociating Ligand? *Dalton Trans.* **2017**, *46* (35), 11529–11532. https://doi.org/10.1039/C7DT02255G.

(76) Cole, H. D.; Roque, J. A.; Shi, G.; Lifshits, L. M.; Ramasamy, E.; Barrett, P. C.; Hodges, R. O.; Cameron, C. G.; McFarland, S. A. Anticancer Agent with Inexplicable Potency in Extreme Hypoxia: Characterizing a Light-Triggered Ruthenium Ubertoxin. *J. Am. Chem. Soc.* **2022**, *144* (22), 9543–9547. https://doi.org/10.1021/jacs.1c09010.

(77) Sun, Y.; Heidary, D. K.; Zhang, Z.; Richards, C. I.; Glazer, E. C. Bacterial Cytological Profiling Reveals the Mechanism of Action of Anticancer Metal Complexes. *Mol. Pharm.* **2018**, *15* (8), 3404–3416. https://doi.org/10.1021/acs.molpharmaceut.8b00407.

(78) Albani, B. A.; Durr, C. B.; Turro, C. Selective Photoinduced Ligand Exchange in a New Tris–Heteroleptic Ru(II) Complex. *The Journal of Physical Chemistry A* **2013**, *117* (50), 13885–13892. https://doi.org/10.1021/jp4085684.

(79) Knoll, J. D.; Albani, B. A.; Durr, C. B.; Turro, C. Unusually Efficient Pyridine Photodissociation from Ru(II) Complexes with Sterically Bulky Bidentate Ancillary Ligands. *The Journal of Physical Chemistry A* **2014**, *118* (45), 10603–10610. https://doi.org/10.1021/jp5057732.

(80) Arora, K.; White, J. K.; Sharma, R.; Mazumder, S.; Martin, P. D.; Schlegel, H. B.; Turro, C.; Kodanko, J. J. Effects of Methyl Substitution in Ruthenium Tris(2-Pyridylmethyl)Amine Photocaging Groups for Nitriles. *Inorganic Chemistry* **2016**, *55* (14), 6968–6979. https://doi.org/10.1021/acs.inorgchem.6b00650.

(81) Huisman, M.; White, J. K.; Lewalski, V. G.; Podgorski, I.; Turro, C.; Kodanko, J. J. Caging the Uncageable: Using Metal Complex Release for Photochemical Control over Irreversible Inhibition. *Chemical Communications* **2016**, *52* (85), 12590–12593. https://doi.org/10.1039/C6CC07083C.

(82) Li, A.; Yadav, R.; White, J. K.; Herroon, M. K.; Callahan, B. P.; Podgorski, I.; Turro, C.; Scott, E. E.; Kodanko, J. J. Illuminating Cytochrome P450 Binding: Ru(II)-Caged Inhibitors of CYP17A1. *Chem. Commun.* **2017**, *53* (26), 3673–3676. https://doi.org/10.1039/C7CC01459G.

(83) Arora, K.; Herroon, M.; Al-Afyouni, M. H.; Toupin, N. P.; Rohrabaugh, T. N.; Loftus, L. M.; Podgorski, I.; Turro, C.; Kodanko, J. J. Catch and Release Photosensitizers: Combining Dual-Action Ruthenium Complexes with Protease Inactivation for Targeting Invasive Cancers. *J. Am. Chem. Soc.* **2018**, *140* (43), 14367–14380. https://doi.org/10.1021/jacs.8b08853.

(84) Li, A.; Turro, C.; Kodanko, J. J. Ru(II) Polypyridyl Complexes Derived from Tetradentate Ancillary Ligands for Effective Photocaging. *Accounts of Chemical Research* **2018**, *51* (6), 1415–1421. https://doi.org/10.1021/acs.accounts.8b00066.

(85) Li, A.; Turro, C.; Kodanko, J. J. Ru(II) Polypyridyl Complexes as Photocages for Bioactive Compounds Containing Nitriles and Aromatic Heterocycles. *Chem. Commun.* **2018**, *54* (11), 1280–1290. https://doi.org/10.1039/C7CC09000E.

(86) Nisbett, K.; Tu, Y.-J.; Turro, C.; Kodanko, J. J.; Schlegel, H. B. DFT Investigation of Ligand Photodissociation in [RuII(Tpy)(Bpy)(Py)]2+ and [RuII(Tpy)(Me2bpy)(Py)]2+ Complexes. *Inorganic Chemistry* **2018**, *57* (1), 231–240. https://doi.org/10.1021/acs.inorgchem.7b02398.

(87) Rohrabaugh, T. N.; Rohrabaugh, A. M.; Kodanko, J. J.; White, J. K.; Turro, C. Photoactivation of Imatinib–Antibody Conjugate Using Low-Energy Visible Light from Ru(II)-Polypyridyl Cages. *Chem. Commun.* **2018**, *54* (41), 5193–5196. https://doi.org/10.1039/C8CC01348A.

(88) Bahreman, A.; Limburg, B.; Siegler, M. A.; Bouwman, E.; Bonnet, S. Spontaneous Formation in the Dark, and Visible Light-Induced Cleavage, of a Ru–S Bond in Water: A Thermodynamic and Kinetic Study. *Inorganic Chemistry* **2013**, *52* (16), 9456–9469. https://doi.org/10.1021/ic401105v.

(89) Bahreman, A.; Rabe, M.; Kros, A.; Bruylants, G.; Bonnet, S. Binding of a Ruthenium Complex to a Thioether Ligand Embedded in a Negatively Charged Lipid Bilayer: A Two-Step Mechanism. *Chemistry - A European Journal* **2014**, *20* (24), 7429–7438. https://doi.org/10.1002/chem.201400377.

(90) Göttle, A. J.; Alary, F.; Boggio-Pasqua, M.; Dixon, I. M.; Heully, J.-L.; Bahreman, A.; Askes, S. H. C.; Bonnet, S. Pivotal Role of a Pentacoordinate ^{3}MC State on the Photocleavage Efficiency of a Thioether Ligand in Ruthenium(II) Complexes: A Theoretical Mechanistic Study. *Inorganic Chemistry* **2016**, *55* (9), 4448–4456. https://doi.org/10.1021/acs.inorgchem.6b00268.

(91) Cuello-Garibo, J.-A.; Pérez-Gallent, E.; van der Boon, L.; Siegler, M. A.; Bonnet, S. Influence of the Steric Bulk and Solvent on the Photoreactivity of Ruthenium Polypyridyl Complexes Coordinated to L-Proline. *Inorganic Chemistry* **2017**, *56* (9), 4818–4828. https://doi.org/10.1021/acs.inorgchem.6b02794.

(92) Sun, W.; Wen, Y.; Thiramanas, R.; Chen, M.; Han, J.; Gong, N.; Wagner, M.; Jiang, S.; Meijer, M. S.; Bonnet, S.; Butt, H.-J.; Mailänder, V.; Liang, X.-J.; Wu, S. Red-Light-Controlled Release of Drug-Ru Complex Conjugates from Metallopolymer Micelles for Phototherapy in Hypoxic Tumor Environments. *Adv. Funct. Mater.* **2018**, *28* (39), 1804227. https://doi.org/10.1002/adfm.201804227.

(93) Meijer, M. S.; Talens, V. S.; Hilbers, M. F.; Kieltyka, R. E.; Brouwer, A. M.; Natile, M. M.; Bonnet, S. NIR-Light-Driven Generation of Reactive Oxygen Species Using Ru(II)-Decorated Lipid-Encapsulated Upconverting Nanoparticles. *Langmuir* **2019**, *35* (37), 12079–12090. https://doi.org/10.1021/acs.langmuir.9b01318.

(94) Havrylyuk, D.; Hachey, A. C.; Fenton, A.; Heidary, D. K.; Glazer, E. C. Ru(II) Photocages Enable Precise Control over Enzyme Activity with Red Light. *Nat Commun* **2022**, *13* (1), 3636. https://doi.org/10.1038/s41467-022-31269-5.

(95) Ryan, R. T.; Havrylyuk, D.; Stevens, K. C.; Moore, L. H.; Parkin, S.; Blackburn, J. S.; Heidary, D. K.; Selegue, J. P.; Glazer, E. C. Biological Investigations of Ru(II) Complexes with Diverse β-Diketone Ligands. *Eur. J. Inorg. Chem.* **2021**, *2021* (35), 3611–3621. https://doi.org/10.1002/ejic.202100468.

(96) Huang, H.; Banerjee, S.; Qiu, K.; Zhang, P.; Blacque, O.; Malcomson, T.; Paterson, M. J.; Clarkson, G. J.; Staniforth, M.; Stavros, V. G.; Gasser, G.; Chao, H.; Sadler, P. J. Targeted Photoredox Catalysis in Cancer Cells. *Nat. Chem.* **2019**, *11* (11), 1041–1048. https://doi.org/10.1038/s41557-019-0328-4.

(97) Baptista, M. S.; Cadet, J.; Di Mascio, P.; Ghogare, A. A.; Greer, A.; Hamblin, M. R.; Lorente, C.; Nunez, S. C.; Ribeiro, M. S.; Thomas, A. H.; Vignoni, M.; Yoshimura, T. M. Type I and Type II Photosensitized Oxidation Reactions: Guidelines and Mechanistic Pathways. *Photochemistry and Photobiology* **2017**, *93* (4), 912–919. https://doi.org/10.1111/php.12716.

(98) Shi, G.; Monro, S.; Hennigar, R.; Colpitts, J.; Fong, J.; Kasimova, K.; Yin, H.; DeCoste, R.; Spencer, C.; Chamberlain, L.; Mandel, A.; Lilge, L.; McFarland, S. A. Ru(II) Dyads Derived from α-Oligothiophenes: A New Class of Potent and Versatile Photosensitizers for PDT. *Coord. Chem. Rev.* **2015**, *282–283*, 127–138. https://doi.org/10.1016/j.ccr.2014.04.012.

(99) Lifshits, L. M.; Roque, J. A.; Cole, H. D.; Thummel, R. P.; Cameron, C. G.; McFarland, S. A. NIR-Absorbing Ru II Complexes Containing α-Oligothiophenes for Applications in Photodynamic Therapy. *ChemBioChem* **2020**, *21*, 3594–3607. https://doi.org/10.1002/cbic.202000419.

(100) Luis, E. T.; Ball, G. E.; Gilbert, A.; Iranmanesh, H.; Newdick, C. W.; Beves, J. E. Efficient Microwave-Assisted Synthesis and Characterization of Key Ruthenium(II) Polypyridyl Complexes $[Ru(Bpy)_3](PF_6)_2$, $[Ru(Phen)_3](PF_6)_2$, $[Ru(Bpy)_2(Phen)](PF_6)_2$ and $[Ru(Phen)_2(Bpy)](PF_6)_2$. *Journal of Coordination Chemistry* **2016**, *69* (11–13), 1686–1694. https://doi.org/10.1080/00958972.2016.1194404.

(101) Sullivan, B.; Salmon, D.; Meyer, T. Mixed Phosphine 2,2’-Bipyridine Complexes of Ruthenium. **1978**, *17*, 3334–3341.

(102) Wang, Z. *Comprehensive Organic Name Reactions and Reagents*; John Wiley & Sons, Inc.: Hoboken, NJ, USA, 2010. https://doi.org/10.1002/9780470638859.

(103) Ghosh, G.; Colón, K. L.; Fuller, A.; Sainuddin, T.; Bradner, E.; McCain, J.; Monro, S. M. A.; Yin, H.; Hetu, M. W.; Cameron, C. G.; McFarland, S. A. Cyclometalated Ruthenium(II) Complexes Derived from α-Oligothiophenes as Highly Selective Cytotoxic or Photocytotoxic Agents. *Inorg. Chem.* **2018**, *57* (13), 7694–7712. https://doi.org/10.1021/acs.inorgchem.8b00689.

(104) Chen, R.; Yang, X.; Tian, H.; Wang, X.; Hagfeldt, A.; Sun, L. Effect of Tetrahydroquinoline Dyes Structure on the Performance of Organic Dye-Sensitized Solar Cells. *Chem. Mater.* **2007**, *19* (16), 4007–4015. https://doi.org/10.1021/cm070617g.

(105) Casida, M. E. Time–Dependent Density Functional Response Theory of Molecular Systems: Theory, Computational Methods, and Functionals. In *Recent developments and applications of modern density functional theory*; Seminario, J. M., Ed.; Theoretical and computational chemistry; Elsevier: Amsterdam; Netherlands, 1996; pp 155–192.

(106) Frisch, M. J.; Trucks, G. W.; Schlegel, H. B.; Scuseria, G. E.; Robb, M. A.; Cheeseman, J. R.; Scalmani, G.; Barone, V.; Petersson, G. A.; Nakatsuji, H.; Li, X.; Caricato, M.; Marenich, A. V.; Bloino, J.; Janesko, B. G.; Gomperts, R.; Mennucci, B.; Hratchian, H. P.; Ortiz, J. V.; Izmaylov, A. F.; Sonnenberg, J. L.; Williams-Young, D.; Ding, F.; Lipparini, F.; Egidi, F.; Goings, J.; Peng, B.; Petrone, A.; Henderson, T.; Ranasinghe, D.; Zakrzewski, V. G.; Gao, J.; Rega, N.; Zheng, G.; Liang, W.; Hada, M.; Ehara, M.; Toyota, K.; Fukuda, R.; Hasegawa, J.; Ishida, M.; Nakajima, T.; Honda, Y.; Kitao, O.; Nakai, H.; Vreven, T.; Throssell, K.; Montgomery, J. A., Jr.; Peralta, J. E.; Ogliaro, F.; Bearpark, M. J.; Heyd, J. J.; Brothers, E. N.; Kudin, K. N.; Staroverov, V. N.; Keith, T. A.; Kobayashi, R.; Normand, J.; Raghavachari, K.; Rendell, A. P.; Burant, J. C.; Iyengar, S. S.; Tomasi, J.; Cossi, M.; Millam, J. M.; Klene, M.; Adamo, C.; Cammi, R.; Ochterski, J. W.; Martin, R. L.; Morokuma, K.; Farkas, O.; Foresman, J. B.; Fox, D. J. *Gaussian 16 Revision C.01*; 2016.

(107) Ponte, F.; Alberto, M. E.; De Simone, B. C.; Russo, N.; Sicilia, E. Photophysical Exploration of Dual-Approach Pt^{II}–BODIPY Conjugates: Theoretical Insights. *Inorg. Chem.* **2019**, *58* (15), 9882–9889. https://doi.org/10.1021/acs.inorgchem.9b01002.

(108) Alberto, M. E.; Francés-Monerris, A. A Multiscale Free Energy Method Reveals an Unprecedented Photoactivation of a Bimetallic Os(II)–Pt(II) Dual Anticancer Agent. *Phys. Chem. Chem. Phys.* **2022**, *24* (32), 19584–19594. https://doi.org/10.1039/D2CP02128E.

(109) Alberto, M. E.; Russo, N.; Adamo, C. Synergistic Effects of Metals in a Promising Ru^{II}−Pt^{II} Assembly for a Combined Anticancer Approach: Theoretical Exploration of the Photophysical Properties. *Chemistry - A European Journal* **2016**, *22* (27), 9162–9168. https://doi.org/10.1002/chem.201601089.

(110) Alberto, M. E.; Pirillo, J.; Russo, N.; Adamo, C. Theoretical Exploration of Type I/Type II Dual Photoreactivity of Promising Ru(II) Dyads for PDT Approach. *Inorg. Chem.* **2016**, *55* (21), 11185–11192. https://doi.org/10.1021/acs.inorgchem.6b01782.

(111) Bertini, L.; Alberto, M. E.; Arrigoni, F.; Vertemara, J.; Fantucci, P.; Bruschi, M.; Zampella, G.; De Gioia, L. On the Photochemistry of $Fe_2(Edt)(CO)_4(PMe_3)_2$, a [FeFe]-Hydrogenase Model: A DFT/TDDFT Investigation. *Int J Quantum Chem* **2018**, *118* (9), e25537. https://doi.org/10.1002/qua.25537.

(112) Alberto, M. E.; Adamo, C. Synergistic Effects in Pt^{II}-Porphyrinoid Dyes as Candidates for a Dual-Action Anticancer Therapy: A Theoretical Exploration. *Chemistry - A European Journal* **2017**, *23* (60), 15124–15132. https://doi.org/10.1002/chem.201702876.

(113) Francés-Monerris, A.; Magra, K.; Darari, M.; Cebrián, C.; Beley, M.; Domenichini, E.; Haacke, S.; Pastore, M.; Assfeld, X.; Gros, P. C.; Monari, A. Synthesis and Computational Study of a Pyridylcarbene Fe(II) Complex: Unexpected Effects of *Fac*/ *Mer* Isomerism in Metal-to-Ligand Triplet Potential Energy Surfaces. *Inorg. Chem.* **2018**, *57* (16), 10431–10441. https://doi.org/10.1021/acs.inorgchem.8b01695.

(114) Alberto, M. E.; Mazzone, G.; Regina, C.; Russo, N.; Sicilia, E. Theoretical Exploration of the Photophysical Properties of Two-Component Ru^{II}–Porphyrin Dyes as Promising Assemblies for a Combined Antitumor Effect. *Dalton Trans.* **2020**, *49* (36), 12653–12661. https://doi.org/10.1039/D0DT02197K.

(115) Adamo, C.; Barone, V. Toward Reliable Density Functional Methods without Adjustable Parameters: The PBE0 Model. *The Journal of Chemical Physics* **1999**, *110* (13), 6158–6170. https://doi.org/10.1063/1.478522.

(116) Andrae, D.; Häußermann, U.; Dolg, M.; Stoll, H.; Preuß, H. Energy-Adjusted Ab Initio Pseudopotentials for the Second and Third Row Transition Elements. *Theoret. Chim. Acta* **1990**, *77* (2), 123–141. https://doi.org/10.1007/BF01114537.

(117) Cossi, M.; Barone, V. Solvent Effect on Vertical Electronic Transitions by the Polarizable Continuum Model. *The Journal of Chemical Physics* **2000**, *112* (5), 2427–2435. https://doi.org/10.1063/1.480808.

(118) Tomasi, J.; Mennucci, B.; Cammi, R. Quantum Mechanical Continuum Solvation Models. *Chemical Reviews* **2005**, *105* (8), 2999–3094. https://doi.org/10.1021/cr9904009.

(119) Cossi, M.; Rega, N.; Scalmani, G.; Barone, V. Energies, Structures, and Electronic Properties of Molecules in Solution with the C-PCM Solvation Model. *J. Comput. Chem.* **2003**, *24* (6), 669–681. https://doi.org/10.1002/jcc.10189.

(120) Hirata, S.; Head-Gordon, M. Time-Dependent Density Functional Theory within the Tamm–Dancoff Approximation. *Chemical Physics Letters* **1999**, *314* (3–4), 291–299. https://doi.org/10.1016/S0009-2614(99)01149-5.

(121) Peach, M. J. G.; Williamson, M. J.; Tozer, D. J. Influence of Triplet Instabilities in TDDFT. *J. Chem. Theory Comput.* **2011**, *7* (11), 3578–3585. https://doi.org/10.1021/ct200651r.

(122) Skripnikov, L. *Chemissan*, 43rd ed.; Vol. 4.

(123) Plasser, F. TheoDORE: A Toolbox for a Detailed and Automated Analysis of Electronic Excited State Computations. *The Journal of Chemical Physics* **2020**, *152* (8), 084108. https://doi.org/10.1063/1.5143076.

(124) Scherrer, R. A.; Howard, S. M. Use of Distribution Coefficients in Quantitative Structure-Activity Relations. *J. Med. Chem.* **1977**, *20* (1), 53–58. https://doi.org/10.1021/jm00211a010.

(125) Alberto, M. E.; De Simone, B. C.; Mazzone, G.; Sicilia, E.; Russo, N. The Heavy Atom Effect on Zn(II) Phthalocyanine Derivatives: A Theoretical Exploration of the Photophysical Properties. *Physical Chemistry Chemical Physics* **2015**, *17* (36), 23595–23601. https://doi.org/10.1039/C5CP03833B.

(126) DeRosa, M. Photosensitized Singlet Oxygen and Its Applications. *Coordination Chemistry Reviews* **2002**, *233–234*, 351–371. https://doi.org/10.1016/S0010-8545(02)00034-6.

(127) Young, R. C.; Meyer, T. J.; Whitten, D. G. Electron Transfer Quenching of Excited States of Metal Complexes. *J. Am. Chem. Soc.* **1976**, *98* (1), 286–287. https://doi.org/10.1021/ja00417a073.

(128) Becker, R. S.; Seixas de Melo, J.; Maçanita, A. L.; Elisei, F. Comprehensive Evaluation of the Absorption, Photophysical, Energy Transfer, Structural, and Theoretical Properties of α-Oligothiophenes with One to Seven Rings. *J. Phys. Chem.* **1996**, *100*, 18683–18695. https://doi.org/10.1021/jp960852e.

(129) Juris, A.; Balzani, V.; Barigelletti, F.; Campagna, S.; Belser, P.; von Zelewsky, A. Ru(II) Polypyridine Complexes: Photophysics, Photochemistry, Eletrochemistry, and Chemiluminescence. *Coordination Chemistry Reviews* **1988**, *84*, 85–277. https://doi.org/10.1016/0010-8545(88)80032-8.

(130) Elfring, W. H.; Crosby, G. A. Excited States of Mixed-Ligand Chelates of Ruthenium(II). Quantum Yield and Decay Time Measurements. *J. Am. Chem. Soc.* **1981**, *103* (10), 2683–2687. https://doi.org/10.1021/ja00400a032.

(131) Hissler, M.; Connick, W. B.; Geiger, D. K.; McGarrah, J. E.; Lipa, D.; Lachicotte, R. J.; Eisenberg, R. Platinum Diimine Bis(Acetylide) Complexes: Synthesis, Characterization, and Luminescence Properties. *Inorg. Chem.* **2000**, *39* (3), 447–457. https://doi.org/10.1021/ic991250n.

(132) Lincoln, R.; Kohler, L.; Monro, S.; Yin, H.; Stephenson, M.; Zong, R.; Chouai, A.; Dorsey, C.; Hennigar, R.; Thummel, R. P.; McFarland, S. A. Exploitation of Long-Lived 3IL Excited States for Metal–Organic Photodynamic Therapy: Verification in a Metastatic Melanoma Model. *J. Am. Chem. Soc.* **2013**, *135* (45), 17161–17175. https://doi.org/10.1021/ja408426z.

(133) DeRosa, M. C.; Crutchley, R. J. Photosensitized Singlet Oxygen and Its Applications. *Coord. Chem. Rev.* **2002**, *233–234*, 351–371. https://doi.org/10.1016/S0010-8545(02)00034-6.

(134) Montalti, M.; Credi, A.; Prodi, L.; Gandolfi, M. T. *Handbook of Photochemistry*; CRC Press, 2006. https://doi.org/10.1201/9781420015195.

(135) Lifshits, L. M.; Roque III, J. A.; Konda, P.; Monro, S.; Cole, H. D.; von Dohlen, D.; Kim, S.; Deep, G.; Thummel, R. P.; Cameron, C. G.; Gujar, S.; McFarland, S. A. Near-Infrared Absorbing Ru(II) Complexes Act as Immunoprotective Photodynamic Therapy (PDT) Agents against Aggressive Melanoma. *Chem. Sci.* **2020**, *11* (43), 11740–11762. https://doi.org/10.1039/D0SC03875J.

(136) Chettri, A.; Roque, J. A.; Schneider, K. R. A.; Cole, H. D.; Cameron, C. G.; McFarland, S. A.; Dietzek, B. It Takes Three to Tango: The Length of the Oligothiophene Chain Determines the Nature of the Long-Lived Excited State and the Resulting Photocytotoxicity of a Ruthenium(II) Photodrug. *ChemPhotoChem* **2021**, *5* (5), 421–425. https://doi.org/10.1002/cptc.202000283.

(137) McCain, J.; Colón, K. L.; Barrett, P. C.; Monro, S. M. A.; Sainuddin, T.; Roque III, J.; Pinto, M.; Yin, H.; Cameron, C. G.; McFarland, S. A. Photophysical Properties and Photobiological Activities of Ruthenium(II) Complexes Bearing π-Expansive Cyclometalating Ligands with Thienyl Groups. *Inorg. Chem.* **2019**, *58* (16), 10778–10790. https://doi.org/10.1021/acs.inorgchem.9b01044.

(138) Monro, S.; Cameron, C. G.; Zhu, X.; Colón, K. L.; Yin, H.; Sainuddin, T.; Hetu, M.; Pinto, M.; Fuller, A.; Bennett, L.; Roque, J.; Sun, W.; McFarland, S. A. Synthesis, Characterization and Photobiological Studies of Ru(II) Dyads Derived from α-Oligothiophene Derivatives of 1,10-Phenanthroline. *Photochem. Photobiol.* **2019**, *95* (1), 267–279. https://doi.org/10.1111/php.13012.

(139) Ghosh, G.; Colón, K. L.; Fuller, A.; Sainuddin, T.; Bradner, E.; McCain, J.; Monro, S. M. A.; Yin, H.; Hetu, M. W.; Cameron, C. G.; McFarland, S. A. Cyclometalated Ruthenium(II) Complexes Derived from α-Oligothiophenes as Highly Selective Cytotoxic or Photocytotoxic Agents. *Inorg. Chem.* **2018**, *57* (13), 7694–7712. https://doi.org/10.1021/acs.inorgchem.8b00689.

(140) Diaz, A. F.; Crowley, J.; Bargon, J.; Gardini, G. P.; Torrance, J. B. Electrooxidation of Aromatic Oligomers and Conducting Polymers. *Journal of Electroanalytical Chemistry and Interfacial Electrochemistry* **1981**, *121*, 355–361. https://doi.org/10.1016/S0022-0728(81)80592-X.

(141) Tokel-Takvoryan, N. E.; Hemingway, R. E.; Bard, A. J. Electrogenerated Chemiluminescence. XIII. Electrochemical and Electrogenerated Chemiluminescence Studies of Ruthenium Chelates. *J. Am. Chem. Soc.* **1973**, *95* (20), 6582–6589. https://doi.org/10.1021/ja00801a011.

(142) Camarada, M. B.; Jaque, P.; Díaz, F. R.; del Valle, M. A. Oxidation Potential of Thiophene Oligomers: Theoretical and Experimental Approach. *J. Polym. Sci. B Polym. Phys.* **2011**, *49* (24), 1723–1733. https://doi.org/10.1002/polb.22360.

(143) Vlcek, A. A.; Dodsworth, E. S.; Pietro, W. J.; Lever, A. B. P. Excited State Redox Potentials of Ruthenium Diimine Complexes; Correlations with Ground State Redox Potentials and Ligand Parameters. *Inorg. Chem.* **1995**, *34* (7), 1906–1913. https://doi.org/10.1021/ic00111a043.

(144) Chettri, A.; Schneider, K. R. A.; Cole, H. D.; Roque, J. A.; Cameron, C. G.; McFarland, S. A.; Dietzek, B. String-Attached Oligothiophene Substituents Determine the Fate of Excited States in Ruthenium Complexes for Photodynamic Therapy. *J. Phys. Chem. A* **2021**, *125* (32), 6985–6994. https://doi.org/10.1021/acs.jpca.1c04900.

2.8 SUPPORTING INFORMATION

2.8.1 Description of Methodology

Lipophilicity

The lipophilicities of the complexes were assessed as log distribution coefficients (log $D_{o/w}$) determined by the “shake-flask” method using three technical replicates. A saturated solution of 1-octanol with phosphate buffer (pH 7.4) was prepared by mixing 16 mL of 1-octanol (99.9%) with 4 mL of 10 mM phosphate buffer (4:1). A saturated solution of phosphate buffer with 1-octanol was prepared by mixing 16 mL of 10 mM phosphate buffer with 4 mL of 1-octanol. The saturated solutions were shaken for 24 hours at room temperature using a vortex mixer at 300 rpm. For determining log $D_{o/w}$, $[Ru(phen)_3](Cl)_2$, **Ru-0T**, **Ru-1T**, and **Ru-2T** were dissolved in 500 µL of the saturated phosphate buffer and diluted with an equal volume of saturated 1-octanol to achieve a final volume of 1 mL and concentration of 25 µM; **Ru-3T** and **Ru-4T** were dissolved in 500 µL of the saturated 1-octanol and diluted with an equal volume of saturated phosphate buffer to achieve a final volume of 1 mL and concentration of 25 µM. The solutions were inverted 200 times by hand and allowed to stand at ambient temperature for 24 h to give time for the complex to disburse between the two layers. The 1-octanol and phosphate buffer layers were then carefully separated using a syringe and transferred to a 96-well microtiter plate for absorbance to be read at wavelengths corresponding to the absorption maxima of the complexes using a SpectraMax M2e microplate reader. The concentration of metal complex in each layer was determined from standard curves prepared with the saturated solution used for the initial dilution and then used to calculated log $D_{o/w}$ as the ratio of the concentrations of compound detected in the 1-octanol layer to phosphate buffer. The averages of the three technical replicates are reported.

Spectroscopy

Unless described otherwise, spectroscopy was performed on dilute (5−20 µM) solutions of the PF_6^- salts of the complexes in spectroscopy grade acetonitrile that had distilled over calcium hydride and stored under N_2. Solutions were deoxygenated by five freeze-pump-thaw cycles in custom Schlenk-style cuvettes. Emission spectra were internally corrected for nonlinear lamp output and detector response.

UV−Visible spectroscopy

Ultraviolet−visible (UV-vis) absorption spectra were collected with a Jasco V730 spectrometer in 5 mm quartz cuvettes. Extinction coefficients were determined by regressing absorption versus concentration for five dilutions at room temperature.

Emission Spectroscopy at Room Temperature

Steady-state emission spectra were acquired on deoxygenated solutions by sparging 30 min with argon using a PTI Quantamaster spectrofluorometer equipped with a K170B PMT (maximum useable wavelength ≈ 800 nm). Wavelength-dependent nonlinearities in lamp output and detector sensitivities were corrected by the software. Generally, the most intense and longest-wavelength peak in the excitation spectrum was chosen for λ_{ex}. Appropriate optical filters were installed to reduce artifacts from scatter and harmonics. Solutions were deoxygenated by argon-sparging in septum-capped 10 mm quartz cuvettes.

Emission Spectroscopy at 77 K

The complexes were immobilized as glasses of 10 μM solutions of the PF_6^- salts in 4:1 ethanol:methanol, contained in 5 mm NMR tubes, and frozen in liquid nitrogen. The solvent was not deaerated. Otherwise, spectra were acquired as described above in section 2.2.3.

Singlet Oxygen Quantum Yield

The quantum yields for singlet oxygen production (Φ_Δ) were measured from dilute (≈5 μM) solutions in spectroscopic grade acetonitrile (not deaerated) at room temperature, and calculated from the intensity of the $^1O_2$ emission centered near 1276 nm using the relative actinometric method depicted in Equation S1, where *I* is the integrated intensity of the emission, *A* is the absorbance of the solution at the excitation wavelength, and η is the refractive index of the solvent. The subscript *S* denotes the standard solution, in this case $[Ru(bpy)_3](PF_6)_2$, for which $\Phi_{\Delta,s}=0.56$,[1] and $(\eta^2/\eta_S^2)=1$ since MeCN was used for both. These experiments used the PF_6^- salts in air-saturated MeCN because water and other protic solvents quench the $^1O_2$ emission.

The emission was measured on a PTI Quantamaster spectrofluorometer with a Hamamatsu R5509-42 PMT that was cooled to −80 °C. The emission spectrum was measured over 1200–1350 nm with a 1000 nm long pass filter in place and integrated with baseline correction. The excitation wavelength was chosen as the wavelength in the MLCT absorption region that produced the most intense signal in the excitation spectrum.

$$\Phi_\Delta = \Phi_{\Delta,s}\left(\frac{I}{I_s}\right)\left(\frac{A_s}{A}\right)\left(\frac{\eta^2}{\eta_s^2}\right) \qquad \text{Equation S1}$$

Transient Absorption Spectroscopy

Dilute (≈5 μM) solutions of the complexes in spectroscopy grade acetonitrile were degassed by five freeze-pump-thaw cycles in custom Schlenk-style cuvettes. Transient absorption (TA) lifetimes and differential excited-state absorption (ESA) spectra were measured with an Edinburgh Instruments LP-980 spectrometer equipped with the PMT-LP detector. 355 nm excitation pulses (0.1 Hz, ~5 ns pulse width, ~7−9 mJ per pulse) were generated by the third harmonic of a Continuum Minilite Nd:YAG laser. The ESA spectra were measured at 10 nm steps and corrected for luminescence, and single-wavelength TA lifetime measurements were optimized for detector response. This system was also used to measure the phosphorescence lifetimes (without a probe beam).

Triplet Energy Determination by Stern-Volmer Quenching

The energy of the ^{3}ILCT states was determined by Stern-Volmer quenching of the excited state lifetime as observed at the TA maximum of the PS signal in the near infrared. The transient lifetime of a dilute (≈5 μM) solution of PS in CH_2Cl_2 was measured at varying (0 – ≈100 μM) concentrations of π-expansive quenchers with known triplet energies,[2] in accordance with Equation S2 (where τ and τ_0 are the TA lifetimes in presence and absence of quencher Q, respectively, and k_q is the quenching constant). The 532 nm second harmonic of a Continuum Minilite Nd:YAG laser (0.1 Hz, ~5 ns pulse width, ~7−9 mJ per pulse) was used to excite the edge of the PS ^{1}MLCT band, while avoiding direct excitation of the quencher.

$$\frac{1}{\tau} = \frac{1}{\tau_0} + k_q[\mathrm{Q}] \qquad \text{Equation S2}$$

Ru(II) compound solutions

For **Ru-4T**, stock solutions were prepared 25 mM in 100% DMSO. For the rest of the compounds, stock solutions were prepared at 5 mM in 10% v/v DMSO:water. Dilutions were prepared in serial with 1x Dulbecco's Phosphate-Buffered Saline (DPBS) without Ca^{2+} or Mg^{2+} that was diluted from 10x DPBS (Corning 20-031-CV). Less than 1.2 % v/v DMSO was applied at the highest concentration (300 μM) Glass vials with PTFE-lined caps were used for stock solutions. The vials were wrapped with aluminum foil to protect from light and stored at −20°C when not in use. When not in use, all stock solutions were stored at −20°C wrapped in foil.

Cell culture

Non-pigmented male human melanoma (SK-MEL-28, ATCC HTB-72) cells were cultured and maintained in EMEM (BioWhittaker, 12-125Q) media, which was further enriched with 10% FB essence (VWR, 10803-034) and 1% glutagro (L-alanyl-L-glutamine; VWR 45001-086). Cells were kept at 37°C under ≥ 90% humidity and 5% USP-grade CO_2 in a water-jacketed incubator (ThermoFisher, Thermo Scientific 4110). Split ratios between 1:2–1:5 were used to achieve 150,000–400,000 cells mL^{-2} at the start of each passage. Cells were used within 15 passages from being purchased. Unless otherwise stated, a seeding density of 3000 cells $well^{-1}$ was used in each (photo)cytotoxicity screen in 384-well plates.

Cellular assays

The photobiological efficacy of each complex was evaluated using dose-response cell viability assays on 384-well plates in concentrations that range from 1×10^{-3} to 300 µM for all and from 1×10^{-12} to 300 µM for **Ru-4T** due to its greater phototoxicity. Under all circumstances, well plates were only stacked 2-plates high in the incubator to facilitate rapid heat exchange. To evaluate inter-assay reproducibility, **Ru-3T** and **Ru-4T** were evaluated in several additional assays (Table S7–S10).

Following our recent examples,[3,4] the compounds were screened for (photo)cytotoxicity via a dose-response resazurin assay in a 384-well plate format. Into 384-well plates (Greiner Bio-One, 781182), DPBS was added into the outmost two wells (144 well count) at 75 µL $well^{-1}$ as a perimeter in the biosafety cabinet. An electronic multichannel pipettor was used for the experimental set-up. There was 40 µL $well^{-1}$ in total for all the inner wells including sample wells, positive and negative control wells. Sample wells were composed of 10 µL $well^{-1}$ complete media, 20 µL $well^{-1}$ cell slurry (3000 $well^{-1}$ SKMEL28 cells) and 10 µL $well^{-1}$ compound dilutions in DPBS. Positive control wells (12 count) were composed of 10 µL $well^{-1}$ complete media, 20 µL $well^{-1}$ cell slurry (3000 cells $well^{-1}$) and 10 µL $well^{-1}$ DPBS. Negative control wells (12 count) consisted of 30 µL $well^{-1}$ complete media and 10 µL $well^{-1}$ DPBS. Before cells were seeded in log-phase growth with >90% viability, the well plates were preincubated (37°C, 5% CO_2, ≥90% RH) with dispensed media. After cell seeding, plates were mixed (up, down, left, right tilting) and then placed in the incubator and incubated 2–3 h to facilitate cell attachment.

During the incubation, serial dilutions were prepared across 9 concentrations from 1×10^{-3} to 300 µM for all compounds and additional 9 concentrations from 1×10^{-12} to 1×10^{-3} µM for **Ru-4T** in sterile 384-well plates using DPBS as solvent. The lights in biosafety cabinet were kept off to minimize exposure to light preventing premature activation in cells. The 384-well plates were incubated with lids for 2–3 h before the compound dilutions were dispensed at 10 µL well^{-1}. Replicates (triplicates) were dispensed row-wise and spaced every 4 rows.

The 384-well plates were incubated overnight (13–20 h drug-to-light interval, DLI), followed by light treatments. Light treatment was approximately 100 J cm^{-2} delivered at 18–24 mW cm^{-2} with cool white Visible (400–700 nm), Blue (Prizmatix LED, 453 nm), Green (Prizmatix LED, 523 nm), and Red (Prizmatix LED, 633 nm). After illumination, plates were further incubated for 1 day before final viability measurements. Edge effects were noted on the 384-well plate; therefore, the post-PDT period was set for one day (20–23 h) to equilibrate cell viability instead of 48 h. Prewarmed 0.3 mM sterifiltered resazurin in 0.2 M phosphate buffer (pH = 7.4) was dispensed across all well plates at 10 µL well^{-1}. Resazurin dyed plates were incubated for 4 h before reading fluorometrically on a Molecular Devices M2e (30 s shake, bottom-read, λ_{exc} 530 nm, long-pass 570 nm, λ_{em} 620 nm).

Hypoxia protocol

The compounds were screened in parallel under normoxia (~18.5% O_2) and hypoxia (1% O_2). For hypoxic-treated plates, the cells were incubated 1–2 h under normoxia (37°C, 5% CO_2, ≥90% RH) to allow time for cells to adhere. Then the plates were incubated at 1% O_2 (37°C, 5% CO_2, ≥90% RH) in a Biospherix Xvivo X3 chamber for 2–3 h before compound dilutions were dispensed in the biosafety cabinet. Plates were then incubated in Biospherix chamber for 17–19 h (DLI). Before light treatment (while still inside the Biospherix chamber), the dissolved oxygen concentration was measured in one randomly chosen well in each plate using an immersive optical probe (Ohio Lumex, PyroScience OXSOLV). The optical probe was calibrated using deaerated, deionized water before each experiment. For measurements, the probe was carefully positioned in the center of the chosen well at a depth of approximately 3 mm. We found that 7–9 µM O_2 was optimal under a 1% O_2 atmosphere, where the dissolved O_2 decreases with more depth (in normoxia-treated cells, the dissolved O_2 concentration is approximately 100 µM O_2). The hypoxia-treated plates to be light-treated were then sealed inside the Biospherix chamber using low-gas permeable and high transparency qPCR films (VWR, 89134-428) to maintain hypoxic conditions during light treatment, which is the most critical point for testing oxygen-dependence of a PS. After light treatment, the films were removed in the biosafety cabinet and all hypoxic-treated plates were moved to the normoxic incubator (37°C, 5% CO_2, ≥90% RH). Alongside the normoxic-treated plates, the hypoxic-treated plates were incubated for 20–23 h before cell viability determination.

Biological replicates

To verify reproducibility across assays for the more active **Ru-3T** and **Ru-4T** complexes, biological replicates were performed as longitudinal studies following our previously reported examples.[3,4] Biological replicates were assigned randomized and unique plate maps, and different pipet tips were used for repeat #1 (Sartorius 790352), #2–3 (VWR 83007-352), and #4–5 (low retention Sartorius LH-L790352). To minimize any possible contribution from stray light, the overhead lights in the lab space were turned off for repeat #5. All cells used in these assays were between 10–15 passages, and all assays were performed within one month of each other.

Light devices and protocols

Unless otherwise noted, each biological assay used a fluence of 100 J cm^{-2} and an irradiance of 18-22 mW cm^{-2}. Three different light sources were used for visible, green, and red light treatments: a cool white LED panel (SOLLA-CREE, 400–700 nm, maxima ~450 nm) and two UHP-LEDs (Prizmatix, 523 and 633 nm). Their spectral outputs are shown in Figure S33.

Data analysis and statistics

Data from the resazurin cell viability assay were corrected for background by subtracting the signal from wells that contained only media and DPBS (no cells) and normalized relative to untreated cells. Because the absorbance and emission of the metal complexes can interfere with the resazurin fluorescence signal, wells treated with the highest concentrations of metal complex were also observed under a microscope. If no cells were detected, these wells were assigned a value of zero. A more detailed discussion of assay limitations for this class of complexes is provided in our 2019 review.[5]

Data points obtained from resazurin fluorescence were fit to a three-parameter log-logistic (Equation S3) and logistic model (Equation S4) using GraphPad Prism 8.4.0. We use Equation S3 for summary log(EC$_{50}$) plots (Figure 12a) and in the dose-response curves shown in Figure 13, but we use Equation S4 for data in log(PI) plots (Figure 12b) as well as the tabulated EC$_{50}$ and PI values (Table S6–S10).

$$Y = \mathrm{Bottom} + \frac{(Top - Bottom)}{(1 + (10^{Log(EC_{50} - X) \times Hillslope})} \qquad \text{Equation S3}$$

$$Y = \mathrm{Bottom} + \frac{(Top - Bottom)}{\left(1 + (EC_{50}/X)^{Hillslope}\right)} \qquad \text{Equation S4}$$

Experiments were completed in triplicate and replicated data points are always plotted with error bars denoting the standard deviation (SD). All EC_{50} values are reported alongside the standard error of the mean (SEM). In cases where the hill slope was too steep to calculate a representative SEM, the SEM was labelled as not determined (n.d.). Phototherapeutic indices (PI) are reported as the ratio of dark to light EC_{50} values and serve as a phototherapeutic efficacy benchmark. Any summary plots showing Log EC_{50} and Log PI values of the entire series of complexes are plotted with SEMs from log-logistic fits.

2.8.2 Synthetic Characterization

Description of NMR Assignments. The proton signals of tris-homoleptic compound $[Ru(phen)_3](Cl)_2$ are characterized in detail by Pazderski *et al.*,[6] and were used to establish the location of the phenanthroline proton signals in compounds **Ru-0T**–**Ru-4T**. In compounds **Ru-0T**–**Ru-4T**, protons *2* and *9* are electromagnetically distinct from one another. It is expected that the protons *2* would be more deshielded than protons *9* due to their relative proximity to the imidazole-phenanthroline (IP) π-system. In compounds **Ru-0T–Ru-4T**, the furthest downfield signal is assigned as *c* due to its proximity to the imidazole's nitrogens. This signal often appears as a broad singlet due to prototropic tautomerization of the neighboring imidazole. In compounds **Ru-0T**–**Ru-4T**, protons *3*, *8*, and *b* are similar in their offsets and splitting characteristics and were assigned using ^1H-^1H COSY correlations with their neighboring protons (*2*/*4*, *7*/*9*, *a*/*c*, respectively). In the case of compounds **Ru-3T** and **Ru-4T**, protons *4* and *7* are distinguishable from one another, which allows for protons *3* and *8* to also be identified more accurately through ^1H-^1H COSY correlations. In compound **Ru-1T**, the thiophene proton *d* is relatively deshielded due to through-space induction with the imidazole's nitrogens, and because of proton *e*'s distinct splitting proton *f*'s location is determined by process of elimination and observed ^1H-^1H COSY correlations. In compounds **Ru-1T–Ru-4T**, the proton signals corresponding to the thiophene closest to the imidazole were all assigned by locating the chemically distinct *d* signal, then assigning the other proton(s) in the spin system using ^1H-^1H COSY correlations. The terminal thiophene's protons in compounds **Ru-2T–Ru-4T** may be assigned using the doublet of doublets observed in monosubstituted thienyl ^1H NMR spectra. Using that signal as a starting point, the other two proton signals may be found through ^1H-^1H COSY correlations, with the proton next to sulfur appearing more downfield. After that, for **Ru-3T** and **Ru-4T**, the only remaining signals are those which correspond to the "internal" thiophenes, which are surrounded by other thiophenes. This is somewhat straightforward for compound **Ru-3T**, which only contains one internal thiophene, but determining which proton is *f* and which one is *g* remains a challenge without ^{13}C -^1H HSQC and ^{13}C -^1H HMBC. For compound **Ru-4T**, the internal thiophene signals are more difficult to assign. Here, the two spin systems (*f*–*g* and *h*–*i*) were first established using ^1H-^1H COSY correlations.

Then, ^{13}C -^{1}H HSQC was used to identify which ^{13}C peaks correspond to the thiophene protons *d*–*k*. Then, ^{13}C -^{1}H HMBC was used to establish neighboring proton peaks. For example, *e* and *f* both correlate to two of the same ^{13}C peaks (141.46 ppm and 136.24 ppm), which are assumed to be carbons *12* and *13*. Proton *e* correlates more strongly to the peak at 141.46 ppm, and proton *f* correlates more strongly to the 136.24 ppm peak, which allowed for carbon *12* and carbon *13* to also be assigned as signals at 141.46 and 136.24, respectively. Because proton *f* was identified, proton *g* was also identified by process of elimination. Proton *g* and proton *h* both correlate to the ^{13}C peaks at 138.30 ppm and 136.36 ppm, which are designated as carbons *14* and *15*. Again, *h* correlated more strongly to *15* and *g* correlated more strongly to *14*. In addition, *i* and *j* both correlate to ^{13}C peaks 137.78 ppm and 138.13 ppm, with *k* weakly correlating to the 137.78 peak. Using these correlations, carbons *16* and *17* were assigned to the 138.13 and 137.78 peaks, respectively. This provided a working assignment of all of compound **Ru-4T**'s protons and some key carbons. The remaining quaternary carbons (10-11, 19-24) were assigned using ^{13}C -^{1}H HMBC correlations and process of elimination. Carbon *10* shows a weak 3-bond correlation to proton *d* and is relatively downfield at 150.01 ppm. Carbon *11* was assigned based on the strong 2-bond HMBC correlation with proton *d*. Carbons *19* and *20* were assigned based on 2-bond and 3-bond correlations shared with protons 5/6 and 3/8, respectively. There are correlations between carbons *21*–*22* with protons *2*, *9*, *4*, *7*, *5*, and *6*, (but not *3* or *8*) which allowed for carbons *21* and *22* to be identified. Carbon *23* was identified using a strong correlation with proton *a*. Because proton *c* is decoupled, and no 2-bond or 3-bond correlations are observed from that proton signal, the location of the signals corresponding to carbons *24* and *25* remains unsolved; it is assumed that they overlap with other carbon signals. An artefact appears near 138 ppm in the ^{13}C NMR spectrum, which is attributed to the surrounding area's various radio stations.

NMR spectra

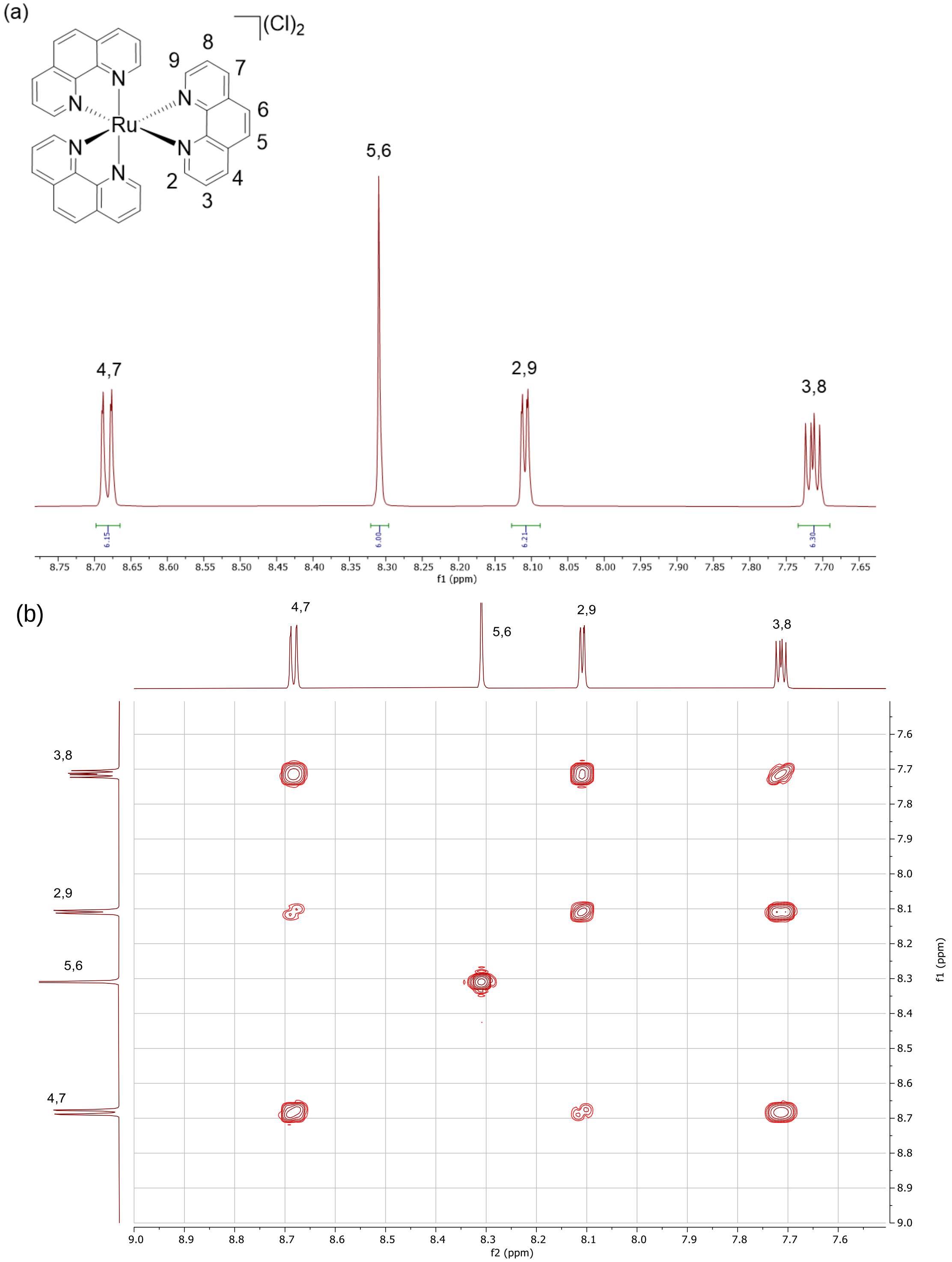

Figure S1. (a) Aromatic ^{1}H NMR (700MHz, MeOD-d_3, 298 K) spectrum and assignments for [Ru(phen)$_3$](Cl)$_2$. (b) Aromatic ^{1}H-^{1}H COSY NMR (700MHz, MeOD-d_3, 289 K) spectrum and assignments for [Ru(phen)$_3$](Cl)$_2$.

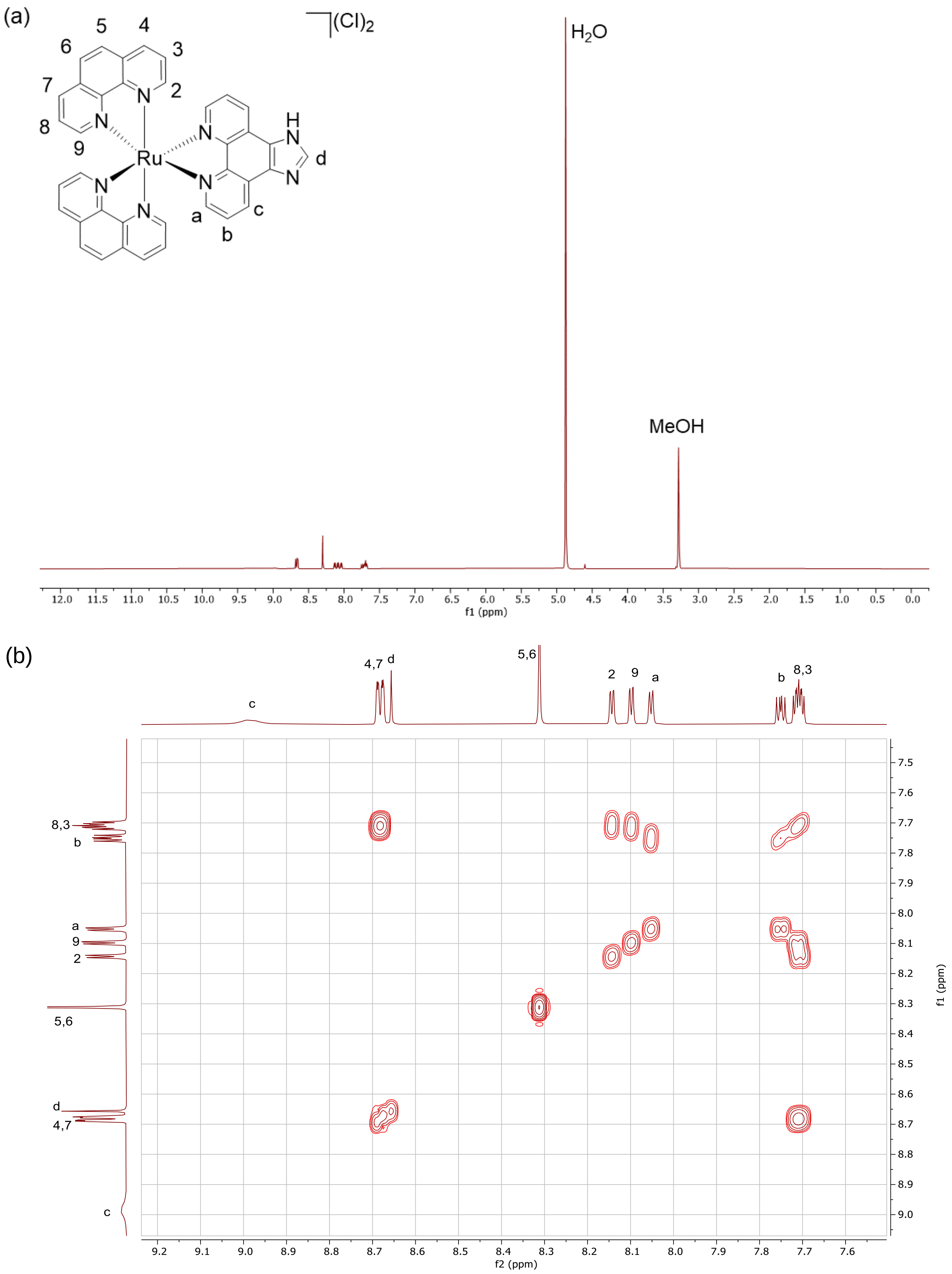

Figure S2. (a) Aromatic ^{1}H NMR (700MHz, MeOD-d_3, 298 K) spectra and assignments for **Ru-0T**. (b) Aromatic ^{1}H-^{1}H COSY NMR (700MHz, MeOD-d_3, 298 K) assignments for **Ru-0T**.

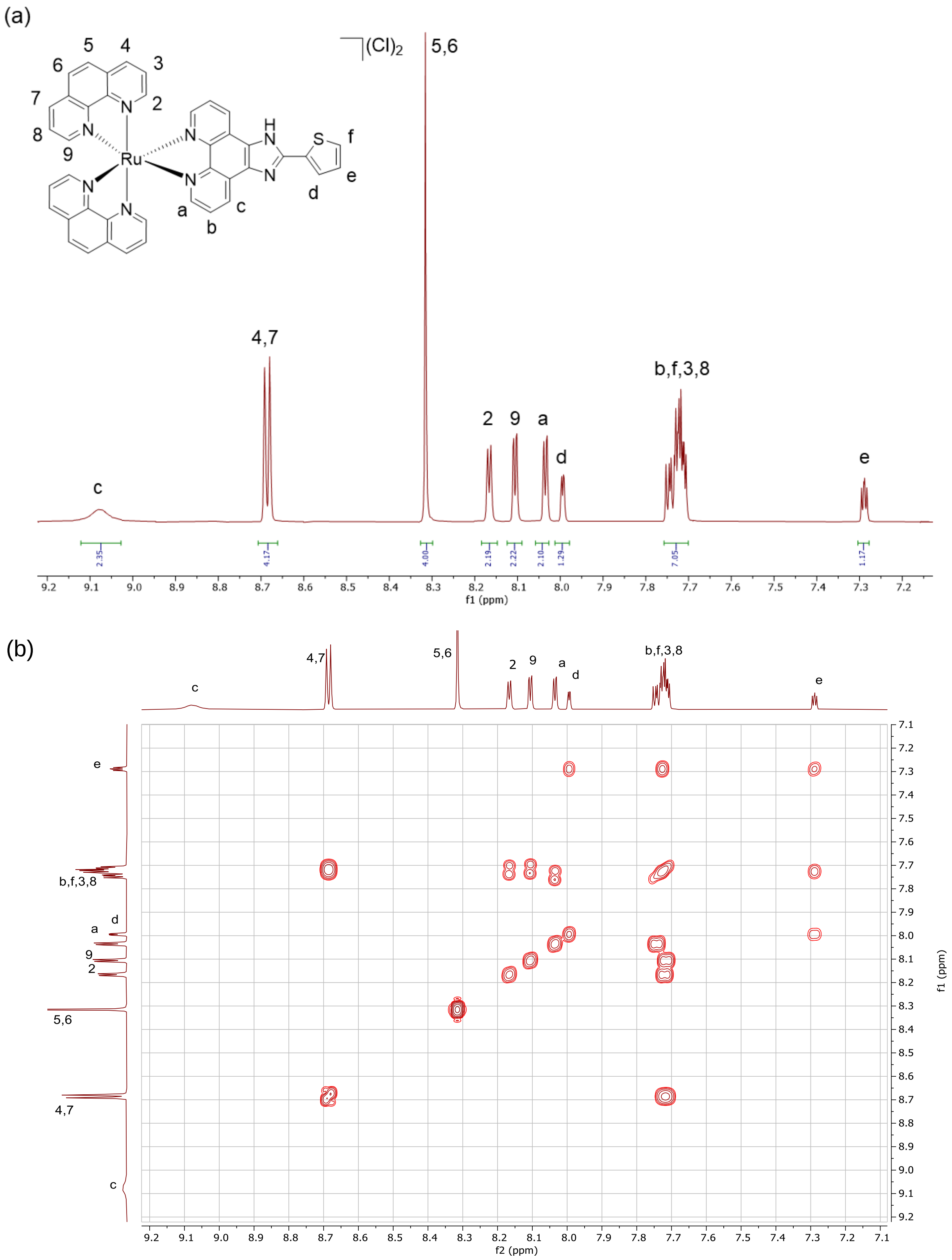

Figure S3. (a) Aromatic ^{1}H NMR (700MHz, MeOD-d_3, 298 K) spectra and assignments for **Ru-1T**. (b) Aromatic ^{1}H-^{1}H COSY NMR (700MHz, MeOD-d_3, 298 K) assignments for **Ru-1T**.

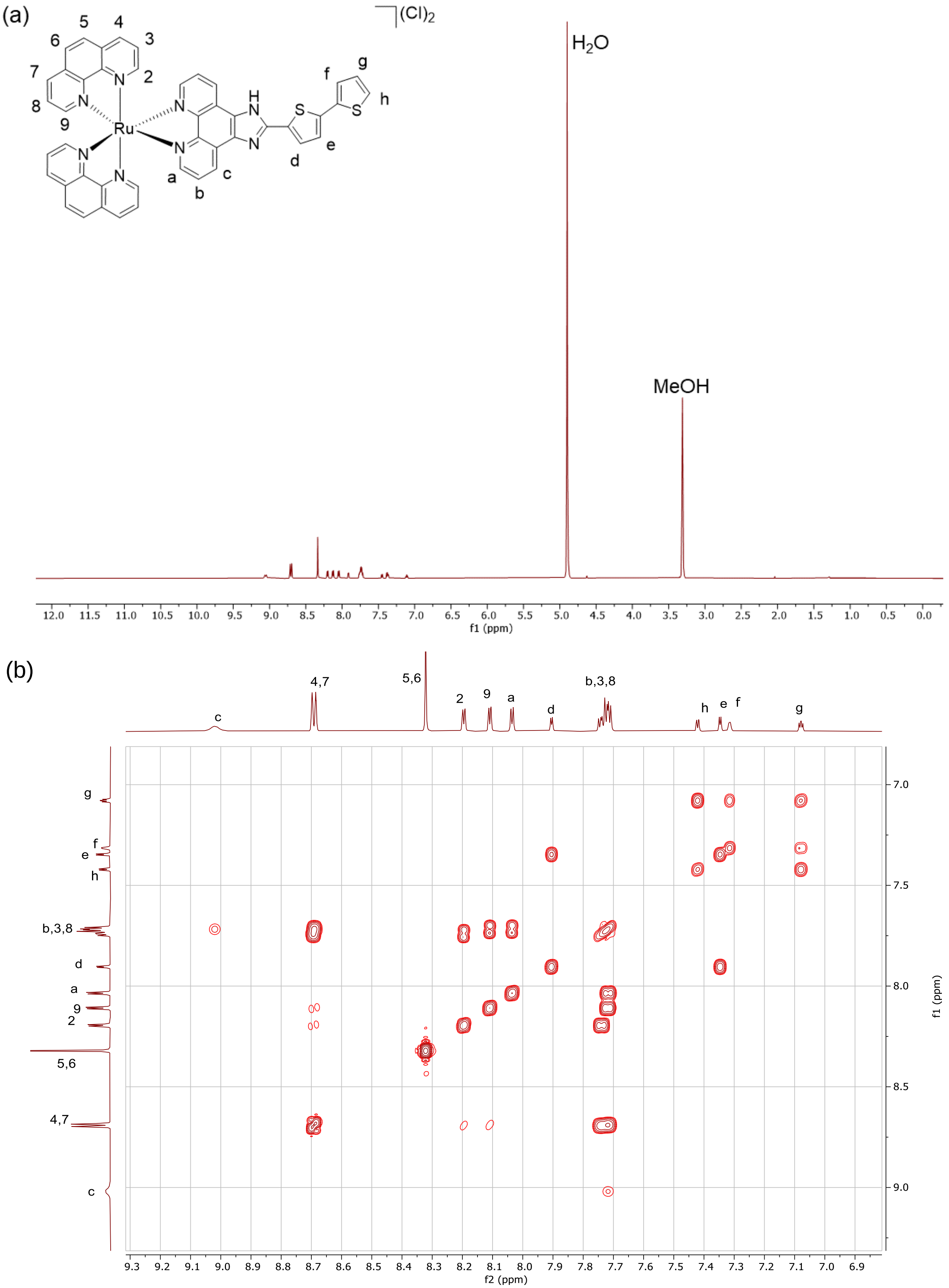

Figure S4. (a) Aromatic ^1H NMR (700MHz, MeOD-*d*$_3$, 298 K) spectra and assignments for compound **Ru-2T**. (b) Aromatic ^1H-^1H COSY NMR (700MHz, MeOD-*d*$_3$, 298 K) assignments for compound **Ru-2T**.

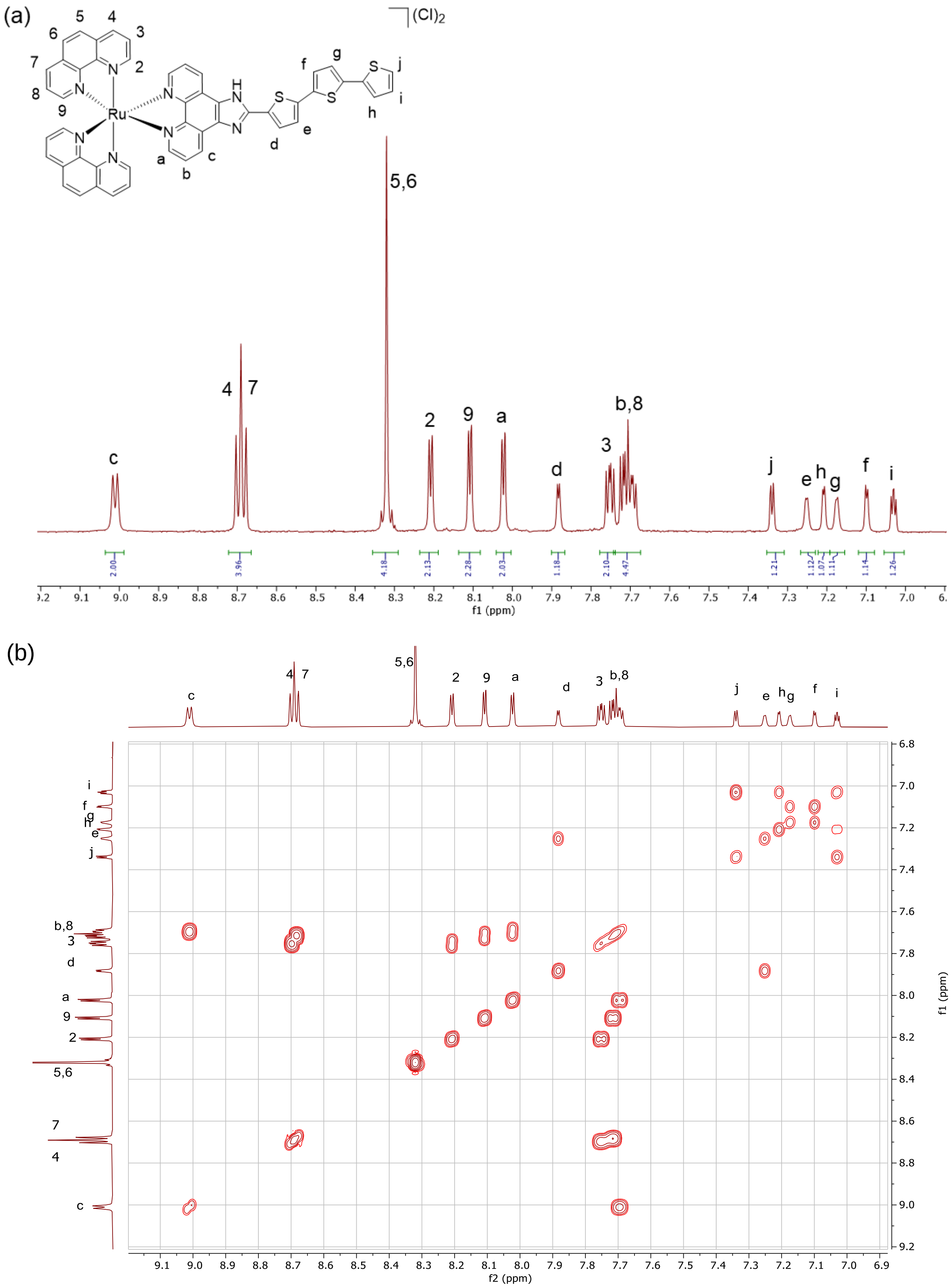

Figure S5. (a) Aromatic ^{1}H NMR (700MHz, MeOD-d_3, 298 K) spectra and assignments for **Ru-3T**. (b) Aromatic ^{1}H-^{1}H COSY NMR (700MHz, MeOD-d_3, 298 K) assignments for **Ru-3T**.

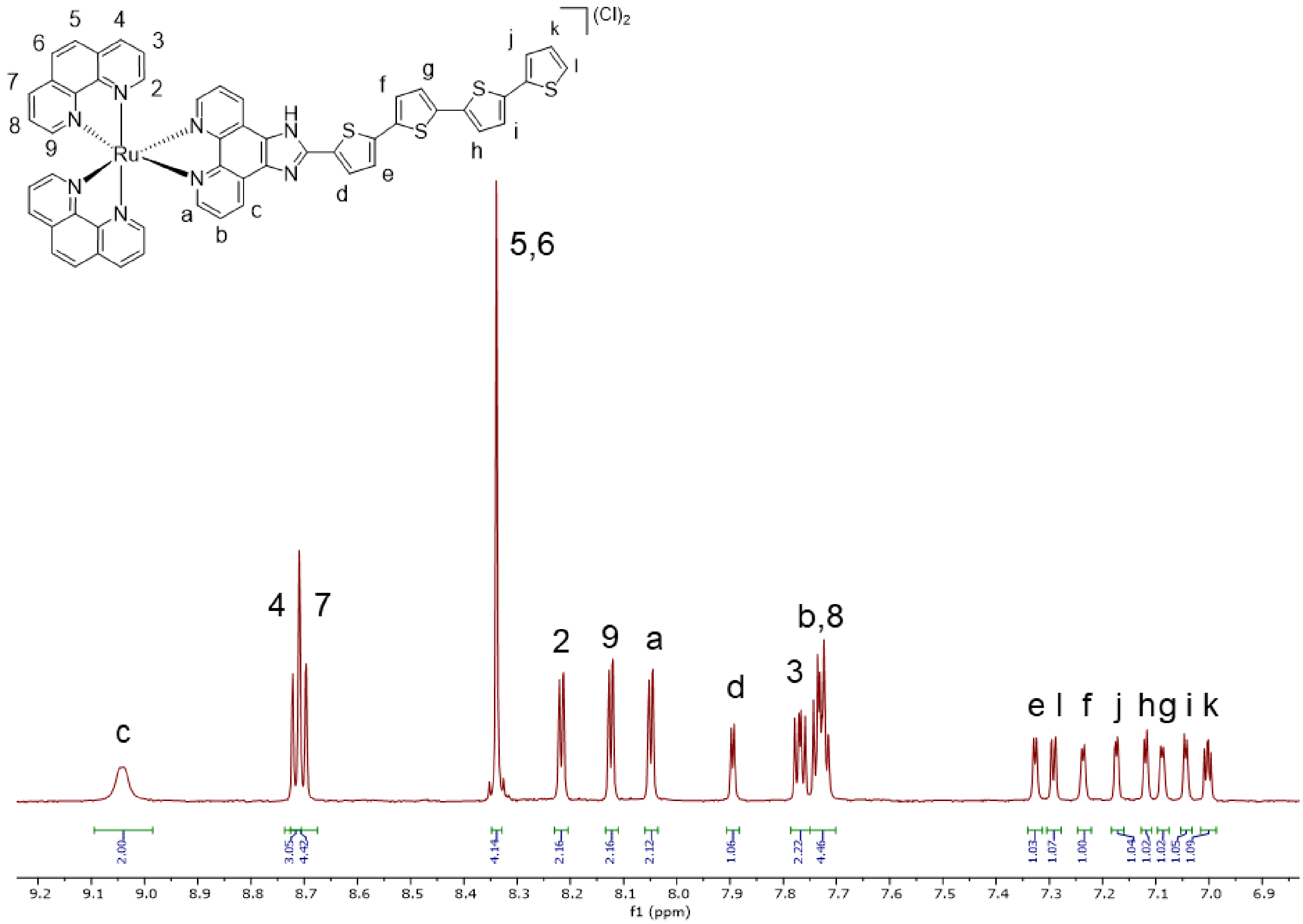

Figure S6. Aromatic ^{1}H NMR (700MHz, MeOD-d_3, 298 K) spectra and assignments for **Ru-4T**.

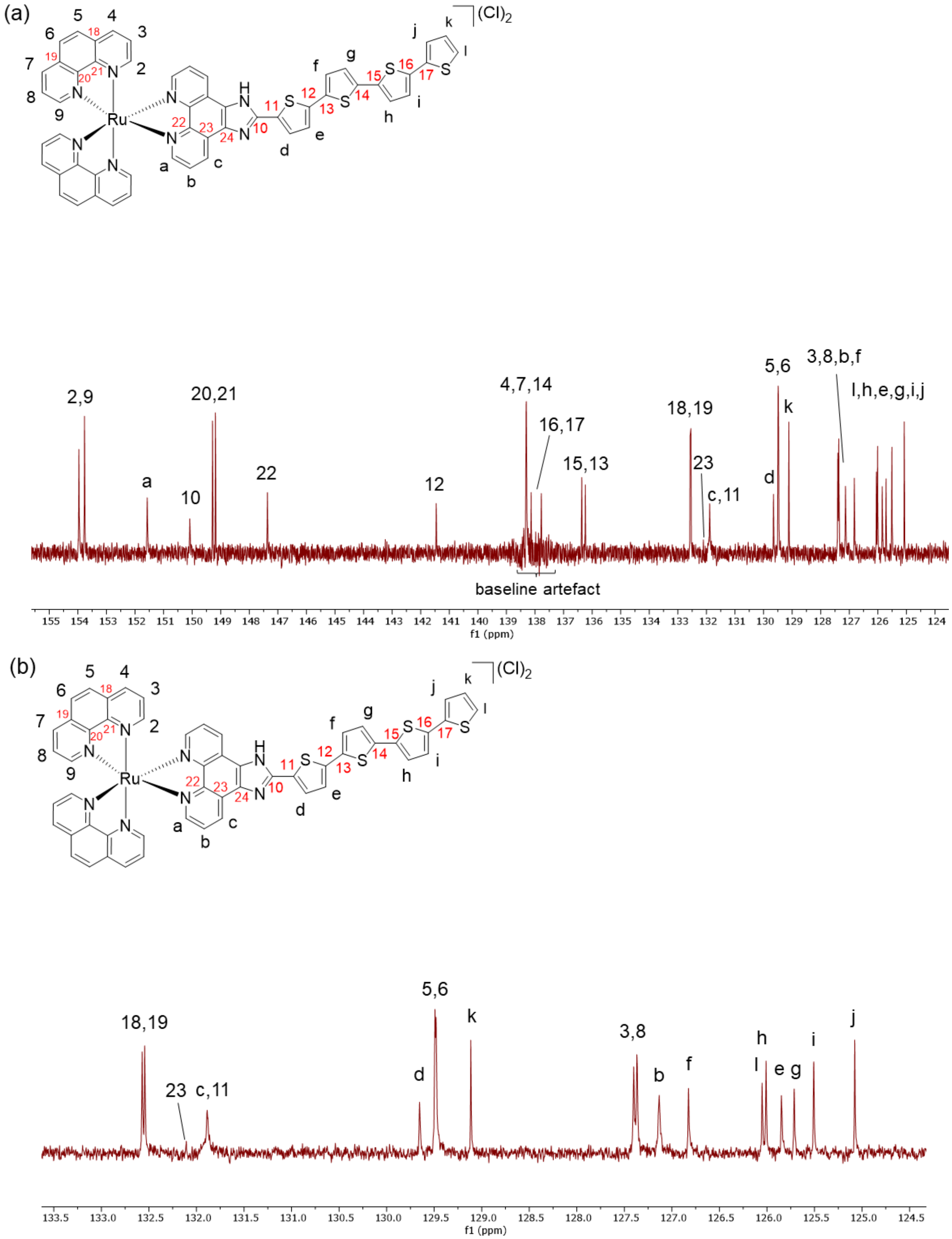

Figure S7. (a) Zoom of ^{13}C NMR (700 MHz, MeOD-d_3, 298 K) spectrum from 124-155 ppm with assignments for **Ru-4T**. (b) Zoom of ^{13}C NMR (700 MHz, MeOD-d_3, 298 K) spectrum from 124.5-133.5 ppm for **Ru-4T**.

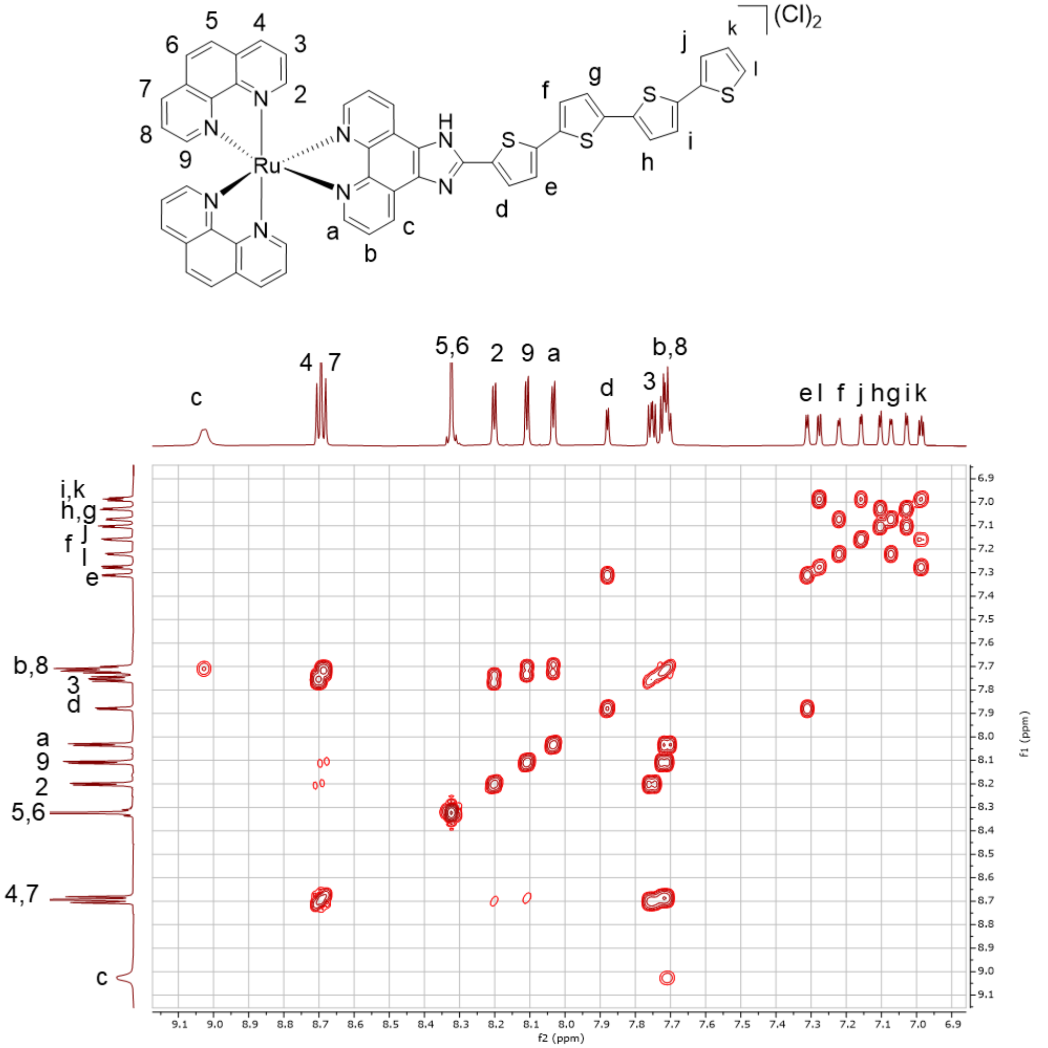

Figure S8. Aromatic ^{1}H-^{1}H COSY NMR (700 MHz, MeOD-d_3, 298 K) spectrum and assignments for **Ru-4T**.

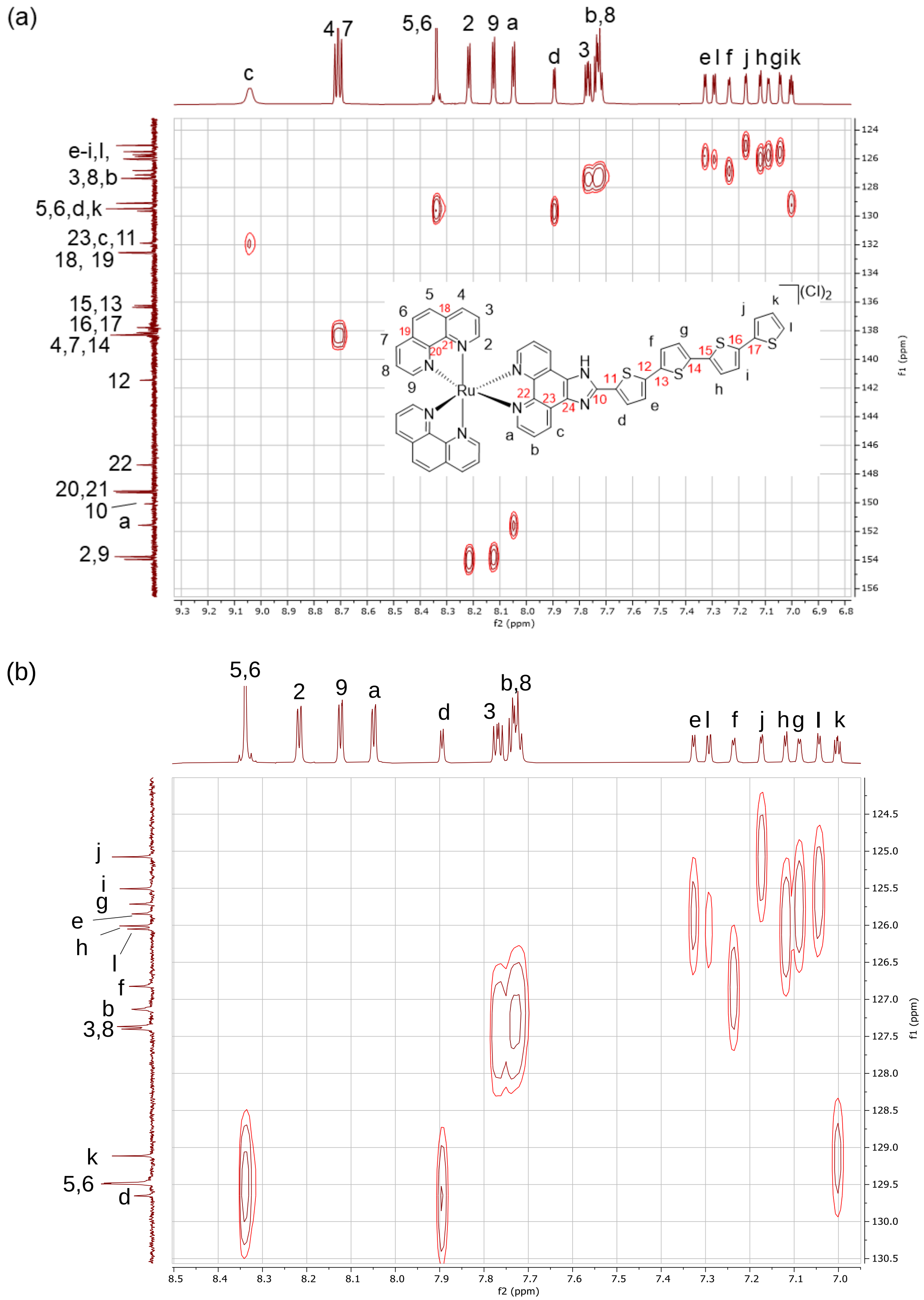

Figure S9. (a) ^{13}C-^{1}H HSQC NMR (700 MHz, MeOD-d_3, 298 K) spectrum of **Ru-4T** with assignments. (b) Zoom of ^{13}C -^{1}H HSQC NMR (700 MHz, MeOD-d_3, 298 K) spectrum for **Ru-4T** with assignments.

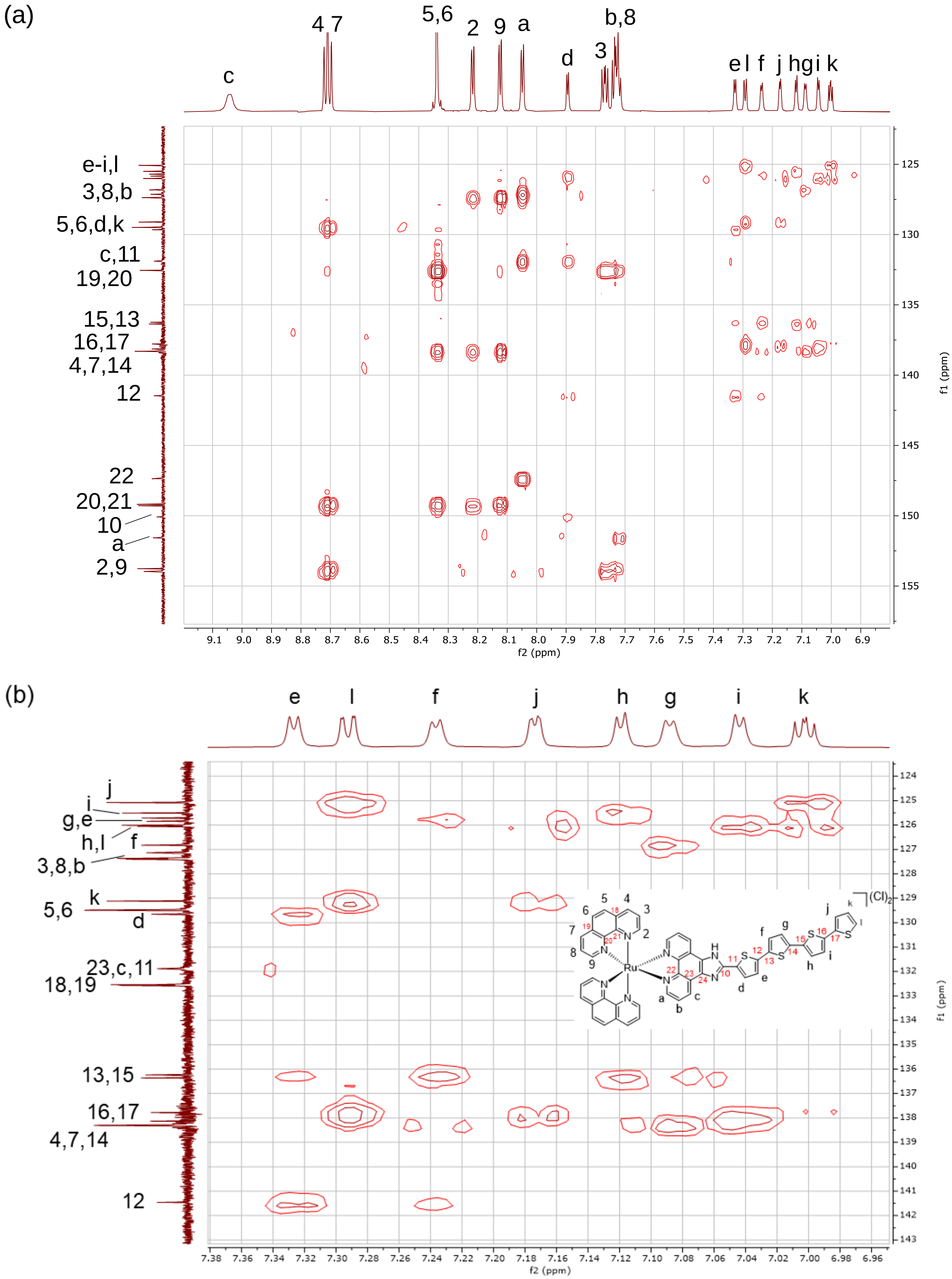

Figure S10. (a) ^{13}C-^{1}H HMBC NMR (700 MHz, MeOD-d_3, 298 K) of **Ru-4T** with assignments. (b) Zoom of ^{13}C -^{1}H HMBC NMR (700 MHz, MeOD-d_3, 298 K) spectrum for **Ru-4T** with assignments.

HRMS spectra

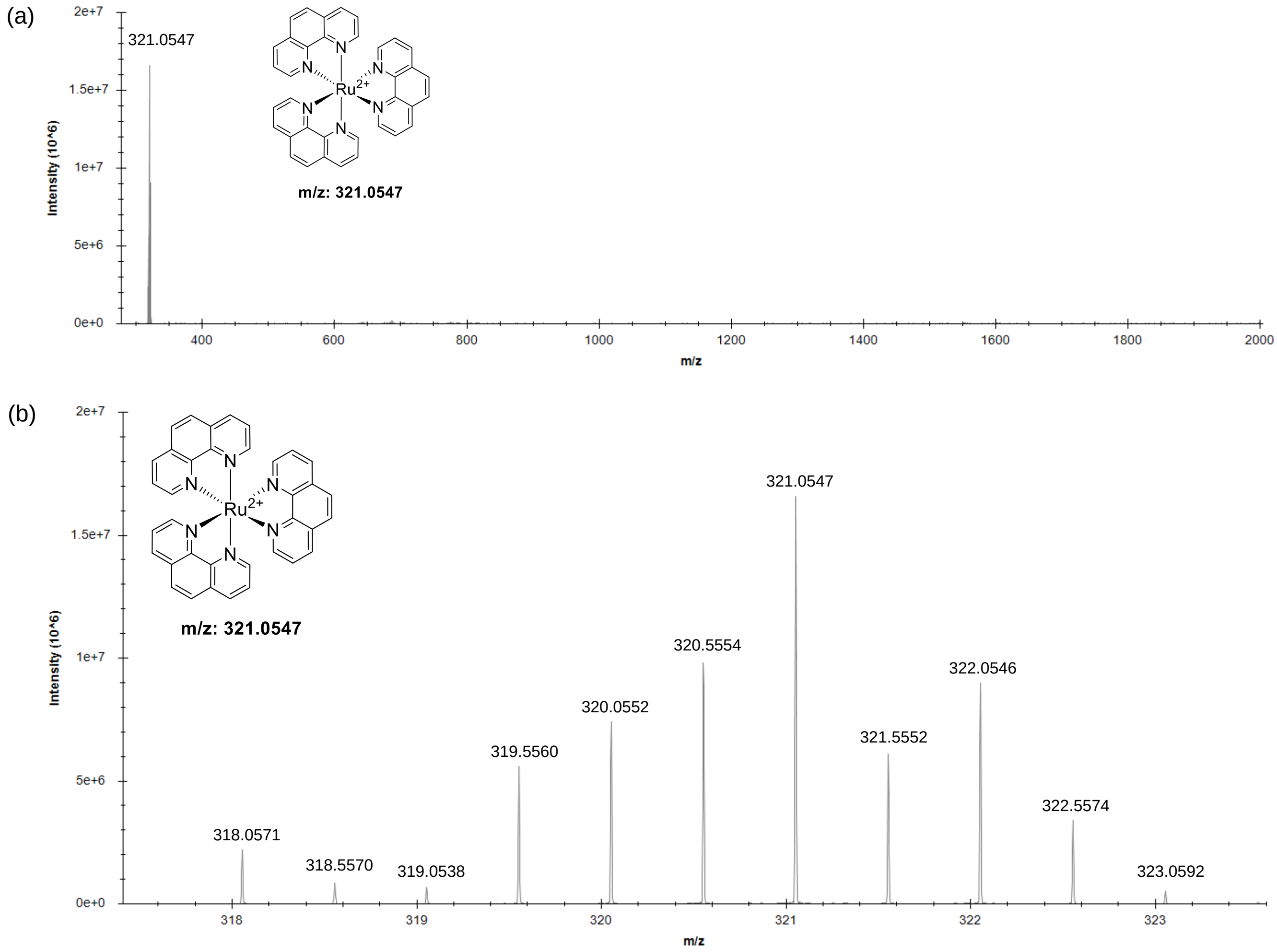

Figure S11. (a) High resolution ESI⁺-MS spectrum for $[Ru(phen)_3](Cl)_2$. (b) Zoom of 321.0547 m/z showing isotopic distribution.

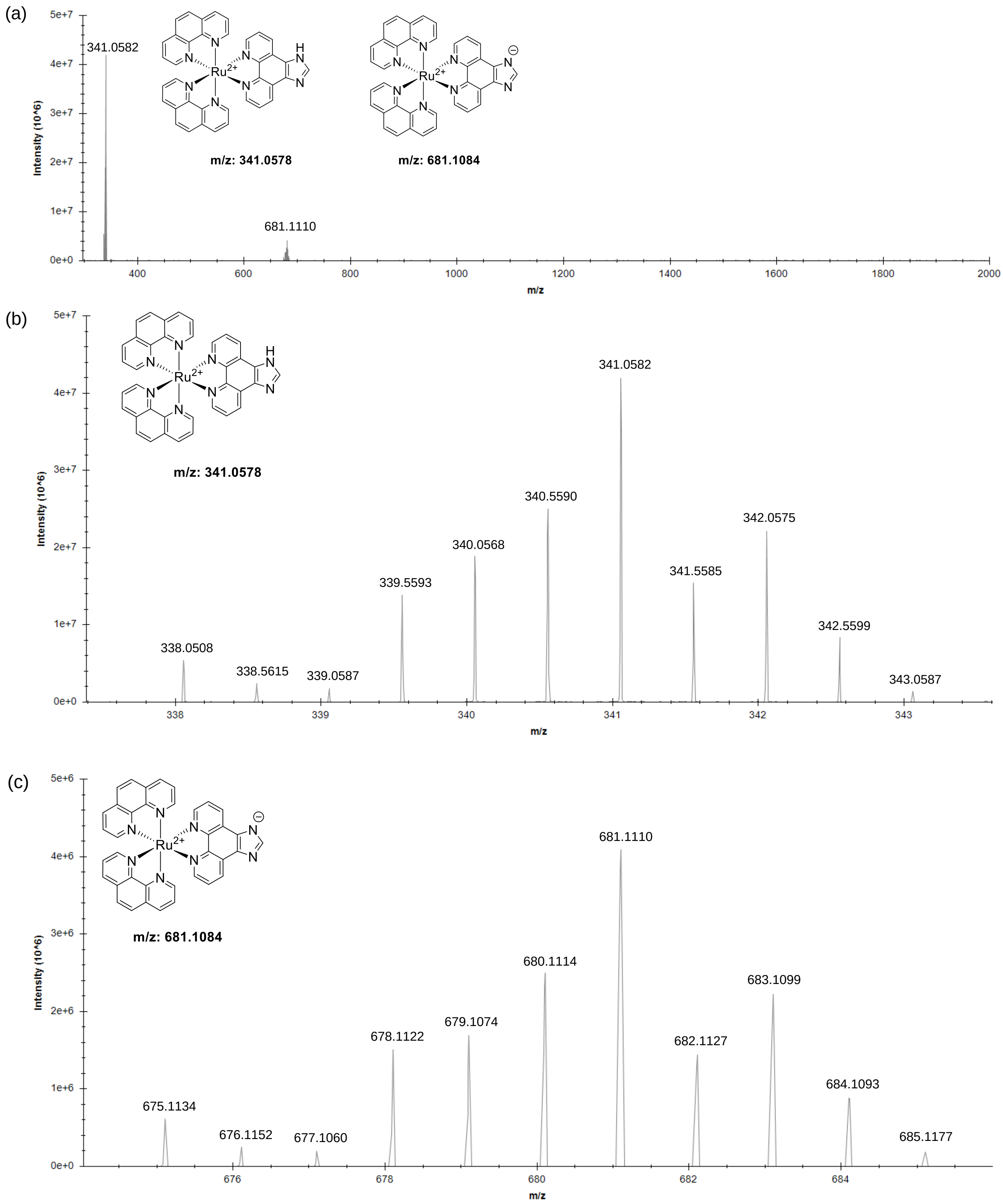

Figure S12. (a) High resolution ESI$^+$-MS spectrum for **Ru-0T**. (b) Zoom of 341.0582 m/z showing isotopic distribution. (c) Zoom of 681.1110 m/z showing isotopic distribution.

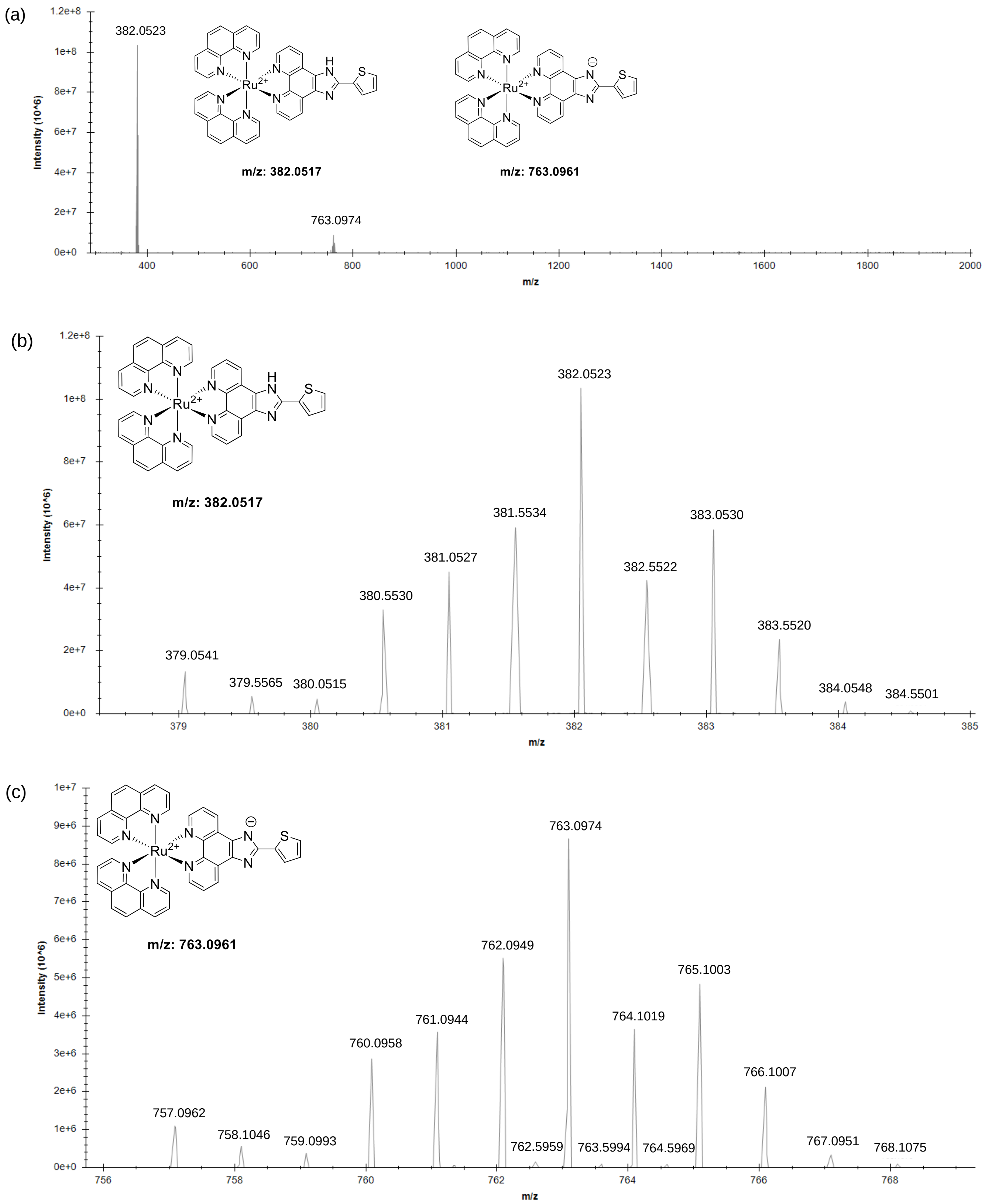

Figure S13. (a) High resolution ESI$^+$-MS spectrum for **Ru-1T**. (b) Zoom of 382.0523 m/z showing isotopic distribution. (c) Zoom of 763.0974 m/z showing isotopic distribution.

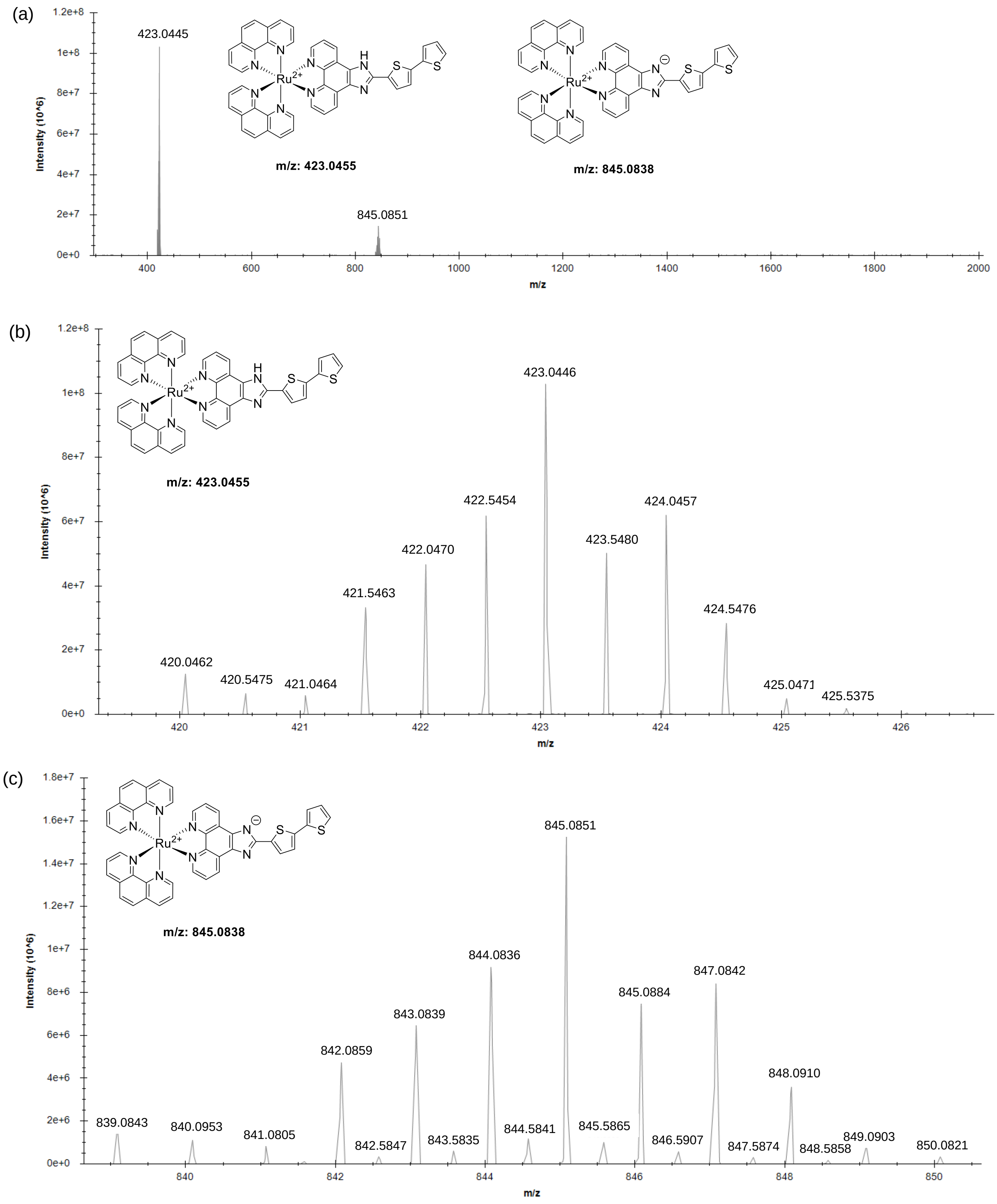

Figure S14. (a) High resolution ESI$^+$-MS spectrum for **Ru-2T**. (b) Zoom of 423.0445 m/z showing isotopic distribution. (c) Zoom of 845.0851 m/z showing isotopic distribution.

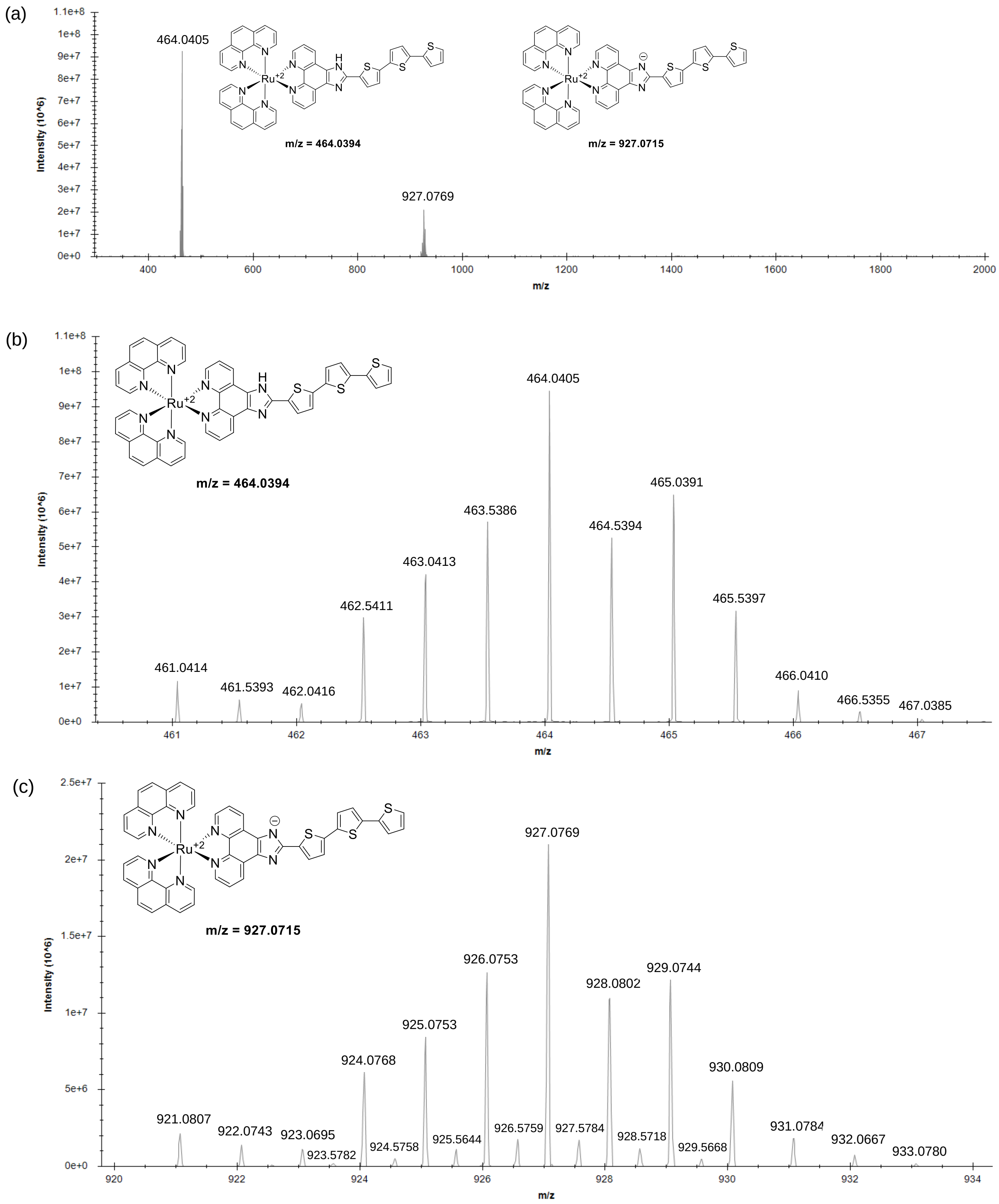

Figure S15. (a) High resolution ESI$^+$-MS spectrum for **Ru-3T**. (b) Zoom of 464.0405 m/z showing isotopic distribution. (c) Zoom of 927.0769 m/z showing isotopic distribution.

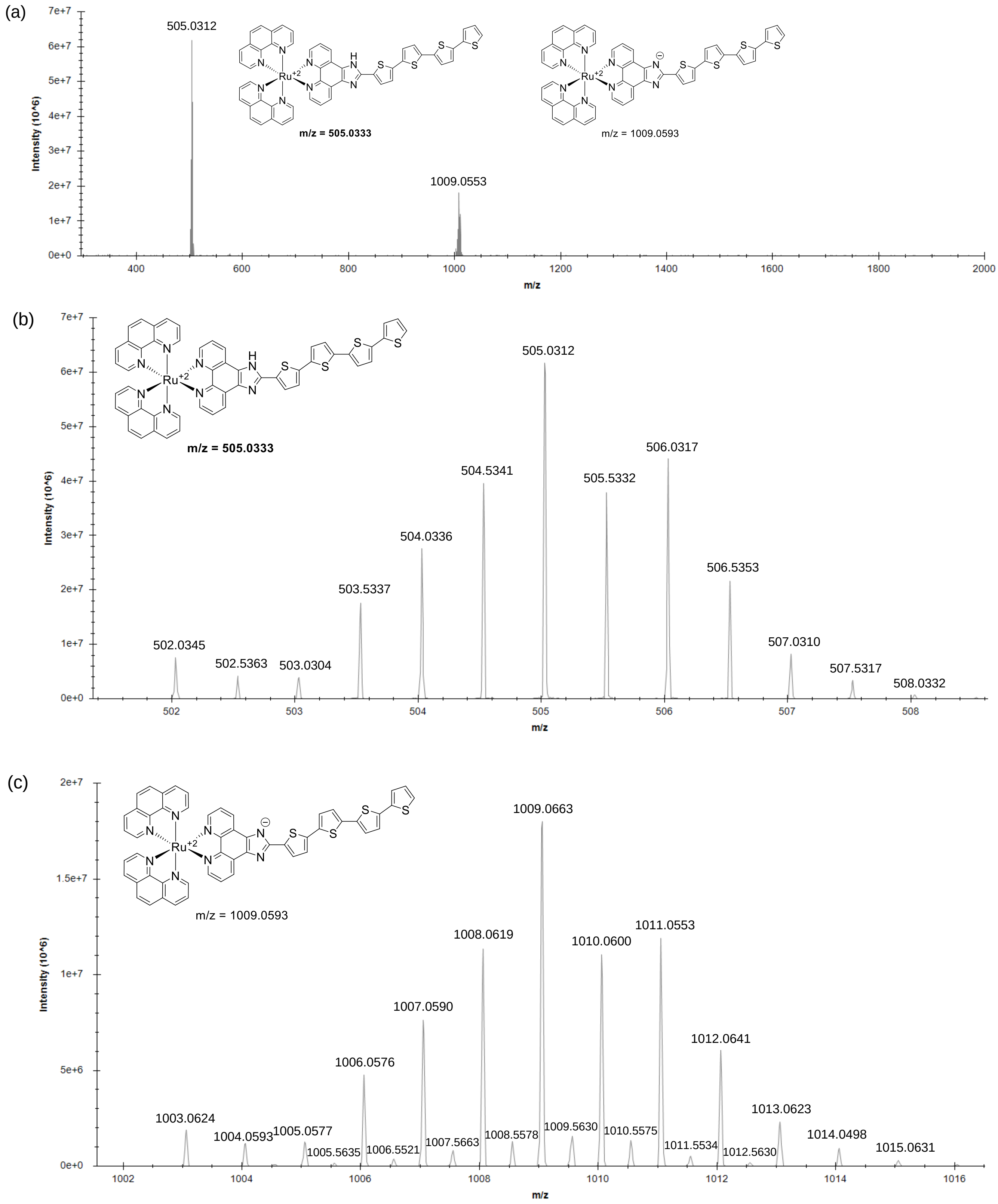

Figure S16. (a) High resolution ESI$^+$-MS spectrum for **Ru-4T**. (b) Zoom of 505.0312 m/z showing isotopic distribution. (c) Zoom of 1009.0663 m/z showing isotopic distribution.

HPLC chromatograms

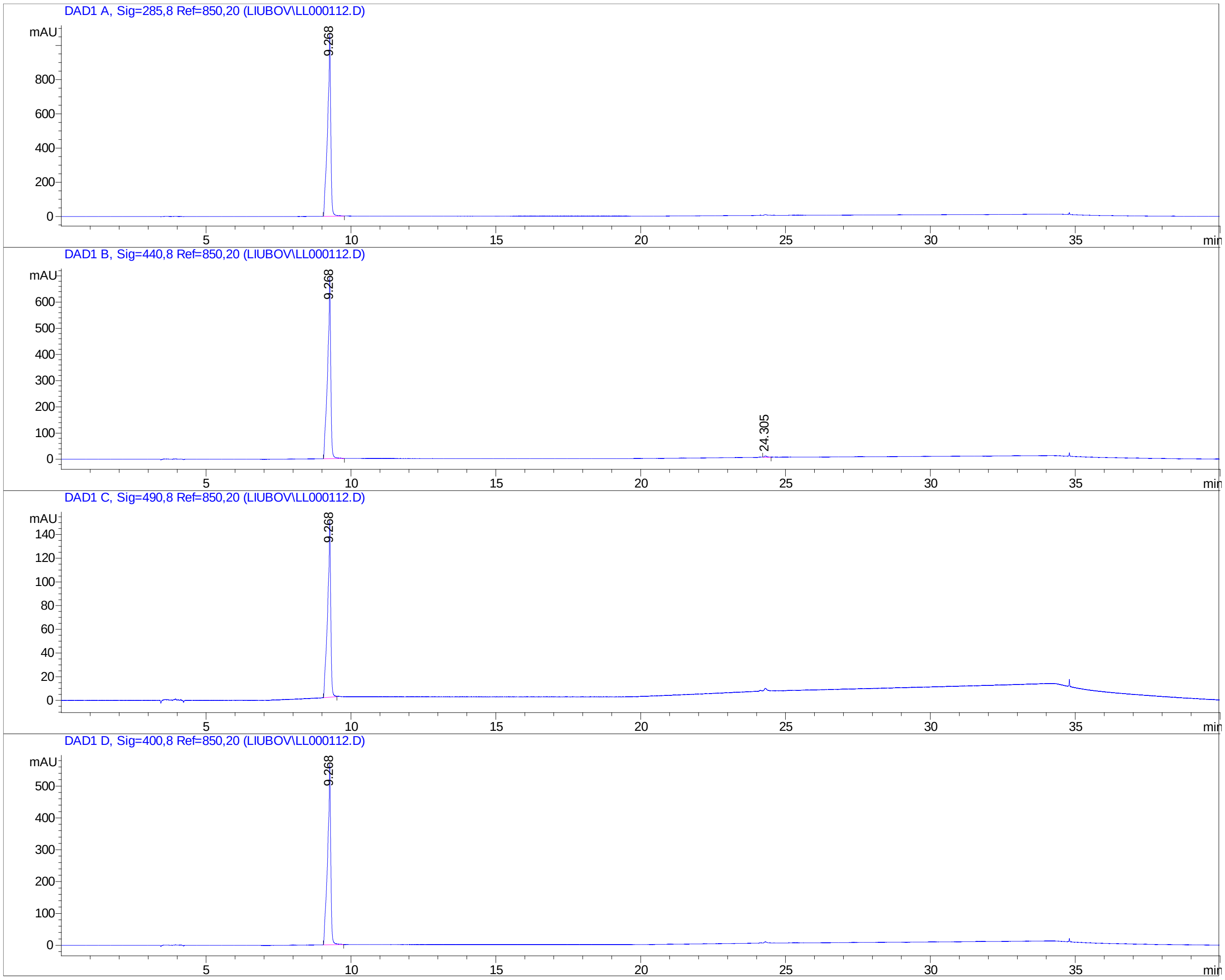

Figure S17. HPLC chromatogram for $[Ru(phen)_3](Cl)_2$ collected at the following wavelengths: 285, 400, 440, and 490 nm (99.5% purity by peak area).

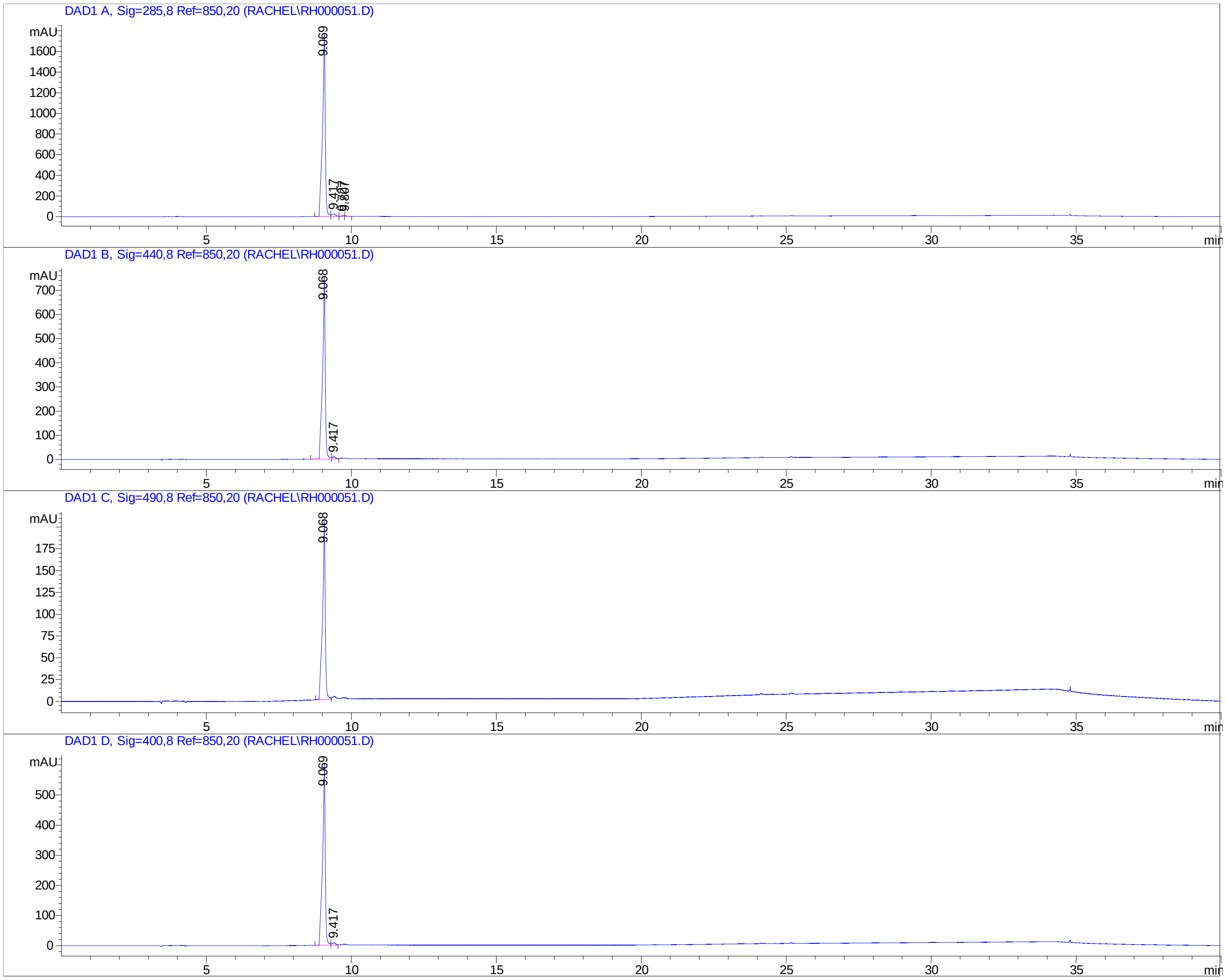

Figure S18. HPLC chromatogram for **Ru-0T** collected at the following wavelengths: 285, 400, 440, and 490 nm. (98% purity by peak area).

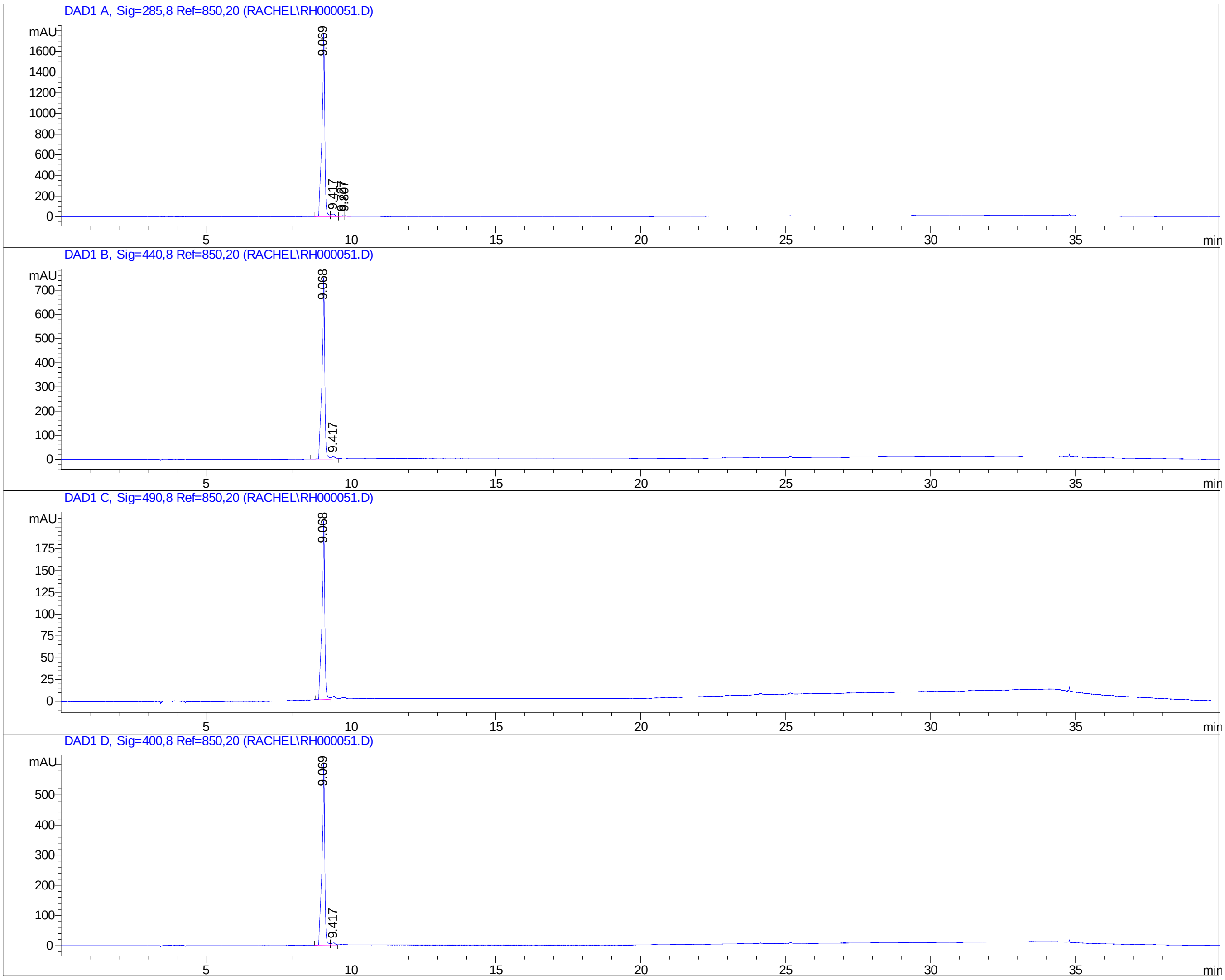

Figure S19. HPLC chromatogram for **Ru-1T** collected at the following wavelengths: 285, 400, 440, and 490 nm (99.5% purity by peak area).

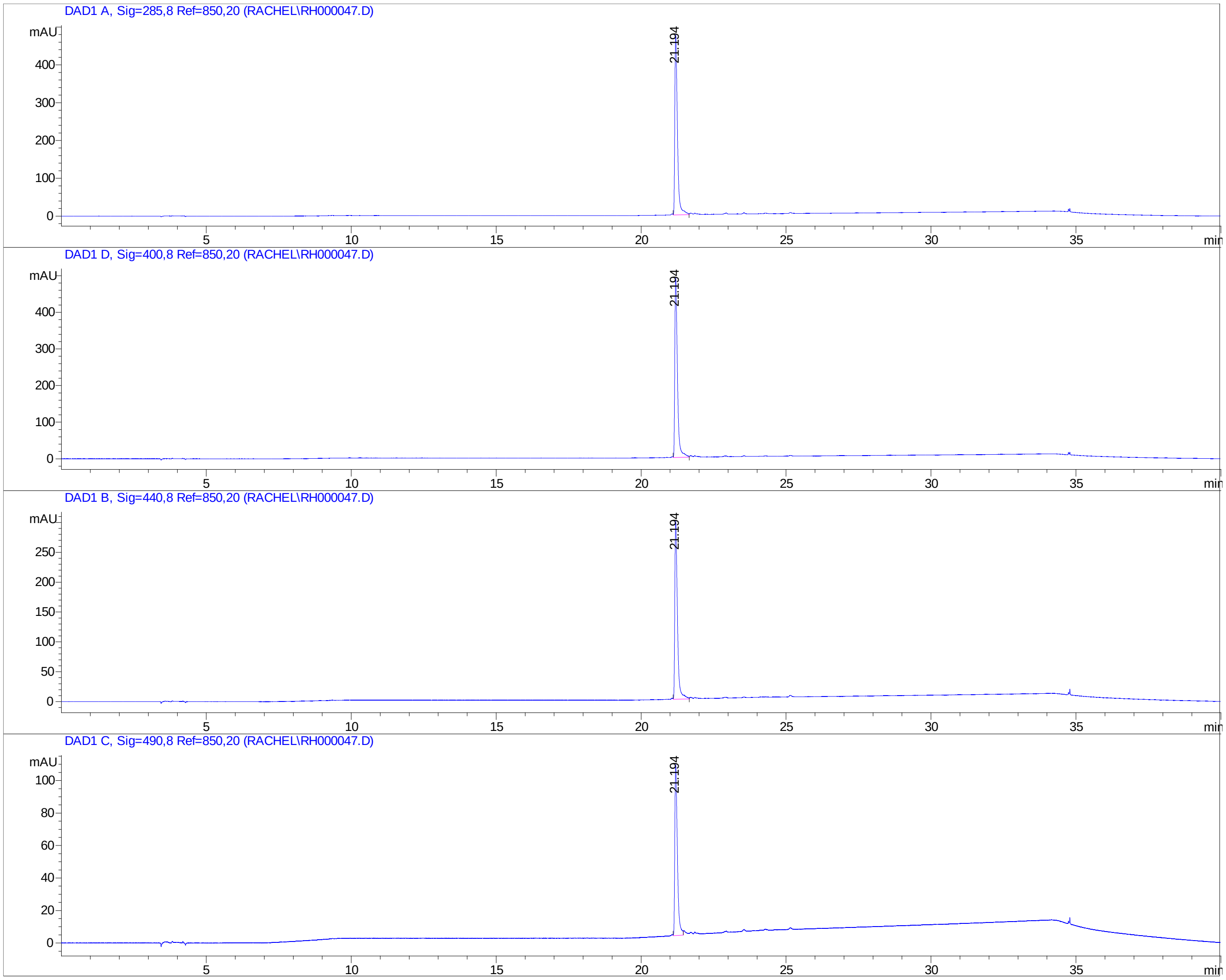

Figure S20. HPLC chromatogram for **Ru-2T** collected at the following wavelengths: 285, 400, 440, and 490 nm (99.5% purity by peak area).

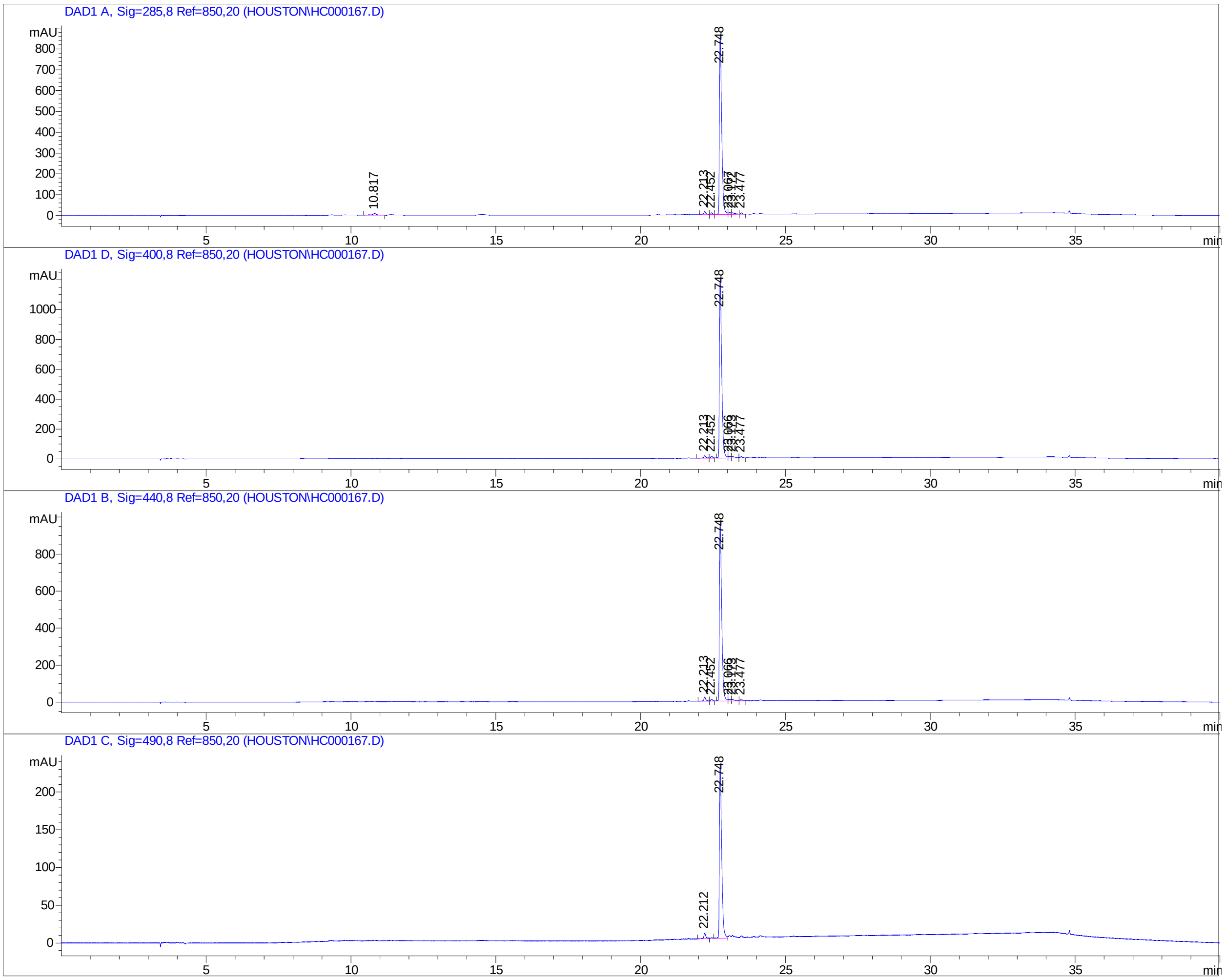

Figure S21. (a) HPLC chromatogram for **Ru-3T** collected at the following wavelengths: 285, 400, 440, and 490 nm (96% purity by peak area).

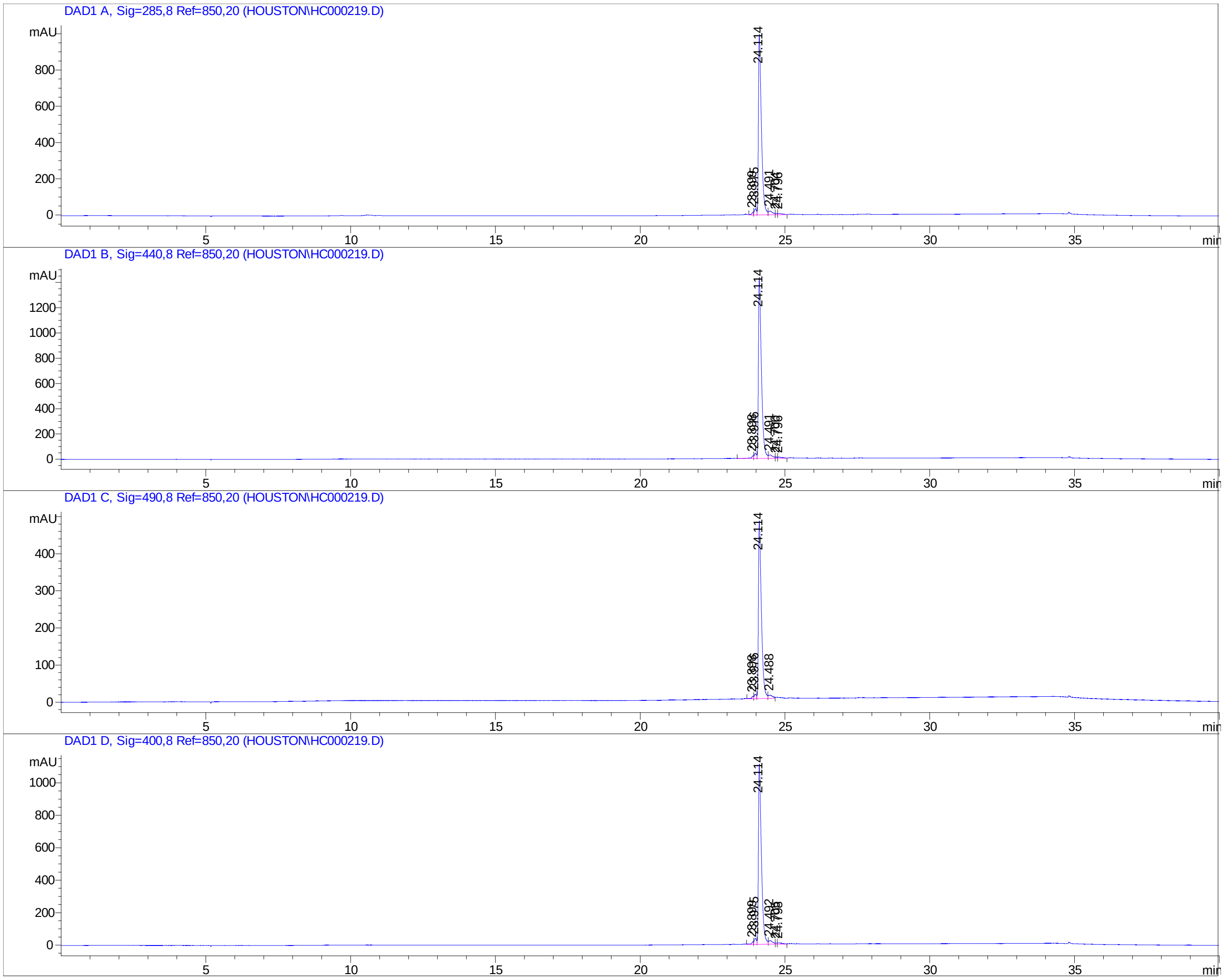

Figure S22. HPLC chromatogram for **Ru-4T** collected at the following wavelengths: 400, 285, 440, and 490 nm (99.5% purity by peak area).

Lipophilicity measurements

Table S1. Log distribution coefficient (log $D_{o/w}$) of 50 μM $[Ru(phen)_3](Cl)_2$ and **Ru-*n*T** (*n*=0–4) in 1-octanol and 10 mM phosphate buffer (pH = 7.4) using the shake-flask method.

Compound	log ($D_{o/w}$ ± SD)
$[Ru(phen)_3](Cl)_2$	– 1.853 ± 0.076
Ru-0T	– 1.524 ± 0.017
Ru-1T	– 0.810 ± 0.023
Ru-2T	– 0.212 ± 0.028
Ru-3T	+ 0.772 ± 0.188
Ru-4T	n.d.[a]

[a] log $D_{o/w}$ for **Ru-4T** was undefined due to precipitation at the octanol:phosphate buffer interface leading to no measurable amount of Ru-4T in the phosphate buffer phase.

2.8.3 Computational Studies

Table S2. (a) Dihedral angles φ1–φ4 (degree) and Ru-N distances (Å) values obtained for singlet (^{1}GS) and triplet (T_1) optimized $[Ru(phen)_3]^{2+}$ and **Ru-*n*T** geometries in a water environment at the PBE0/6-31+G**/SDD/level of theory. (b) Ru-N bond labels and dihedral angles defined for the table.

(a)	$[Ru(phen)_3]^{2+}$		**Ru-0T**		**Ru-1T**		**Ru-2T**		**Ru-3T**		**Ru-4T**	
	^{1}GS	**T_1**	**^{1}GS**	**T_1**	**^{1}GS**	**T_1**	**^{1}GS**	**T_1**	**^{1}GS**	**T_1**	**^{1}GS**	**T_1**
ű 1	/	/	/	/	177.08	-176.24	176.36	-179.67	177.15	-179.75	-177.59	-179.74
ű 2	/	/	/	/	/	/	-163.28	179.94	-166.40	179.91	-166.59	179.87
ű 3	/	/	/	/	/	/	/	/	162.62	-179.94	164.80	-179.92
ű 4	/	/	/	/	/	/	/	/	/	/	-161.41	179.82
Ru-N1	2.08	2.05	2.07	2.05	2.07	2.05	2.07	2.07	2.07	2.07	2.07	2.07
Ru-N2	2.08	2.05	2.07	2.05	2.07	2.05	2.07	2.07	2.07	2.07	2.07	2.07
Ru-N3	2.08	2.08	2.08	2.08	2.08	2.08	2.08	2.08	2.08	2.08	2.08	2.08
Ru-N4	2.08	2.10	2.08	2.10	2.08	2.10	2.08	2.08	2.08	2.08	2.08	2.08
Ru-N5	2.08	2.10	2.08	2.10	2.08	2.10	2.08	2.08	2.08	2.08	2.08	2.08
Ru-N6	2.08	2.08	2.08	2.08	2.08	2.08	2.08	2.08	2.08	2.08	2.08	2.08

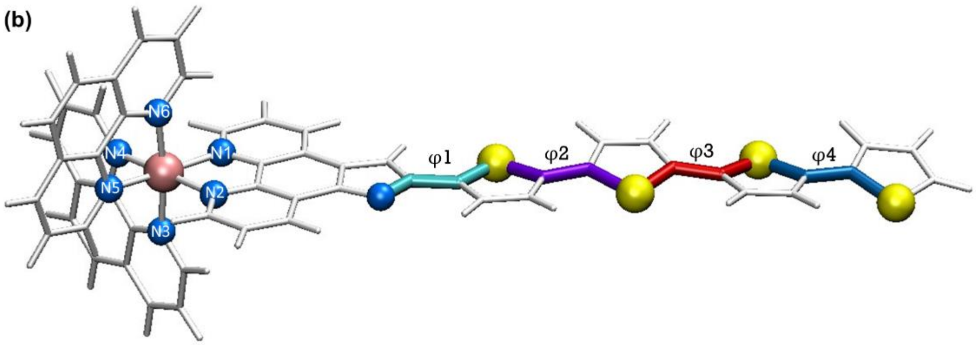

Table S3. Calculated percent contribution of the Ru *d*-orbital and the orbitals involving phen, IP, and *n*T chain to the frontier orbitals (HOMO-1, HOMO, LUMO, LUMO+1) for $[Ru(phen)_3]^{2+}$ and **Ru-*n*T** in the singlet ground state (^{1}GS).

	HOMO-1				**HOMO**				**LUMO**				**LUMO+1**			
%	Ru	phen	IP	*n*T	Ru	phen	IP	*n*T	Ru	phen	IP	*n*T	Ru	phen	IP	*n*T
$[Ru(phen)_3]^{2+}$	47	53	/	/	61	39	/	/	2	98	/	/	1	99	/	/
Ru-0T	46	29	25	/	58	26	16	/	2	57	41	/	2	69	29	/
Ru-1T	18	42	36	4	55	26	19	/	2	57	41		2	72	25	1
Ru-2T	55	25	19	1	1	39	35	26	2	56	39	3	2	68	25	5
Ru-3T	55	26	19	0	0	36	18	46	3	55	40	2	3	64	23	10
Ru-4T	55	27	18	0	0	27	13	61	3	52	38	7	3	40	21	36

Table S4. Computed absorption transitions >400 nm (λ and λ$_{exp}$), oscillator strength (*f*), theoretical peak assignment, and predominant configuration.

Cmpd	***ə˞ /***	***ə$_{exp}$ / nm***	***f***	**Assignment**	**Main Configuration**
[Ru(phen)$_3$]$^{2+}$	432	*444*	0.112	H-2→L+1 H-1→L+2	^{1}MLCT (65%)
Ru-0T	434	*450*	0.149	H-1→L+1; H-2→L+2	^{1}MLCT (62%)
	433		0.119	H-1→L+2; H-2→L+1	^{1}MLCT (62%)
Ru-1T	438	*457*	0.207	H-1→L+1; H-2→L+2	^{1}MLCT (55%)
	434		0.118	H-1→L+2; H-2→L+1	^{1}MLCT (65%)
Ru-2T	455	*457*	0.247	H-3→L H→L	^{1}MLCT (52%)/^{1}LLCT (30%)
	443		0.247	H-3→L+1 H→L+1	^{1}MLCT (47%)/^{1}LLCT (30%)
	434		0.118	H-1→L+1; H-2→L+2	^{1}MLCT (62%)
Ru-3T	466	*460*	1.034	H→L	^{1}ILCT/^{1}IL (58%)/^{1}LLCT(20%)
	449		0.266	H→L+1; H-3→L	^{1}MLCT (47%)/^{1}LLCT (35%)
	438		0.771	H→L+3	^{1}ILCT/^{1}IL (58%) /^{1}LLCT (20%)
	410	*413*	0.110	H→L+4; H-1→L+3; H-3→L+3	^{1}MLCT (42%)/^{1}LLCT(40%)
Ru-4T	488	*465*	2.231	H→L+1	^{1}ILCT/^{1}IL (77%)
	462		0.185	H→L; H→L+3	^{1}ILCT/^{1}IL (53%)/^{1}LLCT (30%)
	435	*436*	0.110	H-3→L+1; H-2→L+2	^{1}MLCT (56%)

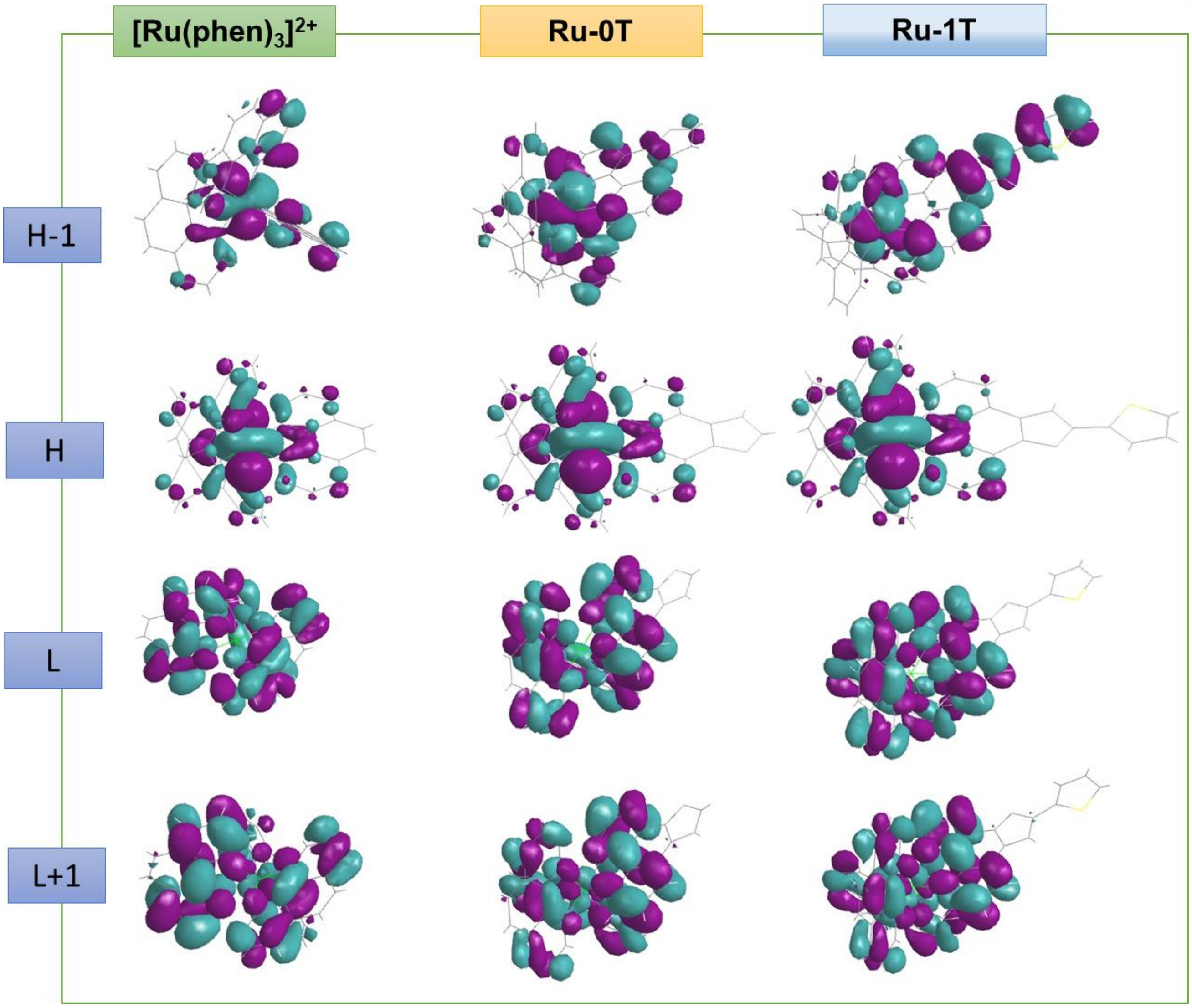
[Ru(phen)$_3$]$^{2+}$
Ru-0T
Ru-1T
H-1
H
L
L+1

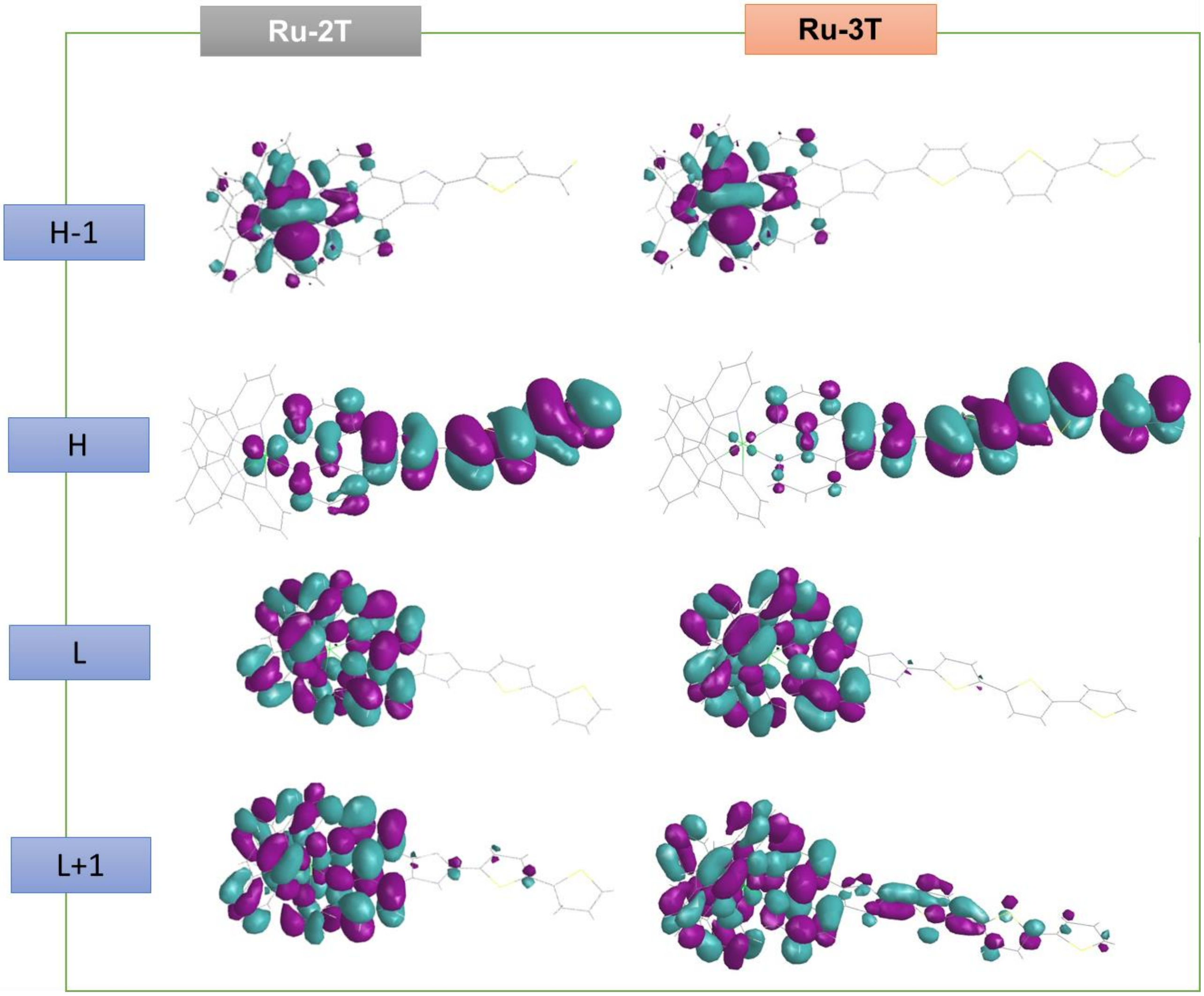
Ru-2T
Ru-3T
H-1
H
L
L+1

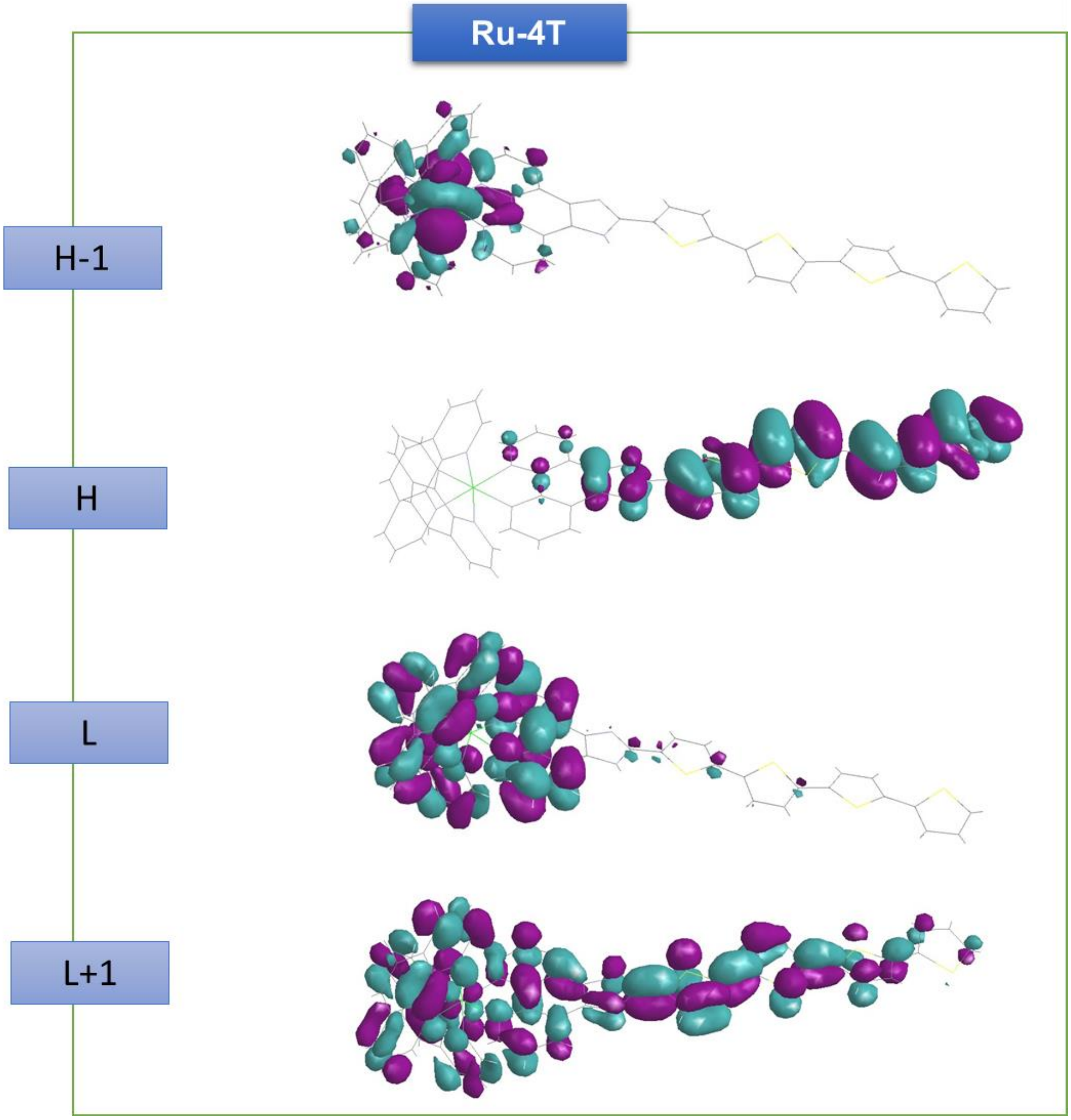

Figure S23. Plots of HOMO-1 (H-1), HOMO (H), LUMO (L) and LUMO+1 (L+1) molecular orbitals for $[Ru(phen)_3]^{2+}$ and **Ru-*n*T** computed in water at the M06/6-31+G(d,p)/SDD/ level of theory.

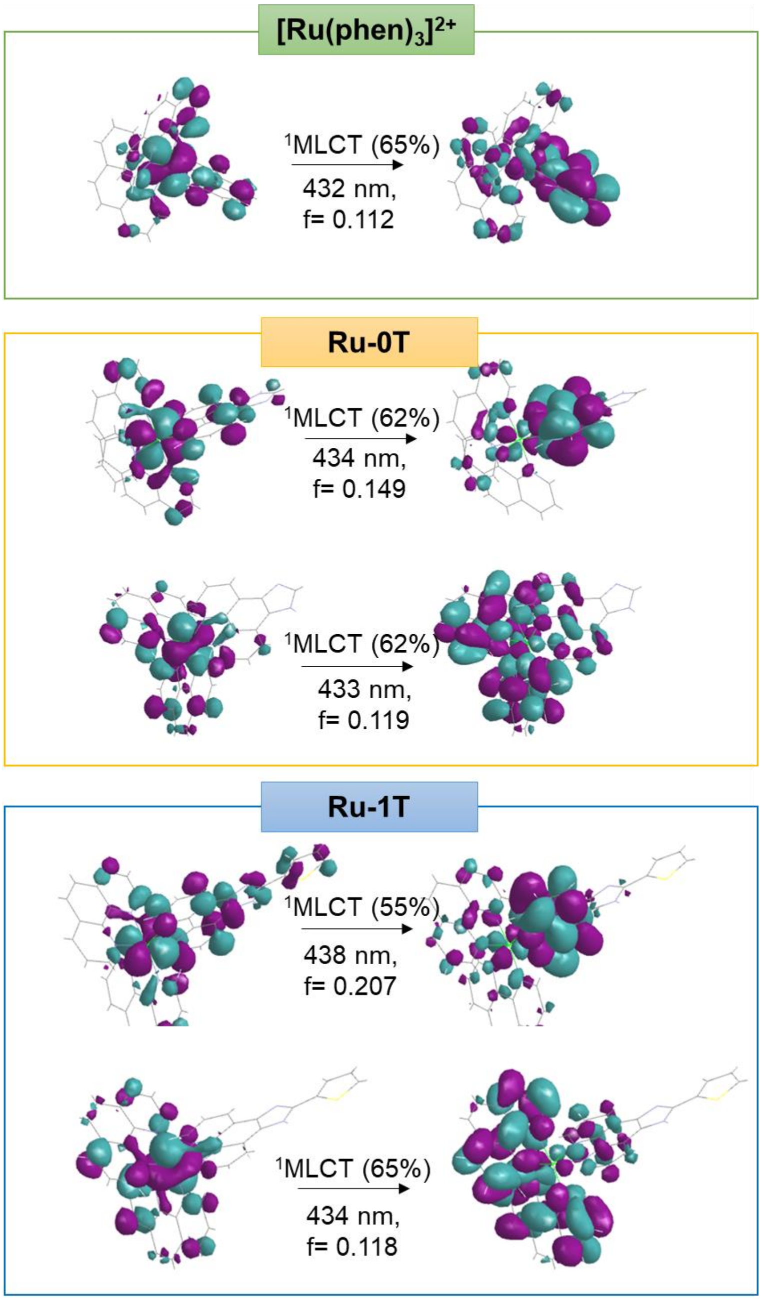
[Ru(phen)3]2+
1MLCT (65%)
432 nm,
f= 0.112
Ru-0T
1MLCT (62%)
434 nm,
f= 0.149
1MLCT (62%)
433 nm,
f= 0.119
Ru-1T
1MLCT (55%)
438 nm,
f= 0.207
1MLCT (65%)
434 nm,
f= 0.118

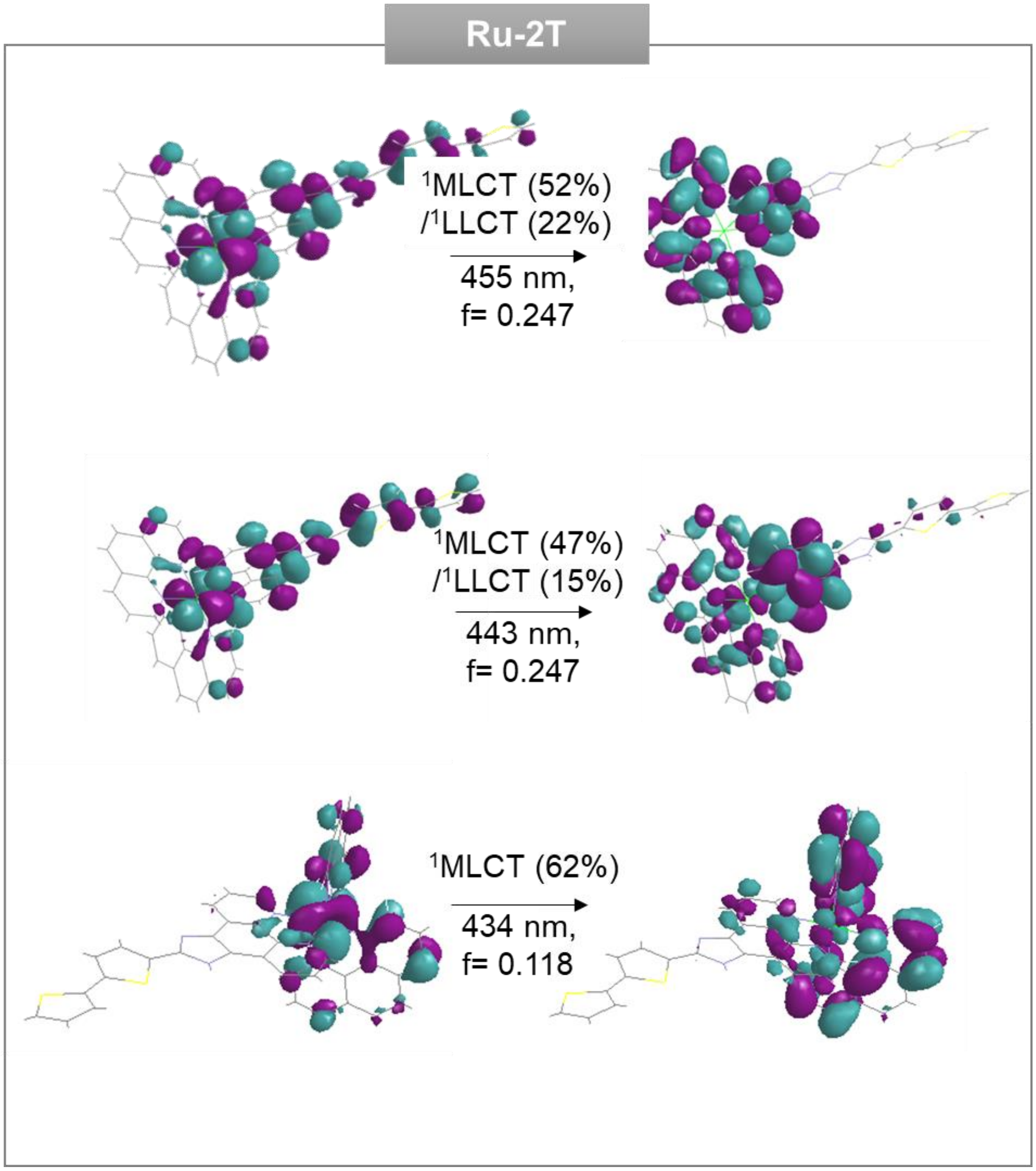
Ru-2T
^{1}MLCT (52%) /^{1}LLCT (22%)
455 nm, f= 0.247
^{1}MLCT (47%) /^{1}LLCT (15%)
443 nm, f= 0.247
^{1}MLCT (62%)
434 nm, f= 0.118

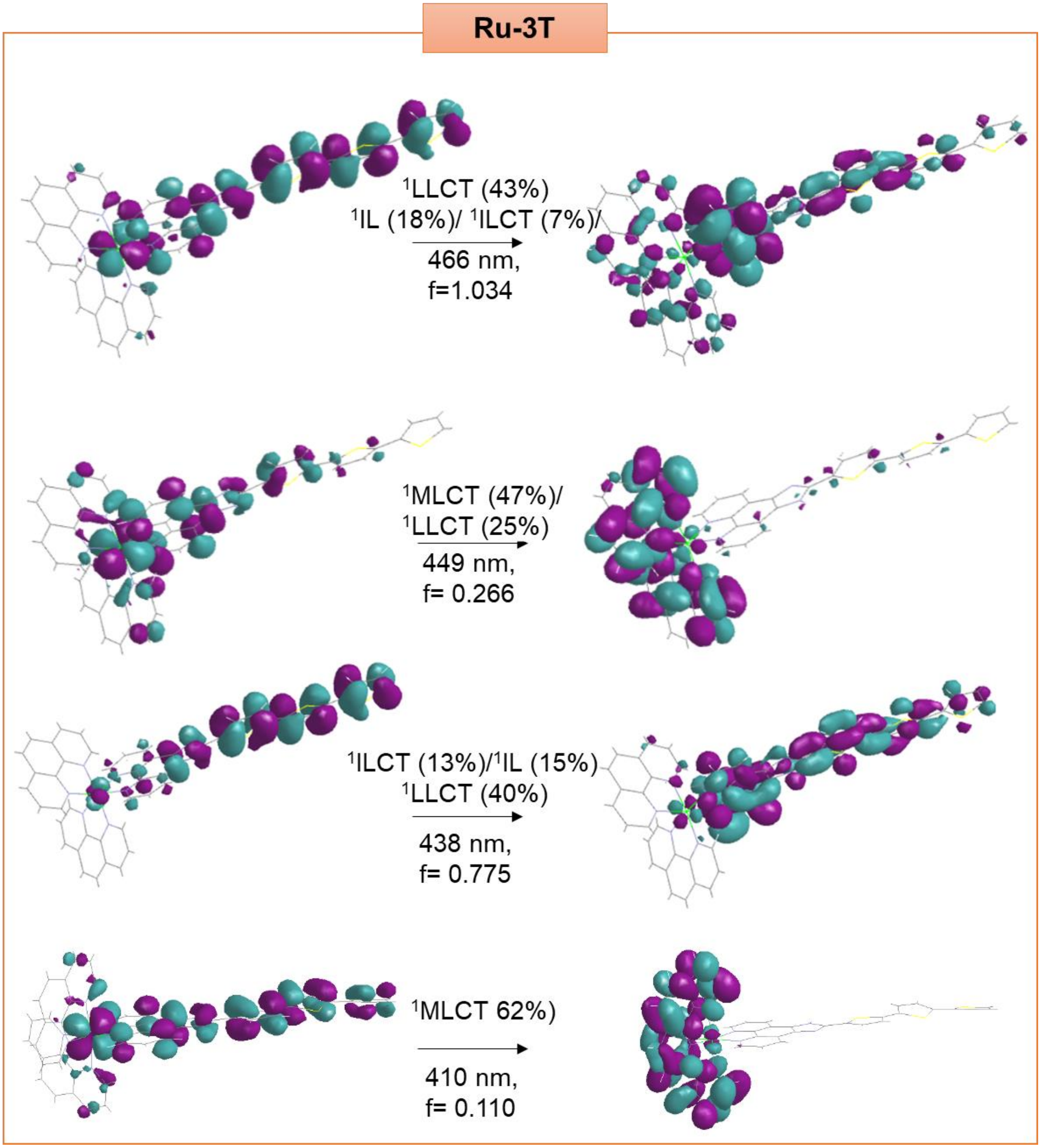
Ru-3T
^{1}LLCT (43%)
^{1}IL (18%)/ ^{1}ILCT (7%)/
466 nm,
f=1.034
^{1}MLCT (47%)/
^{1}LLCT (25%)
449 nm,
f= 0.266
^{1}ILCT (13%)/^{1}IL (15%)
^{1}LLCT (40%)
438 nm,
f= 0.775
^{1}MLCT 62%)
410 nm,
f= 0.110

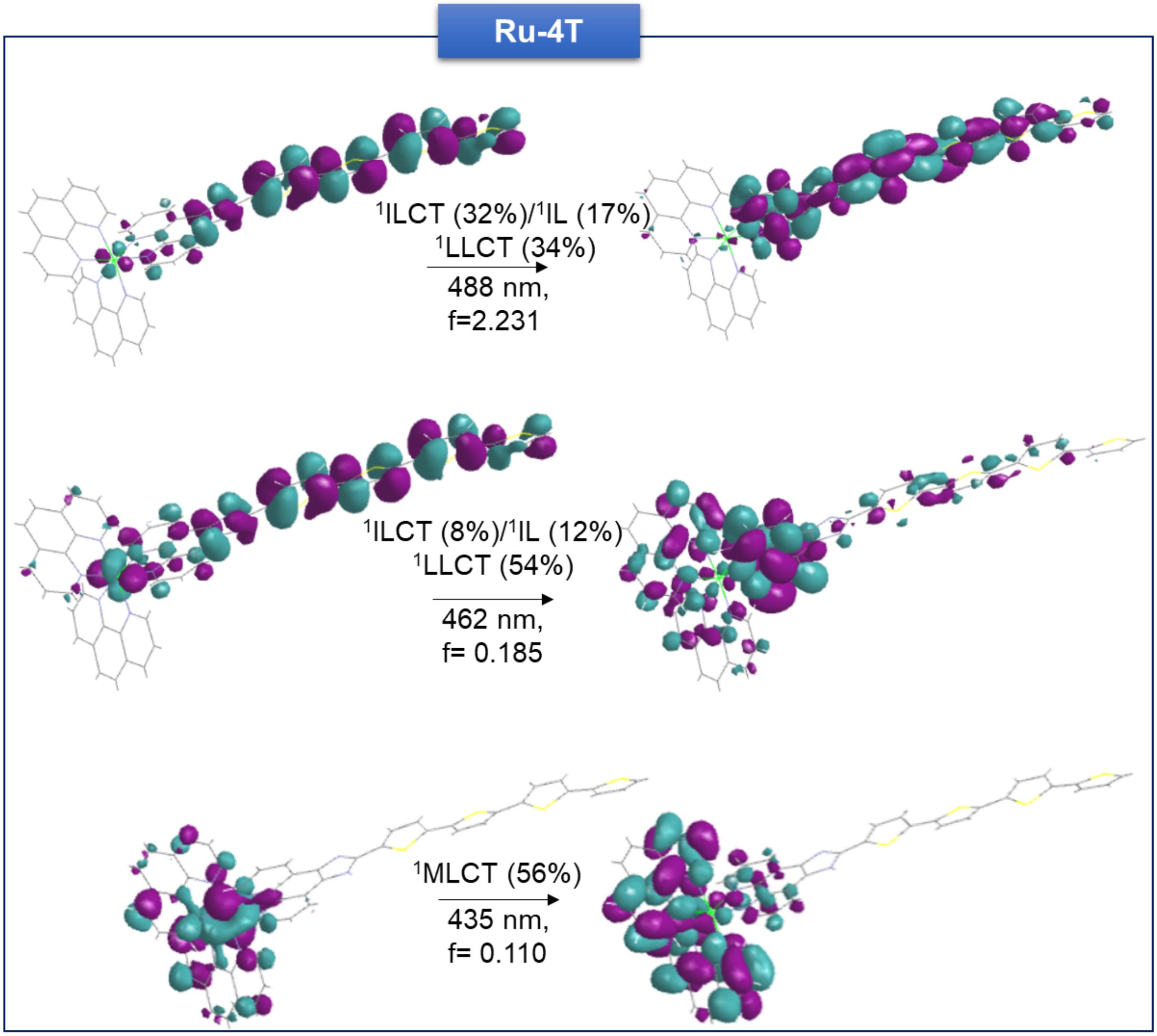

Figure S24. Occupied and virtual NTOs and predominant configuration of the computed absorption wavelengths >400 nm reported in Table S4.

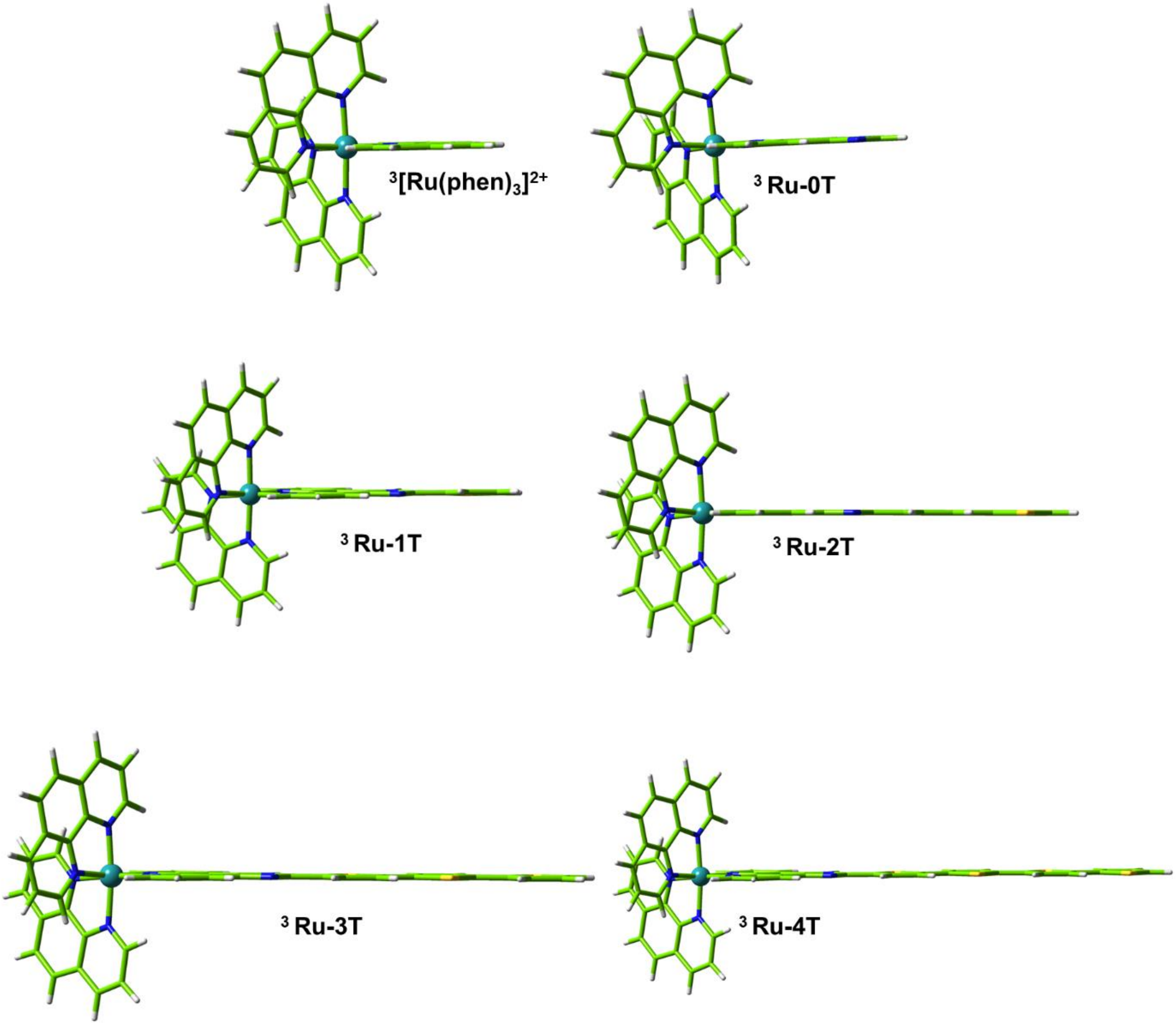

Figure S25. Optimized T_1 geometries for $[Ru(phen)_3]^{2+}$ and **Ru-*n*T** in a water environment at the PBE0/6-31+G(d,p)/SDD/ level of theory.

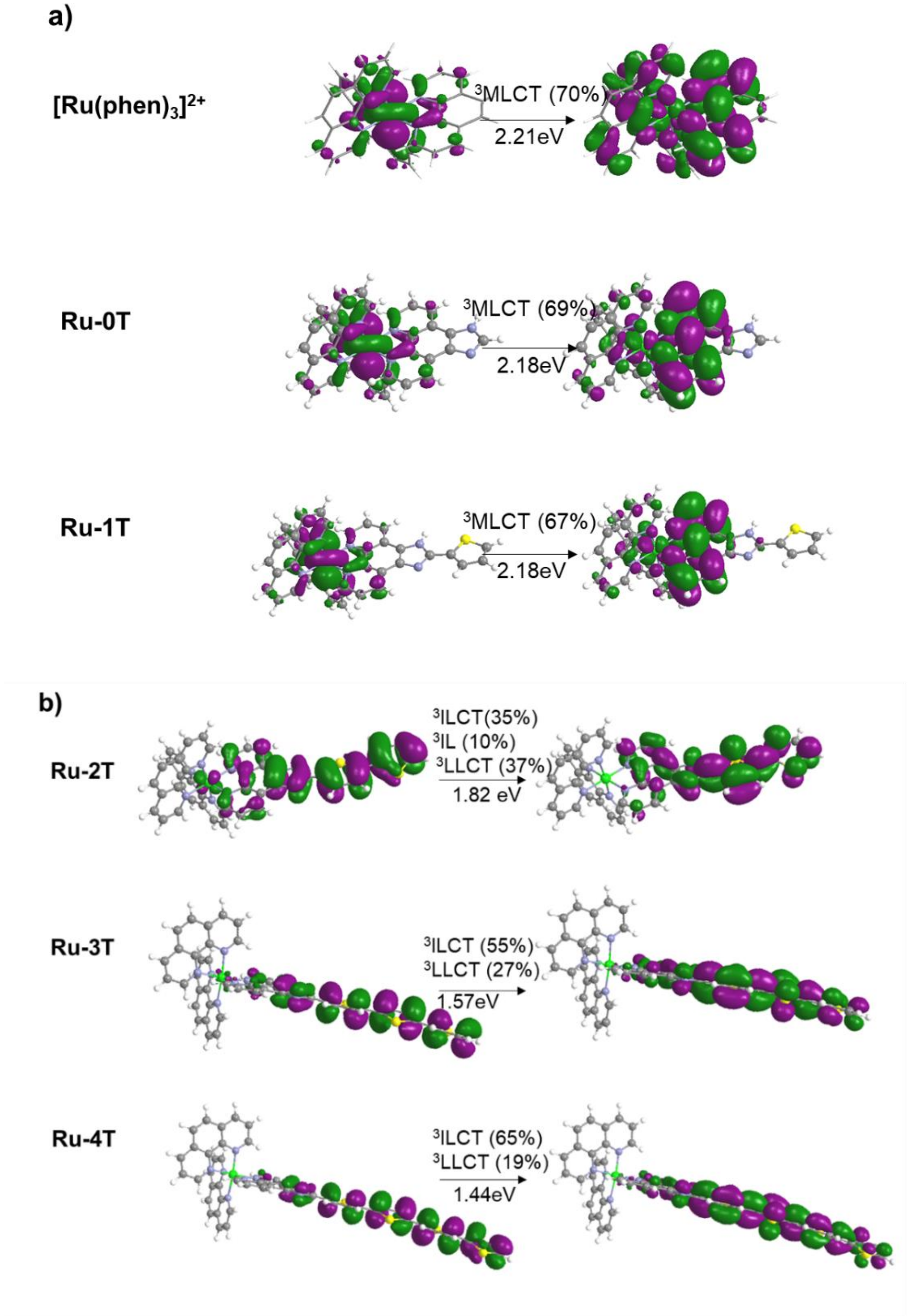

Figure S26. Occupied and Virtual Natural Transition Orbitals (NTOs) of the lowest energy triplet excited states (T_1): (a) ^{3}MLCT T_1 states of $[Ru(phen)_3]^{2+}$ and **Ru-*n*T** (*n*=0,1). (b) Mixed ligand-based ^{3}ILCT/^{3}LLCT T_1 states of **Ru-2T**, **Ru-3T**, and **Ru-4T**, in a water environment at the M06/6-31+G**/SDD level of theory.

Table S5. Adiabatic labels and vertical energies (ΔE_{vert}) of the lowest ^{3}MLCT, ^{3}ILCT, and ^{3}MC states, along with the corresponding adiabatic ^{3}MLCT and ^{3}ILCT energies (ΔE_{adia}) computed with respect to the S_0 minima, and emission energies (ΔE_{em}) for the ^{3}MLCT states for $[\text{Ru(phen)}_3]^{2+}$ and **Ru-*n*T** (*n*=0–4) in a water environment at the TD-M06/6-31+G**/SDD level of theory. The experimental ^{3}MLCT emission energies at 77 and 298 K and the energies estimated for ^{3}ILCT states from Stern-Volmer quenching rates are also provided for comparison.

	^{3}MLCT (eV)					**^{3}ILCT (eV)**				**^{3}MC (eV)**	
Compound	State	ΔE_{vert}	ΔE_{adia}	ΔE_{em}	$\Delta E_{\text{em, 77 K, 298 K}}$ Expt	State	ΔE_{vert}	ΔE_{adia}	$E^{0\text{-}0}$ Expt	State	ΔE_{vert}
$[\text{Ru(phen)}_3]^{2+}$	T_1	2.43	2.21	2.01	2.19, 2.06				n.d.	T_{21}	3.28
Ru-0T	T_1	2.40	2.18	1.99	2.18, 2.01				n.d.	T_{18}	3.07
Ru-1T	T_1	2.40	2.18	1.98	2.16, 2.05				n.d.	T_{19}	3.06
Ru-2T	T_2	2.40	2.17	1.98	2.15, 2.03	T_1	2.23	1.82	n.d.	T_{19}	3.06
Ru-3T	T_2	2.40	2.16*	1.99*	2.16, 2.02	T_1	1.97	1.57	~1.5	T_{22}	3.06
Ru-4T	T_2	2.37	2.12	1.99	2.16, 2.02	T_1	1.84	1.44	~1.5	T_{25}	3.06

*Not fully converged due to degeneracy with the ^{3}ILCT state; n.d.=not determined.

2.8.4 Spectroscopic Characterization

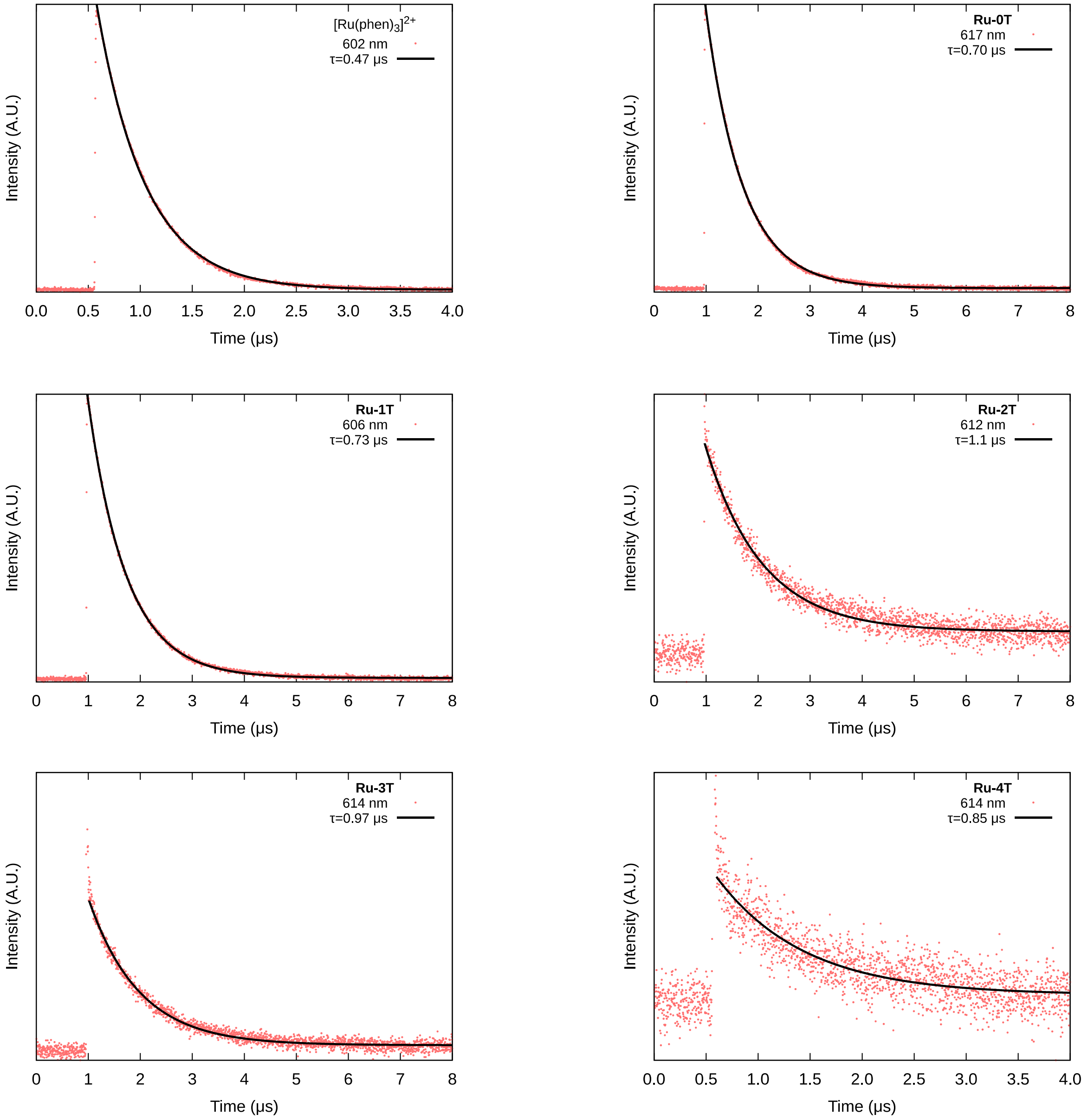

Figure S27: Emission decays measured as ≈5 μM solutions in degassed MeCN at RT, with a 355 nm excitation.

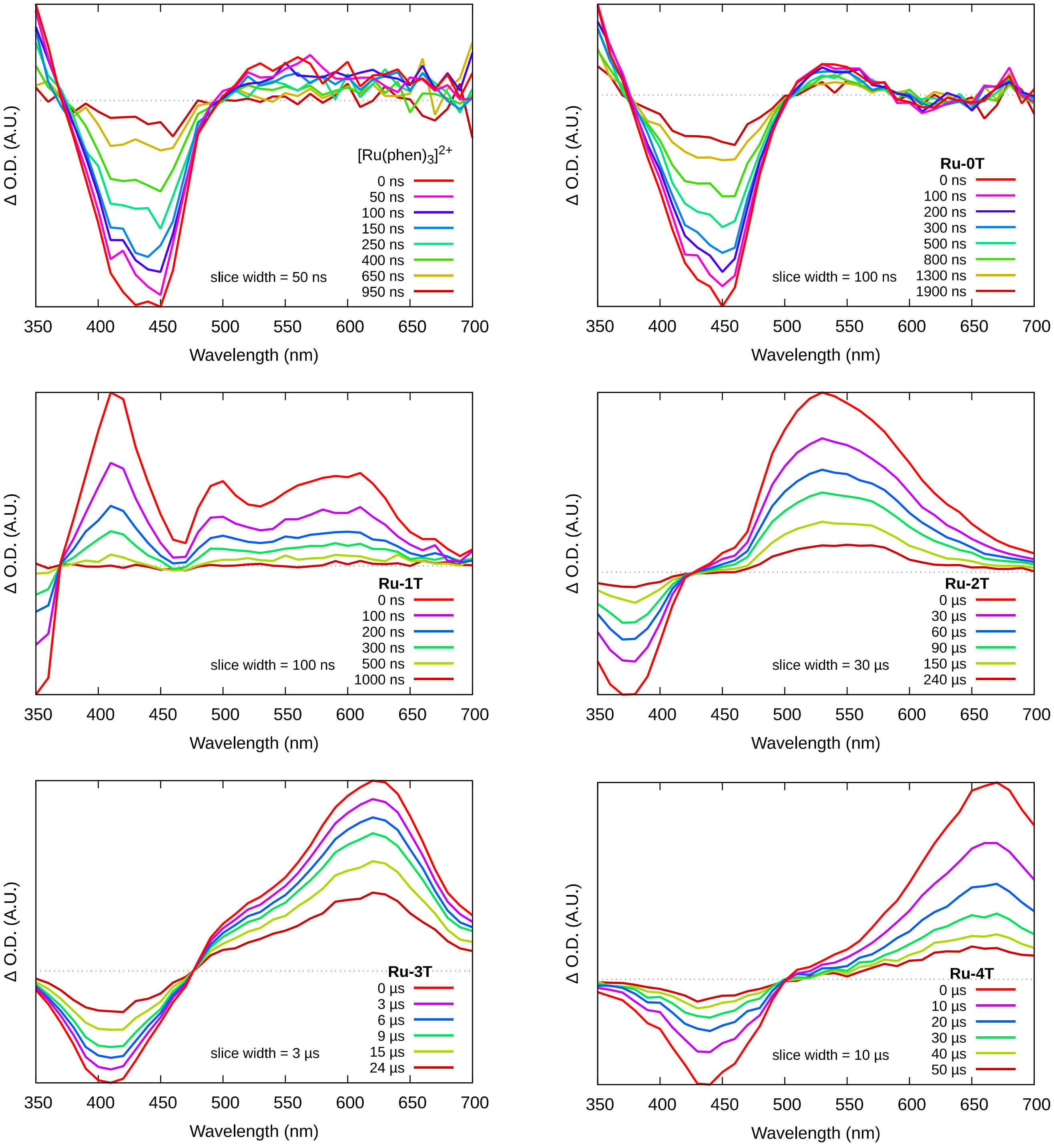

Figure S28. Excited state absorption profiles of the series, measured as ≈5 µM solutions in degassed MeCN at RT, with a 355 nm excitation.

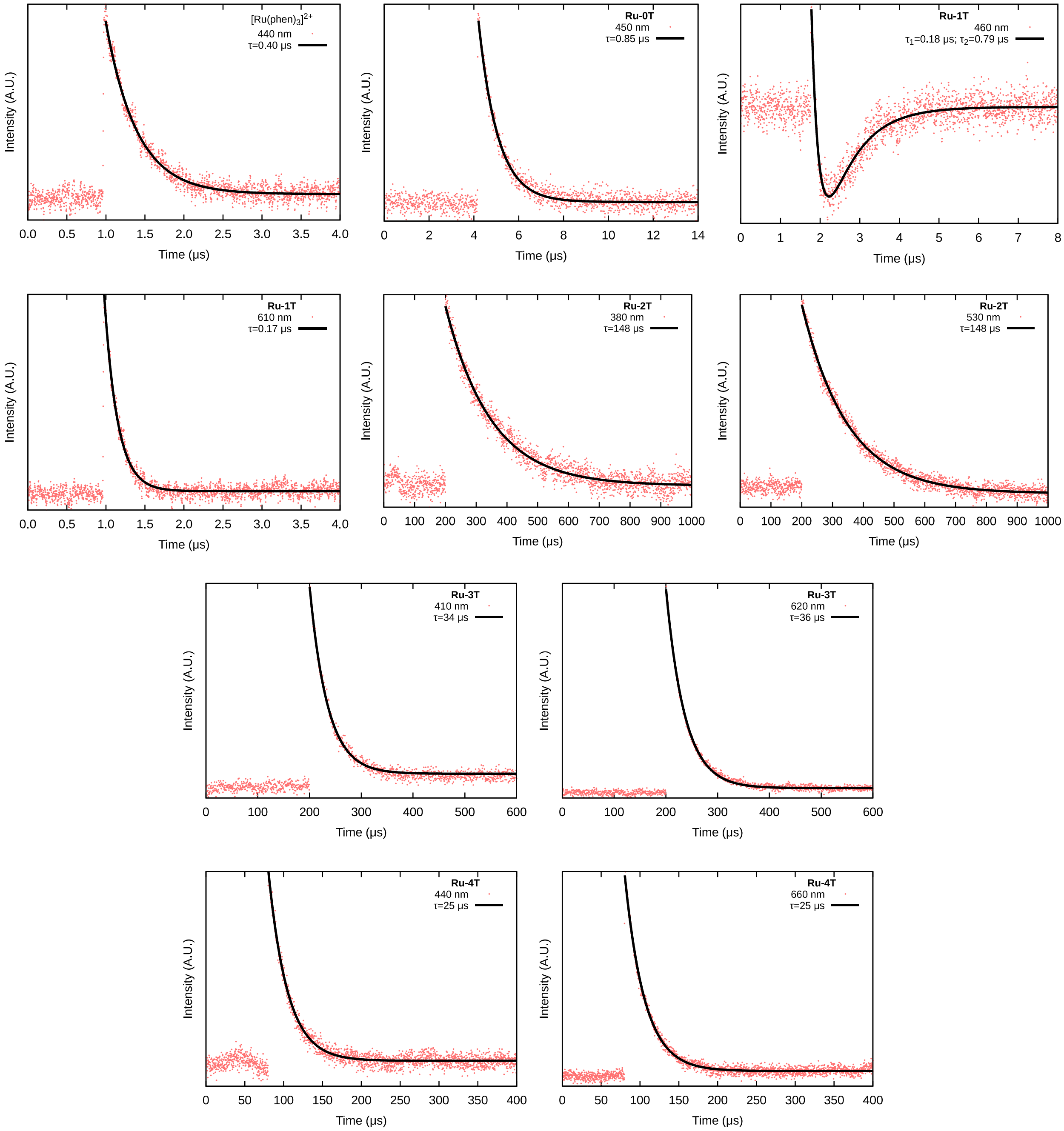

Figure S29: Transient absorption decays measured as ≈5 μM solutions in degassed MeCN at RT, with a 355 nm excitation.

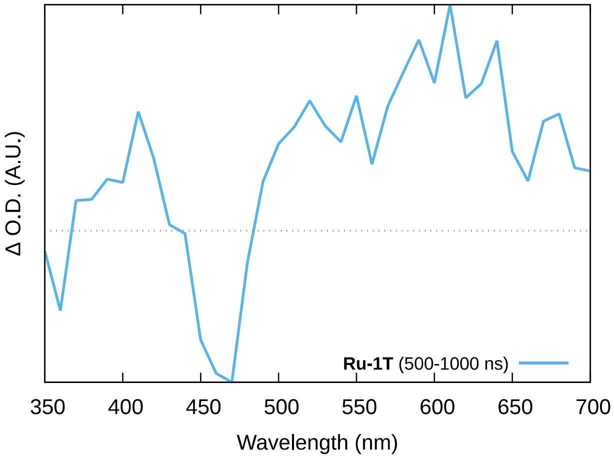

Figure S30. ESA profile of **Ru-1T** at a longer time slice, showing a bleach near 460 nm and an absorption at longer wavelengths, typical of a ^{3}MLCT state.

2.8.5 Electrochemical Characterization

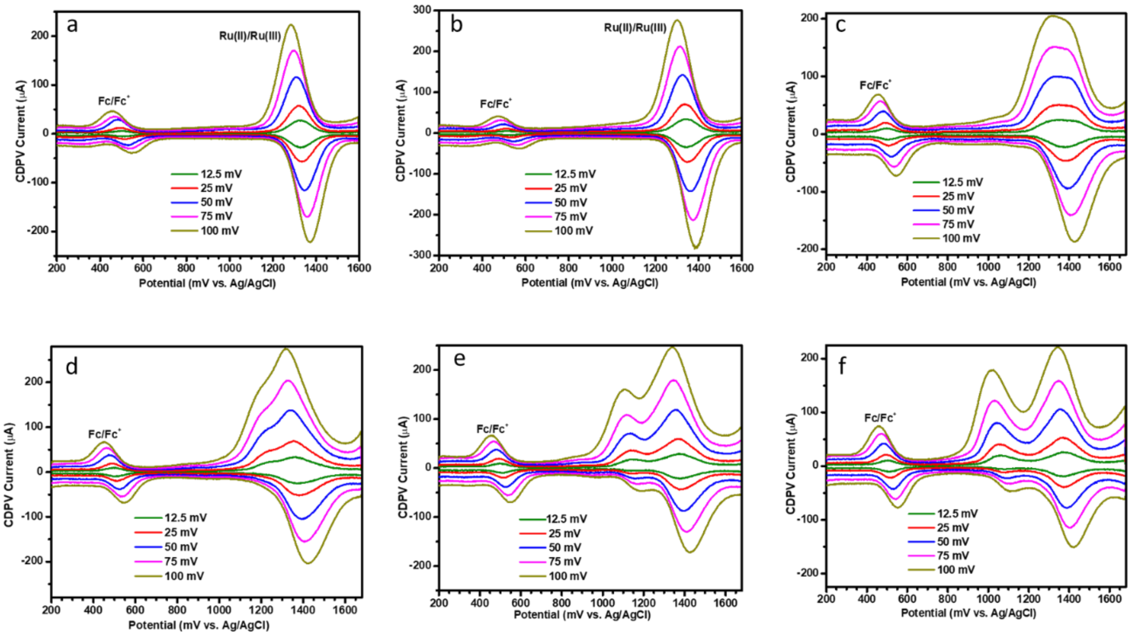

Figure S31. CDPV for the oxidation of (a) [Ru(phen)$_3$]$^{2+}$, (b) **Ru-0T**, (c) **Ru-1T**, (d) **Ru-2T**, (e) **Ru-3T**, and (f) **Ru-4T** in DMF containing 0.1 M tetrabutylammonium hexafluorophosphate and ferrocene as an internal standard.

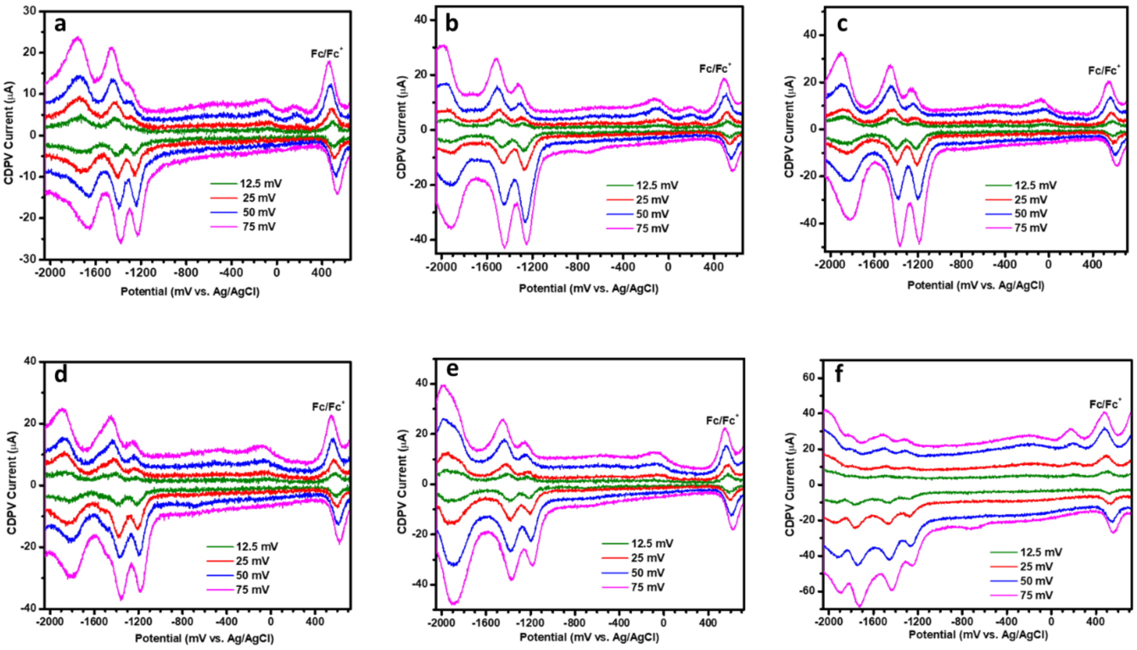

Figure S32. CDPV for the reduction of (a) $[Ru(phen)_3]^{2+}$, (b) **Ru-0T**, (c) **Ru-1T**, (d) **Ru-2T**, (e) **Ru-3T**, and (f) **Ru-4T** in DMF containing 0.1 M tetrabutylammonium hexafluorophosphate and ferrocene as an internal standard.

2.8.6 Biological and Photobiological Characterization

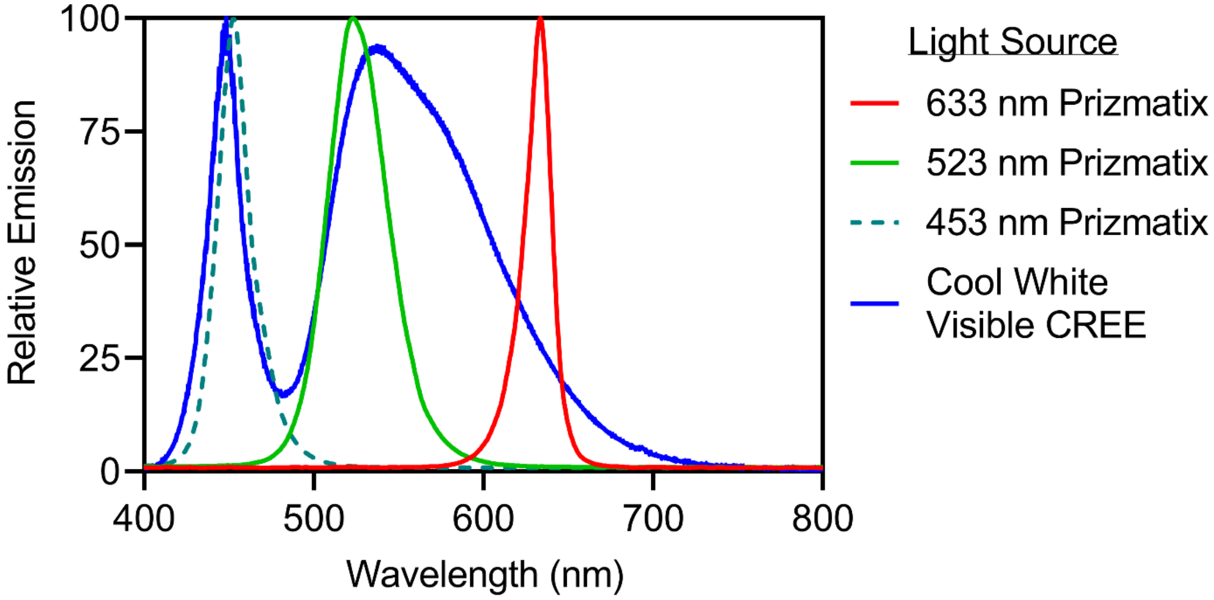

Figure S33. Spectral outputs of light sources used in photobiological experiments.

Table S6: Cytotoxicity and photocytotoxicity of [Ru(phen)$_3$](Cl)$_2$ and **Ru-0T**–**Ru-4T** in normoxic (~18.5% O$_2$, top) or hypoxic (1% O$_2$, bottom) treated SK-MEL-28 melanoma cells. Values correspond to the biological replicate shown in Figure 13.

		Resazurin-Cell Viability						
		EC$_{50}$ ± SEM (μM)				PI^d		
Complex	Oxygen%	Dark	Visible^a	Green^b	Red^c	Visible^a	Green^b	Red^c
[Ru(phen)$_3$](Cl)$_2$	~18.5	>300	22.2 ± 5.4	>300	>300	~14	~1	~1
Ru-0T	~18.5	>300	6.80 ± 2.49	>300	>300	~44	~1	~1
Ru-1T	~18.5	138 ± 6	0.626 ± 0.198	5.94 ± 0.17	144 ± 4	220	23	1
Ru-2T	~18.5	113 ± 5	0.583 ± n.d.	0.536 ± 0.144	116 ± 6	194	211	1
Ru-3T	~18.5	66.4 ± 3.3	0.057 ± 0.037	0.247 ± 0.015	59.5 ± 1.7	1165	269	1
Ru-4T	~18.5	84.0 ± 2.5	(7.39 ± n.d.)*10^{-4}	0.062 ± 0.0076	16.3 ± 1.6	113731	1364	5
[Ru(phen)$_3$](Cl)$_2$	1	>300	>300	>300	>300	~1	~1	~1
Ru-0T	1	>300	>300	>300	>300	~1	~1	~1
Ru-1T	1	147 ± 5	172 ± 6	147 ± 4	156 ± 5	1	1	1
Ru-2T	1	120 ± 5	137 ± 9	128 ± 7	122 ± 5	1	1	1
Ru-3T	1	52.5 ± 1.7	75.3 ± 5.8	64.1 ± 4.7	54.0 ± 2.1	1	1	1
Ru-4T	1	86.2 ± 2.1	2.05 ± 0.38	1.34 ± 0.74	91.9 ± 3.0	42	64	1

Light treatments were approximately 100 J cm^{-2} delivered at 18–22 mW cm^{-2} with ^{a}cool white visible (400–700 nm), ^{b} green 523 nm, ^{c}red 633 nm, and ^{d} PI = phototherapeutic index. Hypoxia and normoxia experiments were ran in parallel. PI not determined when dark EC$_{50}$ exceeded 300 μM. SEM not determined when hill slope was too steep.

Table S7. Inter-assay performance: cytotoxicity and photocytotoxicity of **Ru-3T** in normoxic-treated (~18.5% O_2) SK-MEL-28 melanoma cells.

	Resazurin-Normoxia (18.5% O_2) Ru-3T Repeats						
	EC_{50} ± SEM (μM)				PI^d		
Repeat	Dark	Visible[a]	Green[b]	Red[c]	Visible[a]	Green[b]	Red[c]
0	66.4 ± 3.3	0.0570 ± 0.0368	0.247 ± 0.015	59.5 ± 1.7	1165	269	1
1	122 ± 5	0.0767 ± 0.0075	0.395 ± 0.251	3.29 ± 0.34	1591	309	37
2	124 ± 4	0.0689 ± n.d.	0.219 ± 0.037	3.77 ± 0.05	1800	566	33
3	92.1 ± 2.0	0.0786 ± n.d.	0.638 ± n.d.	3.37 ± 0.09	1172	144	27
4	82.9 ± 2.3	0.0715 ± n.d.	0.164 ± n.d.	50.3 ± n.d.	1159	505	2
5	110 ± 3	0.0642 ± n.d.	0.264 ± 0.032	34.8 ± 2.9	1713	417	3
6	70.4 ± 3.1	0.0277 ± 0.0033	0.186 ± 0.038	69.4 ± 3.4	2542	378	1
Mean ± SD[e]	95.4 ± 23.7	0.0635 ± 0.0174	0.302 ± 0.166	32.1 ± 28.7	1592 ± 501	370 ± 144	14.9 ± 16.6
min	66.4	0.057	0.164	3.29	1159	144	1
max	124	0.0786	0.638	69.4	2542	566	37

Light treatments were approximately 100 J cm^{-2} delivered at 18–22 mW cm^{-2}. [a]cool white visible (400–700 nm), [b] green 523 nm, [c]red 633 nm, [d] PI = phototherapeutic index (dark EC_{50} / light EC_{50}), and n.d. = SEM not determined due to overly steep hill slope. [e] Did not test for outliers or run meta-analysis, use with caution.

Repeats used different plate maps (all), different tips (Sartorius 790352 repeat #0, VWR 83007-352 repeats #1–2, low retention Sartorius LH-L790352 repeats #3–4), changed cell parent seed stock for repeats 3–6, and overhead lights were off in #4–6. Serum and consumable lots were identical for repeats 0–6. Cell passage numbers were within 15. Run in parallel with normoxic repeats.

Table S8. Inter-assay performance: cytotoxicity and photocytotoxicity of **Ru-3T** in hypoxic-treated (1% O_2) SK-MEL-28 melanoma cells.

	Resazurin-Hypoxia (1% O_2) Ru-3T Repeats						
	EC_{50} ± SEM (μM)				PI[d]		
Repeat	Dark	Visible[a]	Green[b]	Red[c]	Visible[a]	Green[b]	Red[c]
0	52.5 ± 1.7	75.3 ± 5.8	64.1 ± 4.7	54.0 ± 2.1	1	1	1
1	120 ± 4	112 ± n.d.	120 ± 68	115 ± 5	1	1	1
2	118 ± 3	1.00 ± 0.07	0.352 ± 0.018	68.8 ± 3.2	118	335	2
3	98.5 ± 2.7	1.15 ± n.d.	1.04 ± 0.73	93.6 ± 3.3	86	95	1
4	78.6 ± 1.6	1.14 ± n.d.	1.11 ± n.d.	77.9 ± 1.2	69	71	1
5	109 ± 2	0.215 ± 0.061	0.420 ± 0.056	111 ± 4	507	260	1
6	72.1 ± 3.3	0.447 ± 0.067	0.813 ± 0.310	62.5 ± 3.5	161	89	~1
Mean ± SD[e]	92.7 ± 25.6	27.3 ± 46.5	26.8 ± 47.4	83.3 ± 23.8	135 ± 174	122 ± 128	1.14 ± 0.38
min	52.5	0.215	0.352	54.0	1	1	1
max	120	112	120	115	507	335	2

Light treatments were approximately 100 J cm^{-2} delivered at 18–22 mW cm^{-2}. [a]cool white visible (400–700 nm), [b] green 523 nm, [c]red 633 nm, [d] PI = phototherapeutic index (dark EC_{50} / light EC_{50}), and n.d. = SEM not determined due to overly steep hill slope. [e] Did not test for outliers or run meta-analysis, use with caution.

Repeats used different plate maps (all), different tips (Sartorius 790352 repeat #0, VWR 83007-352 repeats #1–2, low retention Sartorius LH-L790352 repeats #3–4), changed cell parent seed stock for repeats 3–6, and overhead lights were off in #4–6. Serum and consumable lots were identical for repeats 0–6. Cell passage numbers were within 15. Run in parallel with normoxic repeats.

Table S9. Inter-assay performance: cytotoxicity and photocytotoxicity of **Ru-4T** in normoxic-treated (~18.5% O$_2$) SK-MEL-28 melanoma cells.

	Resazurin-Normoxia (18.5% O$_2$) Ru-4T Repeats						
	EC$_{50}$ ± SEM (μM)				PI[d]		
Repeat	Dark	Visible[a]	Green[b]	Red[c]	Visible[a]	Green[b]	Red[c]
0	84.0 ± 2.5	(7.39 ± n.d.)x10^{-4}	0.0616 ± 0.0076	16.3 ± 1.6	1.14x10^{5}	1364	5
1	106 ± 3	(4.01 ± 0.51)x10^{-8}	0.147 ± 0.019	1.38 ± n.d.	2.64x10^{9}	721	77
2	101 ± 2	(3.22 ± 0.19)x10^{-7}	0.0306 ± 0.004	1.88 ± 0.11	3.14x10^{8}	3301	54
3	92.0 ± 2.3	(8.04 ± 0.55)x10^{-4}	0.257 ± 0.015	1.44 ± 0.68	1.14x10^{5}	358	64
4	90.9 ± 1.9	(8.58 ± n.d.)x10^{-3}	0.0792 ± n.d.	11.4 ± 0.5	1.06x10^{4}	1148	8
5	85.5 ± 1.3	(6.38 ± 3.86)x10^{-4}	0.0321 ± 0.0020	7.69 ± 0.16	1.34x10^{5}	2664	11
6	101 ± 2	(4.85 ± 0.44)x10^{-3}	0.0593 ± 0.0074	50.6 ± n.d.	2.08x10^{4}	1703	2
Mean ± SD[e]	94.3 ± 8.4	(2.23 ± 3.26)x10^{-3}	0.095 ± 0.081	12.96 ± 17.55	(4.22 ± 9.86)x10^{8}	1608 ± 1050	31.6 ± 32.1
min	84	4.01x10^{-8}	0.0306	1.38	1.06x10^{4}	358	2
max	106	8.58x10^{-3}	0.257	50.6	2.64x10^{9}	3301	77

Light treatments were approximately 100 J cm^{-2} delivered at 18–22 mW cm^{-2}. [a]cool white visible (400–700 nm), [b] green 523 nm, [c]red 633 nm, [d] PI = phototherapeutic index (dark EC$_{50}$ / light EC$_{50}$), n.d. = SEM not determined due to overly steep hill slope. [e] Did not test for outliers or run meta-analysis, use with caution.

Repeats used different plate maps (all), different tips (Sartorius 790352 repeat #0, VWR 83007-352 repeats #1–2, low retention Sartorius LH-L790352 repeats #3–4), changed cell parent seed stock for repeats 3–6, and overhead lights were off in #4–6. Serum and consumable lots were identical for repeats 0–6. Cell passage numbers were within 15. Run in parallel with normoxic repeats.

Table S10. Inter-assay performance: cytotoxicity and photocytotoxicity of **Ru-4T** in hypoxic-treated (1% O$_2$) SK-MEL-28 melanoma cells.

	Resazurin-Hypoxia (1% O$_2$) Ru-4T Repeats						
	EC$_{50}$ ± SEM (μM)				PI[d]		
Repeat	Dark	Visible[a]	Green[b]	Red[c]	Visible[a]	Green[b]	Red[c]
0	86.2 ± 2.1	2.05 ± 0.38	1.34 ± 0.74	91.9 ± 3.0	42	64	1
1	95.5 ± 2.4	6.44 ± 8.22	19.2 ± 15.6	22.0 ± 15.4	15	5	4
2	98.3 ± 2.3	0.0323 ± 0.0039	0.199 ± 0.012	6.19 ± 0.25	3043	494	16
3	87.4 ± 2.1	0.299 ± 0.172	0.809 ± 0.451	4.55 ± 1.84	292	108	19
4	81.8 ± 1.2	0.252 ± 0.060	0.562 ± 0.052	85.7 ± 2.3	325	146	1
5	92.5 ± 2.7	0.0537 ± 0.0040	0.229 ± 0.011	97.0 ± 4.2	1723	404	1
6	102 ± 2	0.0701 ± n.d.	0.211 ± 0.040	106 ± 2	1455	483	1
Mean ± SD[e]	92.0 ± 7.2	1.31 ± 2.37	3.22 ± 7.06	59.0 ± 45.8	985 ± 1136	243 ± 209	6.14 ± 7.88
min	81.8	0.0323	0.199	4.55	15	5	1
max	102	6.44	1.34	106	3043	494	19

Light treatments were approximately 100 J cm^{-2} delivered at 18–22 mW cm^{-2}. [a]cool white visible (400–700 nm), [b] green 523 nm, [c]red 633 nm, [d] PI = phototherapeutic index (dark EC$_{50}$ / light EC$_{50}$), n.d. = SEM not determined due to overly steep hill slope. [e] Did not test for outliers or run meta-analysis, use with caution.

Repeats used different plate maps (all), different tips (Sartorius 790352 repeat #0, VWR 83007-352 repeats #1–2, low retention Sartorius LH-L790352 repeats #3–4), changed cell parent seed stock for repeats 3–6, and overhead lights were off in #4–6. Serum and consumable lots were identical for repeats 0–6. Cell passage numbers were within 15. Run in parallel with normoxic repeats.

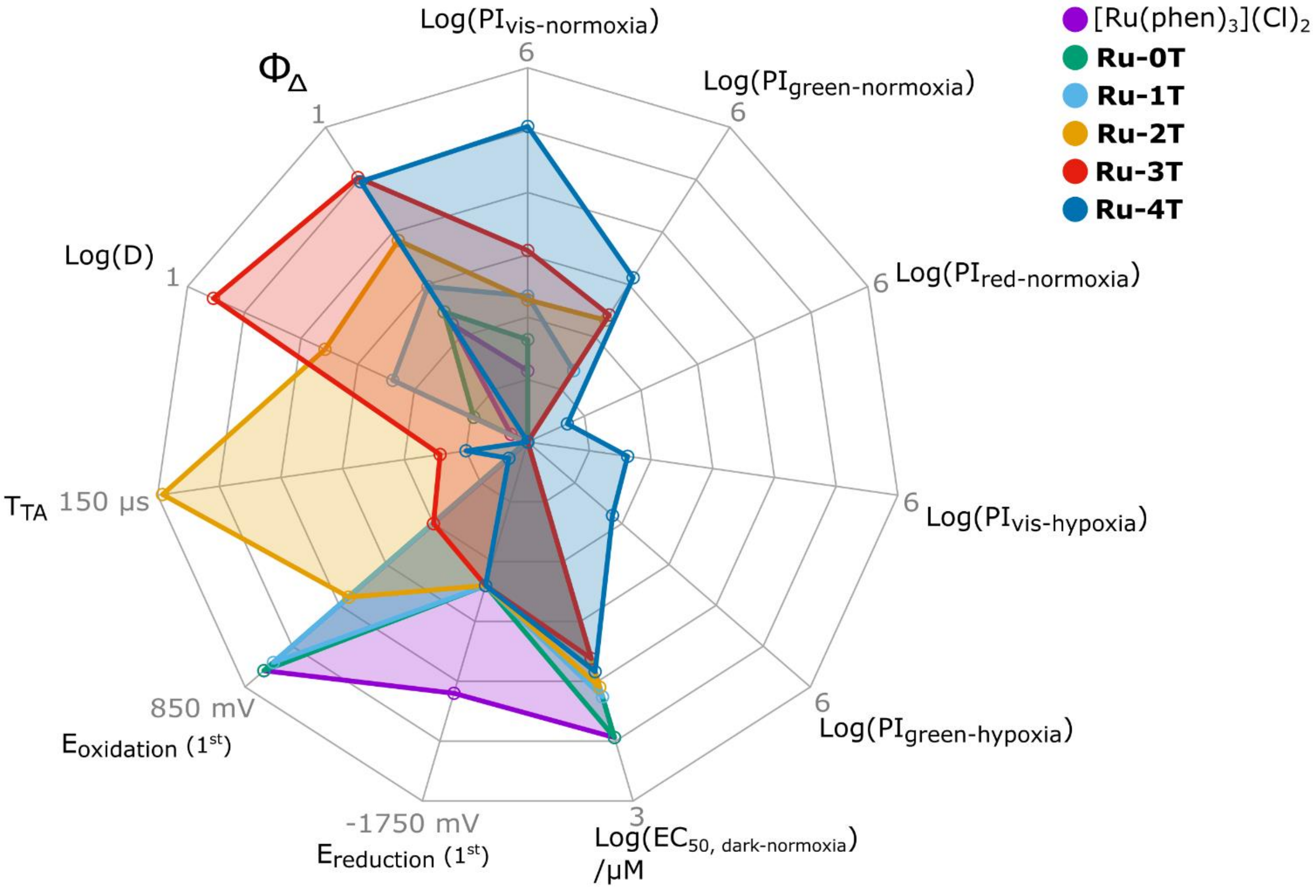

Figure S34. Radar plot of [Ru(phen)$_3$](Cl)$_2$ and **Ru-0T**–**Ru-4T** concerning relevant (photo)physical, electrochemical, and (photo)biological values. Upper bounds are labelled for respective values and lower bounds converge on the origin. Log(PI) values and EC$_{50}$'s are derived from the data shown in Table S6, and the lower bounds are 0. The lower bounds of the other values were chosen to emphasize trends among the series, and are as follows: Φ$_{\Delta}$=0.25, Log(D)= -2, T$_{TA}$=0, E$_{oxidation}$ (1st)=550 mV, E$_{reduction}$ (1st)= -1850 mV, Log(EC$_{50, dark-normoxia}$)=0.

Photophysical values are derived from Table 2, electrochemical values from Table 4, and Log(D) values are from

This radar plot was generated using R (version 4.3.1)[7] with the fsmb package.[8] The text was formatted using Inkscape.[9]

2.8.7 References

(1) DeRosa, M. C.; Crutchley, R. J. Photosensitized Singlet Oxygen and Its Applications. *Coord. Chem. Rev.* **2002**, *233–234*, 351–371. https://doi.org/10.1016/S0010-8545(02)00034-6.

(2) Montalti, M.; Credi, A.; Prodi, L.; Gandolfi, M. T. *Handbook of Photochemistry*; CRC Press, 2006. https://doi.org/10.1201/9781420015195.

(3) Cole, H. D.; Roque, J. A.; Shi, G.; Lifshits, L. M.; Ramasamy, E.; Barrett, P. C.; Hodges, R. O.; Cameron, C. G.; McFarland, S. A. Anticancer Agent with Inexplicable Potency in Extreme Hypoxia: Characterizing a Light-Triggered Ruthenium Ubertoxin. *J. Am. Chem. Soc.* **2022**, *144* (22), 9543–9547. https://doi.org/10.1021/jacs.1c09010.

(4) Roque III, J. A.; Cole, H. D.; Barrett, P. C.; Lifshits, L. M.; Hodges, R. O.; Kim, S.; Deep, G.; Francés-Monerris, A.; Alberto, M. E.; Cameron, C. G.; McFarland, S. A. Intraligand Excited States Turn a Ruthenium Oligothiophene Complex into a Light-Triggered Ubertoxin with Anticancer Effects in Extreme Hypoxia. *J. Am. Chem. Soc.* **2022**, *144* (18), 8317–8336. https://doi.org/10.1021/jacs.2c02475.

(5) Monro, S.; Colón, K. L.; Yin, H.; Roque, J.; Konda, P.; Gujar, S.; Thummel, R. P.; Lilge, L.; Cameron, C. G.; McFarland, S. A. Transition Metal Complexes and Photodynamic Therapy from a Tumor-Centered Approach: Challenges, Opportunities, and Highlights from the Development of TLD1433. *Chem. Rev.* **2019**, *119* (2), 797–828. https://doi.org/10.1021/acs.chemrev.8b00211.

(6) Pazderski, L.; Pawlak, T.; Sitkowski, J.; Kozerski, L.; Szłyk, E. ^{1}H NMR Assignment Corrections and ^{1}H, ^{13}C, ^{15}N NMR Coordination Shifts Structural Correlations in Fe(II), Ru(II) and Os(II) Cationic Complexes with 2,2′-Bipyridine and 1,10-Phenanthroline. *Magnetic Resonance in Chemistry* **2010**, *48* (6), 450–457. https://doi.org/10.1002/mrc.2600.

(7) R Core Team. *R: A Language and Environment for Statistical Computing*; R Foundation for Statistical Computing: Vienna, Austria, 2020.

(8) Nakazawa, M. *Fmsb: Functions for Medical Statistics Book with Some Demographic Data*; 2019.

(9) Inkscape Project. Inkscape, 2020. https://inkscape.org.

CHAPTER 3. RU(II) TRIFLUOROMETHYL BIPYRIDINE-BASED OLIGOTHIENYL COMPLEXES FOR PHOTODYNAMIC THERAPY

Houston D. Cole,[a] Abbas Vali,[a] John A. Roque III,[a,b,] Ge Shi,[a] Alisher Talgatov,[a] Gurleen Kaur,[a] Wesley McDonald,[a] Elamparuthi Ramasamy,[a] Colin G. Cameron,[a*] Sherri A. McFarland[a*]

[a] *Department of Chemistry and Biochemistry, The University of Texas at Arlington, Arlington, Texas, 76019-0065 United States*

[b] *Department of Chemistry and Biochemistry, The University of North Carolina at Greensboro, Greensboro, North Carolina 27402, USA*

[c] *Department of Chemistry, University of Houston, 112 Fleming Building, Houston, Texas, 77204-5003, USA*

**Corresponding authors:* C.G.C. <colin.cameron@uta.edu> ORCID 0000-0003-0978-0894, S.A.M. <sherri.mcfarland@uta.edu> ORCID 0000-0002-8028-5055

3.1 ABSTRACT

In our recent investigations, we have developed and extensively studied a new series of Ru(II) polypyridyl complexes featuring two 4,4'-bis(trifluoromethyl)-2,2'-bipyridine (4,4'-btfmb) ligands and one imidazo[4,5-*f*][1,10]phenanthroline (IP) tethered to thiophene rings (nT) as secondary ligands. The [Ru(4,4'-btfmb)$_2$(IP-nT)]$^{2+}$ scaffold represents a unique class of photosensitizers in the field of photodynamic therapy (PDT) bearing several electron-deficient trifluoromethyl groups (-CF$_3$). Electrochemically, these complexes demonstrated significant shifts in the oxidation potentials of the nT moiety, ranging between +580 mV and +1020 mV. Reductions in the nT units were particularly notable, recorded from −2230 mV in **Ru-3T** to as low as −2960 mV in **Ru-4T**. The series exhibited a range of singlet oxygen quantum yields from 0.13 to 0.66, with **Ru-3T** showing the highest efficiency. From a spectroscopic perspective, the lower thiophene-substituted complexes (**Ru-0T**–**2T**) predominantly exhibited metal-to-ligand charge transfer (^{3}MLCT) states with lifetimes around 0.61–1.5 µs. In contrast, the higher thiophene-substituted variants (**Ru-3T**–**4T**) displayed longer-lived intraligand charge transfer (^{3}ILCT) states, lasting ~20 µ. The photobiological efficacy of these complexes against melanoma cells (SK-MEL-28) demonstrated a dependence on the number of thiophene rings. While **Ru-0T** was minimally active, a notable increase in cytotoxicity was observed with increasing thiophene content, culminating in the exceptional potency of **Ru-4T** (EC_{50}=10 nM, PI=10,000). The complexes in this series stand out as being highly reproducible in their photobiological efficacy, with all EC_{50} values falling within one order of magnitude of one another over five biological replicates. The activity was also influenced by the wavelength of light, with significant persistence under hypoxic conditions, especially noted in **Ru-3T** and **Ru-4T**. These results highlight the significance of the extended ^{3}ILCT states in the higher thiophene-substituted complexes, suggesting their vital role in enhancing photocytotoxicity. This research not only contributes to our understanding of the structure-activity relationships in Ru(II) polypyridyl complexes but also underscores their potential as robust and effective photosensitizers in PDT.

Keywords: Ruthenium, metal-to-ligand charge transfer (MLCT), intraligand (IL), melanoma, photodynamic therapy

3.2 INTRODUCTION

Cancer continues to be a leading cause of mortality worldwide, second only to heart diseases.[1] Despite substantial progress in available medical treatments,[2–6] there remains a critical need for innovative therapeutic strategies and supplementary treatments to enhance the efficacy of traditional methods like surgery, radiotherapy, and chemotherapy. In this regard, photodynamic therapy (PDT) is a distinct and promising method for targeted cancer therapy. It employs a non-toxic photosensitizer (PS), harmless light, and molecular oxygen to produce cytotoxic reactive oxygen species (ROS) that target tumor cells. PDT is advantageous due to its localized approach and minimal invasiveness, resulting in reduced side effects and improved patient quality of life.[7,8] PDT's precision comes from the selective accumulation of PSs in tumor tissues and the controlled activation by light. Consequently, phototoxic effects are restricted to areas where the PS, light, and oxygen coexist in time and space. Optimizing the light protocol, including wavelength, fluence, irradiance, and dosimetry, as well as the drug-to-light interval (DLI), is key to maximizing PDT's effect. The oxygen-dependent nature of PDT is challenging when addressing hypoxic tumors. Moreover, PDT can exacerbate hypoxia by depleting oxygen during irradiation, limiting ROS production and thus reducing the efficacy against cancer cells.

Therefore, there is a drive to develop light-activated compounds that function through oxygen-independent mechanisms. Metal complexes, particularly Ru(II) polypyridyl systems, are of significant interest in this regard. The strategic selection of ligand-metal combinations allows for a range of excited state configurations with unique photophysical and reactive properties. Approaches have included the photorelease of bulky ligands to expose phototoxic metals and/or ligands,[9–17] photocaging of chemotherapeutics and enzyme inhibitors,[14,18–39] photoredox reactions,[40,41] and enhancing ROS production even under low oxygen conditions.[13,16,42]

Our research group has a strong focus on metal complexes as PSs for their diverse mechanisms of action. Their modular design and relatively straightforward synthesis allow for rapid alteration of their physicochemical, photophysical, and biological characteristics, and aligns with our tumor-specific approach to PS development. We advocate that no singular ideal PS exists; rather, PS design should be tailored to the intended application. Our Ru(II) polypyridyl complex, TLD1433, is a prime example, currently in Phase II clinical trials for treating non-muscle invasive bladder cancer (NMIBC) with PDT.[7,43] It exhibits significant phototoxicity towards cancer cells while maintaining low dark toxicity. Clinically, it is activated using green light to prevent harm to underlying muscles.

To expand our understanding of oligothiophene-based metal complexes and to develop new PSs, we are exploring variations in metal ions, coligands, thienyl groups, counter ions, and coordination structures.[7,10,13,16,42,44,45] Our long-term aim is to establish structure-activity relationships (SARs) for photoactive metal complexes, considering their physicochemical, photophysical, electrochemical, and biological properties. Part of our SAR study involves replacing certain hydrogens with fluorine in order to study the effects of electronegativity on the properties of metal-centered PSs. In this study we introduce a series of Ru(II) PSs, each featuring two 4,4'-bis(trifluoromethyl)-2,2'-bipyridine (4,4'-btfmb) coligands and a imidazo[4,5-f][1,10]phenanthroline (IP) ligand with n=0–4 thiophene rings (nT). The syntheses and structural characterization of complexes **Ru-3T** and **Ru-4T** were previously published,[46,47] and in this study the photocytotoxic effects of the five $[Ru(4,4'\text{-btfmb})_2(IP\text{-}nT)]^{2+}$ variants and the reference compound $[Ru(4,4'\text{-btfmb})_3]^{2+}$ were examined on melanoma cells under various light conditions and oxygen levels. Their lipophilicities, ground state absorption and emission characteristics, excited state configurations and lifetimes, and redox properties have been systematically studied.

The remarkable activities of these complexes, particularly those with longer thienyl chains, are of considerable interest to us. This research offers a comprehensive insight into the photophysical and biological behaviors of these complexes, providing a robust platform for future biological studies into the underlying dynamics of PDT efficacy in a range of oligothiophene-containing metal complexes. Furthermore, it introduces two new hypoxia-active PSs, presenting potential avenues for further exploration and development.

3.3 MATERIALS AND METHODS

The complexes in this series were characterized by ^{1}H NMR, HPLC, and ESI$^+$ MS. They were evaluated for lipophilicity, ground and excited state characteristics using absorption and emission spectroscopy, electrochemistry, and (photo)cytotoxicity. Further details regarding procedures and characterization data are available in the Supplementary Information.

3.3.1 Instrumentation

A CEM Discover microwave reactor was used to perform microwave reactions. Flash column chromatography was carried out on the Teledyne ISCO EZ Prep UV model of CombiFlash® EZ Prep using SILICYCLE SiliaSep™ 25 g prepacked silica cartridges. Size-exclusion chromatography was performed using a gravity column packed with Sephadex® LH-20. The NMR spectra were collected on JEOL 500 MHz spectrometers (University of North Carolina at Greensboro, University of Texas at Arlington) operating at 500 MHz for ^{1}H experiments, and on an Agilent 700 MHz Magnet spectrometer (The Joint School of Nanoscience and Nanoengineering at Greensboro) operating at 700 MHz for ^{1}H experiments. The chemical shifts are reported in parts per million (ppm) and were referenced to the residual solvent peaks. High resolution ESI$^+$ mass spectra were obtained using a Thermo Fisher Scientific LTQ Orbitrap XL instrument (Triad Mass Spectrometry Laboratory at University of North Carolina at Greensboro) and Shimadzu IT-TOF instrument (Shimadzu Center for Advanced Analytical Chemistry at University of Texas at Arlington). HPLC analyses were carried out on an Agilent/Hewlett Packard 1100 series instrument in 100 µM solutions in methanol using a

Hypersil GOLD C18 reversed-phase column with an A→B gradient (98% → 5% A; A=0.1% formic acid in H_2O, B=0.1% formic acid in MeCN). Reported retention times are accurate to within ±0.1 min.

3.3.2 Synthesis and Characterization

We previously published the synthetic methods and structural characterization of **Ru-3T** and **Ru-4T**,[46,47] and $Ru(4,4'\text{-btfmb})_3]^{2+}$ has been reported by others.[48–51] To the best of our knowledge, all other complexes presented in this study have not been reported. All solvents and reagents were purchased from commercial sources and used without further purification. Water used for all biological experiments was deionized to a resistivity ≥ 18.2 MΩ using either a Barnstead or Milli-Q® filtration system. Methanol was purchased from Fisher Scientific (ACS grade for synthesis, HPLC grade for LC eluent, Optima™ grade for HPLC and MS sample preparation). Deuterated solvents for NMR were purchased from Cambridge Isotope Laboratories. Ruthenium(III) trichloride trihydrate was purchased from Ark Pharm and Acros Organics. $Ru(4,4'\text{-btfmb})_2Cl_2{\bullet}2H_2O$[52] and IP-based ligands[53] were prepared according to adapted literature procedures. The synthesis of IP-based ligands follows that described below for IP-4T. [2,2′:5′,2″:5″,2‴-quaterthiophene]-5-carbaldehyde (4T-CHO) was prepared as previously described.[54,55] Final products are synthetically characterized in Figure S1–Figure S21 via ^1H NMR, $^1H–^1H$ COSY NMR, HPLC, and ESI^+–MS. The Cl^- salts of final complex products were obtained *via* anion metathesis on HCl-treated Amberlite IRA-410 resin with methanol as eluent and isolated in vacuo. Final complexes are a mixture of Δ/Λ isomers.

$[Ru(4,4'\text{-btfmb})_3](Cl)_2$ $Ru(Cl)_3{\cdot}xH_2O$ (58 mg, 0.2 mmol) and 4,4'-btfmb (175 mg, 0.6 mmol) was added to a microwave vessel containing argon-purged ethylene glycol (3 mL), then the mixture was subject to microwave irradiation at 180°C for 45 min with stirring. The resulting dark red solution was then transferred to a separatory funnel with deionized water (25 mL) and CH_2Cl_2 (25 mL). After gentle agitation, the CH_2Cl_2 was drained and the remaining aqueous layer was washed with CH_2Cl_2 (25 mL) until the CH_2Cl_2 layer was colorless. Then, CH_2Cl_2 (25 mL) and saturated aqueous KPF_6 (5 mL) was added, and the mixture was shaken gently. The CH_2Cl_2 layer was drained and the product was further extracted from the aqueous layer with CH_2Cl_2 (25 mL) until the aqueous layer was colorless. The CH_2Cl_2 extracts were then combined and

concentrated under reduced pressure. The crude product was then purified using silica gel flash column chromatography with a gradient of MeCN to 10% water in MeCN, followed by 7.5% water in MeCN with 0.5% KNO_3. The product-containing fractions were then combined and concentrated under vacuum, then transferred to a separatory funnel with CH_2Cl_2 (25 mL), deionized water (25 mL), and saturated aqueous KPF_6 (1 mL). The resulting mixture was gently agitated and the CH_2Cl_2 layer was drained. Additional CH_2Cl_2 (25 mL) was used to extract the remaining product until the aqueous layer was colorless. The CH_2Cl_2 layers were then combined and dried under vacuum. This was then converted to the corresponding Cl^- salt in quantitative yield using Amberlite IRA-410 with MeOH as the eluent, then purifying further using Sephadex LH-20 with MeOH as the eluent, affording a dark red solid (50 mg, 20%). ^{1}H NMR (400MHz, MeOD-*d₃*, ppm): δ 9.41 (d, *J*=1.9 Hz, 6H), 8.15 (d, *J*=5.9 Hz, 6H), 7.86 (dd,*J*=6.0, 1.8 Hz, 6H). HRMS (ESI+) *m/z* for $[M\text{-}2Cl^-]^{2+}$ calcd: 489.0169. Found: 488.9529. HPLC retention time 22.41 min (99.5% purity by peak area).

[Ru(4,4'-btfmb)₂(phen)](Cl)₂ (**Ru-phen**) Ru(4,4'-btfmb)$_2$Cl$_2$·2H$_2$O (91 mg, 0.12 mmol) and phen (22 mg, 0.1 mmol) were added to a microwave vessel containing argon-purged ethylene glycol (4 mL) and subjected to microwave irradiation at 180°C for 15 min. The resulting dark red mixture was then isolated and purified in the same manner as [Ru(4,4'-btfmb)$_3$](Cl)$_2$, yielding the desired product as a dark red solid (43 mg, 45%). ^{1}H NMR (400MHz, MeOD-*d₃*, ppm): δ 9.38 (d, *J*=14.1 Hz, 4H), 8.81 (d, *J*=8.0 Hz, 2H), 8.36 (s, 2H), 8.28 (d, *J*=5.9 Hz, 2H), 8.23 (d, *J*=5.3 Hz, 2H), 7.94 – 7.84 (m, 6H), 7.67 (dd, *J*=6.0, 1.8 Hz, 2H). HRMS (ESI+) *m/z* for $[M\text{-}2Cl^-]^{2+}$ calcd: 433.0295. Found: 432.9739. HPLC retention time 22.41 min (99.5% purity by peak area).

[Ru(4,4'-btfmb)₂(IP)](Cl)₂ (**Ru-0T**) Ru(4,4'-btfmb)$_2$Cl$_2$·2H$_2$O (91 mg, 0.12 mmol) and IP (22 mg, 0.1 mmol) were added to a microwave vessel containing argon-purged ethylene glycol (4 mL) and subjected to microwave irradiation at 180°C for 15 min. The resulting dark red mixture was then isolated and purified in the same manner as [Ru(4,4'-btfmb)$_3$](Cl)$_2$, yielding the desired product as a dark red solid (81.3 mg, 51%). ^{1}H NMR (400MHz, MeOD-*d₃*, ppm): δ 9.38 (dd, *J*=16.6, 1.9 Hz, 4H), 9.10 (d, *J*=8.4 Hz, 2H), 8.68 (s, 1H), 8.29 (d, *J*=5.9 Hz, 2H), 8.15 (dd, *J*=5.3, 1.3 Hz, 2H), 7.95 (d, *J*=6.0 Hz, 2H), 7.92 (dd, *J*=8.3, 5.3 Hz, 2H), 7.87 (dd, *J*=6.0, 1.9

Hz, 2H), 7.66 (dd, *J*=6.0, 1.9 Hz, 2H). HRMS (ESI+) *m/z* for $[M\text{-}2Cl^-]^{2+}$ calcd: 453.0326. Found: 452.9735. HPLC retention time 20.33 min (>98% purity by peak area).

[Ru(4,4'-btfmb)$_2$(IP-1T)](Cl)$_2$ (**Ru-1T**). Ru(4,4'-btfmb)$_2$Cl$_2$·2H$_2$O (91 mg, 0.12 mmol) and IP-1T (30 mg, 0.1 mmol) were added to a microwave vessel containing ethylene glycol (4 mL) and subjected to microwave irradiation at 180°C for 15 min. The dark red solution was transferred to a separatory funnel with H_2O (25 mL) and CH_2Cl_2 (25 mL). CH_2Cl_2 layer was used to wash the aqueous layer. CH_2Cl_2 (25 mL) and saturated aqueous KPF_6 (5 mL) were used to extract the product from the aqueous layer. The product was then purified using silica gel flash column chromatography. The product-containing fractions were transferred to a separatory funnel with CH_2Cl_2 (25 mL), H_2O (25 mL), and saturated aqueous KPF_6 (1 mL) and the [Ru(4,4'-btfmb)$_2$(IP-1T)](PF$_6$)$_2$ product was isolated via extraction. The PF_6^- salt was then converted to the corresponding Cl^- salt in quantitative yield using Amberlite IRA-410 with MeOH as the eluent, followed by further purification using Sephadex LH-20 with MeOH as the eluent, yielding [Ru(4,4'-btfmb)$_2$(IP-1T)](Cl)$_2$ as a dark red solid (43 mg, 25%). ^{1}H NMR (400MHz, MeOD-*d$_3$*, ppm): δ 9.40 (d, *J*=1.9 Hz, 2H), 9.36 (d, *J*=1.8 Hz, 2H), 9.19 (s, 2H), 8.29 (d, *J*=5.8 Hz, 2H), 8.12 (d, *J*=5.2 Hz, 2H), 8.01 (d, *J*=3.6 Hz, 1H), 7.97 (d, *J*=6.1 Hz, 2H), 7.91 (dd, *J*=8.3, 5.2 Hz, 2H), 7.88 (dd, *J*=6.0, 1.9 Hz, 2H), 7.74 (d, *J*=5.0 Hz, 1H), 7.68 (dd, *J*=6.1, 1.8 Hz, 2H), 7.31 (dd, *J*=5.0, 3.7 Hz, 1H). HRMS (ESI+) *m/z* for $[M\text{-}2Cl]^{2+}$ calcd: 494.0265. Found: 494.0261, *m/z* for $[M\text{-}2Cl\text{-}H]^+$ calcd: 987.0456. Found: 987.0474. HPLC retention time 21.75 min (99% purity by peak area).

[Ru(4,4'-btfmb)$_2$(IP-2T)](Cl)$_2$ (**Ru-2T**). Ru(4,4'-btfmb)$_2$Cl$_2$·2H$_2$O (91 mg, 0.12 mmol) and IP-2T (38 mg, 0.1 mmol) were added to a microwave vessel containing argon-purged ethylene glycol (4 mL) and subjected to microwave irradiation at 180°C for 15 min. The resulting dark red mixture was then isolated and purified in the same manner as **Ru-1T**, yielding the desired product as a dark solid (33 mg, 29%). ^{1}H NMR (400MHz, MeOD-*d$_3$*, ppm): δ 9.40 (d, *J*=1.9 Hz, 2H), 9.37 (d, *J*=1.9 Hz, 2H), 9.17 (s, 2H), 8.29 (d, *J*=5.8 Hz, 2H), 8.13 (dd, *J*=5.2, 1.2 Hz, 2H), 7.99 (d, *J*=6.1 Hz, 2H), 7.94 (d, *J*=3.8 Hz, 1H), 7.91 (dd, *J*=8.3, 5.2 Hz, 2H), 7.88 (dd, *J*=5.9, 1.9 Hz, 2H), 7.71 – 7.67 (m, 2H), 7.47 (dd, *J*=5.1, 1.1 Hz, 1H), 7.43 – 7.38 (m, 2H), 7.13 (dd, *J*=5.1, 3.6 Hz, 1H). HRMS (ESI+) *m/z* for $[M\text{-}2Cl^-]^{2+}$ calcd: 535.0203. Found: 535.0201, *m/z* for

$[M-2Cl^{-}-H]^{+}$ calcd: 1069.0333. Found: 1069.0353. HPLC retention time 22.86 min (95.2% purity by peak area).

[Ru(4,4'-btfmb)$_2$(IP-3T)](Cl)$_2$ (**Ru-3T**). Ru(4,4'-btfmb)$_2$Cl$_2$·2H$_2$O (151 mg, 0.2 mmol) and IP-3T (76 mg, 0.164 mmol) were added to a microwave vessel containing argon-purged ethylene glycol (4 mL) and subjected to microwave irradiation at 180°C for 15 min. The resulting dark red mixture was then isolated and purified in the same manner as **Ru-1T**, yielding the desired product as a dark red solid (55 mg, 27%). ^{1}H NMR (700MHz, MeOD-*d$_3$*, ppm): δ 9.40 (d, *J*=2.0 Hz, 2H), 9.37 (d, *J*=1.9 Hz, 2H), 9.26 (s, 1H), 9.11 (s, 1H), 8.29 (d, *J*=5.8 Hz, 2H), 8.14 (dd, *J*=5.2, 1.3 Hz, 2H), 7.99 (s, 2H), 7.95 – 7.90 (m, 3H), 7.88 (dd, *J*=6.0, 1.9 Hz, 2H), 7.69 (dd, *J*=6.1, 1.9 Hz, 2H), 7.40 (d, *J*=3.8 Hz, 1H), 7.35 (d, *J*=3.8 Hz, 1H), 7.31 (dd, *J*=3.5, 1.1 Hz, 1H), 7.23 (d, *J*=3.8 Hz, 1H), 7.09 (dd, *J*=5.1, 3.6 Hz, 1H). ^{13}C NMR (700MHz, MeOD-*d$_3$*, ppm): δ 163.28, 163.08, 162.89, 159.60, 159.43, 155.07, 154.53, 150.34, 141.88, 140.97, 140.81, 140.77, 140.60, 139.10, 137.67, 135.97, 131.57, 129.82, 129.20, 126.94, 126.39, 125.84, 125.75, 125.40, 125.33, 125.23, 124.45, 124.34, 123.11, 123.02, 122.89, 122.79, 119.88. HRMS (ESI+) *m/z* for $[M-2Cl^{-}]^{2+}$ calcd: 576.0142. Found: 576.0141, *m/z* for $[M-2Cl^{-}-H]^{+}$ calcd: 1151.0211. Found: 1151.0232. HPLC retention time 23.80 min (95.4% purity by peak area).

[Ru(4,4'-btfmb)$_2$(IP-4T)](Cl)$_2$ (**Ru-4T**). Ru(4,4'-btfmb)$_2$Cl$_2$·2H$_2$O (114 mg, 0.2 mmol) and IP-4T (90 mg, 0.164 mmol) were added to a microwave vessel containing argon-purged ethylene glycol (4 mL) and subjected to microwave irradiation at 180°C for 15 min. The reaction mixture was transferred to a 100mL beaker and diluted with ~30 mL H$_2$O, then treated with 3 mL of saturated aqueous KPF$_6$ and stirred for 5 minutes. At this time, a red precipitate formed, and was collected using a Büchner filtration apparatus. The product was then purified following the same procedure as described for **Ru-1T**, yielding [Ru(4,4'-btfmb)$_2$(IP-4T)](Cl)$_2$ as a dark red solid (77 mg, 35%). ^{1}H NMR (700 MHz, MeOD-*d$_3$*, ppm): δ 9.40 (d, *J*=2.0 Hz, 2H), 9.37 (d, *J*=1.9 Hz, 2H), 9.26 (s, 1H), 9.11 (s, 1H), 8.29 (d, *J*=5.8 Hz, 2H), 8.14 (dd, *J*=5.2, 1.3 Hz, 2H), 7.99 (s, 2H), 7.95 – 7.90 (m, 3H), 7.88 (dd, *J*=6.0, 1.9 Hz, 2H), 7.69 (dd, *J*=6.1, 1.9 Hz, 2H), 7.40 (d, *J*=3.8 Hz, 1H), 7.35 (d, *J*=3.8 Hz, 1H), 7.31 (dd, *J*=3.5, 1.1 Hz, 1H), 7.23 (d, *J*=3.8 Hz, 1H), 7.09 (dd, *J*=5.1, 3.6 Hz, 1H). ^{13}C NMR (175 MHz, MeOD-*d$_3$*, ppm): δ 163.28, 163.08, 162.89, 159.60, 159.43, 155.07, 154.53, 150.34, 141.88, 140.97, 140.81, 140.77, 140.60,

139.10, 137.67, 135.97, 131.57, 129.82, 129.20, 126.94, 126.39, 125.84, 125.75, 125.40, 125.33, 125.23, 124.45, 124.34, 123.11, 123.02, 122.89, 122.79, 119.88. HRMS (ESI+) *m*/*z*: $[M–2Cl]^{2+}$ calcd for $C_{49}H_{26}F_{12}N_8RuS_3$ 576.0142; Found: 576.0141. $[M–2Cl–H]^+$ calcd for $C_{49}H_{25}F_{12}N_8RuS_3$ 1151.0211; Found: 1151.0232. HPLC retention time 23.80 min (99% purity by peak area).

3.3.3 Electrochemistry

Voltammetry was performed in dimethylformamide (DMF, Fisher HPLC grade) that had been dried and deoxygenated with an Inert PureSolv MD7 solvent purification system, with 100 mM tetrabutylammonium hexafluorophosphate ($TBAPF_6$) (Fisher) as the supporting electrolyte, in a two-compartment low volume cell with the three-electrode configuration under argon. A 3 mm glassy carbon disc was used as the working electrode with a platinum wire counter electrode and a Ag/AgCl/4M KCl reference electrode. Ferrocene (Fc) was used as an internal standard. The complex solutions were approximately 4 mM for oxidation sweeps and 0.25 mM for reduction sweeps.

Measurements were conducted at room temperature using a WaveNow potentiostat (Pine Research Company) with Aftermath software. Cyclic differential-pulse voltammetry (CDPV) measurements used a sweep rate of 2 $mV·s^{-1}$ with a modulation amplitude varying from 12.5 to 100 mV. For reversible processes, the formal redox potential $E°'$ was taken as the average of E_{pa} (anodic peak potential) and E_{pc} (cathodic peak potential). For quasi-reversible processes, only E_{pa} or E_{pc} is reported.

3.4 RESULTS AND DISCUSSION

3.4.1 Synthesis and Characterization

$[Ru(4,4'\text{-btfmb})_3]^{+2}$ and **Ru-nT** were synthesized utilizing our established method for related Ru(II) 4,4'-bis(trifluoromethyl)-2,2'-bipyridine-based complexes.[13] The complexes were initially isolated as PF6− salts and subsequently purified using flash chromatography on silica. These PF_6^- salts were then efficiently converted to their corresponding Cl^- salts through anion metathesis with Amberlite IRA-410, followed by further purification using size-exclusion chromatography on Sephadex LH-20. The final yields were approximately 60% for [Ru(4,4'-btfmb)$_3$]$^{+2}$, **Ru-0T**, **Ru-1T**, and **Ru-3T**, around 40% for **Ru-2T**, and close to 30% for **Ru-4T**. These complexes underwent thorough characterization by 1D and 2D ^{1}H NMR spectroscopy

(Figure 1, Figure S1–Figure S7), with signal assignments for [Ru(4,4'-btfmb)$_3$]$^{+2}$ and **Ru-0T**–**Ru-4T** conducted using ^{1}H–^{1}H COSY NMR. The assignments aligned with those of our previously reported, related compounds.[13,16,42] Additionally, these complexes were characterized by high-resolution ESI+ mass spectrometry (Figure S8–Figure S14). HPLC analyses confirmed that the complexes were ≥95% pure, as determined by integration (Figure S15–Figure S21).

The lipophilicities of the chloride salts of complexes were determined by measuring their distribution between 1-octanol and 10 mM phosphate buffer (pH 7.4) following the “shake-flask” method as we described previously.[44] The log $D_{o/w}$ values for this series span four orders of magnitude, with [Ru(4,4'-btfmb)$_3$]$^{2+}$ being the most hydrophilic at about -2 and **Ru-4T** most lipophilic near +2 (Figure 2). The three reference compounds lacking thiophene rings ([Ru(4,4'-btfmb)$_3$]$^{2+}$, **Ru-phen**, and **Ru-0T**) as well as **Ru-1T** show a preference for the aqueous buffer and accordingly have negative log $D_{o/w}$ values. In contrast, complexes with two to four thiophenes (**Ru-2T**, **Ru-3T**, **Ru-4T**) have positive log $D_{o/w}$ values and increase on going from *n*=2 to 4. The addition of the trifluoromethyl group qualitatively improved the overall aqueous solubility of the complexes with positive log $D_{o/w}$ values compared to analogous Ru(II) and Os(II) complexes with other coligands where 4T often leads to precipitation at the octanol/buffer interface.[42,44]

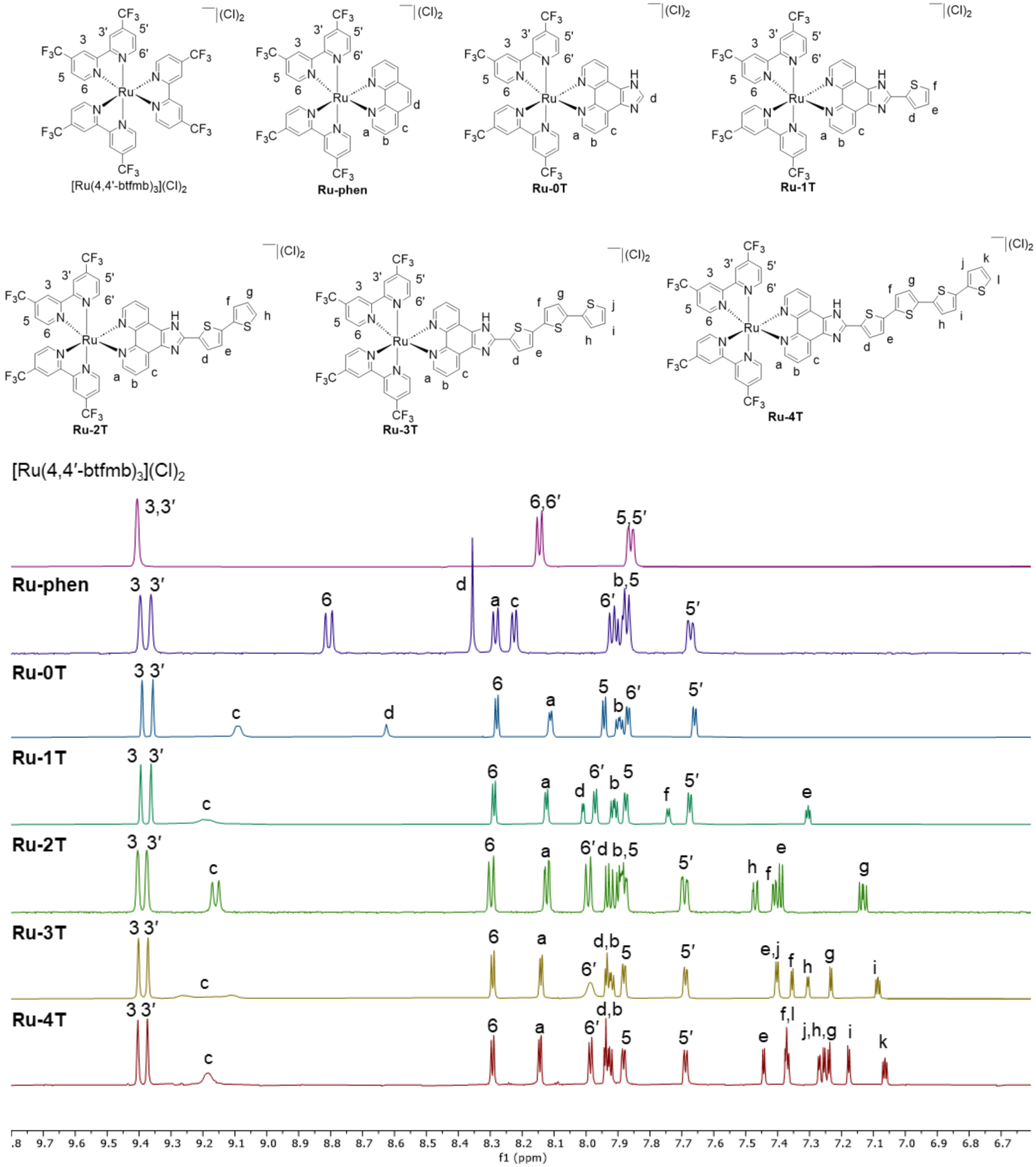

Figure 1. Labelled structures and ^{1}H NMR spectra showing aromatic region for [Ru(4,4'-btfmb)$_3$](Cl)$_2$ and **Ru-*n*T** (*n*=0−4) in MeOD-d$_3$ (Cl$^-$ salts; 298 K). All spectra were collected at 500 MHz, except for **Ru-4T**, which was collected at 700 MHz.

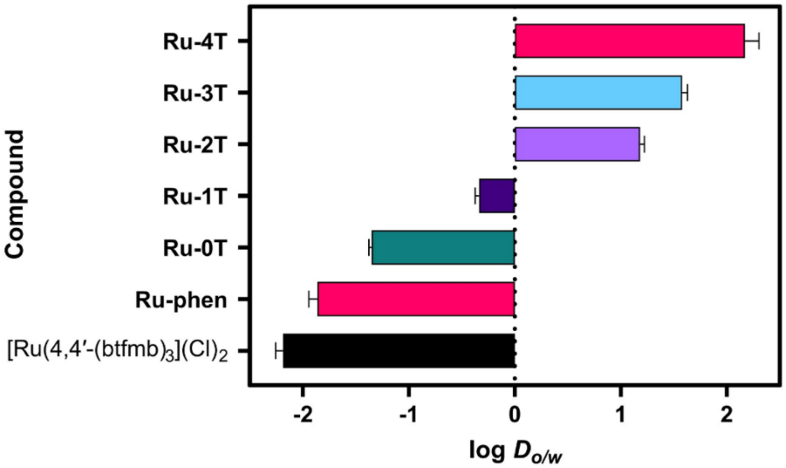

Figure 2. Lipophilicity of [Ru(4,4'-btfmb)$_3$](Cl)$_2$, **Ru-phen**, and **Ru-*n*T** (*n*=0–4) in 1-octanol and phosphate buffer using the in-house “shake-flask” method.

3.4.2 Spectroscopy

Electronic Absorption

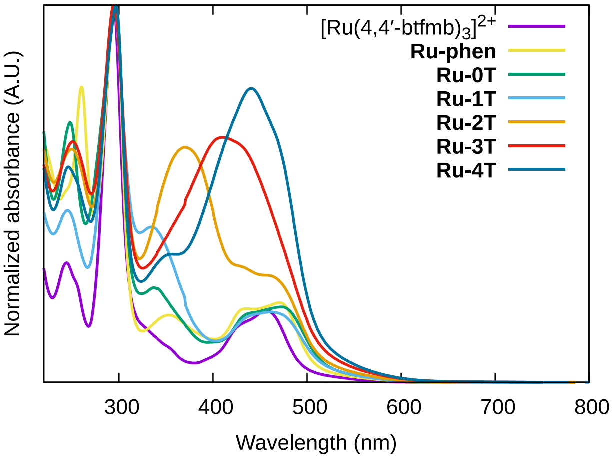

Figure 3: UV-vis spectra of [Ru(4,4'-btfmb)$_3$]$^{2+}$, **Ru-phen**, and **Ru-nT** (*n*=0–4) normalized to the π–π* peak near 295 nm.

The UV-vis absorption spectra of the series are overlaid in Figure 3, and the corresponding molar extinction coefficients for various peak maxima are summarized in Table 1. The sharp peaks near 295 nm and below are due to π–π* transitions involving the 4,4'-btfmb ligand,[49] as well as phen and/or IP in the cases of **Ru-phen** and **Ru-nT**. The energies of these transitions are not affected by the length of the thiophene chain appended to the IP ligand. The broader and less intense peak between 400 and 500 nm with a local maximum at 456 nm in [Ru(4,4'-btfmb)$_3$]$^{+2}$ is due to Ru^{2+}(dπ)→L(π*) ^{1}MLCT transitions. The substitution of one 4,4'-btfmb ligand for phen or IP causes the lowest energy ^{1}MLCT transitions to red-shift by 10–20 nm, suggesting more electron density on the metal center as would be expected for these heteroleptic complexes. Assuming that the 4,4'-btfmb π* orbital remains the acceptor orbital for the lowest energy ^{1}MLCT transitions in all cases, the effect of phen or IP is primarily on the dπ orbital energy. This effect is most evident for **Ru-phen**, **Ru-0T**, and **Ru-1T**. For complexes containing the IP-*n*T ligand, additional ligand-localized transitions overlap the ^{1}MLCT transitions. These isolated transitions can be seen in the absorption spectra of the analogous uncomplexed IP-*n*T ligands and free oligothiophenes.[56] **Ru-2T** through **Ru-4T** have contributions from ^{1}LLCT (*n*TŸ IP) and ^{1}ILCT (*n*TŸ *n*T) transitions that shift to longer wavelengths and increase in ^{1}ILCT character with increasing *n*. The lowest energy singlet-singlet transitions tend to be mixed ^{1}MLCT/^{1}LLCT states for **Ru-2T** and mixed ^{1}ILCT/^{1}LLCT for **Ru-3T** and **Ru-4T**, based on what has been observed previously in related compounds.[7,13,42,43]

Table 1: Molar Extinction coefficients at Selected Wavelengths for the Complexes of This Study.

cmpd	λ_{abs} (nm) (log (ε / M^{-1} cm^{-1}))
[Ru(4,4'-btfmb)$_3$]$^{+2}$	244 (4.34), 294 (4.84), 427 (4.01), 456 (4.12),
Ru-phen	260 (4.69), 296 (4.80), 353 (4.05), 432 (4.09), 471 (4.12)
Ru-0T	248 (4.68), 296 (4.84), 341 (4.13), 435 (4.12), 470 (4.13)
Ru-1T	245 (4.57), 294 (4.92), 335 (4.51), 462 (4.20)
Ru-2T	250 (4.68), 295 (4.89), 370 (4.69), 462 (4.35)
Ru-3T	251 (4.58), 294 (4.76), 410 (4.57)
Ru-4T	246 (4.57), 297 (4.81), 351 (4.33), 441 (4.70)

Singlet Oxygen Sensitization

The singlet oxygen quantum yields (Φ_Δ) of the complexes were calculated by measuring the intensity of O$_2$ phosphorescence ($^1\Delta_g \rightarrow {}^3\Sigma_g$) centered at 1260 nm against [Ru(bpy)$_3$]$^{2+}$ as the standard (Φ_Δ=0.56).[57] These are reported in Table 2. [Ru(4,4'-btfmb)$_3$]$^{+2}$, **Ru-phen**, and **Ru-0T** are moderately efficient ^{1}O$_2$ generators (Φ_Δ=0.47–0.64) and similar to [Ru(bpy)$_3$]$^{2+}$. However, the thiophene-containing complexes **Ru-1T**–**Ru-4T** exhibit larger differences (Φ_Δ=0.13–0.66) and are less efficient than what has been observed for related compounds.[7,43] The largest $^1O_2$ quantum yield was measured for **Ru-3T** at 66%. While all of the complexes show a wavelength-dependence for Φ_Δ, **Ru-4T** exhibits a notable concentration dependence for the $^1O_2$ quantum yield (Figure S22 and Table S1). These differences in Φ_Δ appear to be unrelated to differences in other photophysical parameters such as emission wavelengths and triplet lifetimes (vide infra).

Emission

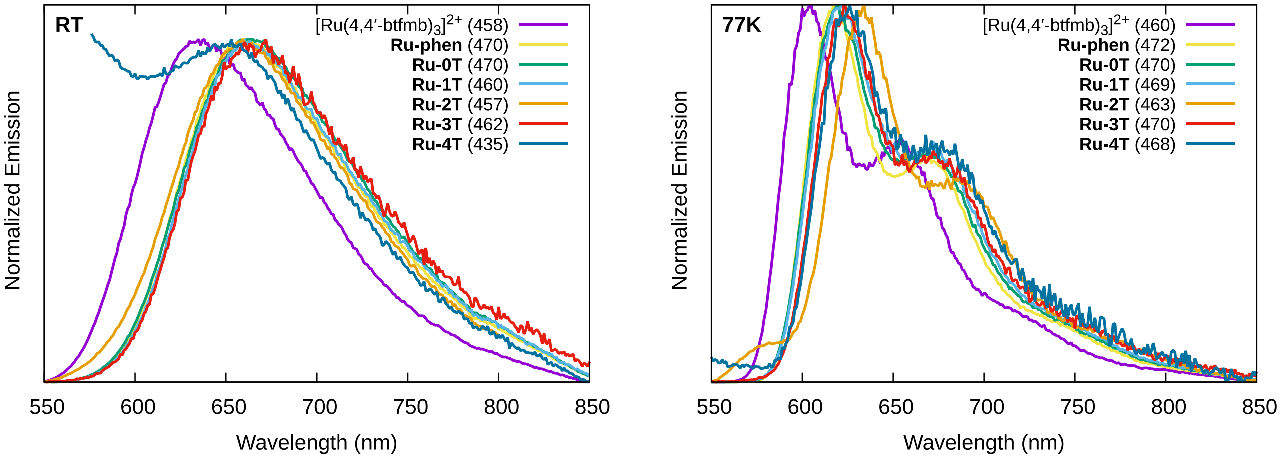

Figure 4: Normalized emission spectra $[Ru(4,4'\text{-btfmb})_3]^{2+}$ and the **Ru-*n*T** series as PF_6^- salts at RT and at 77K. The RT emission was measured in MeCN degassed by freeze-pump-thaw (5 cycles). The 77K emission was measured in a 4:1 EtOH:MeOH glass. Excitation wavelengths are noted in parentheses.

All of the complexes in the series exhibited a broad, featureless red emission band at room temperature (Figure 4a, Table 2). This emission was centered around 636 nm (τ_{em} =1.5 μs) for the parent $[Ru(4,4'\text{-btfmb})_3]^{2+}$ complex in MeCN at room temperature (RT) and shifted to shorter wavelengths with vibronic intervals of around 1350 cm^{-1} at 77 K (Figure 4b).[48–51] Such behavior is consistent with emissive ^{3}MLCT states in Ru(II) complexes with polypyridyl ligands.[58] The thermally induced Stokes shift (ΔE_S) of around 830 cm^{-1} is slightly smaller than the related model complex $[Ru(bpy)_3]^{2+}$ (ΔE_S= 1127 cm^{-1}).[59] Similar to what was observed for the ^{1}MLCT absorption bands, the introduction of a phen or an IP ligand results in bathochromic shifts of up to 30 nm but otherwise similar spectra and lifetimes (τ_{em} =0.8–0.9 μs). The ^{3}MLCT emission energies and lifetimes (τ_{em} =0.6–0.8 μs) also do not depend of the number of thiophenes in the IP-*n*T ligand, suggesting that the π* acceptor orbitals in the Ru(dπ)→L(π*) transitions are localized to the phen/IP portion of the IP-*n*T ligands. However, the emission quantum yield (Φ_{em}) decreases from 16% for [Ru(4,4'-btfmb)$_3$]$^{2+}$ to 9% for **Ru-phen** and **Ru-0T**. Addition of one thiophene drops the value of Φ_{em} to around 2%, and additional thienyl rings further decrease the emission output to <1%. Although **Ru-4T** produces weak but detectable emission, a value for Φ_{em} was not calculated due to the extremely low signal-to-noise ratio. The values for Φ_{em} increase up to ten-fold at 77 K but **Ru-4T** is still only about 0.14%. While the nature of the emissive ^{3}MLCT state does not appear to change across the series, the lower emissive quantum yields with increasing *n* point toward the involvement of additional excited states.

Table 2: Spectroscopic data for compounds [Ru(4,4'-btfmb)$_3$](PF$_6$)$_2$, **Ru-phen**, and **Ru-0Ti Ru-4T** as PF$_6^-$ salts. Excitation wavelengths are indicated in parenthesis. Emission lifetimes were measured following a <5 ns 355 nm laser pulse.

cmpd	RT emission			77K emission		Φ_Δ (λ_{ex} / nm)	τ_{TA} / μs)	
	$\lambda_{em.}$ (λ_{ex}) / nm	Φ_{em}	τ_{em} / μs	$\lambda_{em.}$ (λ_{ex}) / nm	$\Phi_{em,77K}$		λ_{ex}=355 nm	λ_{ex}=532 nm
[Ru(4,4'-btfmb)$_3$]$^{2+}$	636 (458)	1.6×10^{-1}	1.5	604, 653 (460)	2.5×10^{-1}	0.47 (462)	1.5	1.5
Ru-phen	660 (470)	9.0×10^{-2}	0.89	619, 668 (472)	2.4×10^{-1}	0.64 (470)	0.89–0.94	0.77–0.92
Ru-0T	662 (470)	9.1×10^{-2}	0.83	619, 669 (470)	1.9×10^{-1}	0.50 (469)	0.78–0.86	0.78–0.87
Ru-1T	661 (460)	1.8×10^{-2}	0.79	620, 670 (469)	2.0×10^{-1}	0.13 (462)	0.81–0.93	0.71–0.87
Ru-2T	659 (457)	4.1×10^{-3}	0.62	634, 687 (463)	4.3×10^{-2}	0.28 (466)	0.61–0.72	0.63–0.71
Ru-3T	664 (462)	1.3×10^{-3}	0.79	623, 673 (470)	9.7×10^{-3}	0.66 (470)	20–21	22–24
Ru-4T	650 (435)	v. wk.	0.64	625, 672 (468)	1.4×10^{-3}	0.40 (467)	19–20	20–21

Transient Absorption and Excited State Pathways

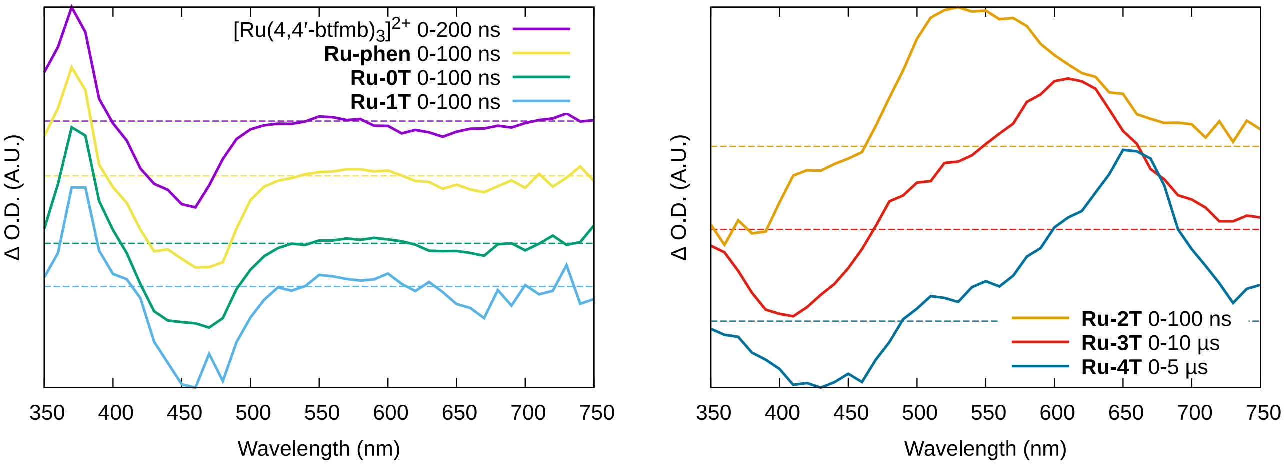

Figure 5: Transient absorption (TA) spectra of [Ru(4,4'-btfmb)$_3$](PF$_6$)$_2$, **Ru-phen**, and **Ru-*n*T** as PF$_6^-$ salts in degassed MeCN at RT (λ$_{ex}$=355 nm). The profiles for λ$_{ex}$=532 nm are similar (Figure S24). The dotted line indicates ΔO.D.=0.

The triplet excited states were investigated using nanosecond transient absorption (TA) spectroscopy with excitation from a 355 nm or 532 nm laser of ≤5 ns pulse width. The responses with the two different excitation wavelengths are similar so only the shorter wavelength excitation is shown in Figure 5. The differential excited state absorption (ESA) spectra were collected using solutions of the PF$_6^-$ salts of the compounds in degassed (5x freeze-pump-thaw) MeCN. Early time slices are presented in Figure 5 and the full relaxation spectra are collected in Figure S23 and Figure S24. Transient lifetimes were measured at the ESA maxima and bleach minima and are listed in Table 2.

The ESA profiles of the [Ru(4,4'-btfmb)$_3$](PF$_6$)$_2$, **Ru-phen**, **Ru-0T**, and **Ru-1T** are similar, consisting primarily of a strong ^{1}MLCT ground state bleach near 450 nm superimposed with new ESA characteristic of the ^{3}MLCT state. The stronger ESA near 375 nm involves bftmb$^-$ transitions, and the extremely weak and broad absorption past 525 nm is due to 4,4'-btfmb$^-$ or LMCT transitions involving Ru(II). With TA lifetimes match the emission lifetimes and support lowest lying ^{3}MLCT states for these complexes.

The ESA profile of **Ru-2T** exhibits features consistent with an IP-*n*T ligand-localized triplet excited state, as we have previously reported.[7,13,45,60–62] This broad and rather intense ESA near 450–700 nm is superimposed on the bleach with its minimum near 370 nm due to a strong ground state absorption contributed by the IP-2T ligand (Figure 3). **Ru-2T** has the signature of an ^{3}IL-based excited state, but its TA lifetime matches the ^{3}MLCT emissive lifetime at all wavelengths. This suggests an equilibrium between ^{3}MLCT and ^{3}IL-based states that are close in energy and decay with a common lifetime.[63]

The ESA spectra of **Ru-3T** and **Ru-4T** are characteristic of oligothiophene-based ^{3}ILCT states, with longer TA lifetimes. The excited state relaxation pathways are proposed in Scheme 1. **Ru-3T** shows a bleach corresponding to the ground state ππ* transition near 410 nm and a broad ESA with its maximum near 610 nm. For **Ru-4T** these were shifted to around 430 nm and 655 nm, respectively. These ESA features are similar to those of the free IP-3T and IP-4T ligands.[42,44] The decays are monoexponential, with τ=~20 μs for both complexes, indicating that the long-lived ^{3}ILCT is decoupled from the shorter-lived emissive ^{3}MLCT, and further supported by the very low emission quantum yields for **Ru-3T** and **Ru-4T**.

The TA spectra for each compound was also collected with 532 nm excitation, and there is little difference between the two wavelengths (compare Figure S24 and Figure S25). This suggests that the excited state dynamics on the ns to μs timescales are independent of the excitation wavelength.

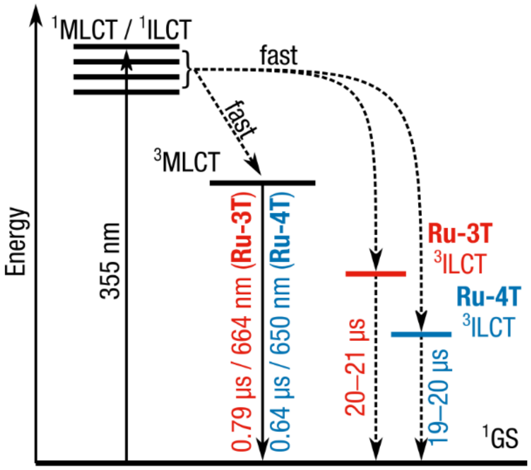

Scheme 1: Jablonski diagram illustrating the excited state relaxation pathways of complexes **Ru-3T** and **Ru-4T**. Energies are not to scale.

3.4.3 Electrochemistry

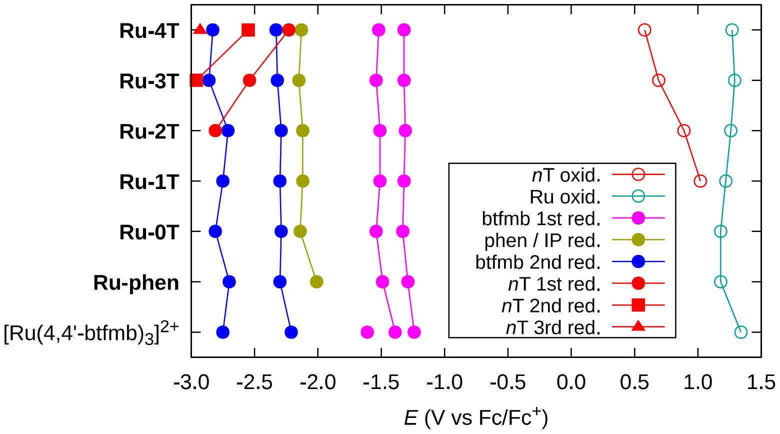

Figure 6: Redox potentials (vs. Fc) of $[Ru(4,4'\text{-btfmb})_3]^{2+}$, **Ru-phen**, and **Ru-*n*T** as PF_6^- salts in degassed MeCN at RT and their tentative assignments.

The electrochemistry of Ru(II) polypyridyl complexes is typified by single electron processes involving one-electron oxidation of the metal center and three sequential reductions on each of the ligands.[64] Oxidation of the Ru^{2+} center (+0.98 V versus Fc, MeCN) tends to be electrochemically reversible, and the ensuing low spin $4d^5$ complex is chemically stable. In complexes like $[Ru(bpy)_3]^{2+}$, the first reduction (–1.72 V versus Fc, MeCN) involves the lowest-energy ligand π* orbital. Since the low spin $4d^6$ configuration is thereby unaffected, the complex remains substitutionally inert, and the process is also reversible. The added electron is localized on one ligand, and thus $[Ru(bpy)_3]^{2+}$ exhibits three sequential one-electron reductions under straightforward electrochemical conditions. In a potential window widened by low temperature cyclic voltammetry, $[Ru(bpy)_3]^{2+}$ has been shown to participate in a total of six one-electron reductions.[65,66]

There are additional redox processes for some members of the present series due to the presence of the electrochemically active oligothiophene[67] unit in complexes **Ru-2T**–**Ru-4T**. The formal redox potentials of the series were measured by cyclic differential pulse voltammetry (CDPV) to enhance the signal, with ferrocene (Fc) as an internal reference ($E_{1/2}$ $(Fc/Fc^+)=0.380$ V vs SCE[68]). The potentials are tabulated in Table 3 and plotted in Figure 6 with tentative assignments.

The metal oxidation of $[Ru(4,4'\text{-btfmb})_3]^{2+}$ and the three one-electron reductions agree well with published data[49] and are around 0.3–0.5 V more positive than the corresponding processes in $[Ru(bpy)_3]^{2+}$, a consequence of the electron-withdrawing nature of the 4,4′-btfmb ligands. The shift of the $Ru^{2+} \rightarrow Ru^{3+}$ oxidation is slightly attenuated when one 4,4′-btfmb ligand is replaced with phen or IP-*n*T, which mirrors the shift of the MLCT absorption energy (Table 1). The oxidation of *n*T becomes more favorable with increasing *n*, consistent with the behavior of free oligothiophenes.[69] The oxidation potential of the thienyl group ranges from +1.02 V for **Ru-1T** to +0.58 for **Ru-4T** and is less positive than the metal center in all cases, indicating that *n*T is more easily oxidized than Ru(II) regardless of the number of thiophenes. The oxidation of *n*T does shift the $Ru^{2+} \rightarrow Ru^{3+}$ oxidation slightly more positive, consistent with a decrease in electron density on the metal.

$[Ru(4,4'\text{-btfmb})_3]^{2+}$ and the other complexes without thiophenes (**Ru-phen**, **Ru-0T**) as well as **Ru-1T** exhibit five sequential reductions spanning −1.24 to −2.81 V (Figure 6). For $[Ru(4,4'\text{-btfmb})_3]^{2+}$ this involves sequential one-electron reductions on each of the three 4,4′-btfmb ligands followed by second reductions on two of those ligands (within the experimental potential window). We believe this study is the first to report the second reductions of the two 4,4′-btfmb ligands occurring between −2.2 and −2.9 V for $[Ru(4,4'\text{-btfmb})_3]^{2+}$.

When one of the 4,4′-btfmb ligands is replaced by phen, IP-0T, or IP-1T, the third reduction involves phen or IP and is less favorable by around 0.4–0.5 V (owing to their lack of electron-withdrawing –CF_3 substituents). **Ru-2T** to **Ru-4T** exhibit similar reductions involving the 4,4′-btfmb coligands and IP, but they accommodate additional reductions on the oligothienyl groups. For **Ru-2T**, the 2T group accepts only one electron and this sixth reduction is the least favorable and occurs near −2.81 V. The 3T group of **Ru-3T** can be doubly reduced (−2.54 and −2.96 V), where the first *n*T reduction is easier than the last 4,4′-btfmb reduction. Continuing this trend, the 4T group of **Ru-4T** accommodates three electrons (−2.23, −2.55, and −2.93 V), with the first *n*T reduction occurring near that of IP at −2.13 V. The effect of the thiophene chain length is dramatic. The *n*T reduction potential shifts positive by more than 0.5 V on going from two to four thiophenes, and the **Ru-4T** complex can accommodate at least eight extra electrons in its ground state at room temperature!

Table 3. Formal redox potentials for the hexafluorophosphate salts of the complexes measured using CDPV at approximately 1.0 mM in MeCN containing $TBAPF_6$. The potentials are referenced in volts (V) against ferrocene as the internal standard. The working and reference electrodes were glassy carbon and Ag/AgCl/4M KCl, respectively. Overlapping waves were deconvoluted mathematically (error approximately ±0.02 V).

Compound	$n\mathrm{T}^{2-}\rightarrow n\mathrm{T}^{3-}$	$n\mathrm{T}^{-}\rightarrow n\mathrm{T}^{2-}$	$n\mathrm{T}\rightarrow n\mathrm{T}^{-}$	$\mathrm{LL}_2^{-}\rightarrow\mathrm{LL}_2^{2-}$	$\mathrm{LL}_1^{-}\rightarrow\mathrm{LL}_1^{2-}$	$\mathrm{LL}_3\rightarrow\mathrm{LL}_3^{-}$	$\mathrm{LL}_2\rightarrow\mathrm{LL}_2^{-}$	$\mathrm{LL}_1\rightarrow\mathrm{LL}_1^{-}$	$\mathrm{Ru}^{2+}\rightarrow\mathrm{Ru}^{3+}$	$n\mathrm{T}\rightarrow n\mathrm{T}^{+}$
$[\mathrm{Ru(4,4'\text{-}btfmb)_3}]^{2+}$				−2.75	−2.21	−1.61	−1.39	−1.24	+1.34	
Ru-phen				−2.70	−2.30	−2.01	−1.49	−1.29	+1.18	
Ru-0T				−2.81	−2.29	−2.14	−1.54	−1.33	+1.18	
Ru-1T				−2.75	−2.30	−2.12	−1.51	−1.32	+1.22	+1.02
Ru-2T			−2.81	−2.71	−2.29	−2.12	−1.51	−1.31	+1.26	+0.89
Ru-3T		−2.96	−2.54	−2.86	−2.32	−2.15	−1.54	−1.32	+1.29	+0.69
Ru-4T	−2.93	−2.55	−2.23	−2.83	−2.33	−2.13	−1.52	−1.32	+1.27	+0.58

3.4.4 In Vitro Photobiological Activity

The compounds in this series were assessed for their cytotoxicity in the absence of light (dark) as well as their light-triggered cytotoxicity against human skin melanoma cells (SK-MEL-28) and lung carcinoma cells (A549) cultured as 2D monolayers (Figure 7). Details can be found in our previously published work[7,13,16] as well as in the SI.

Normoxia.

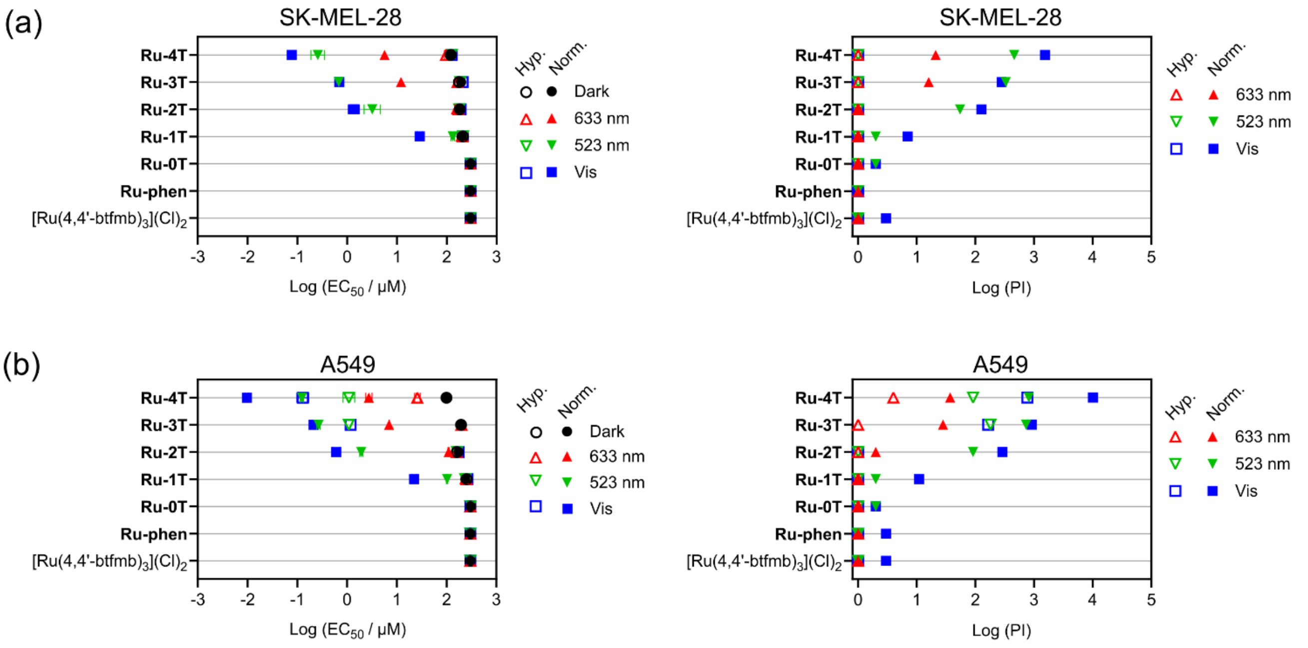

Figure 7. In vitro cytotoxicity and photocytotoxicity log (EC_{50} ± SEM) values (left) and PI values (right) obtained from dose−response curves in the SK-MEL-28 melanoma cell line (a) and A549 cell line (b) with $[Ru(4,4'\text{-}btfmb)_3](Cl)_2$ and **Ru-phen−Ru-4T**. Treatments include dark (black circles) or light delivered at a fluence of 100 J cm^{-2} and irradiance of ~20 mW cm^{-2}. The light wavelengths were broadband visible (400−700 nm, blue squares), 523 nm (green inverted triangles), or 633 nm (red triangles. Data collected under normoxic (~18.5% O_2) and hypoxic (1% O_2) conditions is represented with closed symbols and open symbols, respectively.

For each photobiological assay in normoxia, SK-MEL-28 or A549 cells growing in log phase were seeded into 384-well plates, with one set for dark cytotoxicity evaluation and another set for photocytotoxicity assessment. After allowing the cells to adhere for 3−5 hours at 37°C, they were treated with varying concentrations of the compounds (1 nM to 300 µM for all compounds, 1 aM to 300 µM for **Ru-4T**). After a 13−20 h drug-to-light interval (DLI), the light plates were exposed to specific light treatments, while the dark plates remained in the incubator. The light treatment used a fluence of 100 J cm^{-2} emitted from broadband visible (400−700 nm, 21 mW cm^{-2}) or monochromatic (±2.5 nm) green (523 nm, 18 mW cm^{-2}) or red (633 nm, 18 mW cm^{-2}) LEDs. After light treatment, the plates were allowed to incubate in normoxia at 37°C for 24 h. Cell viability was then assessed indirectly using a resazurin-based cell viability assay. Sigmoidal fits of the dose-response curves were used to calculate the effective concentrations required to reduce cell viability by 50% (EC_{50} values) for both treatment conditions. Phototherapeutic indices (PIs), representing the amplification of cytotoxic effects upon light exposure, were calculated as ratios of dark-to-light EC_{50} values.

In the absence of light activation, the complexes in this series were relatively nontoxic to SK-MEL-28 and A549 cells (Figure 7, Table S4−Table S5). $[Ru(4,4'\text{-btmfb})_3]^{2+}$, **Ru-phen**, and **Ru-0T** exhibited dark EC_{50} values that exceeded the highest concentration tested in the assay (>300 µM), indicating a lack of toxicity. Consequently, the phototherapeutic indices (PIs) for these compounds were technically undefined but were reported as a lower limit using 300 µM as the dark cytotoxicity threshold. **Ru-1T−Ru-3T** were considered nontoxic toward both cell lines, with dark EC_{50} values >100 µM. **Ru-4T** had the lowest dark EC_{50} values, which were still relatively high at 99 µM and 120 µM in in SK-MEL-28 and A549 cells, respectively.

<u>*SKMEL28 cells.*</u> $[Ru(4,4'\text{-btmfb})_3]^{2+}$, **Ru-phen**, and **Ru-0T** were inactive against both cell lines under any light condition. Incorporation of thiophene rings (*n*=1−4 thienyl groups) resulted in progressively higher potency with visible light, spanning from 22 µM (PI=11) for the least active thienyl compound **Ru-1T** to as low as 10 nM (PI=10,000) for the most active compound **Ru-4T** in SK-MEL-28. Appending two thiophenes (**Ru-2T**) improved the potency 37-fold, shifting the EC_{50} values into the sub-micromolar regime near 0.61 µM (PI=290). Another 20-fold enhancement in photocytotoxicity was accomplished on going to three thiophene rings (**Ru-3T**; SK-MEL-28: EC_{50}=0.21 µM, PI=920), and yet another 20-fold improvement occurred with four thiophenes (**Ru-4T**; SK-MEL-28: EC_{50}=10 nM, PI=10,000).

The activity of the series was mostly diminished with longer-wavelength green or red light. With green light, **Ru-1T** lost most of its activity (EC_{50}=103 µM, PI=2). The activity **Ru-2T** dropped by a factor of 3 but was still single-digit micromolar (EC_{50}=1.9 µM, PI=91), and **Ru-4T** dropped by

10-fold but remained sub-micromolar (EC_{50}=0.12 µM, PI=815). **Ru-3T**, on the other hand, maintained its activity (EC_{50}=0.27 µM, PI=731). With red light, **Ru-3T** (EC_{50}=12.1 µM; PI=329) and **Ru-4T** (EC_{50}=5.64 µM; PI=461) showed modest activity. This outcome aligns with the anticipated behavior of compounds that exhibit minimal absorption of red light.[70]

A549 cells. The A549 cell line proved more resistant to the light-triggered compounds than SK-MEL-28 under similar conditions, but the overall trend in activity remained the same (Figure 7, Table S4). The cytotoxicity was minimal for all complexes, with EC_{50} values ranging from 120–300 µM. Compounds $[Ru(4,4'\text{-btfmb})_3](Cl)_2$, **Ru-phen**, and **Ru-0T** were completely inactive under all light conditions, and **Ru-1T** (visible EC_{50}=29 µM, PI=7) was the least active thienyl complex, followed by **Ru-2T** (visible EC_{50}=1.37 µM, PI=127), **Ru-3T** (visible EC_{50}=0.70 µM, PI=280), and finally **Ru-4T** (EC_{50}=0.077 µM, PI=1500). Treatments with red and green light similarly attenuated the overall activity of the series.

Hypoxia.

The assays under hypoxic conditions mirrored the procedure followed for normoxia, with a notable exception: post-cell adhesion, the plates—both for dark and light conditions—were transferred to a hypoxia chamber with 1% O_2 atmosphere for a duration of 2–3 h prior to introducing the compounds. After a DLI of 18 h in the hypoxia chamber, the concentration of dissolved O_2 was verified in the assay wells using an immersive optical probe before sealing the plates to be light treated with transparent qPCR film that has a low gas permeability. Light was delivered outside the hypoxia chamber for approximately 1.5 h, while the dark plates were kept inside an incubator. The films were removed from the light plates at the end of the illumination period. Both dark and light plates were then incubated in normoxia (37°C, 5% CO_2, with relative humidity above 90%) for 20–23 h, after which time the cell viability was assessed.

Hypoxic conditions broadly attenuated the activity of the series in both cell lines, where A549 cells were completely resistant to all treatments and SK-MEL-28 cells were moderately sensitive under certain conditions. Regardless of light-treatment, $[Ru(4,4'\text{-btfmb})_3](Cl)_2$ and compounds **Ru-0T**–**Ru-2T** exhibited no photocytotoxic effect under hypoxic conditions toward SK-MEL-28 cells. On the other hand, **Ru-3T** showed an EC_{50} value of ~1 µM with visible and green light treatments. With red light, **Ru-4T** was less active (EC_{50}=26 µM, PI=4), but otherwise the series was inactive. The dramatic decline in the activity of **Ru-3T** and **Ru-4T**, coupled with the complete inactivity of the other compounds in the series under hypoxic conditions, suggests that oxygen plays a pivotal role in their photocytotoxic mechanisms. This observation solidifies the hypothesis that the primary driver behind the observed photocytotoxicity of these compounds in normoxic conditions stems from oxygen-dependent photophysical processes.

Biological replicates.

Figure 7 and Table S5 show representative activity against SK-MEL-28 for one biological replicate based on the mean values from three technical replicates with minimal standard deviation. Since a greater degree of variation is expected over biological replicates, we assessed the activity of the most potent compounds (**Ru-3T** and **Ru-4T**) over five biological replicates (each performed in triplicate) with SK-MEL-28 cells (Table S6−Table S9). Repeat 0 corresponds to the data in Figure 7 and Table S5. The subsequent biological replicates are labeled Repeats 1–5. SK-MEL-28 cells were selected for these studies because this is the cell line we have historically used to rank potency across all compounds made in our lab. [13]

Without light both **Ru-3T** and **Ru-4T** were completely nontoxic over all biological replicates in both normoxia and hypoxia, with mean EC_{50} of 197 µM for **Ru-3T** and 100 µM for **Ru-4T**. The visible EC_{50} values for **Ru-3T** in normoxia ranged from 70 to 700 nM (mean=440 nM); the corresponding visible PIs ranged from 305–2700 (PI_{avg}=1400). The EC_{50} values for **Ru-4T** under the same conditions ranged from 9–59 nM with a mean of 17 nM (PI=1900–12000, mean=6500). All 6 replicates were within an order of magnitude of each other.

Using green light, the EC_{50} values for **Ru-3T** fluctuated between 0.22–0.66 µM (PI_{avg}=0.29 µM), with PIs between 300–1000 (PI_{avg}=548). The mean values were determined to be 0.29 µM and 548, respectively. For **Ru-4T**, the results were slightly more variable, with green EC_{50} values from 54 to 320 nM, and corresponding PIs extending from 800–3000 range. Even though **Ru-4T** was generally more active than **Ru-3T**, the difference in their activities was only around five-fold.

Under red light illumination in normoxia, the EC_{50} values of both **Ru-3T** and **Ru-4T** were reproducibly in the single digit micromolar regime. **Ru-3T** exhibited red EC_{50} values between 2 and 7 µM (mean=2.2 µM) and PIs ranging from 23 to 101 (PI_{avg}=52). The activity of **Ru-4T** was slightly more consistent than **Ru-3T**, with red EC_{50} values falling between 1.3 to 3.3 µM (mean=2.2 µM) with PIs between 21 and 91 (PI_{avg}=53). The red-derived activity of **Ru-3T** and **Ru-4T** is notable as both complexes exhibit vanishingly low molar extinction coefficients at 633 nm. This characteristic has been reported previously,[70] and tends to require lowest-lying $^3\pi\pi^*$ triplets with prolonged lifetimes such as those observed for **Ru-3T** and **Ru-4T**.

The activity of **Ru-3T** in hypoxia was mostly consistent but repeats 3 and 4 were outliers that should be ignored: repeat 3 displayed unusually high activity compared to the other replicates, and no activity at all was observed in repeat 4 (see Table S16). In repeats 1, 2, and 5, the visible and green activity of **Ru-3T** improved when compared to our initial measurements, but all values were still within one order of magnitude. With visible light, the EC_{50} value was 1.2 µM (PI=170) in repeat 0 but improved to a range of 410–870 nM (PI=230–700, PI_{avg}=300) in repeats 1, 2, and 5. Similarly, the initial green EC_{50} value for **Ru-3T** was 1.1 µM (PI=180), which lowered to 0.3–1.0 µM (PI=200–700, PI_{avg}=270) in subsequent assays. The observation of two distinct outliers, and the fact that the activity of **Ru-3T** was actually greater in subsequent biological replicates, underscores the importance of performing biological replicates when evaluating photobiological efficacy.

The activity of **Ru-4T** varied slightly more in hypoxia than it did in normoxia, but all EC_{50} values were still within roughly one order of magnitude. Using visible light treatment, repeats 0 and 2–5 fell between 0.13–0.54 µM (PI=200–400), but repeat 1 presented a slightly lower EC_{50} of 35 nM (PI=2900). With green and red light treatments, **Ru-4T** proved to be consistently more active than what was originally observed in repeat 0, with initial EC_{50} values of 1.0 µM (PI=90) and 26 µM (PI=4), respectively, which improved to a range of 200–900 nM (PI=100–500, PI_{avg}=210) and 6–9 µM (PI=7–30, PI_{avg}=9) during repeats 1–5. The average hypoxic red activity (<10 µM) of **Ru-4T** is particularly notable for this class of PS, and is comparable to the "ubertoxin" ML19C01 (which presents sub-nanomolar normoxic phototoxicity).[13,16]

In conclusion, across six biological replicates, **Ru-4T** has consistently displayed superior activity compared to **Ru-3T**, particularly when activated with visible light under normoxic conditions. Under these conditions, **Ru-4T** had an average EC_{50} of 13 nM (PI_{avg}=9300). Notably, the values obtained in all biological replicates were within one order of magnitude, making **Ru-4T** more consistent than ML19C01, which varies by up to 6 orders of magnitude.[13,16] This marked improvement in consistency may be related to the improved aqueous solubility observed in this family of complexes, and the effects of fluorination on biological reproducibility is being investigated further.

3.5 CONCLUSIONS

Herein we synthesized a series of Ru(II) polypyridyl complexes featuring two 4,4'-btfmb coligands and the IP-*n*T ligand (*n*=1–4) and compared these systems to the reference compounds $[Ru(4,4'\text{-btfmb})_3]^{+2}$, **Ru-phen**, and **Ru-0T**. This study stands as part of our larger initiative to better understand the impact of structural variations on the photophysical, photobiological, and electrochemical profiles of oligothienyl-containing metal complexes.

The emission quantum yields were moderate for $[Ru(4,4'\text{-btfmb})_3]^{+2}$ and become very low as the number of thiophenes increased in the IP-*n*T ligand. **Ru-3T** and **Ru-4T** displayed the longest T_1 lifetimes in the series at approximately 20 μs. The $^1O_2$ quantum yields ranged from poor to moderate, with **Ru-3T** and **Ru-4T** having the higher quantum yields among the thienyl complexes.

Electrochemically, the Ru(II/III) oxidation processes were typical for this family of complexes. Additional thiophene oxidations ($n\text{T}^{0/+}$) were observed at +1.02 V for **Ru-1T** to as low as +0.58 V for **Ru-4T**. All complexes underwent at least five reductions: two for each 4,4'-btfmb ligand and one for the phen or IP ligands. Complexes **Ru-2T**–**Ru-4T** underwent additional reductions involving their *n*T groups, occurring at potentials ranging from −2.23 V to −2.96 V. Specifically, **Ru-4T** could accommodate 8 additional electrons, highlighting its potential for potential photoredox applications.

Over five biological replicates, **Ru-4T** demonstrated EC_{50} values averaging 13 nM (PI_{avg}=9300) in normoxia under visible light. Notably, all values fell within one order of magnitude of each other, making **Ru-4T** significantly more consistent than some previously studied IP-4T complexes. We attribute this consistency in part to the improved aqueous solubility for these complexes. It is common for IP-4T complexes to precipitate in aqueous solution, but **Ru-4T** dissolves very well.

In summary, this fluorinated family of Ru(II) polypyridyl complexes stands out for its notable water solubility, tight consistency in photobiological assays, and compelling electrochemical properties. These findings highlight **Ru-4T** as an excellent candidate for further applications.

3.6 ASSOCIATED CONTENT

Synthetic characterization (1D and 2D NMR, HPLC, HRMS) and (photo)biological data are included in the Supporting Information. This material is available free of charge via the Internet at https://www.acs.com.

3.7 ACKNOWLEDGEMENTS

S.A.M. and C.G.C. thank the National Cancer Institute (NCI) of the National Institutes of Health (NIH) (Award R01CA222227) and the National Science Foundation (NSF) (Award NSF 2102459) for support. The content in this work is solely the responsibility of the authors and does not necessarily represent the official views of the National Institutes of Health. S.A.M. also thanks Dr. Daniel Todd as UNCG's Triad Mass Spectrometry Facility manager and his assistants Jennifer Simpson and Diane Wallace. S.A.M. likewise thanks Dr. Franklin Moy (UNCG) and Dr. Brian Edwards (UTA) for their experimental support and instrument maintenance as NMR facility managers.

3.8 REFERENCES

(1) Sung, H.; Ferlay, J.; Siegel, R. L.; Laversanne, M.; Soerjomataram, I.; Jemal, A.; Bray, F. Global Cancer Statistics 2020: GLOBOCAN Estimates of Incidence and Mortality Worldwide for 36 Cancers in 185 Countries. *CA A Cancer J Clin* **2021**, *71* (3), 209–249. https://doi.org/10.3322/caac.21660.

(2) Mellman, I.; Coukos, G.; Dranoff, G. Cancer Immunotherapy Comes of Age. *Nature* **2011**, *480* (7378), 480–489. https://doi.org/10.1038/nature10673.

(3) Marabelle, A.; Tselikas, L.; De Baere, T.; Houot, R. Intratumoral Immunotherapy: Using the Tumor as the Remedy. *Annals of Oncology* **2017**, *28*, xii33–xii43. https://doi.org/10.1093/annonc/mdx683.

(4) Meric-Bernstam, F.; Larkin, J.; Tabernero, J.; Bonini, C. Enhancing Anti-Tumour Efficacy with Immunotherapy Combinations. *The Lancet* **2021**, *397* (10278), 1010–1022. https://doi.org/10.1016/S0140-6736(20)32598-8.

(5) Sawyers, C. Targeted Cancer Therapy. *Nature* **2004**, *432* (7015), 294–297. https://doi.org/10.1038/nature03095.

(6) Min, H.-Y.; Lee, H.-Y. Molecular Targeted Therapy for Anticancer Treatment. *Exp Mol Med* **2022**, *54* (10), 1670–1694. https://doi.org/10.1038/s12276-022-00864-3.

(7) Monro, S.; Colón, K. L.; Yin, H.; Roque, J.; Konda, P.; Gujar, S.; Thummel, R. P.; Lilge, L.; Cameron, C. G.; McFarland, S. A. Transition Metal Complexes and Photodynamic Therapy from a Tumor-Centered Approach: Challenges, Opportunities, and Highlights from the Development of TLD1433. *Chem. Rev.* **2019**, *119* (2), 797–828. https://doi.org/10.1021/acs.chemrev.8b00211.

(8) McFarland, S. A.; Mandel, A.; Dumoulin-White, R.; Gasser, G. Metal-Based Photosensitizers for Photodynamic Therapy: The Future of Multimodal Oncology? *Curr. Opin. Chem. Biol.* **2020**, *56*, 23–27. https://doi.org/10.1016/j.cbpa.2019.10.004.

(9) Howerton, B. S.; Heidary, D. K.; Glazer, E. C. Strained Ruthenium Complexes Are Potent Light-Activated Anticancer Agents. *Journal of the American Chemical Society* **2012**, *134* (20), 8324–8327. https://doi.org/10.1021/ja3009677.

(10) Sainuddin, T.; Pinto, M.; Yin, H.; Hetu, M.; Colpitts, J.; McFarland, S. A. Strained Ruthenium Metal–Organic Dyads as Photocisplatin Agents with Dual Action. *J. Inorg. Biochem.* **2016**, *158*, 45–54. https://doi.org/10.1016/j.jinorgbio.2016.01.009.

(11) Roque, J.; Havrylyuk, D.; Barrett, P. C.; Sainuddin, T.; McCain, J.; Colón, K.; Sparks, W. T.; Bradner, E.; Monro, S.; Heidary, D.; Cameron, C. G.; Glazer, E. C.; McFarland, S. A. Strained, Photoejecting Ru(II) Complexes That Are Cytotoxic Under Hypoxic Conditions. *Photochem. Photobiol.* **2020**, *96* (2), 327–339. https://doi.org/10.1111/php.13174.

(12) Cole, H. D.; Roque, J. A.; Lifshits, L. M.; Hodges, R.; Barrett, P. C.; Havrylyuk, D.; Heidary, D.; Ramasamy, E.; Cameron, C. G.; Glazer, E. C.; McFarland, S. A. Fine-Feature Modifications to Strained Ruthenium Complexes Radically Alter Their Hypoxic Anticancer Activity. *Photochem & Photobiology* **2022**, *98* (1), 73–84. https://doi.org/10.1111/php.13395.

(13) Roque III, J. A.; Cole, H. D.; Barrett, P. C.; Lifshits, L. M.; Hodges, R. O.; Kim, S.; Deep, G.; Francés-Monerris, A.; Alberto, M. E.; Cameron, C. G.; McFarland, S. A. Intraligand Excited States Turn a Ruthenium Oligothiophene Complex into a Light-Triggered Ubertoxin with Anticancer Effects in Extreme Hypoxia. *J. Am. Chem. Soc.* **2022**, *144* (18), 8317–8336. https://doi.org/10.1021/jacs.2c02475.

(14) Cuello-Garibo, J.-A.; Meijer, M. S.; Bonnet, S. To Cage or to Be Caged? The Cytotoxic Species in Ruthenium-Based Photoactivated Chemotherapy Is Not Always the Metal. *Chem. Commun.* **2017**, *53* (50), 6768–6771. https://doi.org/10.1039/C7CC03469E.

(15) Azar, D. F.; Audi, H.; Farhat, S.; El-Sibai, M.; Abi-Habib, R. J.; Khnayzer, R. S. Phototoxicity of Strained Ru(II) Complexes: Is It the Metal Complex or the Dissociating Ligand? *Dalton Trans.* **2017**, *46* (35), 11529–11532. https://doi.org/10.1039/C7DT02255G.

(16) Cole, H. D.; Roque, J. A.; Shi, G.; Lifshits, L. M.; Ramasamy, E.; Barrett, P. C.; Hodges, R. O.; Cameron, C. G.; McFarland, S. A. Anticancer Agent with Inexplicable Potency in Extreme Hypoxia: Characterizing a Light-Triggered Ruthenium Ubertoxin. *J. Am. Chem. Soc.* **2022**, *144* (22), 9543–9547. https://doi.org/10.1021/jacs.1c09010.

(17) Sun, Y.; Heidary, D. K.; Zhang, Z.; Richards, C. I.; Glazer, E. C. Bacterial Cytological Profiling Reveals the Mechanism of Action of Anticancer Metal Complexes. *Mol. Pharm.* **2018**, *15* (8), 3404–3416. https://doi.org/10.1021/acs.molpharmaceut.8b00407.

(18) Loftus, L. M.; White, J. K.; Albani, B. A.; Kohler, L.; Kodanko, J. J.; Thummel, R. P.; Dunbar, K. R.; Turro, C. New Ru^{II} Complex for Dual Activity: Photoinduced Ligand Release and $^1O_2$ Production. *Chem. Eur. J.* **2016**, *22* (11), 3704–3708. https://doi.org/10.1002/chem.201504800.

(19) Toupin, N. P.; Nadella, S.; Steinke, S. J.; Turro, C.; Kodanko, J. J. Dual-Action Ru(II) Complexes with Bulky π-Expansive Ligands: Phototoxicity without DNA Intercalation.

Inorganic Chemistry **2020**, *59* (6), 3919–3933. https://doi.org/10.1021/acs.inorgchem.9b03585.

(20) Lameijer, L. N.; Ernst, D.; Hopkins, S. L.; Meijer, M. S.; Askes, S. H. C.; Le Dévédec, S. E.; Bonnet, S. A Red-Light-Activated Ruthenium-Caged NAMPT Inhibitor Remains Phototoxic in Hypoxic Cancer Cells. *Angew. Chem. Int. Ed.* **2017**, *56* (38), 11549–11553. https://doi.org/10.1002/anie.201703890.

(21) Albani, B. A.; Durr, C. B.; Turro, C. Selective Photoinduced Ligand Exchange in a New Tris–Heteroleptic Ru(II) Complex. *The Journal of Physical Chemistry A* **2013**, *117* (50), 13885–13892. https://doi.org/10.1021/jp4085684.

(22) Knoll, J. D.; Albani, B. A.; Durr, C. B.; Turro, C. Unusually Efficient Pyridine Photodissociation from Ru(II) Complexes with Sterically Bulky Bidentate Ancillary Ligands. *The Journal of Physical Chemistry A* **2014**, *118* (45), 10603–10610. https://doi.org/10.1021/jp5057732.

(23) Arora, K.; White, J. K.; Sharma, R.; Mazumder, S.; Martin, P. D.; Schlegel, H. B.; Turro, C.; Kodanko, J. J. Effects of Methyl Substitution in Ruthenium Tris(2-Pyridylmethyl)Amine Photocaging Groups for Nitriles. *Inorganic Chemistry* **2016**, *55* (14), 6968–6979. https://doi.org/10.1021/acs.inorgchem.6b00650.

(24) Huisman, M.; White, J. K.; Lewalski, V. G.; Podgorski, I.; Turro, C.; Kodanko, J. J. Caging the Uncageable: Using Metal Complex Release for Photochemical Control over Irreversible Inhibition. *Chemical Communications* **2016**, *52* (85), 12590–12593. https://doi.org/10.1039/C6CC07083C.

(25) Li, A.; Yadav, R.; White, J. K.; Herroon, M. K.; Callahan, B. P.; Podgorski, I.; Turro, C.; Scott, E. E.; Kodanko, J. J. Illuminating Cytochrome P450 Binding: Ru(II)-Caged Inhibitors of CYP17A1. *Chem. Commun.* **2017**, *53* (26), 3673–3676. https://doi.org/10.1039/C7CC01459G.

(26) Arora, K.; Herroon, M.; Al-Afyouni, M. H.; Toupin, N. P.; Rohrabaugh, T. N.; Loftus, L. M.; Podgorski, I.; Turro, C.; Kodanko, J. J. Catch and Release Photosensitizers: Combining Dual-Action Ruthenium Complexes with Protease Inactivation for Targeting Invasive Cancers. *J. Am. Chem. Soc.* **2018**, *140* (43), 14367–14380. https://doi.org/10.1021/jacs.8b08853.

(27) Li, A.; Turro, C.; Kodanko, J. J. Ru(II) Polypyridyl Complexes Derived from Tetradentate Ancillary Ligands for Effective Photocaging. *Accounts of Chemical Research* **2018**, *51* (6), 1415–1421. https://doi.org/10.1021/acs.accounts.8b00066.

(28) Li, A.; Turro, C.; Kodanko, J. J. Ru(II) Polypyridyl Complexes as Photocages for Bioactive Compounds Containing Nitriles and Aromatic Heterocycles. *Chem. Commun.* **2018**, *54* (11), 1280–1290. https://doi.org/10.1039/C7CC09000E.

(29) Nisbett, K.; Tu, Y.-J.; Turro, C.; Kodanko, J. J.; Schlegel, H. B. DFT Investigation of Ligand Photodissociation in [RuII(Tpy)(Bpy)(Py)]2+ and [RuII(Tpy)(Me2bpy)(Py)]2+ Complexes. *Inorganic Chemistry* **2018**, *57* (1), 231–240. https://doi.org/10.1021/acs.inorgchem.7b02398.

(30) Rohrabaugh, T. N.; Rohrabaugh, A. M.; Kodanko, J. J.; White, J. K.; Turro, C. Photoactivation of Imatinib–Antibody Conjugate Using Low-Energy Visible Light from Ru(II)-Polypyridyl Cages. *Chem. Commun.* **2018**, *54* (41), 5193–5196. https://doi.org/10.1039/C8CC01348A.

(31) Bahreman, A.; Limburg, B.; Siegler, M. A.; Bouwman, E.; Bonnet, S. Spontaneous Formation in the Dark, and Visible Light-Induced Cleavage, of a Ru–S Bond in Water: A Thermodynamic and Kinetic Study. *Inorganic Chemistry* **2013**, *52* (16), 9456–9469. https://doi.org/10.1021/ic401105v.

(32) Bahreman, A.; Rabe, M.; Kros, A.; Bruylants, G.; Bonnet, S. Binding of a Ruthenium Complex to a Thioether Ligand Embedded in a Negatively Charged Lipid Bilayer: A Two-Step Mechanism. *Chemistry - A European Journal* **2014**, *20* (24), 7429–7438. https://doi.org/10.1002/chem.201400377.

(33) Göttle, A. J.; Alary, F.; Boggio-Pasqua, M.; Dixon, I. M.; Heully, J.-L.; Bahreman, A.; Askes, S. H. C.; Bonnet, S. Pivotal Role of a Pentacoordinate ^{3}MC State on the Photocleavage Efficiency of a Thioether Ligand in Ruthenium(II) Complexes: A Theoretical Mechanistic Study. *Inorganic Chemistry* **2016**, *55* (9), 4448–4456. https://doi.org/10.1021/acs.inorgchem.6b00268.

(34) Cuello-Garibo, J.-A.; Pérez-Gallent, E.; van der Boon, L.; Siegler, M. A.; Bonnet, S. Influence of the Steric Bulk and Solvent on the Photoreactivity of Ruthenium Polypyridyl

Complexes Coordinated to L-Proline. *Inorganic Chemistry* **2017**, *56* (9), 4818–4828. https://doi.org/10.1021/acs.inorgchem.6b02794.

(35) Sun, W.; Wen, Y.; Thiramanas, R.; Chen, M.; Han, J.; Gong, N.; Wagner, M.; Jiang, S.; Meijer, M. S.; Bonnet, S.; Butt, H.-J.; Mailänder, V.; Liang, X.-J.; Wu, S. Red-Light-Controlled Release of Drug-Ru Complex Conjugates from Metallopolymer Micelles for Phototherapy in Hypoxic Tumor Environments. *Adv. Funct. Mater.* **2018**, *28* (39), 1804227. https://doi.org/10.1002/adfm.201804227.

(36) Meijer, M. S.; Talens, V. S.; Hilbers, M. F.; Kieltyka, R. E.; Brouwer, A. M.; Natile, M. M.; Bonnet, S. NIR-Light-Driven Generation of Reactive Oxygen Species Using Ru(II)-Decorated Lipid-Encapsulated Upconverting Nanoparticles. *Langmuir* **2019**, *35* (37), 12079–12090. https://doi.org/10.1021/acs.langmuir.9b01318.

(37) Havrylyuk, D.; Hachey, A. C.; Fenton, A.; Heidary, D. K.; Glazer, E. C. Ru(II) Photocages Enable Precise Control over Enzyme Activity with Red Light. *Nat Commun* **2022**, *13* (1), 3636. https://doi.org/10.1038/s41467-022-31269-5.

(38) Ryan, R. T.; Havrylyuk, D.; Stevens, K. C.; Moore, L. H.; Parkin, S.; Blackburn, J. S.; Heidary, D. K.; Selegue, J. P.; Glazer, E. C. Biological Investigations of Ru(II) Complexes with Diverse β-Diketone Ligands. *Eur. J. Inorg. Chem.* **2021**, *2021* (35), 3611–3621. https://doi.org/10.1002/ejic.202100468.

(39) Wachter, E.; Heidary, D. K.; Howerton, B. S.; Parkin, S.; Glazer, E. C. Light-Activated Ruthenium Complexes Photobind DNA and Are Cytotoxic in the Photodynamic Therapy Window. *Chem. Commun.* **2012**, *48* (77), 9649. https://doi.org/10.1039/c2cc33359g.

(40) Huang, H.; Banerjee, S.; Qiu, K.; Zhang, P.; Blacque, O.; Malcomson, T.; Paterson, M. J.; Clarkson, G. J.; Staniforth, M.; Stavros, V. G.; Gasser, G.; Chao, H.; Sadler, P. J. Targeted Photoredox Catalysis in Cancer Cells. *Nat. Chem.* **2019**, *11* (11), 1041–1048. https://doi.org/10.1038/s41557-019-0328-4.

(41) Baptista, M. S.; Cadet, J.; Di Mascio, P.; Ghogare, A. A.; Greer, A.; Hamblin, M. R.; Lorente, C.; Nunez, S. C.; Ribeiro, M. S.; Thomas, A. H.; Vignoni, M.; Yoshimura, T. M. Type I and Type II Photosensitized Oxidation Reactions: Guidelines and Mechanistic Pathways. *Photochemistry and Photobiology* **2017**, *93* (4), 912–919. https://doi.org/10.1111/php.12716.

(42) Roque III, J. A.; Barrett, P. C.; Cole, H. D.; Lifshits, L. M.; Shi, G.; Monro, S.; von Dohlen, D.; Kim, S.; Russo, N.; Deep, G.; Cameron, C. G.; Alberto, M. E.; McFarland, S. A. Breaking the Barrier: An Osmium Photosensitizer with Unprecedented Hypoxic Phototoxicity for Real World Photodynamic Therapy. *Chem. Sci.* **2020**, *11*, 9784–9806. https://doi.org/10.1039/D0SC03008B.

(43) Shi, G.; Monro, S.; Hennigar, R.; Colpitts, J.; Fong, J.; Kasimova, K.; Yin, H.; DeCoste, R.; Spencer, C.; Chamberlain, L.; Mandel, A.; Lilge, L.; McFarland, S. A. Ru(II) Dyads Derived from α-Oligothiophenes: A New Class of Potent and Versatile Photosensitizers for PDT. *Coord. Chem. Rev.* **2015**, *282–283*, 127–138. https://doi.org/10.1016/j.ccr.2014.04.012.

(44) Roque, J. A.; Barrett, P. C.; Cole, H. D.; Lifshits, L. M.; Bradner, E.; Shi, G.; von Dohlen, D.; Kim, S.; Russo, N.; Deep, G.; Cameron, C. G.; Alberto, M. E.; McFarland, S. A. Os(II) Oligothienyl Complexes as a Hypoxia-Active Photosensitizer Class for Photodynamic Therapy. *Inorg. Chem.* **2020**, *59* (22), 16341–16360. https://doi.org/10.1021/acs.inorgchem.0c02137.

(45) Lifshits, L. M.; Roque, J. A.; Cole, H. D.; Thummel, R. P.; Cameron, C. G.; McFarland, S. A. NIR-Absorbing Ru II Complexes Containing α-Oligothiophenes for Applications in Photodynamic Therapy. *ChemBioChem* **2020**, *21*, 3594–3607. https://doi.org/10.1002/cbic.202000419.

(46) Armstrong, D. W.; Yu, J.; Cole, H. D.; McFarland, Sherri. A.; Nafie, J. Chiral Resolution and Absolute Configuration Determination of New Metal-Based Photodynamic Therapy Antitumor Agents. *J. Pharm. Biom. Anal.* **2021**, *204*, 114233. https://doi.org/10.1016/j.jpba.2021.114233.

(47) Handlovic, T. T.; Wahab, M. F.; Cole, H. D.; Alatrash, N.; Ramasamy, E.; MacDonnell, F. M.; McFarland, S. A.; Armstrong, D. W. Insights into Enantioselective Separations of Ionic Metal Complexes by Sub/Supercritical Fluid Chromatography. *Analytica Chimica Acta* **2022**, *1228*, 340156. https://doi.org/10.1016/j.aca.2022.340156.

(48) Farney, E. P.; Chapman, S. J.; Swords, W. B.; Torelli, M. D.; Hamers, R. J.; Yoon, T. P. Discovery and Elucidation of Counteranion Dependence in Photoredox Catalysis. *J. Am. Chem. Soc.* **2019**, *141* (15), 6385–6391. https://doi.org/10.1021/jacs.9b01885.

(49) Furue, M.; Maruyama, K.; Oguni, T.; Naiki, M.; Kamachi, M. Trifluoromethyl-Substituted 2,2'-Bipyridine Ligands. Synthetic Control of Excited-State Properties of Ruthenium(II) Tris-Chelate Complexes. *Inorg. Chem.* **1992**, *31* (18), 3792–3795. https://doi.org/10.1021/ic00044a022.

(50) Maurer, A. B.; Piechota, E. J.; Meyer, G. J. Excited-State Dipole Moments of Homoleptic $[Ru(Bpy')_3]^{2+}$ Complexes Measured by Stark Spectroscopy. *J. Phys. Chem. A* **2019**, *123* (41), 8745–8754. https://doi.org/10.1021/acs.jpca.9b05874.

(51) Nomrowski, J.; Wenger, O. S. Photoinduced PCET in Ruthenium–Phenol Systems: Thermodynamic Equivalence of Uni- and Bidirectional Reactions. *Inorg. Chem.* **2015**, *54* (7), 3680–3687. https://doi.org/10.1021/acs.inorgchem.5b00318.

(52) Sullivan, B.; Salmon, D.; Meyer, T. Mixed Phosphine 2,2'-Bipyridine Complexes of Ruthenium. **1978**, *17*, 3334–3341.

(53) Wang, Z. *Comprehensive Organic Name Reactions and Reagents*; John Wiley & Sons, Inc.: Hoboken, NJ, USA, 2010. https://doi.org/10.1002/9780470638859.

(54) Ghosh, G.; Colón, K. L.; Fuller, A.; Sainuddin, T.; Bradner, E.; McCain, J.; Monro, S. M. A.; Yin, H.; Hetu, M. W.; Cameron, C. G.; McFarland, S. A. Cyclometalated Ruthenium(II) Complexes Derived from α-Oligothiophenes as Highly Selective Cytotoxic or Photocytotoxic Agents. *Inorg. Chem.* **2018**, *57* (13), 7694–7712. https://doi.org/10.1021/acs.inorgchem.8b00689.

(55) Chen, R.; Yang, X.; Tian, H.; Wang, X.; Hagfeldt, A.; Sun, L. Effect of Tetrahydroquinoline Dyes Structure on the Performance of Organic Dye-Sensitized Solar Cells. *Chem. Mater.* **2007**, *19* (16), 4007–4015. https://doi.org/10.1021/cm070617g.

(56) Becker, R. S.; Seixas de Melo, J.; Maçanita, A. L.; Elisei, F. Comprehensive Evaluation of the Absorption, Photophysical, Energy Transfer, Structural, and Theoretical Properties of α-Oligothiophenes with One to Seven Rings. *J. Phys. Chem.* **1996**, *100*, 18683–18695. https://doi.org/10.1021/jp960852e.

(57) DeRosa, M. C.; Crutchley, R. J. Photosensitized Singlet Oxygen and Its Applications. *Coord. Chem. Rev.* **2002**, *233–234*, 351–371. https://doi.org/10.1016/S0010-8545(02)00034-6.

(58) Hissler, M.; Connick, W. B.; Geiger, D. K.; McGarrah, J. E.; Lipa, D.; Lachicotte, R. J.; Eisenberg, R. Platinum Diimine Bis(Acetylide) Complexes: Synthesis, Characterization, and Luminescence Properties. *Inorg. Chem.* **2000**, *39* (3), 447–457. https://doi.org/10.1021/ic991250n.

(59) Lincoln, R.; Kohler, L.; Monro, S.; Yin, H.; Stephenson, M.; Zong, R.; Chouai, A.; Dorsey, C.; Hennigar, R.; Thummel, R. P.; McFarland, S. A. Exploitation of Long-Lived 3IL Excited States for Metal–Organic Photodynamic Therapy: Verification in a Metastatic Melanoma Model. *J. Am. Chem. Soc.* **2013**, *135* (45), 17161–17175. https://doi.org/10.1021/ja408426z.

(60) Monro, S.; Cameron, C. G.; Zhu, X.; Colón, K. L.; Yin, H.; Sainuddin, T.; Hetu, M.; Pinto, M.; Fuller, A.; Bennett, L.; Roque, J.; Sun, W.; McFarland, S. A. Synthesis, Characterization and Photobiological Studies of Ru(II) Dyads Derived from α-Oligothiophene Derivatives of 1,10-Phenanthroline. *Photochem. Photobiol.* **2019**, *95* (1), 267–279. https://doi.org/10.1111/php.13012.

(61) Chettri, A.; Schneider, K. R. A.; Cole, H. D.; Roque, J. A.; Cameron, C. G.; McFarland, S. A.; Dietzek, B. String-Attached Oligothiophene Substituents Determine the Fate of Excited States in Ruthenium Complexes for Photodynamic Therapy. *J. Phys. Chem. A* **2021**, *125* (32), 6985–6994. https://doi.org/10.1021/acs.jpca.1c04900.

(62) Chettri, A.; Roque, J. A.; Schneider, K. R. A.; Cole, H. D.; Cameron, C. G.; McFarland, S. A.; Dietzek, B. It Takes Three to Tango: The Length of the Oligothiophene Chain Determines the Nature of the Long-Lived Excited State and the Resulting Photocytotoxicity of a Ruthenium(II) Photodrug. *ChemPhotoChem* **2021**, *5* (5), 421–425. https://doi.org/10.1002/cptc.202000283.

(63) McClenaghan, N. D.; Leydet, Y.; Maubert, B.; Indelli, M. T.; Campagna, S. Excited-State Equilibration: A Process Leading to Long-Lived Metal-to-Ligand Charge Transfer Luminescence in Supramolecular Systems. *Coordination Chemistry Reviews* **2005**, *249* (13–14), 1336–1350. https://doi.org/10.1016/j.ccr.2004.12.017.

(64) Juris, A.; Balzani, V.; Barigelletti, F.; Campagna, S.; Belser, P.; von Zelewsky, A. Ru(II) Polypyridine Complexes: Photophysics, Photochemistry, Eletrochemistry, and

Chemiluminescence. *Coordination Chemistry Reviews* **1988**, *84*, 85–277. https://doi.org/10.1016/0010-8545(88)80032-8.

(65) Ohsawa, Y.; DeArmond, M. K.; Hanck, K. W.; Morris, D. E.; Whitten, D. G.; Neveux, P. E. Spatially Isolated Redox Orbitals: Evidence from Low-Temperature Voltammetry. *J. Am. Chem. Soc.* **1983**, *105* (21), 6522–6524. https://doi.org/10.1021/ja00359a045.

(66) Ohsawa, Y.; Hanck, K. W.; DeArmond, M. K. A Systematic Electrochemical and Spectroscopic Study of Mixed-Ligand Ruthenium(II) 2,2′-Bipyridine Complexes [Ru(Bpy)3-nLn]2+ (N=0,1,2 and 3). *Journal of Electroanalytical Chemistry and Interfacial Electrochemistry* **1984**, *175* (1–2), 229–240. https://doi.org/10.1016/S0022-0728(84)80358-7.

(67) Roncali, J. Conjugated Poly(Thiophenes): Synthesis, Functionalization, and Applications. *Chemical Reviews* **1992**, *92* (4), 711–738. https://doi.org/10.1021/cr00012a009.

(68) Pavlishchuk, V. V.; Addison, A. W. Conversion Constants for Redox Potentials Measured versus Different Reference Electrodes in Acetonitrile Solutions at 25°C. *Inorganica Chimica Acta* **2000**, *298* (1), 97–102. https://doi.org/10.1016/S0020-1693(99)00407-7.

(69) Diaz, A. F.; Crowley, J.; Bargon, J.; Gardini, G. P.; Torrance, J. B. Electrooxidation of Aromatic Oligomers and Conducting Polymers. *Journal of Electroanalytical Chemistry and Interfacial Electrochemistry* **1981**, *121*, 355–361. https://doi.org/10.1016/S0022-0728(81)80592-X.

(70) Yin, H.; Stephenson, M.; Gibson, J.; Sampson, E.; Shi, G.; Sainuddin, T.; Monro, S.; McFarland, S. A. In Vitro Multiwavelength PDT with 3IL States: Teaching Old Molecules New Tricks. *Inorganic Chemistry* **2014**, *53* (9), 4548–4559. https://doi.org/10.1021/ic5002368.

3.9 SUPPORTING INFORMATION

3.9.1 Synthesis and Characterization

Preparation of Target Complexes

Chart S1. Structures of $[Ru(btfmb)_3](Cl)_2$, **Ru-phen**, and **Ru-0T**–**Ru-4T**.

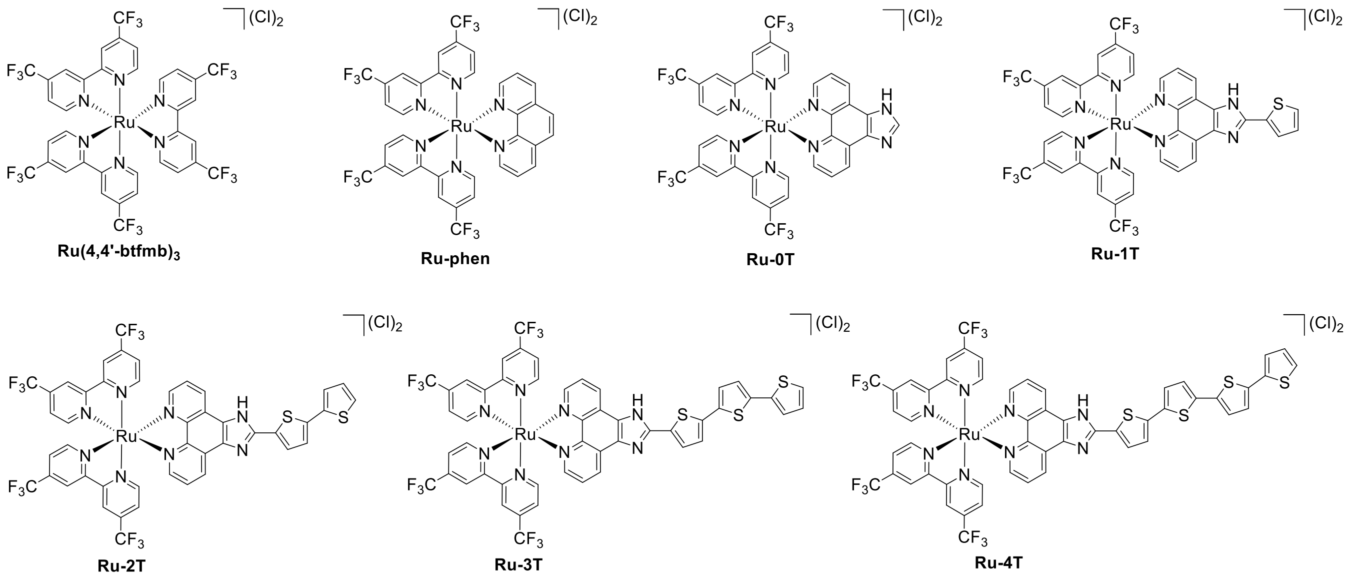

Ru(4,4'-btfmb)$_3$ **Ru-phen** **Ru-0T** **Ru-1T**

Ru-2T **Ru-3T** **Ru-4T**

$Ru(4,4'\text{-}btfmb)_3$ was synthesized using an adapted literature procedure that describes the microwave-assisted synthesis of *tris*-homoleptic Ru(II) polypyridyl complexes.[1] To a solution of Ar-purged ethylene glycol, $Ru(Cl)_3xH_2O$ was combined with 3 equivalents of 4,4′-btfmb ligand and subjected to microwave irradiation for 45 minutes at 180 °C. The crude reaction mixture is then isolated and purified using the same method described above.

Complexes **Ru-phen** and **Ru-0T**–**Ru-3T** were prepared by adapting previously described synthetic methods.[2,3] Briefly, $Ru(4,4'\text{-}btfmb)_2(Cl)_2•2H_2O$ was combined in 20% excess with the corresponding phen or IP-based ligand in a solution of argon-purged ethylene glycol and was subjected to microwave irradiation (hold temperature: 180 °C) for 15 minutes. The complexes were isolated as their PF_6^- salts by transferring the crude reaction mixture to a separatory funnel containing H_2O. The products were then washed with dichloromethane (DCM) several times, which removes any unreacted $Ru(4,4'\text{-}btfmb)_2(Cl)_2•2H_2O$ precursor. An aqueous solution of saturated KPF_6 is then added to the separatory funnel, and then the products were extracted using DCM. The complexes are then purified using flash silica gel chromatography (100% MeCN → 10% water in MeCN → 7.5% H_2O, 0.5% KNO_3, in MeCN) and then converted to their Cl salts via elution through a column of amberlite resin. Finally, the complexes are purified using size-exclusion chromatography, which affords the separation of other Ru(II) species such as $[Ru(4,4'\text{-btfmb})_3](Cl)_2$ that may elute at similar times when using (normal phase) silica chromatography.

The isolation of **Ru-4T** was modified due to its poor solubility in DCM. To circumnavigate this, the crude reaction mixture was diluted with water in a beaker and treated with saturated aqueous KPF_6, and then the solid $[Ru(4,4'\text{-btfmb})_2(IP\text{-}4T)](Cl)_2$ was isolated via a Büchner filtration apparatus and was subsequently washed with 100 mL of H_2O and a few drops of ether. Thereafter, the complex was purified using the same methods described above.

^1H NMR and ^1H–^1H COSY NMR characterization

The Ru(II) polypyridyl complexes with α-oligothiophene chains were characterized in-depth using ^1H NMR spectroscopy. Our strategy for assigning the ^1H signals across all the complexes was centered around identifying each spin system present on the ligands: btfmb, phen, or IP-nT. This began with $[Ru(4,4'\text{-btfmb})_3](Cl)_2$, where three diagnostic signals were observed. These signals enabled the rapid assignment of btfmb signals in all other complexes in the series. The symmetry and electronic properties of the **Ru-phen** complex were altered by replacing one btfmb ligand with phen, resulting in unique phenanthroline-based signals. Their distinct Newtonian characteristics and the through-bond correlations observed in ^1H -^1H COSY aided in their identification.

The assignment of **Ru-0T**–**Ru-3T** was largely straightforward. Specifically, **Ru-0T** and **Ru-1T** were the easiest to assign due to the electromagnetic and chemical distinctions between the imidazole or thiophene peaks from the other pyridyl ^1H signals. However, with each additional thiophene ring on the alpha-oligothiophene chain, the complexity of the assignment increased.

A crucial observation was the distinct chemical shift of the thiophene ring closest to the imidazole unit, attributed to its spatial proximity to nearby nitrogen atoms. This allowed us to distinguish the first ring of the thiophene chain from all other signals in the spectra for **Ru-1T**–**Ru-4T**. In the case of **Ru-2T**, the assignment process was simplified due to the presence of only two thiophene rings: the first positioned next to the imidazole and the second characterized by three signals. The assignment of **Ru-3T** was also straightforward, with thiophene rings being easily discernable.

However, the **Ru-4T** complex posed a unique challenge due to the presence of two electromagnetically similar thiophene rings in the middle of the alpha-oligothiophene chain. To overcome this, we first utilized ^{1}H-^{13}C HSQC NMR to associate the ^{13}C signals with the ^{1}H signals confirmed via ^{1}H-^{1}H COSY NMR. Subsequently, we used ^{13}C-^{1}H HMBC NMR to identify correlations shared between unidentified thienyl ring ^{13}C atoms and previously identified thienyl protons, which were then used to assign the remaining thiophene ring protons in the **Ru-4T** complex.

Characterization with HPLC and ESI+ MS

Each complex was evaluated using HPLC and MS to further confirm their purity. The HPLC method utilized a reverse-phase silica column and a gradient of 98% → 5% A; A = 0.1% formic acid in H_2O, B = 0.1% formic acid in MeCN, and was adopted from previously reported examples,[2–4] In general, the complexes eluted between 20–24 minutes. The purity of the complexes was determined to be at least 98% by integration.

The complexes were evaluated by ESI^{+}-MS via direct injection (Figure S8–Figure S14. In every case, the observed ions shown signature isotopic distributions corresponding to a +2 charged Ru(II) species, where the Cl^{-} counteranions have dissociated, but otherwise the complex was left intact. **Ru-1T**–**Ru-4T** shown a +1 charged peak, which is due to loss of a proton from a nitrogen on the imidazole unit.

Lipophilicity Determination

To determine the lipophilicity (or distribution coefficient, D) of the compounds, an in-house modified "shake-flask" method was employed at pH 7.4.[5] Saturated 1-octanol solution was prepared by mixing 1-octanol with 10 mM phosphate buffer (pH 7.4) in a ratio of 4:1. Similarly, a saturated phosphate buffer solution was prepared by mixing 10 mM phosphate buffer with 1-octanol in the same ratio. These solutions were vigorously shaken at 300 rpm for 24 hours at room temperature using a VWR vortex mixer to achieve saturation. Excess solvent from saturation was removed from both solutions using pipette before further use. For the lipophilicity determination, a 50 μM solution of chloride salt of each compound was prepared in saturated 1-octanol or saturated phosphate buffer (500 μL), then an equal volume (500 μL) of the other saturated solvent was added to the solution, resulting in a final volume of 1 mL. The mixture was then shaken 200 times then centrifuged at 11,000 rpm (~10,000x g) for 2 minutes using a BioRad Model 16K Microcentrifuge, which allowed for separation of the 1-octanol and phosphate buffer layers. The layers were then separated using a syringe, and the amount of the compound in each layer was measured by utilizing the standard curve specific to the compound and solvent. Absorbance measurements were taken at the characteristic longest wavelength peak for each compound using a SpectraMax M2e plate reader.

3.9.2 Spectroscopy

Spectroscopic characterization was undertaken with dilute (5–20 μM) solutions of the complexes as PF_6^- salts in spectroscopic grade MeCN.

UV-visible spectroscopy

Steady state ultraviolet visible near-infrared absorption spectra were measured at room temperature on a Jasco v730 dual beam spectrophotometer with 5 mm pathlength cuvettes. Molar extinction coefficients (ε) were determined at selected peak maxima by regressing the absorption at five different concentrations.

Singlet oxygen quantum yield

The quantum yields of singlet oxygen sensitization (Φ_Δ) were calculated from the steady state intensity of the $^1O_2$ emission band near 1276 nm. This signal was measured on a PTI

Quantamaster emission spectrometer with a 1000 nm long pass filter and a Hamamatsu R5509-42 near-infrared photomultiplier tube detector that was cooled to −80 °C. The instrument internally corrected for any wavelength-dependent nonlinearity in the lamp and detector. The Φ_Δ values were calculated using a relative actinometric formula (Equation S1), where 'I' denotes the integrated emission intensity, 'A' is the absorbance of the UV-vis spectrum at the excitation wavelength, 'η' is the refractive index of the solvent. The symbols 'A_S' and 'I_S' represent the absorbance and refractive index corresponding with the standard, which was $[Ru(bpy)_3](PF_6)_2$ (Φ_Δ=0.56 in aerated MeCN).[6] All measurements were conducted using solutions of the PF_6^- salts of the complexes in air-saturated MeCN.

$$\Phi_\Delta = \Phi_{\Delta,S}\left(\frac{I}{I_S}\right)\left(\frac{A_S}{A}\right)\left(\frac{\eta^2}{\eta_S^2}\right)$$ Equation S1

Steady-state emission

Steady-state emission spectra were measured on a PTI Quantamaster spectrometer with a K170B PMT (max ≈800 nm). Any wavelength-dependent nonlinearity in lamp output and detector sensitivity was corrected internally by the instrument. Suitable long pass filters were employed to minimize artifacts caused by harmonics and scatter. The most intense and longest-wavelength peak in the excitation spectrum was selected for the excitation wavelength (λ_{ex}). Room temperature emission of the new complexes was measured from a solution of spectroscopy-grade MeCN that had been degassed with five free-pump-thaw cycles in a custom Schlenk-style cuvette. Emission at 77K was measured in a 4:1 EtOH:MeOH glass held in a 5 mm NMR tube immersed in liquid nitrogen in a custom apparatus. The quantum yields for emission (Φ_{em}) were calculated using a relative actinometric formula (Equation S2), where 'I' denotes the integrated emission intensity, 'A' is the absorbance of the UV-vis spectrum at the excitation wavelength, 'η' is the refractive index of the solvent. The symbols 'A_S' and 'I_S' represent the absorbance and refractive index corresponding with the standard, which was $[Ru(bpy)_3](PF_6)_2$ (Φ_{em}=0.018 in MeCN left in air,[6] 0.4 in EtOH:MeOH[7] glass).

$$\Phi_{\mathrm{em}} = \Phi_{\mathrm{em},S}\left(\frac{I}{I_S}\right)\left(\frac{A_S}{A}\right)\left(\frac{\eta^2}{\eta_S^2}\right) \qquad \text{Equation S2}$$

Transient Absorption spectroscopy

Transient absorption (TA) lifetimes and differential excited state absorption (ESA) spectra were measured on an Edinburgh Instruments LP-980 spectrometer equipped with the PMT-LP detector. A Continuum Minilite Nd:YAG laser generated 355 or 532 nm excitation pulses (≈5 ns pulse width, ≈7–9 mJ per pulse). Sample solutions were prepared in a custom Schlenk-style cuvettes in spectroscopy-grade MeCN that had been degassed with five free-pump-thaw cycles. The ESA spectra were recorded at 10 nm intervals, and single wavelength TA lifetime measurements were optimized for maximum detector response. Emission lifetimes were also measured with this configuration, less the probe beam.

3.9.3 Photobiology

Following our previous work,[2–4] resazurin-based assays were used to determine the in vitro cytotoxicity and photocytotoxicity of the complexes in this series against normoxic and hypoxic male human melanoma cells (SK-MEL-28, ATCC HTB-72).

Cell culture

The nonpigmented male human melanoma cells (SK-MEL-28, ATCC HTB-72) were cultivated and maintained in EMEM (BioWhittaker, 12-125Q) was used as the basal medium, which was supplemented with 10% FB essence (VWR, 10803-034), 1% glutagro (L-alanyl-L-glutamine; VWR 45001-086), 1% sodium pyruvate (ThermoFisher, 11360070) and 1% NEAA (ThermoFisher, 11140050). The cells were incubated using a water-jacketed incubator (ThermoFisher, Thermo Scientific 4110) at a temperature of 37°C, with humidity levels above or equal to 90%, and a CO_2 concentration of 5%. To initiate each passage, split ratios from 1:2–1:5 were employed to achieve a cell density of 150,000–400,000 cells per milliliter. The cells were utilized within 15 passages from the time of purchase. For photobiological assays, the SK-MEL-28 cells were seeded into 384-well plates with a seeding density of 3000 cells per well.

For the cultivation and screening of male lung carcinoma cells (A549, ATCC CCL-185), EMEM (BioWhittaker, 12-125Q) was used as the basal medium, which was supplemented with 10% FB essence (VWR, 10803-034) and 1% glutagro (L-alanyl-L-glutamine; VWR 45001-086). The cells were incubated using a water-jacketed incubator (ThermoFisher, Thermo Scientific 4110) at a temperature of 37°C, ≥90% humidity, and 5% CO_2. To initiate each passage, split ratios from 1:4–1:6 were employed to achieve a cell density of 150,000–400,000 cells mL^{-1}. The cells were utilized within 15 passages from the time of purchase. The A549 cells were seeded into 384-well plates for cytotoxicity screening with a seeding density of 4,500 cells per well.

Cellular assays

We assessed the photobiological effectiveness of each compound by conducting dose-response cell viability assays on 384-well plates. Concentrations ranging from 1×10^{-3} to 300 µM were used for all compounds, while a broader concentration range of 1×10^{-12} to 300 µM was utilized for **Ru-4T** due to its higher phototoxicity. To ensure quick heat exchange, the well plates were stacked only two plates high in the incubator, irrespective of the experimental conditions. To evaluate the reproducibility between assays, we performed additional assessments of **Ru-3T** and **Ru-4T**.

Ru(II) compound solutions

Stock solutions of **Ru-4T** were prepared at concentrations of 21 mM and 25 mM in 100% DMSO. As for the other compounds, stock solutions were prepared at a concentration of 5 mM in a 10% v/v DMSO:water mixture. Dilutions were then prepared in a serial manner using 1x Dulbecco's Phosphate-Buffered Saline (DPBS) without Ca^{2+} or Mg^{2+}, which was obtained by diluting 10x DPBS (Corning 20-031-CV). The highest concentration (300 µM) of the diluted solutions contained less than 1.2% v/v DMSO. Glass vials with PTFE-lined caps were utilized to store the stock solutions, and these vials were wrapped in aluminum foil to shield them from light. When not in use, all stock solutions were kept at −20°C while wrapped in foil.

Cytotoxicity and photocytotoxicity

In accordance with our recent examples, the compounds were subjected to (photo)cytotoxicity screening using a resazurin assay in a 384-well plate format. Greiner Bio-One 384-well plates

(781182) were used for this purpose. In the biosafety cabinet, DPBS was added to the outermost two wells (a total of 144 wells) at a volume of 75 µL per well, forming a perimeter. An electronic multichannel pipettor was employed for the experimental setup. The total volume for all inner wells, including sample wells, positive control wells, and negative control wells, was 40 µL per well. The sample wells consisted of 10 µL of complete media, 20 µL of cell slurry (3000 SK-MEL-28 cells per well, 4500 A549 cells per well), and 10 µL of compound dilutions in DPBS. The positive control wells (12 in total) were prepared with 10 µL of complete media, 20 µL of cell slurry (3000 cells per well), and 10 µL of DPBS. The negative control wells (12 in total) consisted of 30 µL of complete media and 10 µL of DPBS. Before seeding the cells, the well plates were preincubated with dispensed media at a temperature of 37°C, 5% CO_2, and a relative humidity of at least 90%. After cell seeding, the plates were gently mixed by tilting them up, down, left, and right, and then placed in the incubator for 2–3 hours to facilitate cell attachment.

During the incubation period, we prepared serial dilutions of the compounds in sterile 384-well plates using DPBS as the solvent. For all compounds, dilutions were prepared across nine concentrations ranging from 1×10^{-3} to 300 µM. In addition, for **Ru-4T**, an extra set of nine concentrations ranging from 1×10^{-12} to 1×10^{-3} µM was included. To minimize exposure to light and prevent premature activation in cells, the lights in the biosafety cabinet were kept off during the dilution preparation. The 384-well plates, along with their lids, were incubated for 2–3 hours before the compound dilutions were dispensed at a volume of 10 µL per well. Replicates (triplicates) were dispensed in a row-wise manner with a spacing of every four rows.

The 384-well plates were incubated overnight, with a drug-to-light interval (DLI) ranging from 13 to 20 hours. Following the incubation, light treatments were administered. The light treatment consisted of delivering approximately 100 J cm^{-2} of light at an intensity of 18–24 mW cm^{-2}. The light used included cool white Visible light (400–700 nm), Blue light (Prizmatix LED, 453 nm), Green light (Prizmatix LED, 523 nm), and red light (Prizmatix LED, 633 nm). After the light treatments, the plates were further incubated for 1 day before the final viability measurements were taken. It is worth noting that edge effects were observed on the 384-well plate, which led to the adjustment of the post-photodynamic therapy (PDT) period to one day (20–23 hours) to allow for cell viability equilibration, instead of the standard 48-hour period. Prewarmed sterifiltered resazurin in 0.2 M phosphate buffer (pH = 7.4) at a concentration of 0.3 mM was dispensed into all wells of the plates, with a volume of 10 µL per well. The resazurin-dyed plates were then incubated for 4 hours before fluorometric measurements were taken using a Molecular Devices M2e plate reader. The measurements were conducted with a 30-second shaking step, a bottom-read configuration, an excitation wavelength of 530 nm, a long-pass filter at 570 nm, and an emission wavelength of 620 nm.

Hypoxia cytotoxicity and photocytotoxicity

The screening of the compounds was conducted simultaneously under two different oxygen conditions: normoxia (approximately 18.5% O_2) and hypoxia (1% O_2). For the plates treated with hypoxia, the cells were allowed to incubate for 1–2 hours at 37°C, 5% CO_2, and a relative humidity of at least 90% under normoxia to promote adhesion after seeding. Subsequently, the plates were transferred to a Biospherix Xvivo X3 chamber and incubated for an additional 2–3 hours at 1% O_2, 37°C, 5% CO_2, and a relative humidity of at least 90% before the compound dilutions were dispensed in the biosafety cabinet. The plates were then placed back into the Biospherix chamber and incubated for a DLI of 17–19 hours. To confirm the hypoxic condition, the dissolved oxygen level inside the Biospherix chamber was measured using an immersive optical probe, with a range of 5–7 µM. Following confirmation, the hypoxic-treated plates designated for light treatment were sealed inside the Biospherix chamber using low-gas permeable and highly transparent qPCR films (VWR, 89134-428) to maintain the hypoxic conditions during the light treatment. This step is crucial to evaluate the oxygen-dependence of the photosensitizer (PS). After the light treatment, the films were removed in a biosafety cabinet, and all the hypoxic-treated plates were transferred to a normoxia incubator (37°C, 5% CO_2, and a relative humidity of at least 90%). Like the normoxic-treated plates, the hypoxic-treated plates were incubated for an additional 20–23 hours before the final viability measurements were taken.

Dosimetry Studies

To assess the impact of irradiance on the photoactivity of **Ru-4T**, specialized dosimetry experiments were conducted. The Modulight ML8500 platform was utilized for precise well-by-well illumination, employing lasers with center wavelengths of 525 nm, 630 nm, and 753 nm. Various irradiances ranging from 10 to 100 mW cm^{-2} were applied while maintaining a constant fluence of 100 J cm^{-2}. The spectral output was captured using a Luzchem SPR fiber optic detector in conjunction with an Ocean Optics USB4000 spectrophotometer and an Ocean Optics UV-Vis XSR fiber optic with a diameter of 230 μm (see Figure S26). Irradiance levels were measured using a Thorlabs Optical Power Meter PM100D along with their corresponding thermal power sensor S310C.

Longitudinal studies

The reproducibility of the more active **Ru-3T** and **Ru-4T** complexes was tested across multiple assays using SK-MEL-28. The results of the five repeat assays can be found in Figure S29 and Table S5–S10. For each repeat assay, randomized and unique plate maps were assigned. Different types of pipet tips were utilized for each repeat: Sartorius 790352 for repeat #1, VWR 83007-352 for repeat #2–3, and low retention Sartorius LH-L790352 for repeat #4–5. This approach aimed to minimize any potential contribution from stray light. During repeat #5, the overhead lights in the laboratory space were turned off to further reduce the impact of stray light on the assay results. All cells utilized in these experiments were within the range of 10–15 passages, and all assays were performed within a one-month timeframe to maintain consistency and minimize potential variations.

Light devices and protocols.

For all biological assays, unless stated otherwise, a consistent fluence of 100 J cm^{-2} and an irradiance ranging between 18–22 mW cm^{-2} were employed. The light treatments utilized three different light sources for visible, green, and red light. These sources included a cool white LED panel from SOLLA-CREE, covering a spectral range of 400–700 nm with a maximum absorption around 450 nm. Additionally, two UHP-LEDs from Prizmatix were used, emitting light at 523 nm (green) and 633 nm (red) respectively. The spectral outputs of these light sources can be referenced in Figure S26.

Data manipulation and statistics

Data from the resazurin cell viability assay were corrected for background by subtracting the signal from wells that contained only media and DPBS (no cells) and normalized relative to untreated cells. Because the absorbance and emission of the metal complexes can interfere with the resazurin fluorescence signal, wells treated with the highest concentrations of metal complex were also observed under a microscope. If no cells were detected, these wells were assigned a value of zero. A more detailed discussion of assay limitations for this class of complexes is provided in our 2019 review.[4]

Data points obtained from resazurin fluorescence were fit to a three-parameter log-logistic (Equation S3) and logistic model (Equation S4) using GraphPad Prism 8.4.0. We use Equation S3 for summary log(EC_{50}) plots (Figure 12a) and in the dose-response curves shown in Figure 13, but we use Equation S4 for data in log(PI) plots (Figure 12b) as well as the tabulated EC_{50} and PI values (Table S5–S10).

$$Y = \mathrm{Bottom} + \frac{(Top - Bottom)}{(1 + (10^{Log(EC_{50} - X) \times Hillslope})} \qquad \text{Equation S3}$$

$$Y = \mathrm{Bottom} + \frac{(Top - Bottom)}{\left(1 + (EC_{50}/X)^{Hillslope}\right)}$$

Equation S4

Experiments were completed in triplicate and replicated data points are always plotted with error bars denoting the standard deviation (SD). All EC_{50} values are reported alongside the standard error of the mean (SEM). In cases where the hill slope was too steep to calculate a representative SEM, the SEM was labelled as not determined (n.d.). Phototherapeutic indices (PI) are reported as the ratio of dark to light EC_{50} values and serve as a phototherapeutic efficacy benchmark. Any summary plots showing Log EC_{50} and Log PI values of the entire series of complexes are plotted with SEMs from log-logistic fits.

Maximum tolerated dose in mice

To determine the maximum tolerated dose (MTD) of **Ru-3T** and **Ru-4T**, a cohort of 8-week-old female C57BL/6J mice weighing approximately 20 g each was used. The MTD evaluation was carried out via two different injection routes: intraperitoneal (IP) and intravenous (IV). For IP injections, the mice were dosed with varying concentrations of 25–200 mg kg^{-1}, with a total volume of 200 µL injected into the lower right abdominal quadrant. For IV injections, concentrations of 12.5–50 mg kg^{-1} were administered, with a total volume of 100 µL injected into the tail vein. The vehicle used for both injection routes consisted of a 10% DMSO solution in 0.9% saline. Prior to injection, compound solutions were prepared immediately and sonicated to ensure complete dissolution. Injections were delivered slowly after visually confirming compound dissolution. Following the injections, the mice were continuously monitored for a period of 2 hours, with additional frequent monitoring over 6 hours, and periodic monitoring over a span of 2 weeks. If a combination of moderately severe signs of clinical toxicity appeared, or a single severe sign appeared, or if 2 weeks had passed since the injection, the mice were euthanized. The MTD was determined as the dose that induced moderate signs of clinical toxicity.

3.9.4 Synthetic Characterization

NMR Spectra

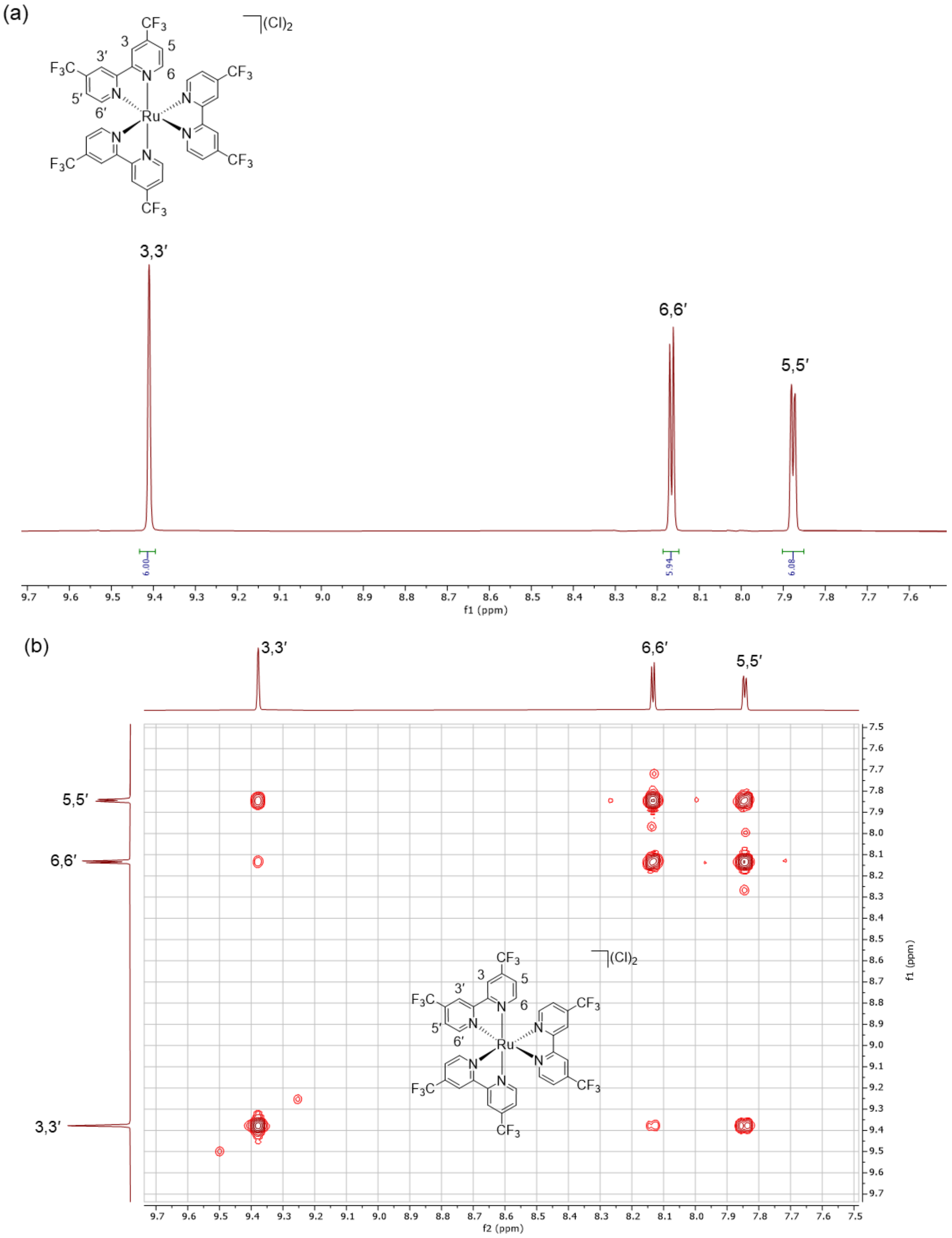

Figure S1. (a) Structure labelling and aromatic ^{1}H NMR (700MHz, 798 K) spectrum of [Ru(4,4'-btfmb)$_3$](Cl)$_2$ with assignments. (b) Aromatic ^{1}H-^{1}H COSY NMR (700MHz, 798 K) spectrum of [Ru(4,4'-btfmb)$_3$](Cl)$_2$.

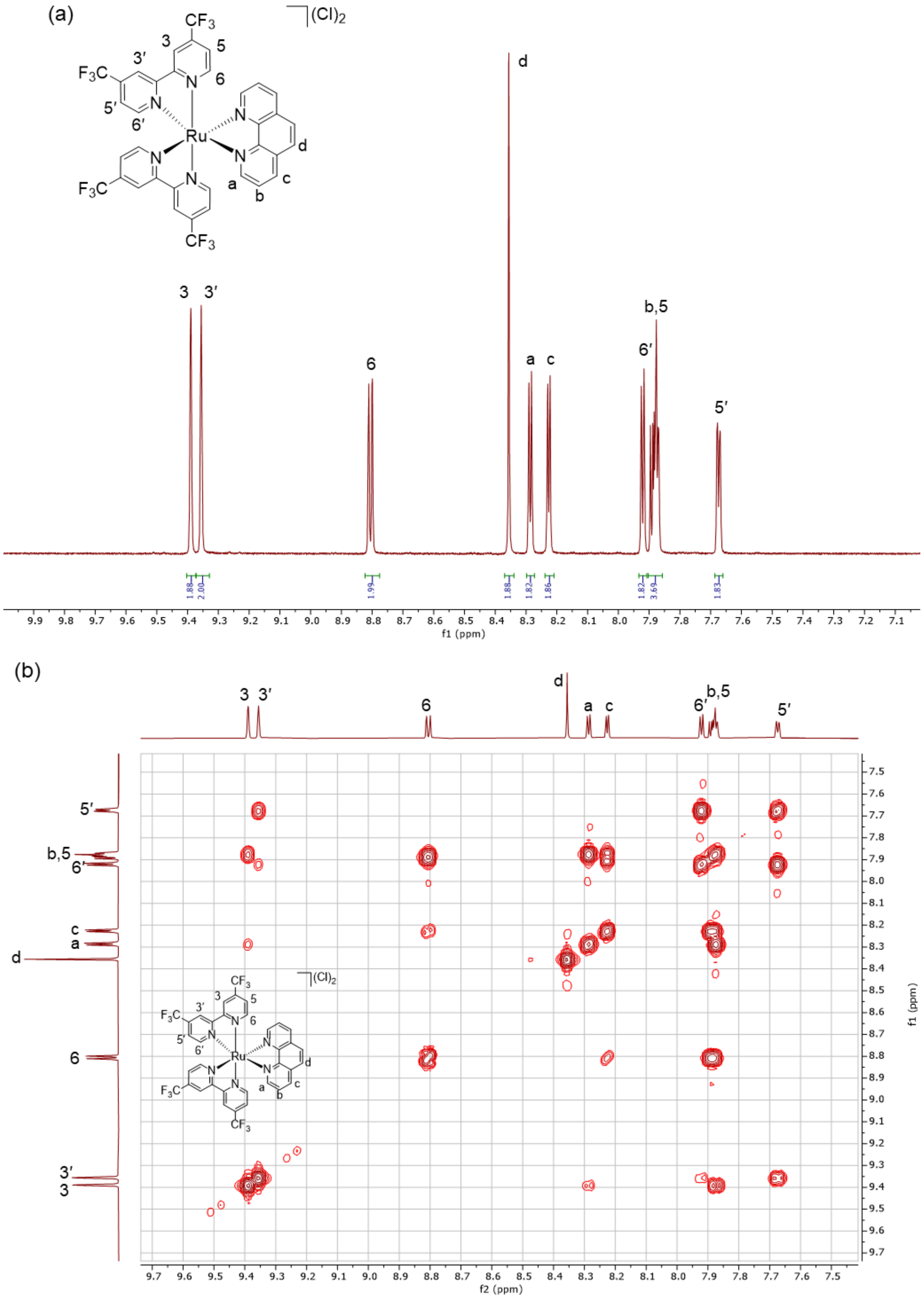

Figure S2. (a) Structure labelling and aromatic ^{1}H NMR (700MHz, 798 K) spectrum of **Ru-phen** with assignments. (b) Aromatic ^{1}H-^{1}H COSY NMR (700MHz, 798 K) assignments for **Ru-phen**.

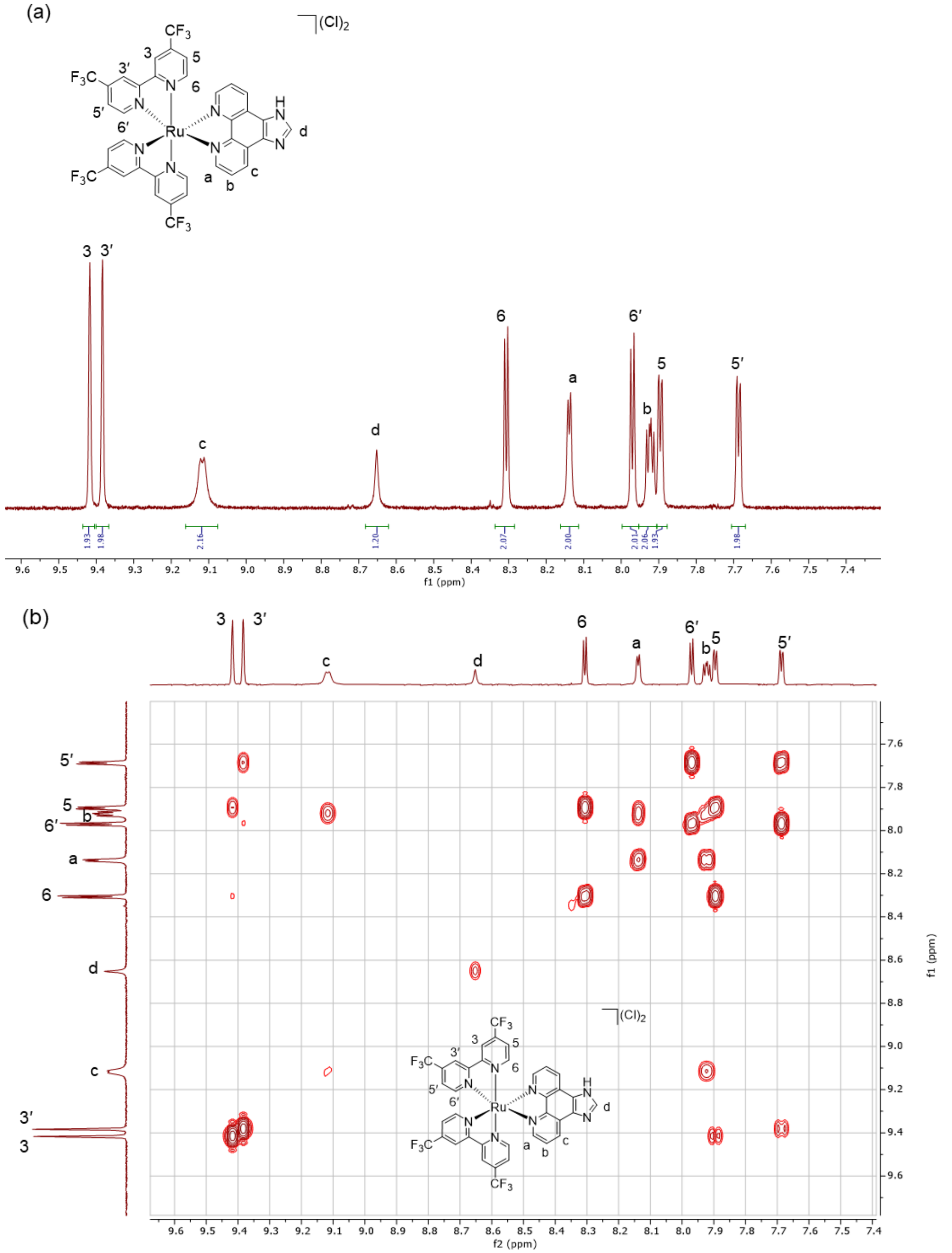

Figure S3. (a) Structure labelling and aromatic ^{1}H NMR (700MHz, 289 K) spectrum of **Ru-0T** with assignments. (b) Aromatic ^{1}H-^{1}H COSY NMR (700MHz, 798 K) assignments for **Ru-0T.**

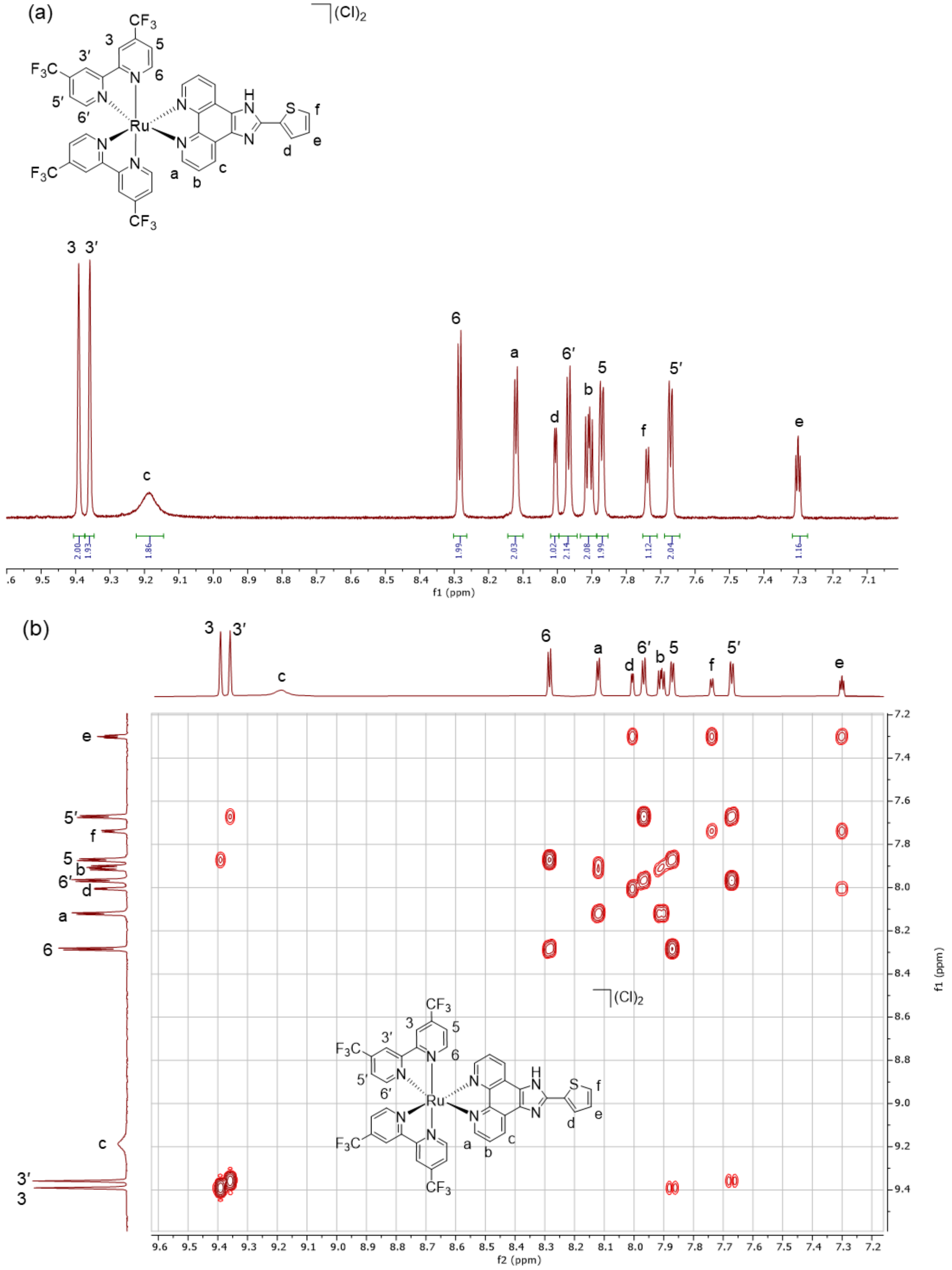

Figure S4. (a) Structure labelling and aromatic ^{1}H NMR (700MHz, 798 K) spectrum of **Ru-1T** with assignments. (b) Aromatic ^{1}H-^{1}H COSY NMR (700MHz, 798 K) assignments for **Ru-1T.**

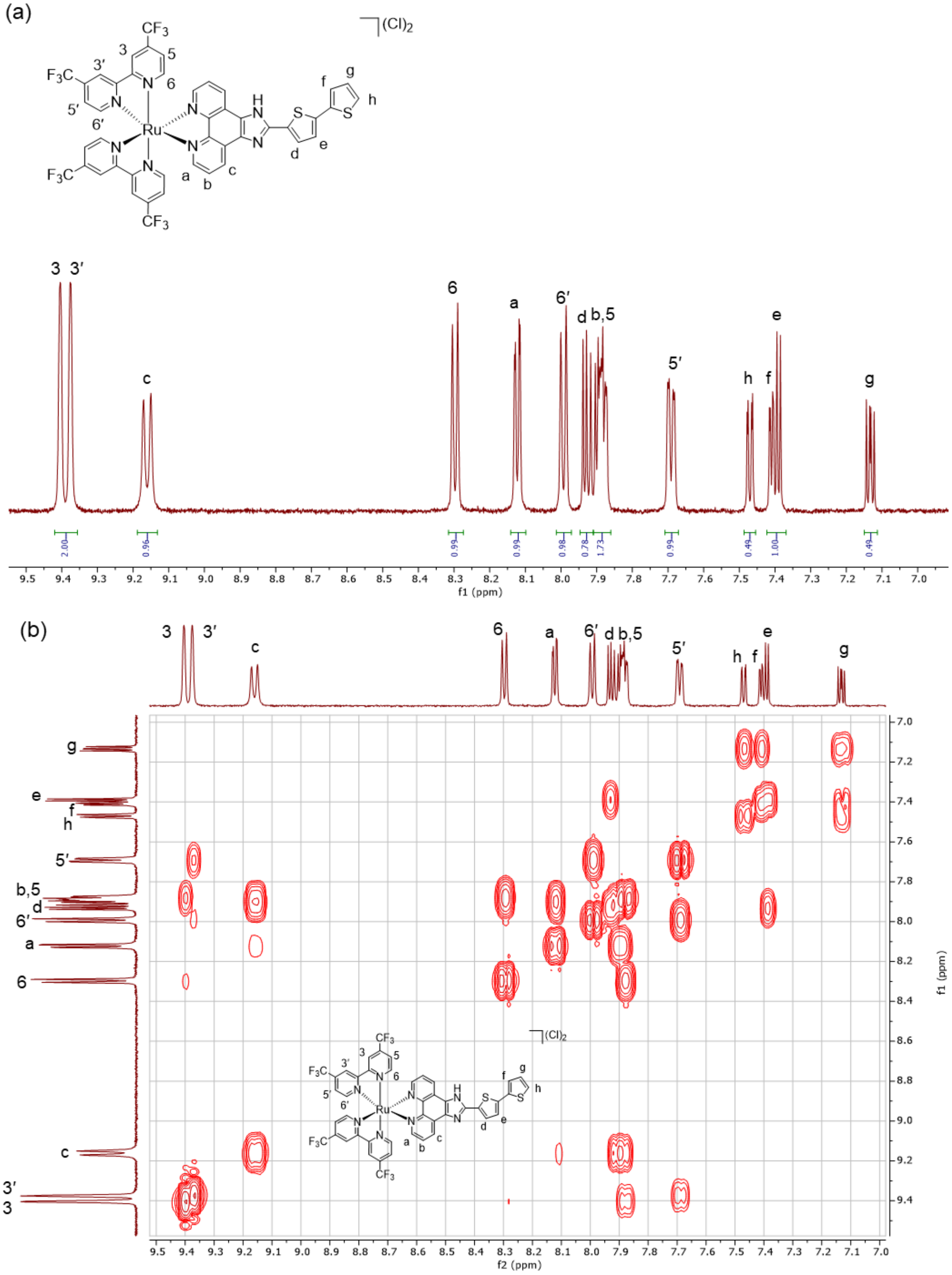

Figure S5. (a) Structure labelling and aromatic ^{1}H NMR (700MHz, 798 K) spectrum of **Ru-2T** with assignments. (b) Aromatic ^{1}H-^{1}H COSY NMR (700MHz, 798 K) assignments for **Ru-2T.**

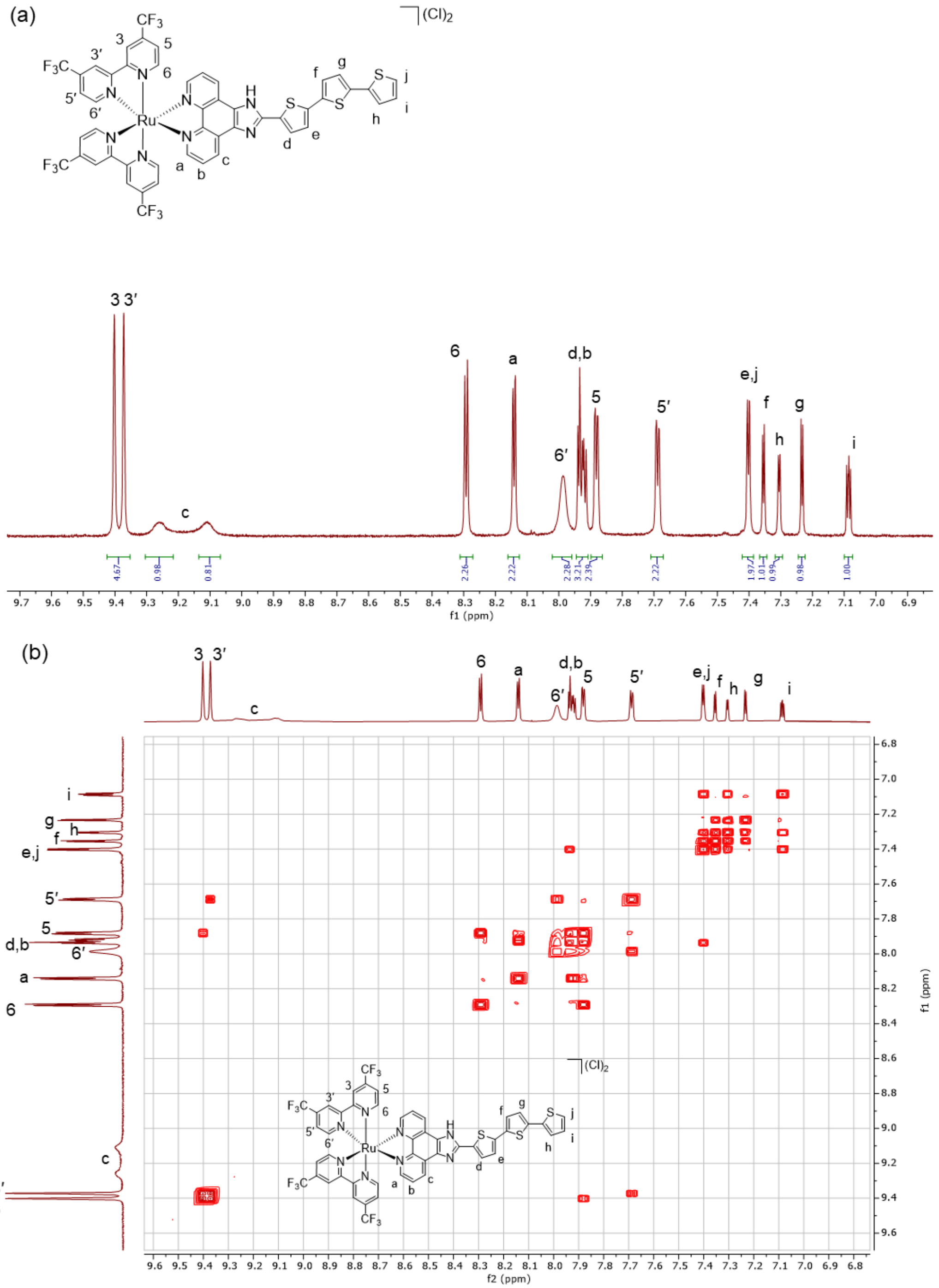

Figure S6. (a) Structure labelling and aromatic ^{1}H NMR (700MHz, 798 K) spectrum of **Ru-3T** with assignments. (b) Aromatic ^{1}H-^{1}H COSY NMR (700MHz, 798 K) assignments for **Ru-3T.**

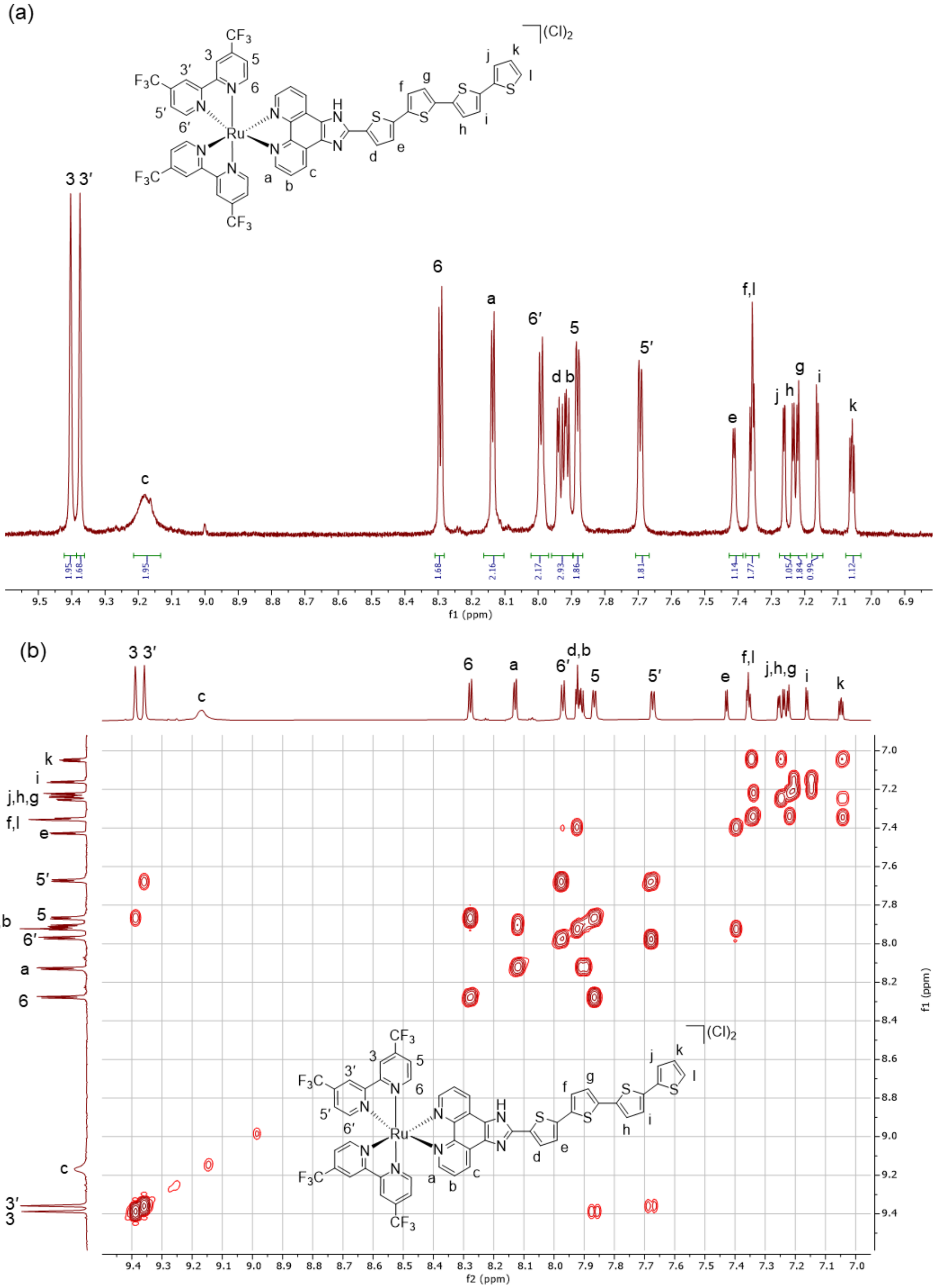

Figure S7. (a) Structure labelling and aromatic ^{1}H NMR (700MHz, 798 K) spectrum of **Ru-4T** with assignments. (b) Aromatic ^{1}H-^{1}H COSY NMR (700MHz, 798 K) assignments for **Ru-4T.**

High-Resolution Mass Spectra (HRMS-ESI+)

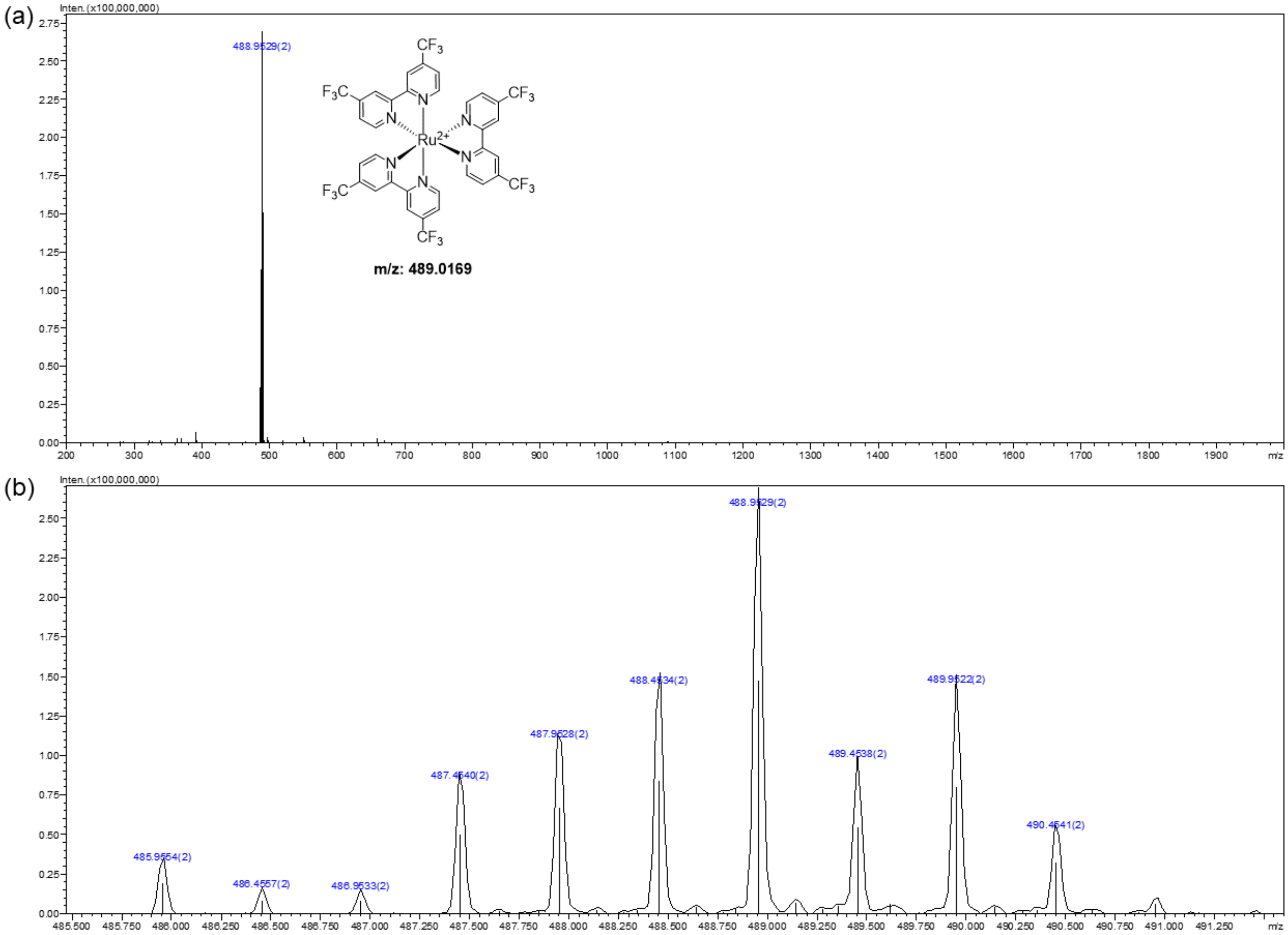

Figure S8. (a) High resolution ESI$^+$-MS spectrum for [Ru(4,4'-btfmb)$_3$](Cl)$_2$ (b) Zoom of 488.9529 m/z showing isotopic distribution.

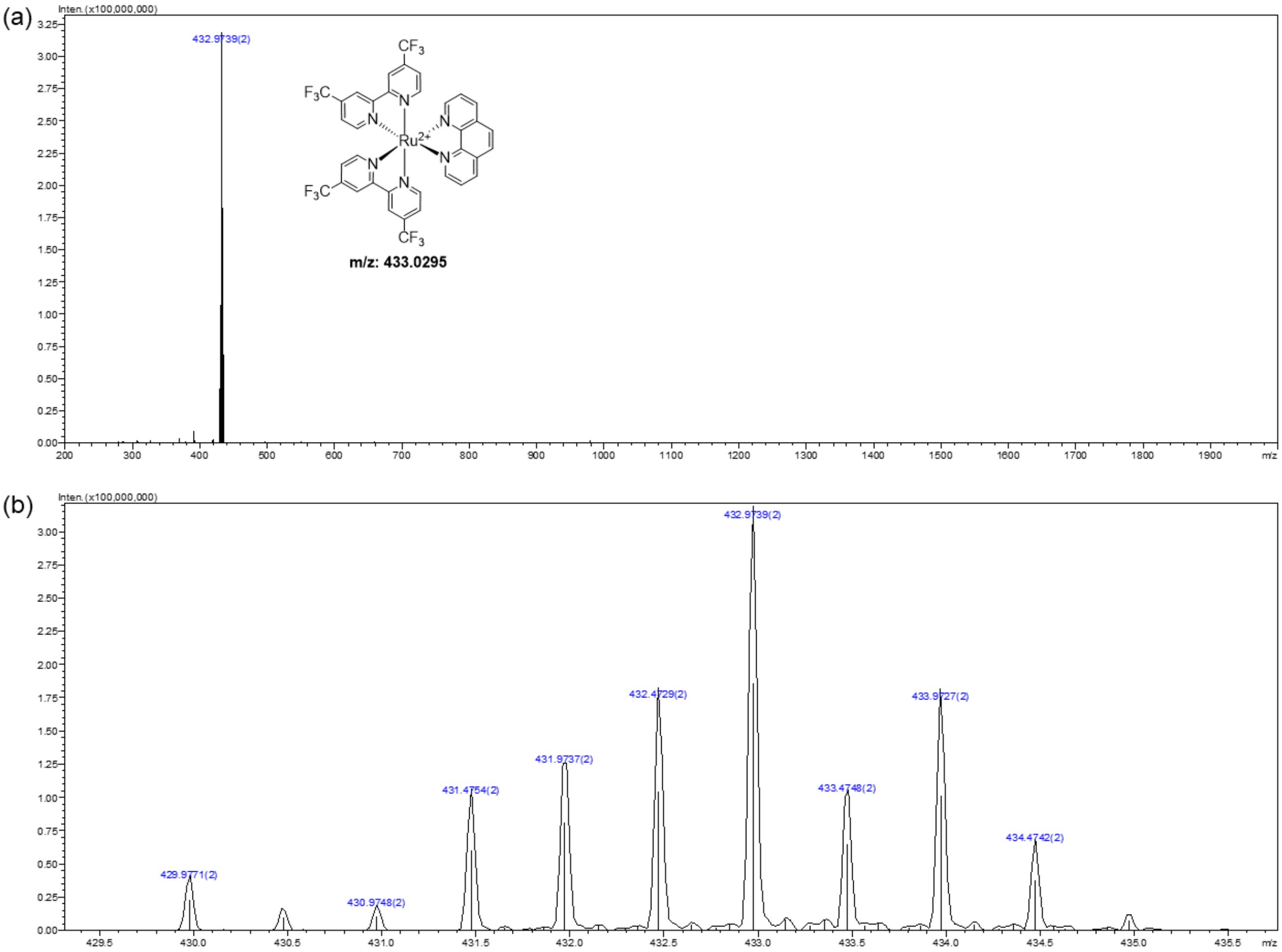

Figure S9. (a) High resolution ESI$^+$-MS spectrum for **Ru-phen** (b) Zoom of 432.9739 m/z showing isotopic distribution.

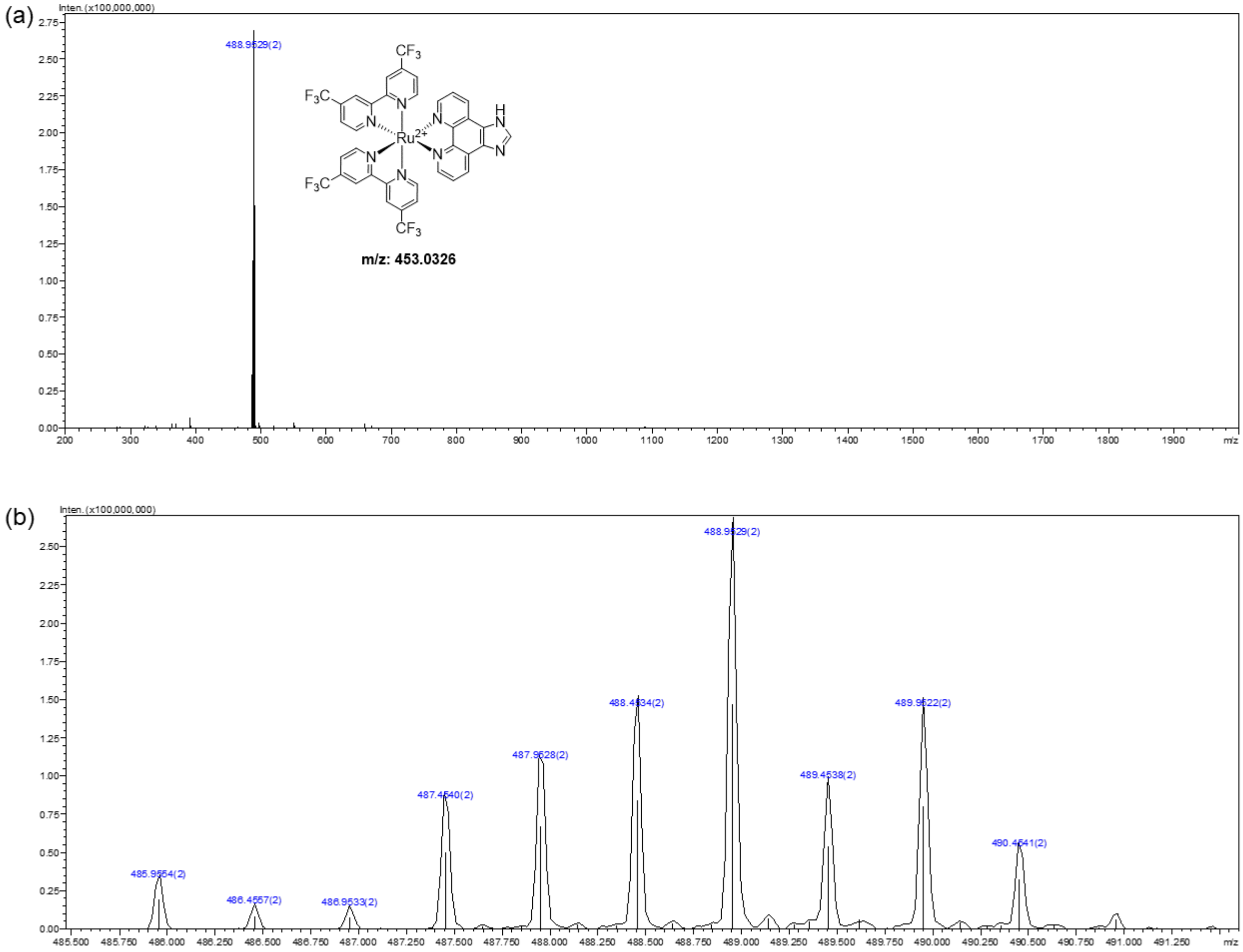

Figure S10. (a) High resolution ESI$^+$-MS spectrum for **Ru-0T** (b) Zoom of 488.9529 m/z showing isotopic distribution.

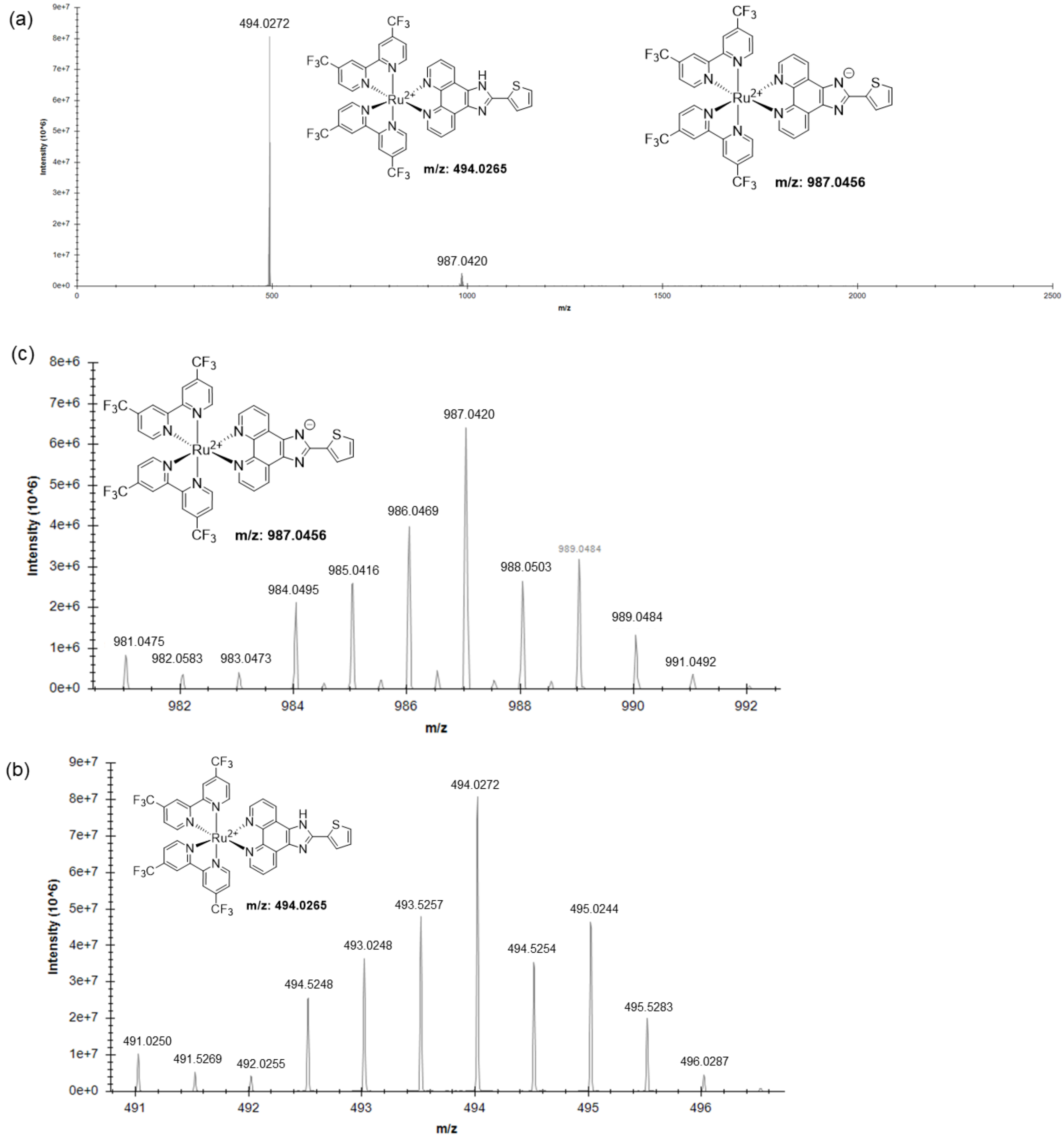

Figure S11. (a) High resolution ESI$^+$-MS spectrum for **Ru-1T**. (b) Zoom of 432.9739 m/z showing isotopic distribution. (c) Zoom of 987.0456 m/z showing isotopic distribution.

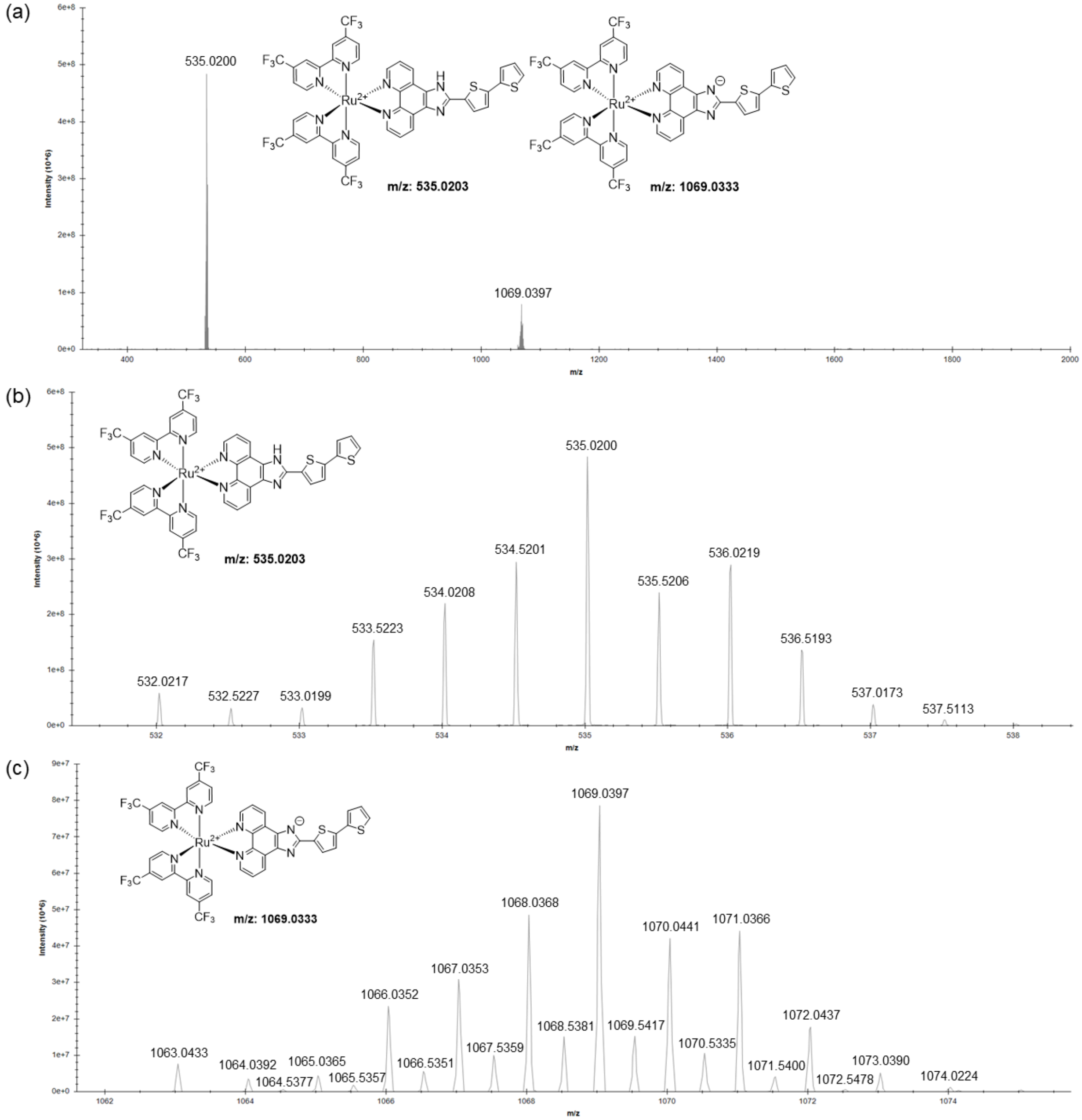

Figure S12. (a) High resolution ESI$^+$-MS spectrum for **Ru-2T** (b) Zoom of 464.0405 m/z showing isotopic distribution. (c) Zoom of 927.0769 m/z showing isotopic distribution.

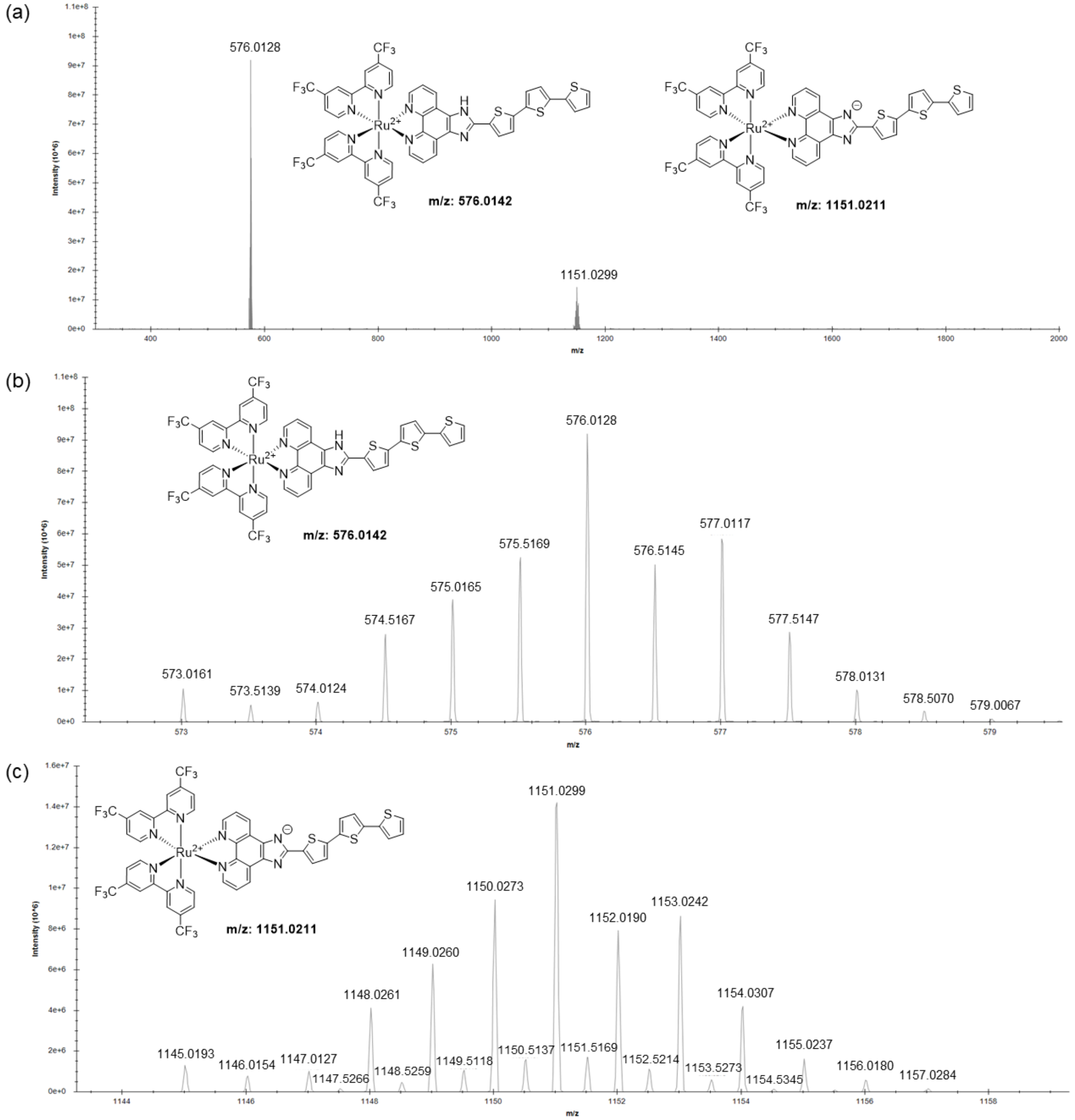

Figure S13. (a) High resolution ESI$^+$-MS spectrum for **Ru-3T** (b) Zoom of 576.0128 m/z showing isotopic distribution. (c) Zoom of 1151.0299 m/z showing isotopic distribution.

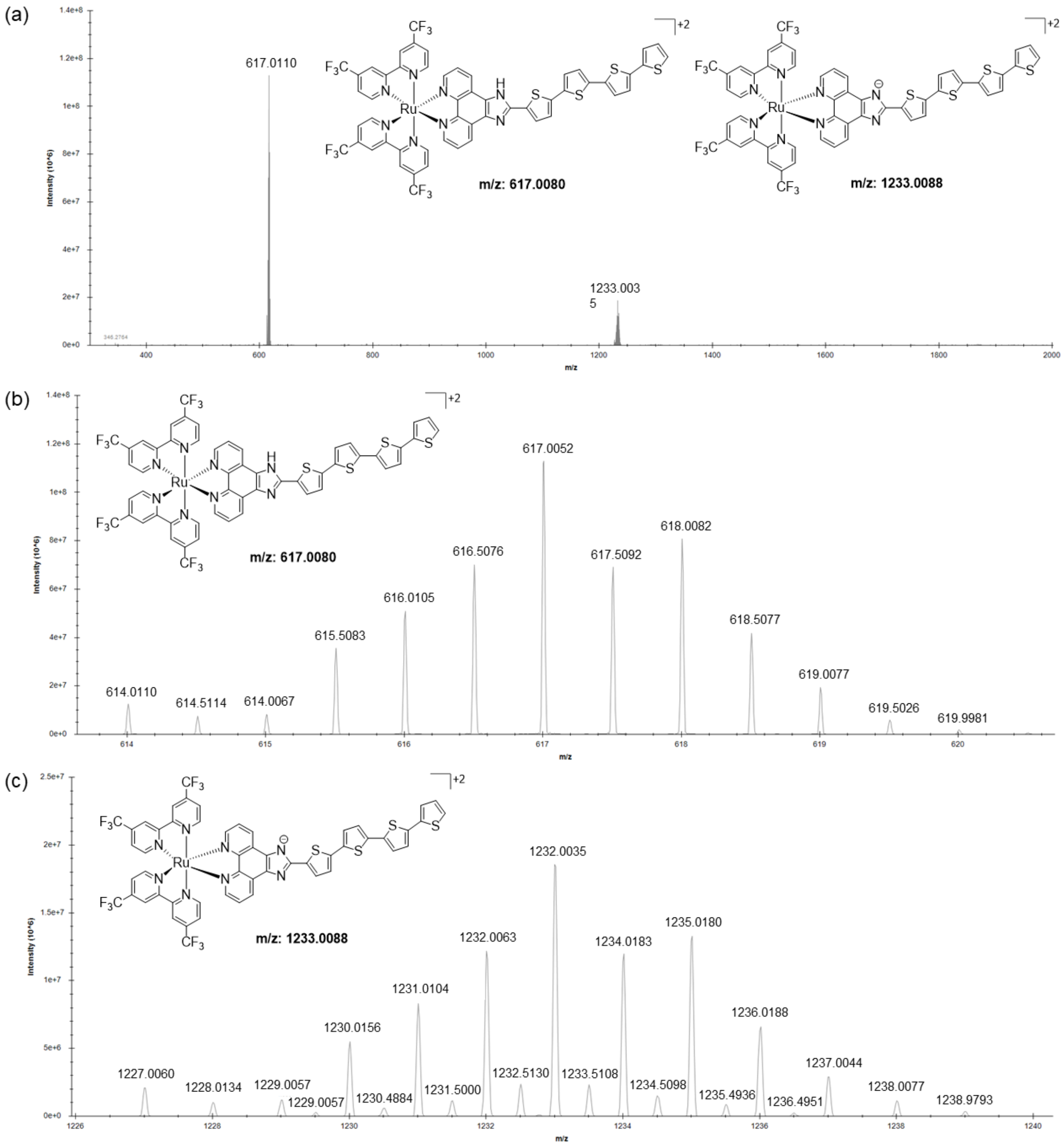

Figure S14. (a) High resolution ESI$^+$-MS spectrum for **Ru-4T** (b) Zoom of 617.0052 m/z showing isotopic distribution. (c) Zoom of 1232.0035 m/z showing isotopic distribution.

HPLC Chromatographs

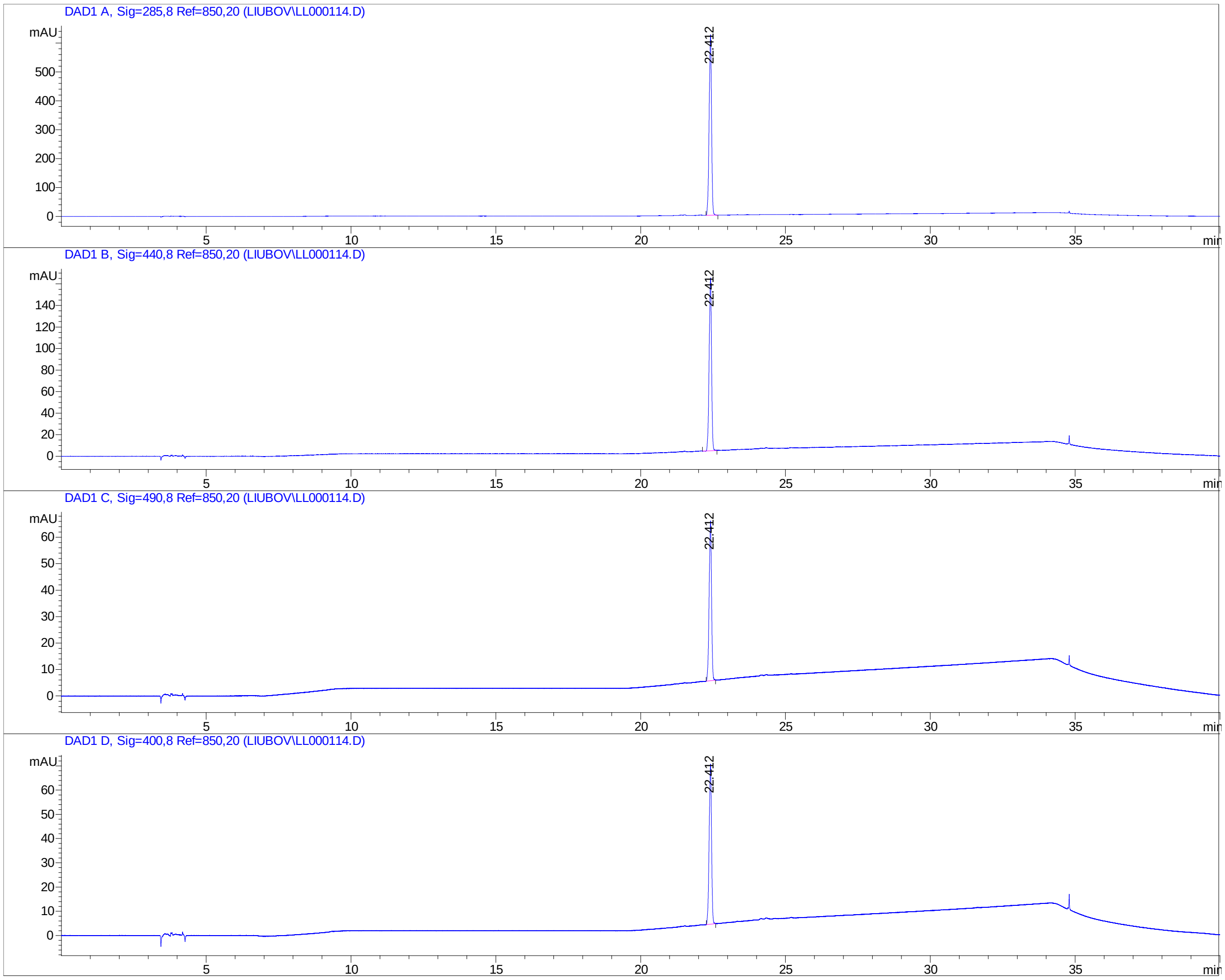

Figure S15. HPLC chromatogram for [Ru(4,4'-dtfmb)$_3$](Cl)$_2$ collected at the following wavelengths: 285, 400, 440, and 490 nm.

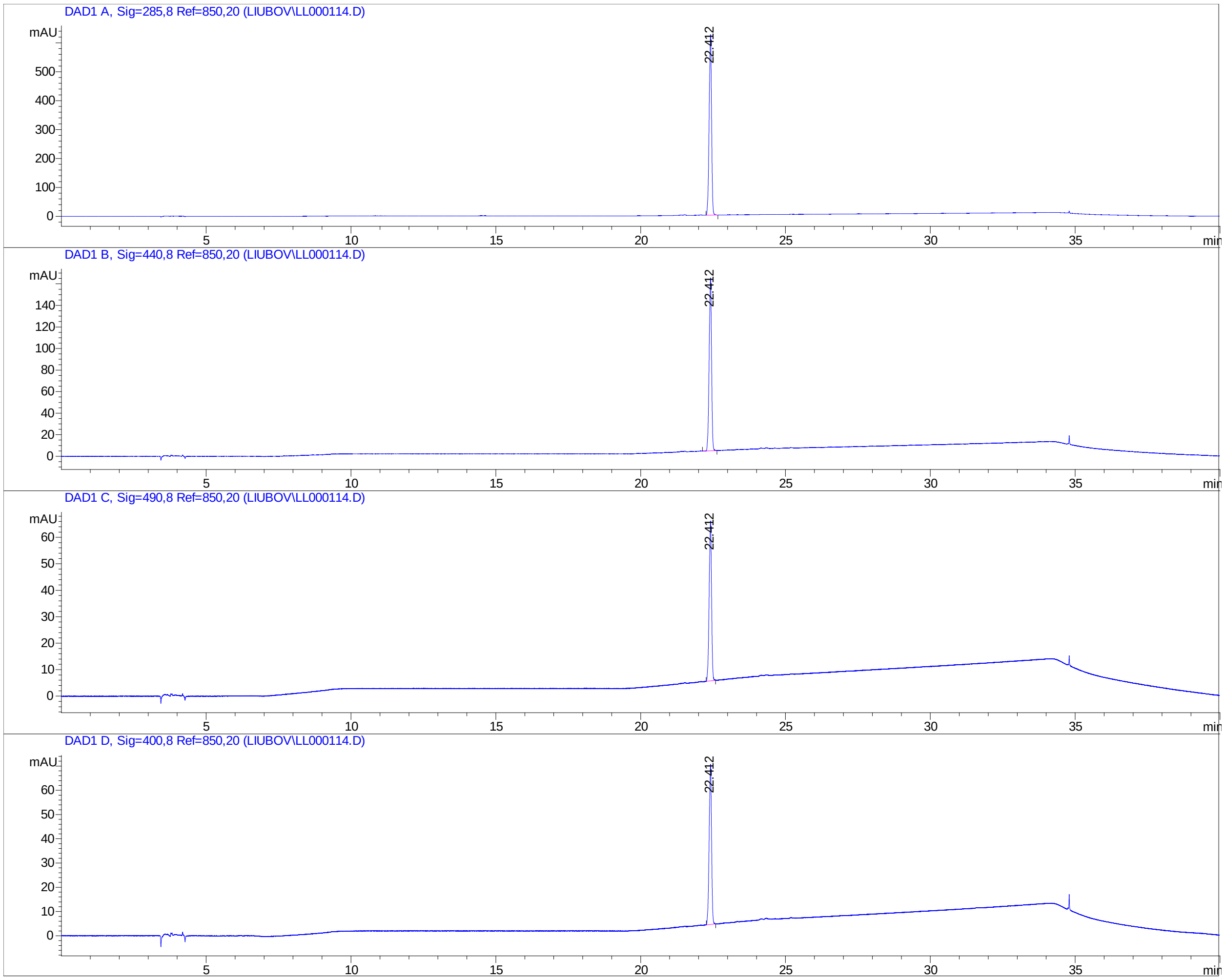

Figure S16. HPLC chromatogram for **Ru-phen** collected at the following wavelengths: 285, 400, 440, and 490 nm.

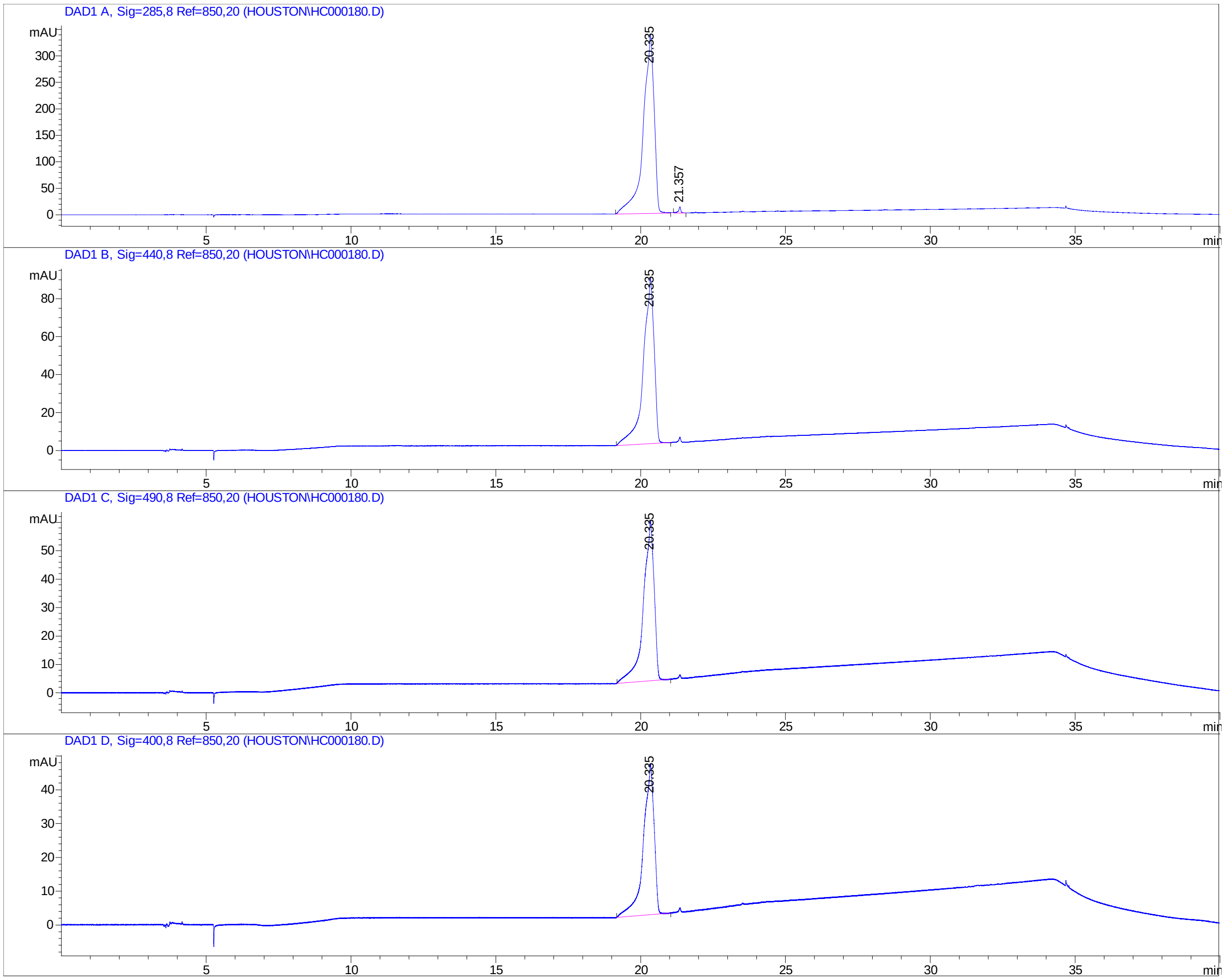

Figure S17. HPLC chromatogram for **Ru-0T** collected at the following wavelengths: 285, 400, 440, and 490 nm.

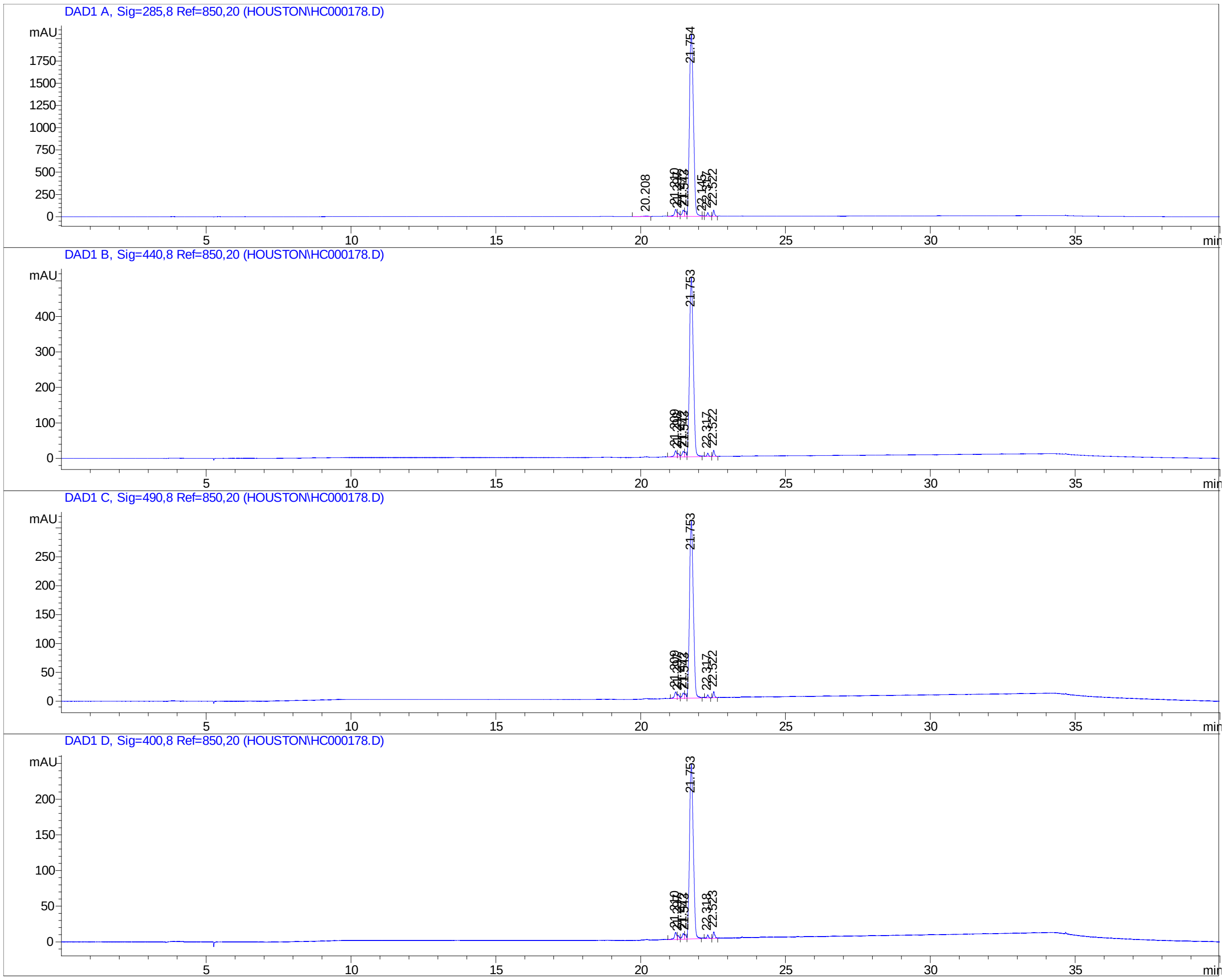

Figure S18. HPLC chromatogram for **Ru-1T** collected at the following wavelengths: 285, 400, 440, and 490 nm.

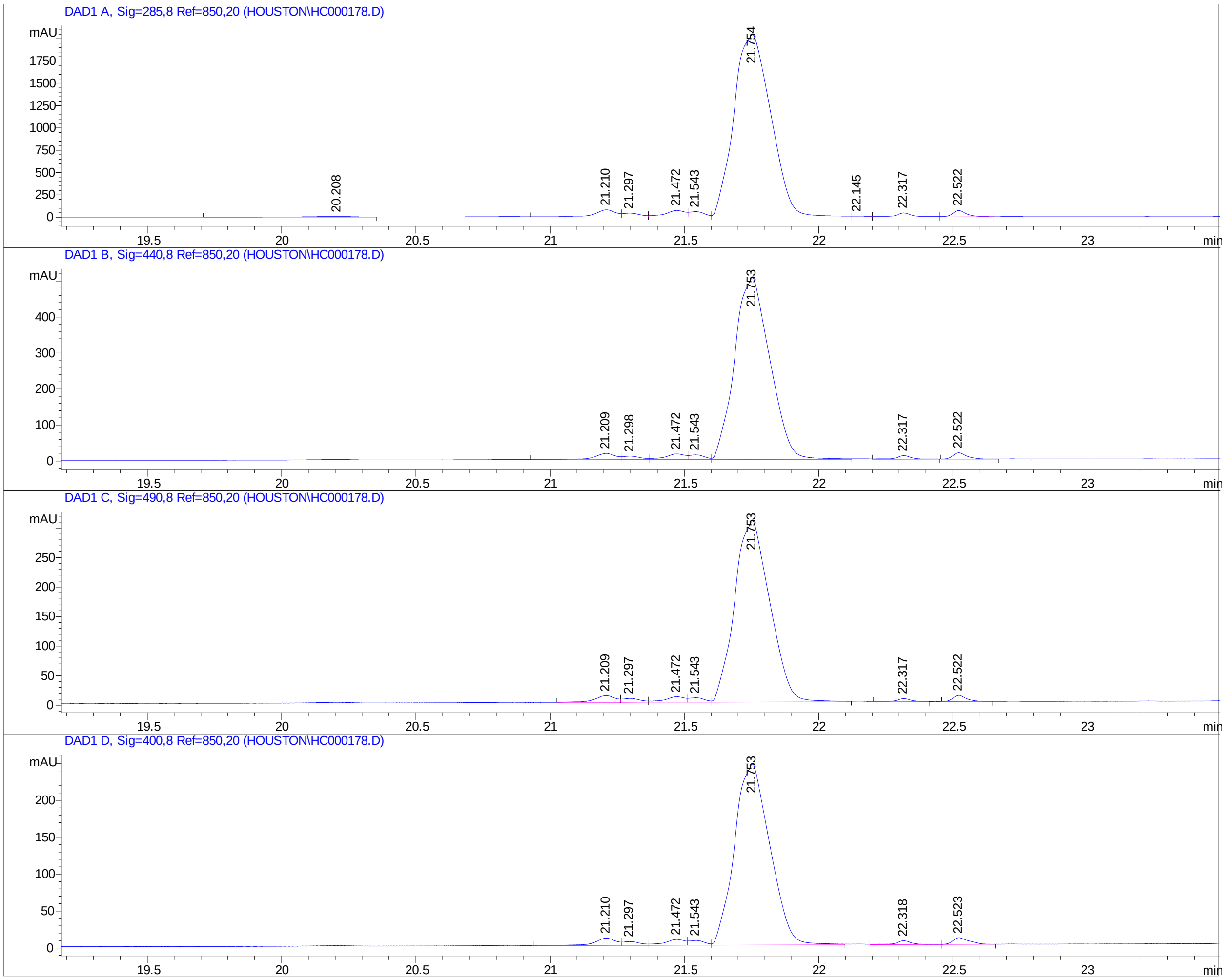

Figure S19. Zoom of HPLC chromatogram for **Ru-2T** collected at the following wavelengths: 285, 400, 440, and 490 nm.

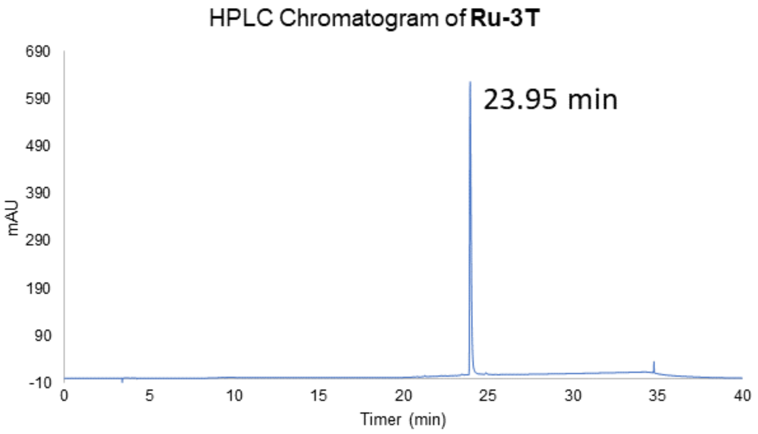

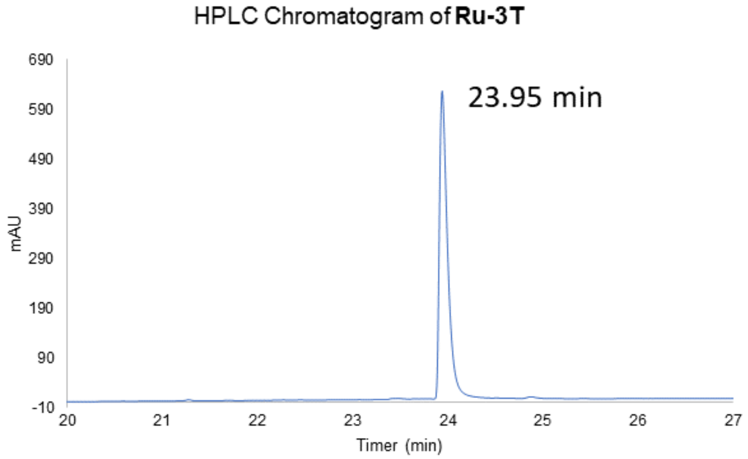

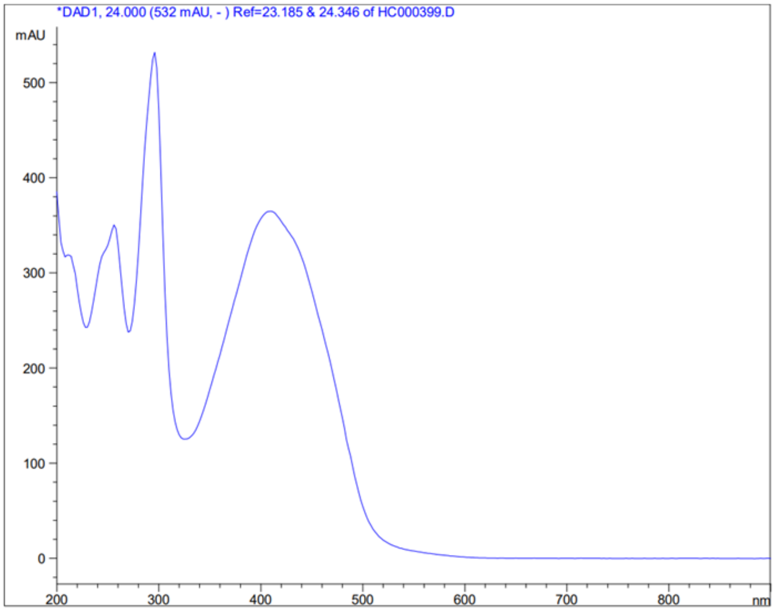

Figure S20. (top) HPLC chromatogram for **Ru-3T** collected at the following wavelengths: 285 nm. (middle) Zoom of HPLC chromatogram for **Ru-3T** collected at 285 nm. (bottom) Overlay of UV-Vis absorption spectra of HPLC Chromatogram peaks of **Ru-3T** at 285 nm.

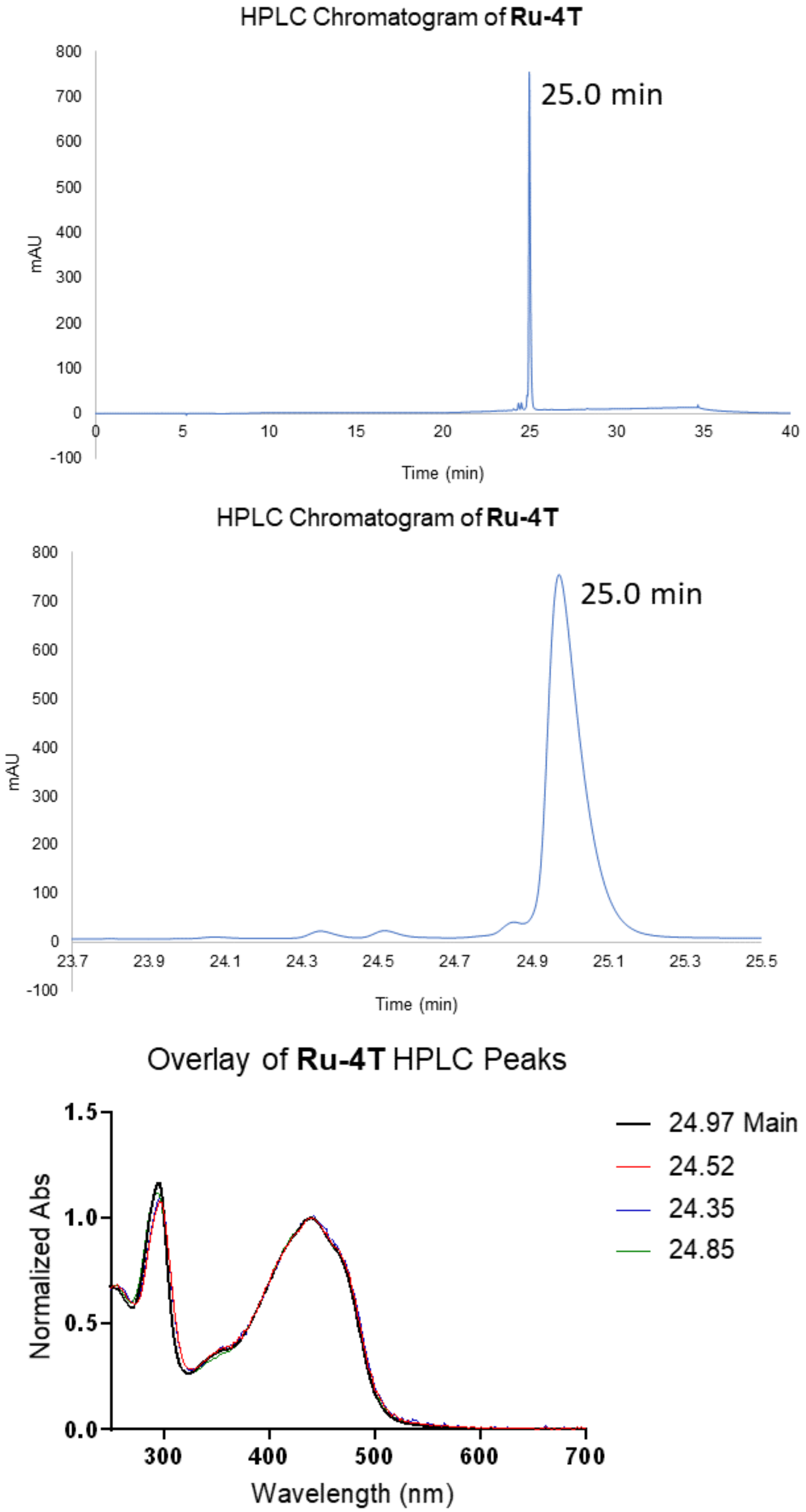

Figure S21. (a) HPLC chromatogram for **Ru-4T** collected at the following wavelengths: 285 nm. (b) Zoom of HPLC chromatogram for **Ru-4T** collected at the following wavelengths: 285 nm. (c) Overlay of UV-Vis absorption spectra of HPLC Chromatogram peaks of **Ru-4T** at 285 nm.

Table S1. Analytical HPLC method using the Hypersil GOLD C_{18} Column.

	time (min)	%MeCN	%Water
Pre-run	20	2	98
Run	0	2	98
	2	5	95
	5	30	70
	15	30	70
	20	60	40
	30	95	5
	35	2	98
	40	2	98
Post-run	10	2	98
Flow rate (mL min^{-1})	1		

Both eluents contain 0.1% optima grade formic acid with runs involving a 20 µL injection at 50–200 µM of metal complex dissolved in optima grade MeOH.

LIPOPHILICITY

Table S2. Log distribution coefficient (log $D_{o/w}$) of chloride salts of [Ru(btfmb)$_3$], **Ru-phen** and **Ru-*n*T** (*n*=0–4) in 1-octanol and 10mM phosphate buffer (pH = 7.4) using the shake-flask method.

Compound	log ($D_{o/w}$ ± SD)
[Ru(4,4'-btfmb)$_3$](Cl)$_2$	– 2.184 ± 0.071
Ru-phen	– 1.862 ± 0.080
Ru-0T	– 1.349 ± 0.026
Ru-1T	– 0.336 ± 0.037
Ru-2T	+ 1.182 ± 0.042
Ru-3T	+ 1.580 ± 0.052
Ru-4T	+ 2.172 ± 0.132

3.9.5 Spectroscopic Characterization

Singlet Oxygen Sensitization

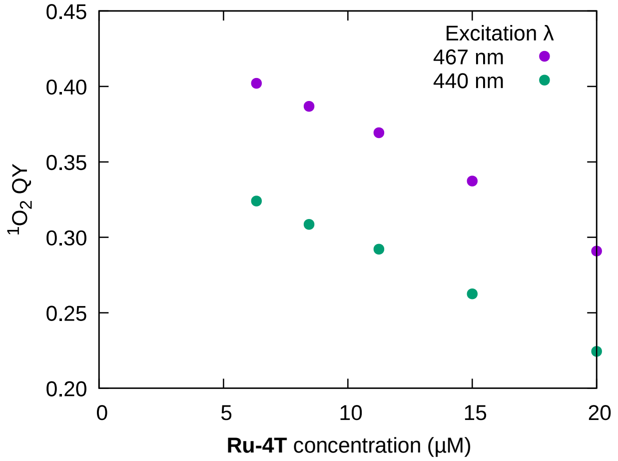

Figure S22: The dependence of $^1O_2$ quantum yield on the concentration of **Ru-4T** in acetonitrile

Table S3: Singlet oxygen sensitization quantum yield and varying concentration and excitation wavelength.

Concentration (μM)	Φ_Δ @ λ_{ex}=440 nm	Φ_Δ @ λ_{ex}=440 nm
20	0.22	0.29
15	0.26	0.34
11	0.29	0.37
8.4	0.31	0.39
6.3	0.32	0.40

Transient Absorption

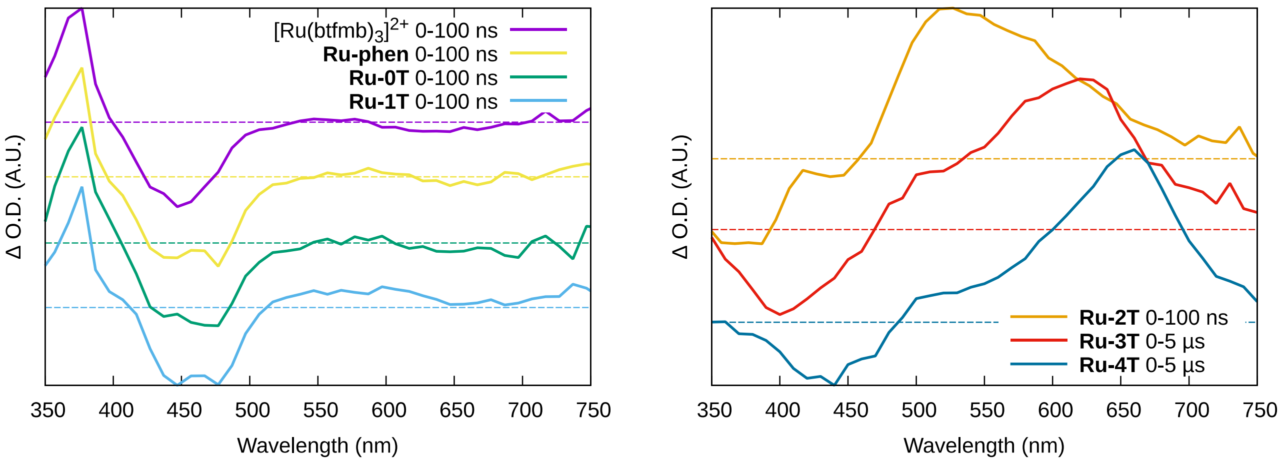

Figure S23: Differential excited state absorption profiles for the series in degassed MeCN at RT, λex=532 nm.

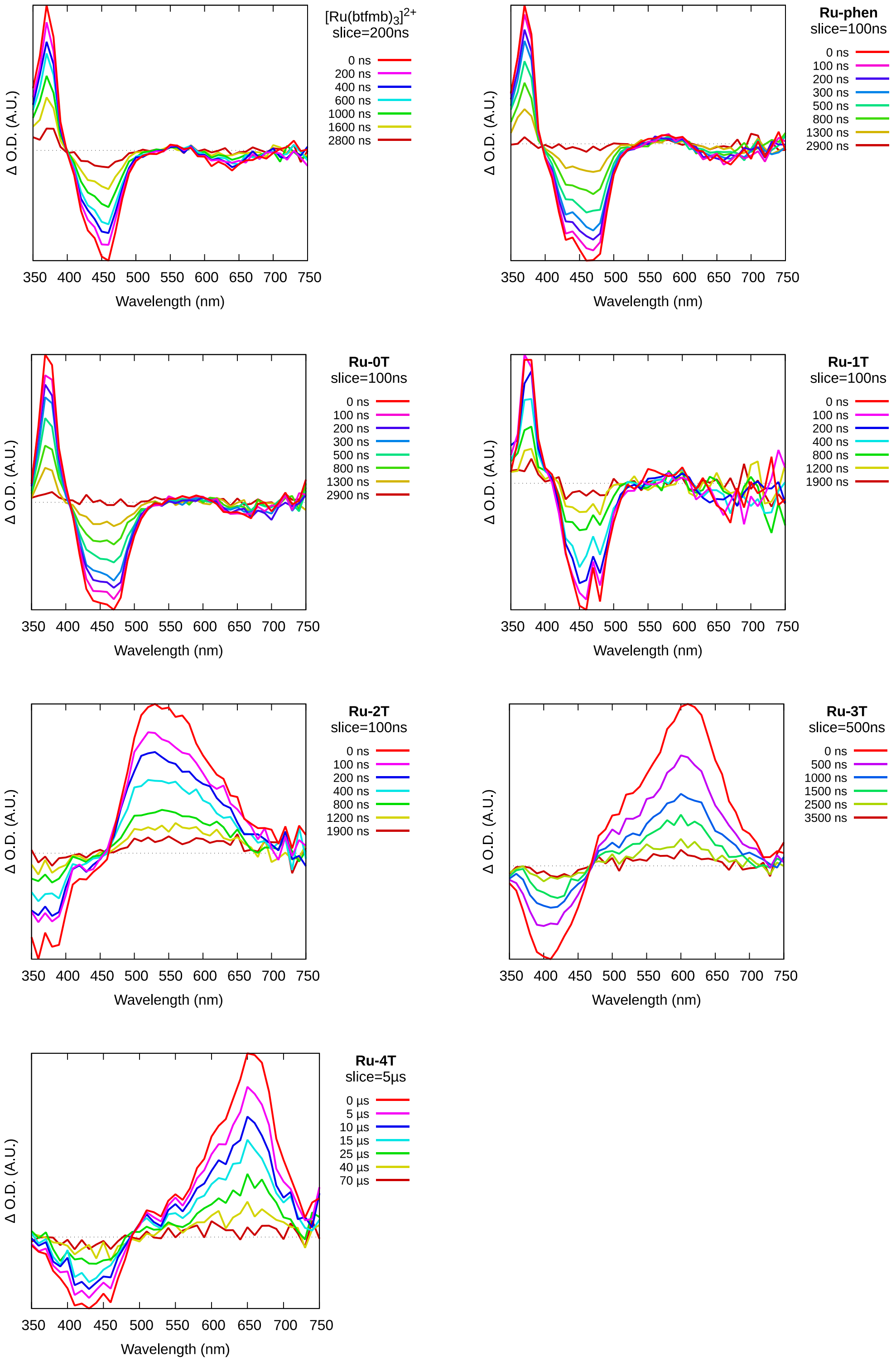

Figure S24: Time-sliced differential excited state absorption spectra, excitation pulse 355 nm.

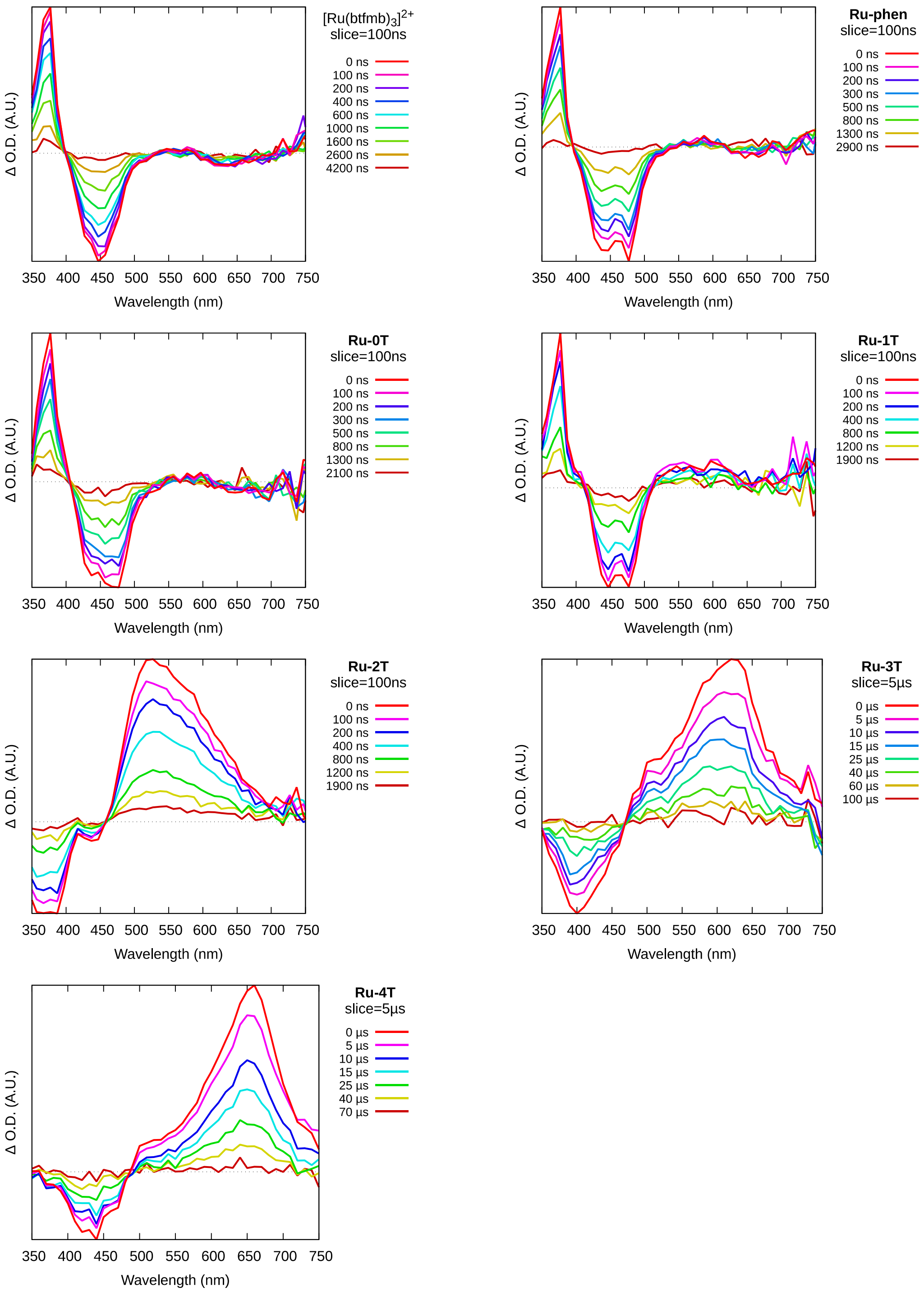

Figure S25: Time-sliced differential excited state absorption spectra, excitation pulse 532 nm.

3.9.6 Photobiological Evaluation

Light Sources and Absorbed Photons

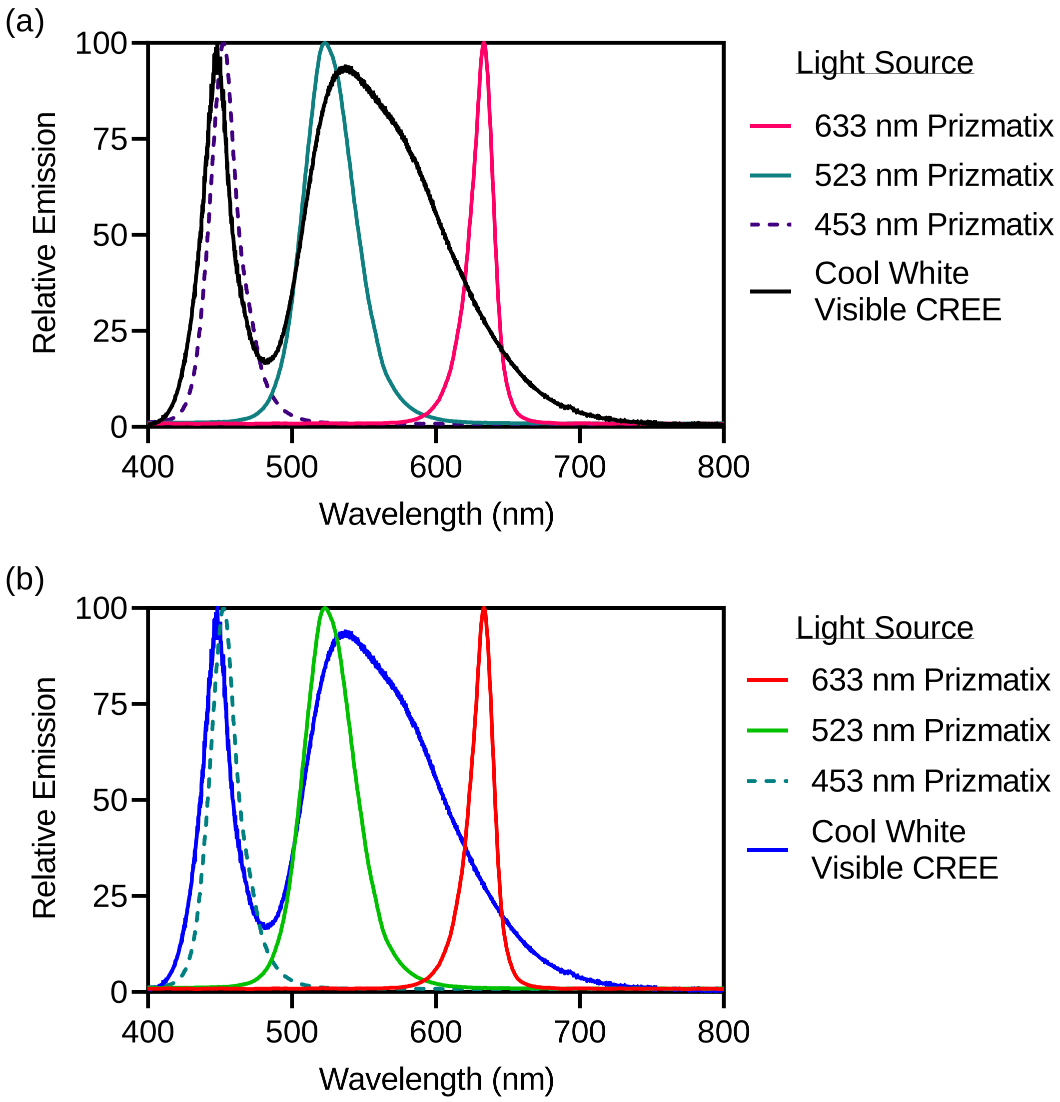

Figure S26. Relative spectral emissions or output of the light sources applied in photobiological studies manufacturer of the LED chip and/or light device is indicated (Prizmatix or CREE). Two color schemes are shown with (a) being colorblind-friendly and (b) matching colors used in reported biological plots (approximately matching apparent colors).

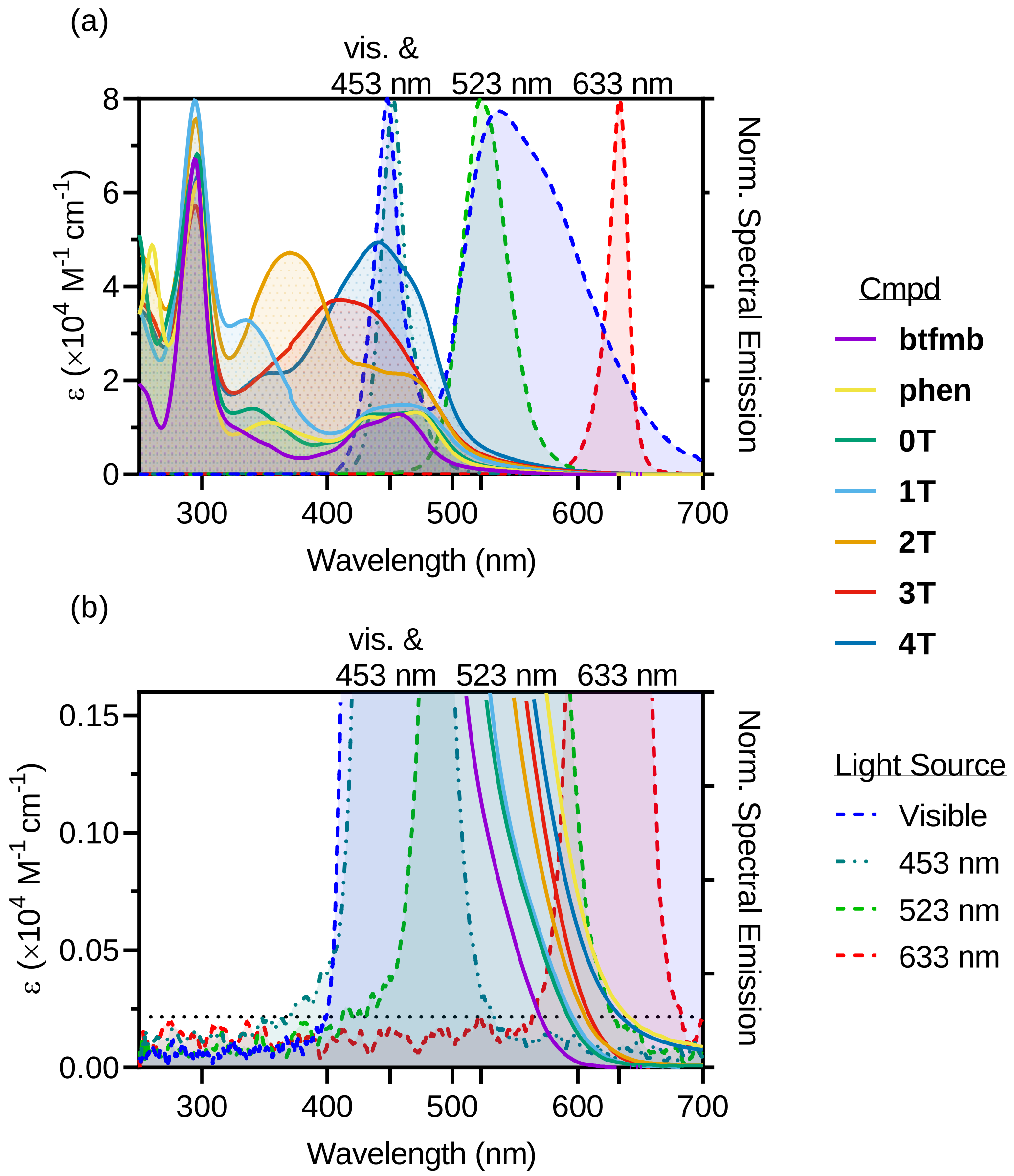

Figure S27. Overlay of [Ru(4,4'-btfmb)$_3$](Cl)$_2$, **Ru-phen**, and **Ru-0T**–**Ru-4T** for their molar extinction coefficients in MeCN (single extrapolated concentration, 20 μM only) and normalized spectral outputs of light sources applied in photobiological studies. Top (a) shows full range and bottom (b) shows the zoom (bottom 1/50th of top y-axis). Color fill was only used in the top plot of the PSs for clarity. The dotted line in (b) indicates the threshold used for the absorbed photon flux estimate (0.27% norm. spectral emission).

Table S4. Approximate photon flux density (mol m^{-2} s^{-1}) absorbed by 20 μM of [Ru(4,4'-btfmb)$_3$](Cl)$_2$, **Ru-phen**, and **Ru-0T**–**Ru-4T** in MeCN (5 mm pathlength). Does not correct for scatter or reflection.

cmpd	633 nm[a]	523 nm[b]	453 nm[c]	Visible[d]	V:R[e]	V:G[f]	B:V[g]	G:R[h]
[Ru(btfmb)$_3$](Cl)$_2$	8.70×10^{-8}	2.47×10^{-5}	1.62×10^{-4}	4.68×10^{-5}	538	2	3	284
Ru-phen	8.44×10^{-7}	4.09×10^{-5}	1.75×10^{-4}	5.67×10^{-5}	67	1	3	49
Ru-0T	9.97×10^{-7}	4.63×10^{-5}	1.81×10^{-4}	5.99×10^{-5}	60	1	3	46
Ru-1T	2.02×10^{-6}	6.64×10^{-5}	2.03×10^{-4}	7.27×10^{-5}	36	1	3	33
Ru-2T	2.05×10^{-6}	8.15×10^{-5}	2.79×10^{-4}	9.73×10^{-5}	48	1	3	40
Ru-3T	6.42×10^{-6}	8.84×10^{-5}	3.36×10^{-4}	1.18×10^{-4}	18	1	3	14
Ru-4T	7.60×10^{-6}	1.24×10^{-4}	4.47×10^{-4}	1.58×10^{-4}	21	1	3	16

[a]red 633 nm, [b]green 523 nm, [c]blue 453 nm, [d]cool white visible (400–700 nm), [e]ratio of visible to red absorbed photon flux, [f]ratio of visible to green absorbed photon flux, [g]ratio of blue to visible absorbed photon flux, and [h]ratio of green to red absorbed photon flux. PS and light source overlay in Table S2.

Note that the values above were calculated from the absorption values reported in the spectroscopy section (5 mm pathlength, 20 μM PF$_6^-$ salts in MeCN) and use an equivalent irradiance (20.5 mW cm^{-2}) to facilitate comparison.

Cytotoxicity and Photocytotoxicity

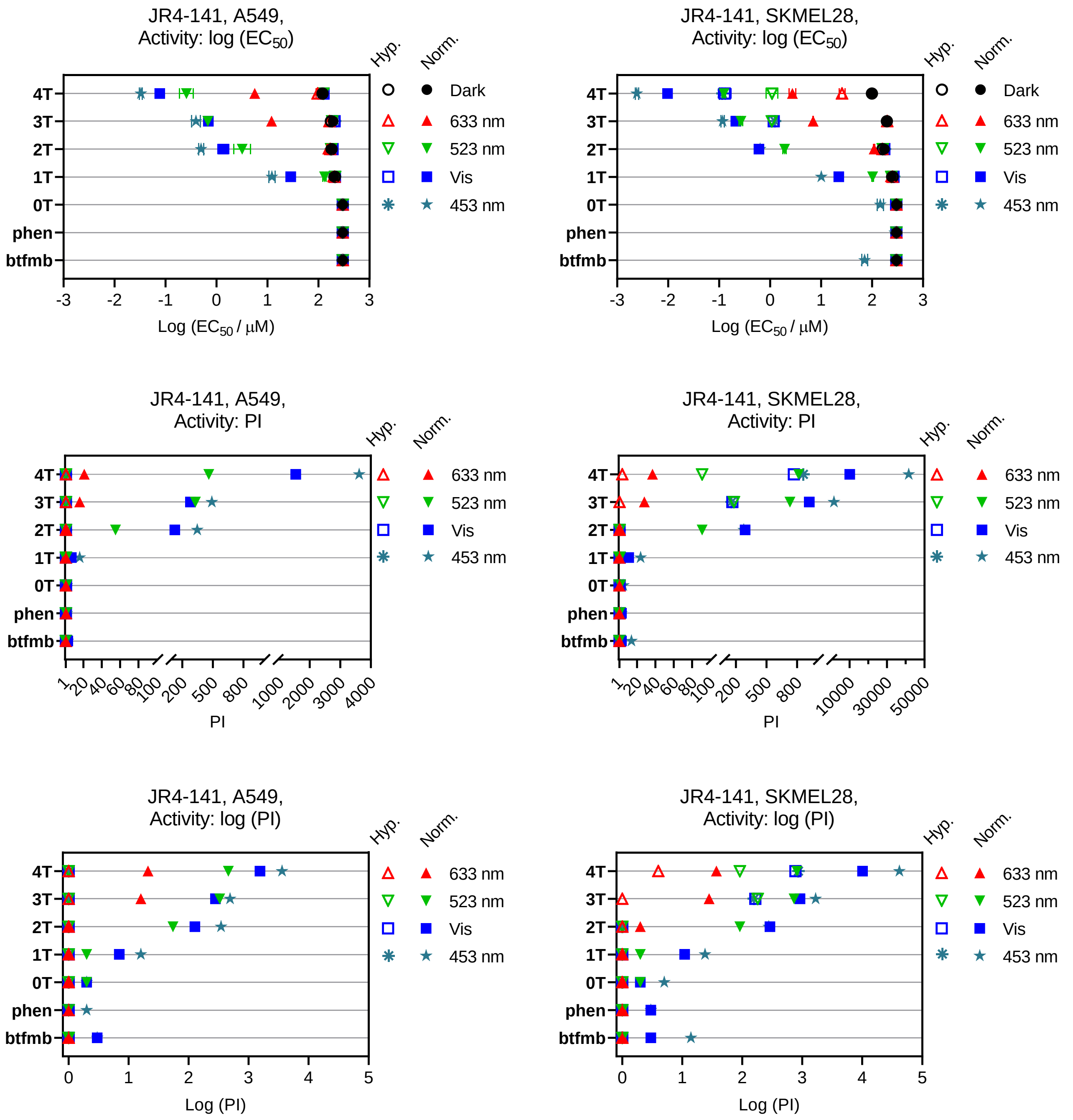

Figure S28. Summary activity plots of Ru complexes [Ru(4,4'-btfmb)$_3$](Cl)$_2$, **Ru-phen**, and **Ru-0T**–**Ru-4T** against A549 cells (left) and SK-MEL-28 (right). Treatments in either hypoxic (1% O_2) or normoxic (18.5–21% O_2) conditions are denoted by symbols for dark (sham, 0 J cm^{-2}) and light treatments (100 J cm^{-2}, ~20 mW cm^{-2}) with red 633 nm, green 523 nm, cool white visible, and blue 453 nm.

Table S5. Comparison of (photo)cytotoxicities of [Ru(4,4'-btfmb)$_3$](Cl)$_2$, **Ru-phen**, and **Ru-0T**–**Ru-4T** in hypoxic (1% O_2) and normoxic (18.5–21% O_2) treated male lung carcinoma A549 cells.

cmpd	O_2%	EC_{50} ± SEM (μM)[a]					PI[b]			
		Dark[c]	633 nm[d]	523 nm[d]	453 nm[d]	Visible[d,e]	633 nm[d]	523 nm[d]	453 nm[d]	Visible[d,e]
[Ru(btfmb)$_3$](Cl)$_2$	1	>300	>300	>300	>300	>300	1	1	1	1
Ru-phen	1	>300	>300	>300	>300	>300	1	1	1	1
Ru-0T	1	>300	>300	>300	>300	>300	1	1	1	1
Ru-1T	1	211 ± 7	208 ± 5	213 ± 5	212 ± 6	212 ± 8	1	1	1	1
Ru-2T	1	182 ± 7	170 ± 4	178 ± 5	176 ± 5	190 ± 5	1	1	1	1
Ru-3T	1	175 ± 12	166 ± 6	187 ± 7	215 ± 9	207 ± 9	1	1	1	1
Ru-4T	1	120 ± 4	96.7 ± 6.5	126 ± 5	126 ± 4	127 ± 6	1	1	1	1
[Ru(btfmb)$_3$](Cl)$_2$	18.5	>300	>300	>300	>300	>300	1	1	3	3
Ru-phen	18.5	>300	>300	>300	>300	>300	1	1	2	1
Ru-0T	18.5	>300	>300	>300	>300	>300	1	2	2	2
Ru-1T	18.5	199 ± 7	189 ± 5	132 ± 11	12.3 ± 1.9	28.6 ± 3.2	1	2	16	7
Ru-2T	18.5	174 ± 4	152 ± 6	3.19 ± 1.19	0.50 ± 0.056	1.37 ± 0.35	1	55	348	127
Ru-3T	18.5	195 ± 10	12.1 ± n.d.	0.59 ± n.d.	0.40 ± 0.08	0.70 ± n.d.	16	329	491	280
Ru-4T	18.5	119 ± 4	5.64 ± n.d.	0.26 ± 0.081	0.033 ± 0.0023	0.077 ± n.d.	21	461	3617	1541

[a]Effective concentration to reduce relative cell viability to 50% (EC_{50}) and standard error of the mean (SEM), [b]phototherapeutic index (PI) provides the ratio of dark (sham) to light EC_{50} values, [c]dark treatment or absence of light during treatment, [d]light treatment uses 100 J cm^{-2} at ~20 mW cm^{-2}, and [e]cool white visible (400–700 nm). *n.d. = SEM not determined to a steep hill slope.

Table S6. Comparison of (photo)cytotoxicities [Ru(4,4'-btfmb)$_3$](Cl)$_2$, **Ru-phen**, and **Ru-0T**–**Ru-4T** in hypoxic (1% O_2) and normoxic (18.5% O_2) SK-MEL-28 cells.

compound	% O_2	EC$_{50}$ ± SEM (μM)[a]					PI[b]			
		Dark[c]	633 nm[d]	523 nm[d]	453 nm[d]	Visible[d,e]	633 nm[d]	523 nm[d]	453 nm[d]	Visible[d,e]
[Ru(btfmb)$_3$](Cl)$_2$	1	>300	>300	>300	>300	>300	1	1	1	1
Ru-phen	1	>300	>300	>300	>300	>300	1	1	1	1
Ru-0T	1	>300	>300	>300	>300	>300	1	1	1	1
Ru-1T	1	254 ± 8	251 ± 5	240 ± 5	271 ± 7	264 ± 9	1	1	1	1
Ru-2T	1	160 ± 4	160 ± 3	163 ± 5	179 ± 5	174 ± 5	1	1	1	1
Ru-3T	1	195 ± 7	198 ± 8	1.08 ± n.d.	1.24 ± n.d.	1.18 ± n.d.	1	181	157	165
Ru-4T	1	99.2 ± 3.6	25.9 ± 3.2	1.09 ± 0.29	0.12 ± 0.015	0.13 ± 0.036	4	91	863	769
[Ru(btfmb)$_3$](Cl)$_2$	18.5	>300	>300	>300	71.8 ± 9.8	>300	1	1	4	1
Ru-phen	18.5	>300	>300	>300	281 ± n.d.	300 ± n.d.	1	1	~1	1
Ru-0T	18.5	>300	>300	>300	145 ± 21	290 ± n.d.	1	1	2	~1
Ru-1T	18.5	238 ± 9	228 ± 5	103 ± 4	10.1 ± n.d.	22.4 ± 2.4	1	2	24	11
Ru-2T	18.5	176 ± 5	110 ± 3	1.93 ± 0.15	0.64 ± n.d.	0.61 ± 0.1	2	91	277	290
Ru-3T	18.5	196 ± 6	7.02 ± 0.1	0.27 ± 0.021	0.12 ± 0.009	0.21 ± 0.032	28	731	1675	920
Ru-4T	18.5	101 ± 3	2.74 ± 0.41	0.12 ± 0.01	0.0024 ± 0.00018	0.010 ± 0.001	37	815	41564	10100

[a] Effective concentration to reduce relative cell viability to 50% (EC$_{50}$) and standard error of the mean (SEM), [b] phototherapeutic index (PI) provides the ratio of dark (sham) to light EC$_{50}$ values, [c] dark treatment or absence of light during treatment, [d] light treatment uses 100 J cm^{-2} at ~20 mW cm^{-2}, and [e] cool white visible (400–700 nm).

*n.d. = SEM not determined to a steep hill slope.

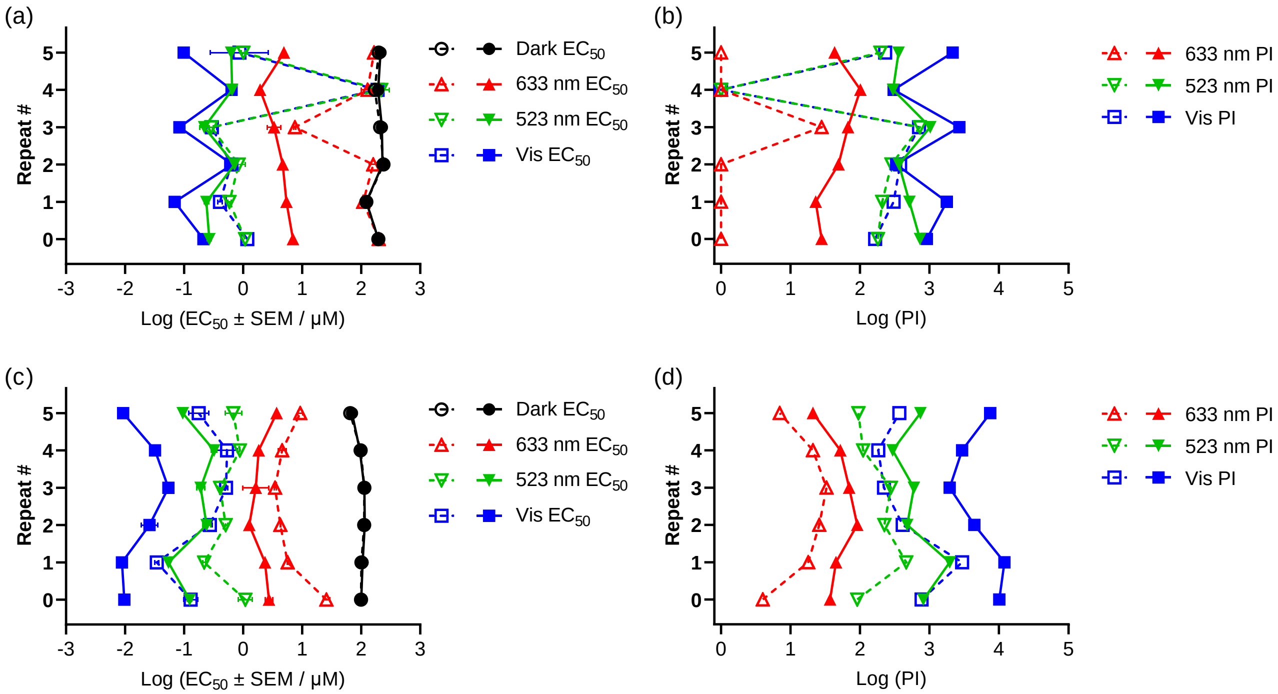

Figure S29. Interassay performance with various factors changed across each repeat as described in the experimental section. Cytotoxicity and photocytotoxicity of **Ru-3T** (top, a+b) and **Ru-4T** (bottom, c+d) in normoxic- (filled symbols, solid lines; ~18.5% O_2) and hypoxic-treated (open symbols, dashed lines; 1% O_2) SK-MEL-28 melanoma cells. Log (EC_{50} ± SEM) values (left) and PI values (right). Treatments included dark (0 J cm^{-2}) and 100 J cm^{-2} doses of 633 nm, 523 nm, and visible (400–700 nm) light.

“Repeat 0” is the data reported in the compound family’s dose-response in SK-MEL-28 about one year after repeats 1–5 (completed over one month).

Table S7. Interassay performance: cytotoxicity and photocytotoxicity of **Ru-3T** in hypoxic-treated (1% O_2) male SK-MEL-28 melanoma cells.

	Resazurin-Hypoxia (1% O_2) Ru-3T Repeats						
	EC_{50} ± SEM (μM)				PI[d]		
Repeat	Dark	Red[a]	Green[b]	Vis[c]	Red[a]	Green[b]	Vis[c]
0*	195 ± 7	198 ± 8	1.08 ± n.d.	1.18 ± n.d.	1	181	165
1	123 ± 6	109 ± 12	0.59 ± 0.04	0.41 ± 0.037	1	209	304
2	238 ± 11	160 ± 24	0.84 ± 0.22	0.63 ± 0.068	1	283	377
3	210 ± 13	7.54 ± 0.29	0.29 ± 0.024	0.30 ± 0.059	28	724	707
4	170 ± 3	128 ± 31	219 ± 69	190 ± 41	1	1	1
5	199 ± 8	165 ± 19	1.01 ± 0.08	0.87 ± 0.98	1	197	230
Mean ± SD[e]	189 ± 39	128 ± 67	37.1 ± 89.1	13.9 ± 30.8	6 ± 11	266 ± 243	297 ± 238
min	123	7.54	0.290	0.297	1	1	1
max	238	198	219	190	28	724	707

Light treatments were approximately 100 J cm^{-2} delivered at 18–22 mW cm^{-2}. [a] red 633 nm, [b] green 523 nm, [c] cool white visible (400–700 nm), [d] PI = phototherapeutic index (dark EC_{50} / light EC_{50}), *original run in repeat 0 from Table S4, and n.d. = SEM not determined due to overly steep hill slope. [e] Did not test for outliers or run meta-analysis, use with caution.

Repeats used different plate maps (all), different tips (Sartorius 790352 repeat #1, VWR 83007-352 repeats #2–3, low retention Sartorius LH-L790352 repeats #4–5), changed cell parent seed stock for repeats 4–5, and overhead lights were off in #5. Serum and consumable lots were identical for repeats 1–5. Cell passage numbers were equal. Run in parallel with normoxic repeats.

Table S8. Interassay performance: cytotoxicity and photocytotoxicity of **Ru-3T** in normoxic-treated (~18.5% O_2) male SK-MEL-28 melanoma cells.

	Resazurin-Normoxia (~18.5% O_2) Ru-3T Repeats						
	EC_{50} ± SEM (μM)				PI[d]		
Repeat	Dark	Red[a]	Green[b]	Vis[c]	Red[a]	Green[b]	Vis[c]
0*	196 ± 6	7.02 ± 0.10	0.27 ± 0.021	0.21 ± 0.032	28	731	920
1	123 ± 6	5.44 ± 0.11	0.24 ± 0.023	0.070 ± n.d.	23	515	1767
2	230 ± 12	4.70 ± n.d.	0.63 ± n.d.	0.70 ± n.d.	49	364	331
3	225 ± 10	3.36 ± 0.9	0.22 ± 0.037	0.084 ± n.d.	67	1023	2691
4	195 ± 9	1.94 ± 0.06	0.65 ± n.d.	0.64 ± n.d.	101	299	305
5	213 ± 10	4.90 ± n.d.	0.60 ± n.d.	0.10 ± n.d.	43	358	2158
Mean ± SD[e]	197 ± 39	4.56 ± 1.75	0.29 ± 0.41	0.44 ± 0.21	52 ± 29	548 ± 280	1362 ± 994
min	123	1.94	0.22	0.070	23	299	305
max	230	7.02	0.66	0.70	101	1023	2691

Light treatments were approximately 100 J cm^{-2} delivered at 18–22 mW cm^{-2}. [a] red 633 nm, [b] green 523 nm, [c] cool white visible (400–700 nm), [d] PI = phototherapeutic index (dark EC_{50} / light EC_{50}), *original run in repeat 0 from Table S4, and n.d. = SEM not determined due to overly steep hill slope. [e] Did not test for outliers or run meta-analysis, use with caution.

Repeats used different plate maps (all), different tips (Sartorius 790352 repeat #1, VWR 83007-352 repeats #2–3, low retention Sartorius LH-L790352 repeats #4–5), changed cell parent seed stock for repeats 4–5, and overhead lights were off in #5. Serum and consumable lots were identical for repeats 1–5. Cell passage numbers were equal. Run in parallel with normoxic repeats.

Table S9. Interassay performance: cytotoxicity and photocytotoxicity of **Ru-4T** in hypoxic-treated (1% O_2) male SK-MEL-28 melanoma cells.

	Resazurin-Hypoxia (1% O_2) Ru-4T Repeats						
	EC$_{50}$ ± SEM (µM)				PI[d]		
Repeat	Dark	Red[a]	Green[b]	Vis[c]	Red[a]	Green[b]	Vis[c]
0*	99.2 ± 3.6	25.9 ± 3.2	1.09 ± 0.29	0.13 ± 0.036	4	91	769
1	102 ± 3	5.71 ± 0.15	0.22 ± 0.013	0.035 ± 0.0026	18	464	2948
2	113 ± 5	4.30 ± 0.06	0.51 ± 0.043	0.28 ± 0.028	26	224	411
3	114 ± 4	3.48 ± 0.13	0.41 ± 0.041	0.52 ± 0.032	33	278	221
4	97.8 ± 4.2	4.59 ± 0.70	0.88 ± 2.24	0.54 ± 0.21	21	111	183
5	65.3 ± 1.5	9.32 ± 0.90	0.68 ± 0.22	0.18 ± 0.069	7	95	369
Mean ± SD[e]	98.6 ± 17.7	8.88 ± 8.58	0.63 ± 0.32	0.47 ± 0.87	18 ± 11	211 ± 146	817 ± 1065
min	65.3	3.48	0.220	0.0346	4	91	183
max	114	25.9	1.09	0.535	33	464	2948

Light treatments were approximately 100 J cm^{-2} delivered at 18–22 mW cm^{-2}. [a] red 633 nm, [b] green 523 nm, [c] cool white visible (400–700 nm), [d] PI = phototherapeutic index (dark EC$_{50}$ / light EC$_{50}$), *original run in repeat 0 from Table S4, and n.d. = SEM not determined due to overly steep hill slope. [e] Did not test for outliers or run meta-analysis, use with caution.

Repeats used different plate maps (all), different tips (Sartorius 790352 repeat #1, VWR 83007-352 repeats #2–3, low retention Sartorius LH-L790352 repeats #4–5), changed cell parent seed stock for repeats 4–5, and overhead lights were off in #5. Serum and consumable lots were identical for repeats 1–5. Cell passage numbers were equal. Run in parallel with normoxic repeats.

Table S10. Interassay performance: cytotoxicity and photocytotoxicity of **Ru-4T** in normoxic-treated (~18.5% O_2) male SK-MEL-28 melanoma cells.

	Resazurin-Normoxia (~18.5% O_2) Ru-4T Repeats						
	EC$_{50}$ ± SEM (μM)				PI[d]		
Repeat	Dark	Red[a]	Green[b]	Vis[c]	Red[a]	Green[b]	Vis[c]
0*	101 ± 3	2.74 ± 0.41	0.12 ± 0.010	0.0097 ± 0.00068	37	815	10402
1	106 ± 3	2.36 ± 0.10	0.054 ± 0.0030	0.0088 ± 0.0012	45	1949	11964
2	115 ± 4	1.27 ± n.d.	0.24 ± 0.037	0.026 ± 0.0083	91	479	4406
3	114 ± 4	1.64 ± 0.83	0.19 ± 0.029	0.059 ± n.d.	70	597	1949
4	95.2 ± 3.0	1.84 ± 0.08	0.32 ± 0.038	0.032 ± 0.0028	52	296	2957
5	69.9 ± 1.1	3.39 ± n.d.	0.095 ± n.d.	0.0093 ± n.d.	21	738	7500
Mean ± SD[e]	100 ± 17	2.21 ± 0.78	0.36 ± 0.35	0.017 ± 0.010	53 ± 25	812 ± 587	6530 ± 4092
min	69.9	1.27	0.054	0.0089	21	296	1949
max	115	3.39	0.32	0.059	91	1949	11964

Light treatments were approximately 100 J cm^{-2} delivered at 18–22 mW cm^{-2} [a]red 633 nm, [b] green 523 nm, [c] cool white visible (400–700 nm), [d] PI = phototherapeutic index (dark EC$_{50}$ / light EC$_{50}$), *original run in repeat 0 from Table S4, and n.d. = SEM not determined due to overly steep hill slope. [e] Did not test for outliers or run meta-analysis, use with caution.

Repeats used different plate maps (all), different tips (Sartorius 790352 repeat #1, VWR 83007-352 repeats #2–3, low retention Sartorius LH-L790352 repeats #4–5), changed cell parent seed stock for repeats 4–5, and overhead lights were off in #5. Serum and consumable lots were identical for repeats 1–5. Cell passage numbers were equal. Run in parallel with normoxic repeats.

CHAPTER 4. CHIRALITY MATTERS: ENANTIOMERICALLY RESOLVED RU(II) OLIGOTHIENYL COMPLEXES FOR PHOTODYNAMIC THERAPY

Houston D. Cole,[a] Troy T. Handlovic,[a] Saba Aslani,[a] John A. Roque III,[a,b,] Ge Shi,[a] Elamparuthi Ramasamy,[a] Colin G. Cameron,[a*] Daniel W. Armstrong,[a] Sherri A. McFarland[a*]

[a] *Department of Chemistry and Biochemistry, The University of Texas at Arlington, Arlington, Texas, 76019-0065 United States*

**Corresponding authors:* C.G.C. <colin.cameron@uta.edu> ORCID 0000-0003-0978-0894, S.A.M. <sherri.mcfarland@uta.edu> ORCID 0000-0002-8028-5055

4.1 ABSTRACT

Keywords: Ruthenium, enantiomers, cancer, metal-to-ligand charge transfer (MLCT), intraligand (IL), melanoma, photodynamic therapy

4.2 INTRODUCTION

The chiral configurations of *bis*-heteroleptic and *tris*-homoleptic Ruthenium polypyridyl complexes are defined as being either the delta (Δ) or lambda (Λ) enantiomer (Scheme 1). The resolution of these chiral complexes may be performed synthetically[1] or through high-pressure liquid chromatography (HPLC) using a chiral stationary phase.[2–4] In collaboration with the Armstrong group, we have previously reported the HPLC-driven separation of various ruthenium and osmium oligothienyl complexes using *R*-napthylenecarbamate cyclofructan 6 (CF6-RN) column matrixes.[5,6] The absolute configurations of these enantiomers may be confirmed using vibrational circular dichroism (VCD).[6]

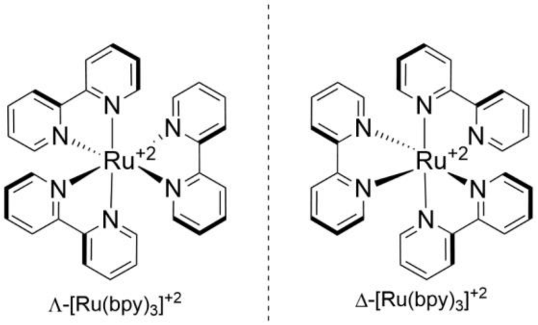

Scheme 1. Structure of lambda (Λ) and delta (Δ) enantiomers of $[Ru(bpy)_3]^{+2}$.

The racemates of certain Ru(II) polypyridyl complexes bearing dipyridophenazine (dppz) or benzodipyridophenazine (dppn) type ligands are known for their DNA binding properties[7–12] as well as their capacity for DNA binding-induced luminescence.[13] A number of studies have expanded upon this by evaluating the binding properties of the delta (Δ) and lambda (Λ) enantiomers with DNA, where they typically found the delta enantiomer to bind more strongly to DNA than the lambda enantiomer. Consequently, the delta enantiomer is also observed to be more cytotoxic than the delta enantiomer and racemate in certain cancerous cell lines,[12,14–20] with studies suggesting that the primary source of this cytotoxicity stems from binding-induced DNA damage or disruption of the mitochondrial membrane.

In the context of photodynamic therapy (PDT), the effect of chirality on the photobiological activity of Ru(II) polypyridyl complexes is far less understood. A study that was published this year (2023)[12] observed that, at the same concentration (30 µM), Δ-$[Ru(DIP)_2(dppz)]^{+2}$ (DIP= 4,7-diphenylphenanthroline) was more phototoxic than the corresponding lambda enantiomer in HeLa cells when exposed to visible light. We seek to expand upon the PDT community's understanding of the effects of chirality on photocytotoxicity by comparing the dose-response activity of enantiomerically pure (Δ/Λ) photosensitizers with their corresponding racemates. In this study, we investigate two previously published Ru(II) oligothienyl complexes bearing 4,4'-btfmb ligands and an imidazo[4,5-*f*][1,10]phenanthroline ligand tethered to *n*=3–4 thiophene rings (IP-*n*T). We selected these complexes because of their highly consistent photobiological activity, which allows us to effectively distinguish between the effects of chirality from other factors that contribute to the photobiological variance observed in certain oligothienyl systems.

4.3 RESULTS AND DISCUSSION

Chart 1. Structures of **æ/ş-Ru-3T** and **æ/ş-Ru-4T**. The racemates are mixtures of both enantiomers.

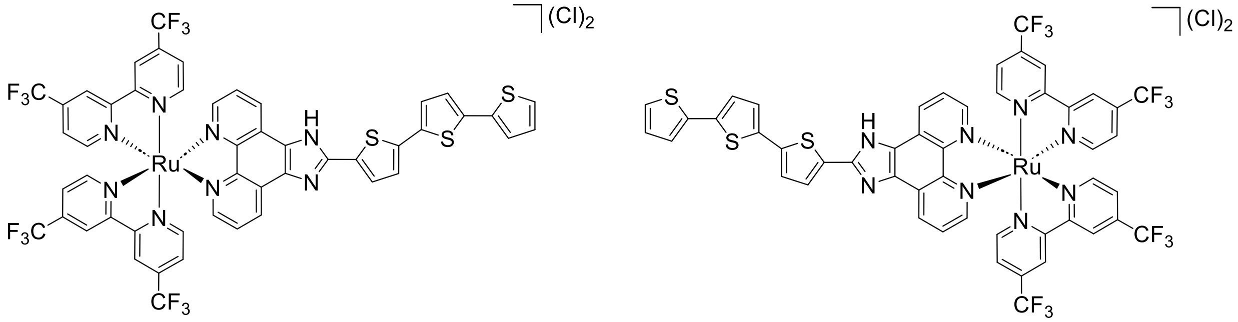

Λ-Ru-3T **Δ-Ru-3T**

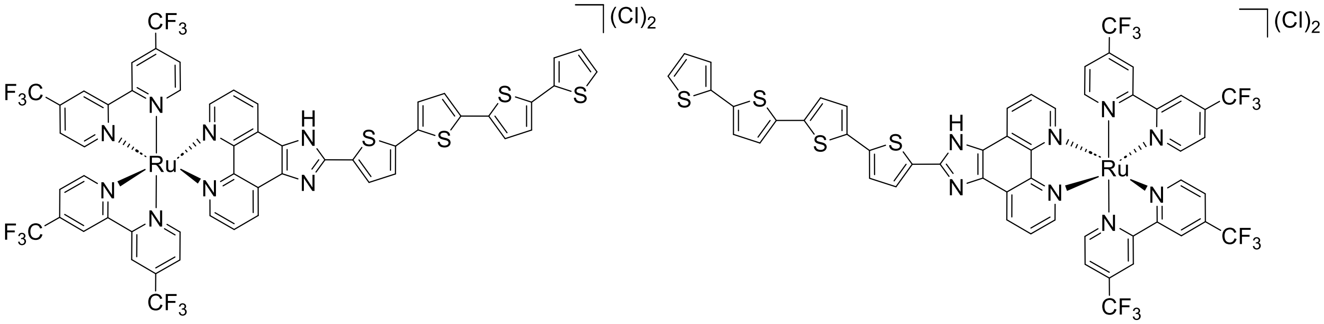

Λ-Ru-4T **Δ-Ru-4T**

4.3.1 Resolution of enantiomers via HPLC

A previously described chiral chromatographic technique was used for **Ru-3T** and **Ru-4T**. Briefly, racemates were eluted through a CF6-RN column matrix using an eluent consisting of MeOH/TFA/TEA. Three batches were prepared in total: A, B, and C. Batch A and B were prepared using the same procedure. Batch B shown evidence of TEA and TFA salts by ^{1}H NMR and ^{19}F NMR and was visibly less soluble than expected, another batch was prepared without the use of triethylamine (TEA).

4.3.2 In Vitro Photobiological Activity

The complexes ***rac*/æ/ş-Ru-3T** and ***rac*/æ/ş-Ru-4T** were thoroughly evaluated for their cytotoxic and photocytotoxic properties against normoxic-treated SKMEL28 cells over several resazurin-based photobiological assays in which we determine the effective concentration to eliminate 50% of cells (EC_{50}) in the dark and under green (523 nm) and cool white visible (400–700 nm) light as well as the phototherapeutic index (PI) of each compound under each light condition (Table 1, Table S3–Table S8). The PI is defined as the ratio of dark to light EC_{50} values; in cases where the dark EC_{50} value exceeds the upper concentration limit of 300 µM, the PI is technically undefined but is estimated using 300 µM as the dark EC_{50} value. Details regarding the cell culture conditions, solution preparation, and photobiological assay procedures may be found in our previous work[8,9] as well as the Supplemental Information. Unless otherwise specified, the racemates of **Ru-3T** and **Ru-4T** were tested alongside their enantiomerically resolved counterparts.

Compound ***rac*-Ru-3T** exhibits minimal activity towards melanoma cells in the dark but reached sub-micromolar EC_{50} values when exposed to visible or green light (visible EC_{50}=16 nM, green EC_{50}=220 nM). Our initial investigations showed that the enantiopure samples were less active overall than the racemate both in the dark and light, but all values were within one order of magnitude of one another. This was further confirmed in two follow-up assays where we tested ***rac*/æ/ş-Ru-3T** alongside one another under the same conditions as the original run (Figure S10, Table S3–Table S5).

Our investigations comparing ***rac*/æ/ş-Ru-4T** shown that the enantiomerically pure compounds shared similar toxicity in the dark. However, in the presence of green or visible light, ***rac*-Ru-4T** (visible EC_{50}= 6.4 nM) and **æ-Ru-4T** (visible EC_{50}= 14 nM) were significantly less photocytotoxic than **ş-Ru-4T** (visible EC_{50}= 0.21 nM), where **ş-Ru-4T** out-performs ***rac*-Ru-4T** by a factor of 35 (visible PI= 16,000 vs. 560,000)!

Table 1. Cytotoxicity and photocytotoxicity of ***rac*/æ/ş-Ru-3T** and ***rac*/æ/ş-Ru-4T** against normoxic-treated SKMEL28 cells (~18.5% O_2).

Compound	Resazurin-Cell Viability				
	EC_{50} ± SEM			PI[c]	
	Dark	Visible[a]	Green[b]	Visible[a]	Green[b]
ȹ/ -şRu-3T	192 ± 8 µM	16 ± n.d. nM	0.22 ± 0.027 µM	12,000	870
ȹ-Ru-3T	210 ± 7 µM	97 ± n.d. nM	0.32 ± 0.031 µM	2200	670
ş-Ru-3T	>300 µM	79 ± n.d. nM	0.25 ± 0.029 µM	3800	1200
ȹ/ -şRu-4T	110 ± 3 µM	6.4 ± 0.6 nM	97 ± 5.8 nM	16,000	1100
ȹ-Ru-4T	127 ± 4 µM	14 ± n.d. nM	180 ± n.d. nM	900	700
ş-Ru-4T	117 ± 3 µM	0.21 ± 0.016 nM	0.85 ± n.d. nM	560,000	14,000

Light treatments were approximately 100 J cm^{-2} delivered at 18–24 mW cm^{-2} with [a] cool white Visible (400–700 nm), [b] Green (523 nm), and [c] PI = phototherapeutic index. Hypoxia and normoxia experiments were ran in parallel. *n.d. = SEM not determined due to steep hill slope.

To confirm our findings in the initial assay described in Table 1**,** we tested the compounds against one another an additional 17 times (18 total assays), where we probed the effects of: 1) inter-assay variability, 2) batch-to-batch variability (of the compounds), and 3) the potential impact/presence of impurities. In order to isolate the effects of inter-assay variability, we kept all conditions exactly the same for 10 additional assays using the same batch of material used in the original run, which are coded as **A1**–**A12** in Table S6–Table S8. In each experiment, we observed that 1) the racemate was typically less toxic than either isolated enantiomer in the dark (by up to a factor of two) and 2) the trend in light-triggered photocytotoxicity was that **ş-Ru-4T** was the most phototoxic by a margin of roughly one order of magnitude, with **æ-Ru-4T** being the least phototoxic among the three and ***rac*-Ru-4T** being somewhere between the two in terms of activity. Notably, the EC_{50} values for each complex under every light condition during all 12 assays were consistently within 1 order of magnitude of one another, which aligns with our previous observations of ***rac*-Ru-3T** and ***rac*-Ru-4T**.

The batch-to-batch variability of ***rac*/æ/ş-Ru-4T** was tested by preparing the racemate two additional times then resolving each new batch of racemate, once using the exact same procedure (Table S6–Table S8, **B1**–**B4**) and another time using a modified purification method (Table S6–Table S8, **C1**–**C2**). The dark toxicity and photobiological efficacies of ***rac*-Ru-4T** and **æRu-4T** from batch **B** were the same as the complexes from batch **A**, with EC$_{50}$ values within one order of magnitude of the original results. Conversely, **ş-Ru-4T** was less toxic in the dark and with light treatments during all four repeat assays. The dark toxicity of **ş-Ru-4T** from batch **B** exceeded the upper concentration limit of 300 µM, and the visible EC$_{50}$ values decreased by a factor of two in two examples (from ~0.5 nM to ~3 nM), and in the other two examples their EC$_{50}$ values dropped by over an order of magnitude (from ~0.5 nM to ~100 nM). The photocytotoxic trends were similar under green light, where the overall activity decreased from 1–10 nM to roughly 300 nM during the four runs.

This sudden decrease in activity was particularly concerning because batches **A** and **B** were identical in their HPLC traces. However, further analysis of their stock solutions revealed that the lambda enantiomer in batch **B** was visibly less water soluble than previous batches (Figure S12), and ^{1}H NMR analysis confirmed the presence of cationic ammonium salts. These kinds of salts are difficult to remove via simple work up procedures because of their similar solubility properties to our complexes as well as their exceedingly high boiling points. We believe the overall attenuation in activity was from the added mass of these salts causing less **ş-Ru-4T** to be added to cells. To circumvent this issue, we were able to prepare batch **C** by removing TEA from the eluent, thus removing the possibility of ammonium salts. Thankfully, the complexes from batch **C** have displayed the same overall trends in activity that were observed in batch **A** in the two biological replicates so far (Table S6–Table S8, **C1**–**C2**). Our observations here further emphasize the importance of biological replication as well as the importance of fully characterizing enantiomerically resolved samples after isolation.

4.4 SUMMARY AND FUTURE DIRECTIONS

In summary, the dark toxicity and photobiological activity of ***rac*-Ru-3T**, **æ-Ru-3T**, and **ş-Ru-3T** were, under these conditions, the same against SKMEL28 cells. However, expanding the IP-*n*T ligand to have *n* = 4 thiophenes caused two major effects: 1) the dark toxicity of the isolated **æ-Ru-4T** and **ş-Ru-4T** complexes was lower than ***rac*-Ru-4T** by roughly a factor of two; 2) **æ-Ru-4T** is the least active with light treatments and **ş-Ru-4T** was the most active under light treatments, with ***rac*-Ru-4T** being in between. This enantioselectivity exceeds an order of magnitude, and our best results displayed an improvement in activity by a factor of 35. To the best of our knowledge, this is the first study to compare the EC_{50} values of racemic PSs with their delta and lambda enantiomers. The source of this specificity is still unknown and is under active investigation.

4.5 ASSOCIATED CONTENT

Synthetic characterization (1D and 2D NMR, HPLC, HRMS) of the racemates and (photo)biological data are included in the Supporting Information.

4.5.1 Acknowledgements

S.A.M. and C.G.C. thank the National Cancer Institute (NCI) of the National Institutes of Health (NIH) (Award R01CA222227) as well as the National Science Foundation (NSF) (Award NSF 2102459) for support. The content in this work is solely the responsibility of the authors and does not necessarily represent the official views of the National Institutes of Health. S.A.M. also thanks Dr. Daniel Todd as UNCG’s Triad Mass Spectrometry Facility manager and his assistants Jennifer Simpson and Diane Wallace. S.A.M. likewise thanks Dr. Franklin Moy (UNCG) and Dr. Brian Edwards (UTA) for their experimental support and instrument maintenance as NMR facility managers.

4.6 REFERENCES

(1) Morgan, O.; Wang, S.; Bae, S.-A.; Morgan, R. J.; Baker, A. D.; Strekas, T. C.; Engel, R. Two Complete Stereochemical Sets of Dinuclear Ruthenium Complexes. J. Chem. Soc., Dalton Trans. 1997, No. 20, 3773–3776. https://doi.org/10.1039/a702829f.

(2) Sun, P.; Krishnan, A.; Yadav, A.; MacDonnell, F. M.; Armstrong, D. W. Enantioseparations of Chiral Ruthenium(II) Polypyridyl Complexes Using HPLC with Macrocyclic Glycopeptide Chiral Stationary Phases (CSPs). J. Mol. Struct. 2008, 890 (1–3), 75–80. https://doi.org/10.1016/j.molstruc.2008.02.030.

(3) Sun, P.; Wang, C.; Breitbach, Z. S.; Zhang, Y.; Armstrong, D. W. Development of New HPLC Chiral Stationary Phases Based on Native and Derivatized Cyclofructans. Anal. Chem. 2009, 81 (24), 10215–10226. https://doi.org/10.1021/ac902257a.

(4) Sun, P.; Wang, C.; Padivitage, N. L. T.; Nanayakkara, Y. S.; Perera, S.; Qiu, H.; Zhang, Y.; Armstrong, D. W. Evaluation of Aromatic-Derivatized Cyclofructans 6 and 7 as HPLC Chiral Selectors. Analyst 2011, 136 (4), 787–800. https://doi.org/10.1039/C0AN00653J.

(5) Handlovic, T. T.; Wahab, M. F.; Cole, H. D.; Alatrash, N.; Ramasamy, E.; MacDonnell, F. M.; McFarland, S. A.; Armstrong, D. W. Insights into Enantioselective Separations of Ionic Metal Complexes by Sub/Supercritical Fluid Chromatography. Analytica Chimica Acta 2022, 1228, 340156. https://doi.org/10.1016/j.aca.2022.340156.

(6) Armstrong, D. W.; Yu, J.; Cole, H. D.; McFarland, Sherri. A.; Nafie, J. Chiral Resolution and Absolute Configuration Determination of New Metal-Based Photodynamic Therapy Antitumor Agents. J. Pharm. Biom. Anal. 2021, 204, 114233. https://doi.org/10.1016/j.jpba.2021.114233.

(7) Wang, X.; Liu, X.; Tan, L. Binding and Stabilizations Effects of RNA Triplex Poly(U*A-U) by Enantiomers of Ruthenium(II) Polypyridyl Complex [Ru(Bpy)2(10-OH-Dppz)]2+. Dyes and Pigments 2023, 216, 111377. https://doi.org/10.1016/j.dyepig.2023.111377.

(8) Cardin, C. J.; Kelly, J. M.; Quinn, S. J. Photochemically Active DNA-Intercalating Ruthenium and Related Complexes – Insights by Combining Crystallography and Transient Spectroscopy. Chem. Sci. 2017, 8 (7), 4705–4723. https://doi.org/10.1039/C7SC01070B.

(9) Hall, J. P.; Cook, D.; Morte, S. R.; McIntyre, P.; Buchner, K.; Beer, H.; Cardin, D. J.; Brazier, J. A.; Winter, G.; Kelly, J. M.; Cardin, C. J. X-Ray Crystal Structure of Rac- [Ru(Phen)

2 Dppz] 2+ with d(ATGCAT) 2 Shows Enantiomer Orientations and Water Ordering. J. Am. Chem. Soc. 2013, 135 (34), 12652–12659. https://doi.org/10.1021/ja403590e.

(10) Hall, J. P.; Keane, P. M.; Beer, H.; Buchner, K.; Winter, G.; Sorensen, T. L.; Cardin, D. J.; Brazier, J. A.; Cardin, C. J. Delta Chirality Ruthenium 'Light-Switch' Complexes Can Bind in the Minor Groove of DNA with Five Different Binding Modes. Nucl. Acids Res. 2016, 44 (19), 9472–9482. https://doi.org/10.1093/nar/gkw753.

(11) Sun, D.; Liu, Y.; Yu, Q.; Liu, D.; Zhou, Y.; Liu, J. Selective Nuclei Accumulation of Ruthenium(II) Complex Enantiomers That Target G-Quadruplex DNA. Journal of Inorganic Biochemistry 2015, 150, 90–99. https://doi.org/10.1016/j.jinorgbio.2015.04.003.

(12) Chao, X.-J.; Huang, C.-H.; Tang, M.; Yan, Z.-Y.; Huang, R.; Li, Y.; Zhu, B.-Z. Unusual Enantioselective Cytoplasm-to-Nucleus Translocation and Photosensitization of the Chiral Ru(II) Cationic Complex via Simple Ion-Pairing with Lipophilic Weak Acid Counter-Anions. Nucleic Acids Research 2023, 51 (7), 3041–3054. https://doi.org/10.1093/nar/gkad155.

(13) Friedman, A. E.; Chambron, J. C.; Sauvage, J. P.; Turro, N. J.; Barton, J. K. A Molecular Light Switch for DNA: Ru(Bpy)2(Dppz)2+. J. Am. Chem. Soc. 1990, 112, 4960–4962. https://doi.org/10.1021/ja00168a052.

(14) Bai, M.; Zeng, Z.; Li, L.; Wu, Q.; Zhang, Y.; Pan, T.; Mu, L.; Zhu, D.; Guan, S.; Xie, Q.; Mei, W. Chiral Ruthenium(II) Complex as Potent Radiosensitizer of 125 I through DNA-Damage-Mediated Apoptosis. RSC Adv. 2018, 8 (37), 20612–20618. https://doi.org/10.1039/C8RA03383H.

(15) De La Cueva-Alique, I.; Sierra, S.; Muñoz-Moreno, L.; Pérez-Redondo, A.; Bajo, A. M.; Marzo, I.; Gude, L.; Cuenca, T.; Royo, E. Biological Evaluation of Water Soluble Arene Ru(II) Enantiomers with Amino-Oxime Ligands. Journal of Inorganic Biochemistry 2018, 183, 32–42. https://doi.org/10.1016/j.jinorgbio.2018.02.018.

(16) Lovison, D.; Alessi, D.; Allegri, L.; Baldan, F.; Ballico, M.; Damante, G.; Galasso, M.; Guardavaccaro, D.; Ruggieri, S.; Melchior, A.; Veclani, D.; Nardon, C.; Baratta, W. Enantioselective Cytotoxicity of Chiral Diphosphine Ruthenium(II) Complexes Against Cancer Cells. Chemistry A European J 2022, 28 (33), e202200200. https://doi.org/10.1002/chem.202200200.

(17) McDonnell, U.; Kerchoffs, J. M. C. A.; Castineiras, R. P. M.; Hicks, M. R.; Hotze, A. C. G.; Hannon, M. J.; Rodger, A. Synthesis and Cytotoxicity of Dinuclear Complexes Containing Ruthenium(Ii) Bipyridyl Units Linked by a Bis(Pyridylimine) Ligand. Dalton Trans. 2008, No. 5, 667–675. https://doi.org/10.1039/B711080D.

(18) Wang, J.-Q.; Zhang, P.-Y.; Ji, L.-N.; Chao, H. A Ruthenium(II) Complex Inhibits Tumor Growth in Vivo with Fewer Side-Effects Compared with Cisplatin. Journal of Inorganic Biochemistry 2015, 146, 89–96. https://doi.org/10.1016/j.jinorgbio.2015.02.003.

(19) Yu, Q.; Liu, Y.; Wang, C.; Sun, D.; Yang, X.; Liu, Y.; Liu, J. Chiral Ruthenium(II) Polypyridyl Complexes: Stabilization of G-Quadruplex DNA, Inhibition of Telomerase Activity and Cellular Uptake. PLoS ONE 2012, 7 (12), e50902. https://doi.org/10.1371/journal.pone.0050902.

(20) Zhang, W.; Sun, Y.; Wang, J.; Ding, X.; Yang, E.; Martin, L. L.; Sun, D. Enantiomeric Selectivity of Ruthenium (II) Chiral Complexes with Antitumor Activity, in Vitro and in Vivo. Journal of Inorganic Biochemistry 2021, 216, 111339. https://doi.org/10.1016/j.jinorgbio.2020.111339.

(21) Ghosh, S.; Jana, B.; Ghosh, A.; Guldi, D. M.; Patra, A. The Impact of Aggregation of Quaterthiophenes on the Excited State Dynamics. J. Phys. Chem. Lett. 2021, 12 (13), 3424–3430. https://doi.org/10.1021/acs.jpclett.1c00440.

(22) Cole, H. D.; Roque, J. A.; Shi, G.; Lifshits, L. M.; Ramasamy, E.; Barrett, P. C.; Hodges, R. O.; Cameron, C. G.; McFarland, S. A. Anticancer Agent with Inexplicable Potency in Extreme Hypoxia: Characterizing a Light-Triggered Ruthenium Ubertoxin. J. Am. Chem. Soc. 2022, 144 (22), 9543–9547. https://doi.org/10.1021/jacs.1c09010.

(23) Roque III, J. A.; Cole, H. D.; Barrett, P. C.; Lifshits, L. M.; Hodges, R. O.; Kim, S.; Deep, G.; Francés-Monerris, A.; Alberto, M. E.; Cameron, C. G.; McFarland, S. A. Intraligand Excited States Turn a Ruthenium Oligothiophene Complex into a Light-Triggered Ubertoxin with Anticancer Effects in Extreme Hypoxia. J. Am. Chem. Soc. 2022, 144 (18), 8317–8336. https://doi.org/10.1021/jacs.2c02475.

4.7 SUPPORTING INFORMATION

4.7.1 Materials and Methods

Synthesis and Characterization of Racemates

The parent complexes ***rac*-Ru-3T** and ***rac*-Ru-4T** was prepared as previously described.[1] The characterization data pertaining to the racemates may be found in Figure S1–S8.

*Enantiomeric resolution of **rac**-**Ru-3T** and **rac**-**Ru-4T***

Parent complexes ***rac*-Ru-3T** and ***rac*-Ru-4T** were resolved and assigned as being the Λ or Δ enantiomer using our previously described techniques.[1] All preparative and analytical separations were conducted using a JASCO (Tokyo, Japan) semi-prep supercritical fluid chromatograph (SFC-2000-7). The instrument allows for flow rates up to 20 mL/min and a pressure limit of 500 bar. The system contains two HPLC pumps (PU-2086), an autosampler (AS-2059-SFC) with a 100 µL loop, a 6-column selector (HV-2080-06), a column oven (CO-2060), a UV detector (UV-2075), and a back pressure regulator (BP-2080). The carbon dioxide pump was held at a constant $^{-}$10 °C by a Julabo (Seelbach, Germany) chiller to ensure the CO_2 stays liquefied, and the column oven was held at a constant 40 °C. Separations were done on the Larihc CF6-RN phase which contains *R*-(-)-1-(1-Napthyl)ethyl (RN) isocyanate functionalized cyclofructan-6 (CF-6) bonded to 5 µm fully porous silica particles. Columns were synthesized and packed by AZYP, LLC (Arlington, Tx) in the dimensions of 250 x 4.6 (i.d.) for analytical separations and 250 x 7.8 (i.d.) for preparative separations. For preparative separations, solutions were made at 10 mg/mL in methanol, introduced to the system every ~7 minutes in 100 µL full loop injections (~1 mg of racemate), signal was monitored at 500 nm, and fractions were collected using the SCF-Vch-Bp automated valve unit. The SFC system and the valve unit were both controlled by JASCO's Chrom Nav (ver. 2). The mobile phase was 50/50 (v/v) CO_2/modifier where the modifier is 100/0.25/0.25 (v/v/v) MeOH/TFA/TEA. For the 4.6 (i.d.) column a flow rate of 4 mL/min was used and for the 7.8 (i.d.) column a flow rate of 12 mL/min was used to approximately match the linear velocity between the columns. The collected fractions were concentrated under reduced pressure, resuspended in water, then extracted with DCM several times to remove any residual ions from the eluent. The DCM fractions were then combined, concentrated under reduced pressure, and passed through a 12-inch column of HCl-treated Amberlite IRA-420 using MeOH as the eluent. The collected fractions were concentrated under reduced pressure and used for subsequent photobiological assays. To evaluate the integrity of each of the enantiomerically resolved samples we evaluated each batch of ***æ/* ş-Ru-4T** via ^{1}H NMR and ^{19}F NMR to confirm that all TFA and TEA had been removed from the sample. The final yields of the enantiomerically resolved complexes are as follows: 50 mg of ***rac*-Ru-3T** yielded 13 mg of **æ-Ru-3T** (99.1% ee), 8 mg of **ş-Ru-3T** (>99.8% ee by HPLC) (42% rec); 70 mg of ***rac*-Ru-4T** yielded 20 mg of **æ-Ru-4T** (98.4% ee by HPLC), 20 mg of **ş-Ru-4T** (98.8% ee by HPLC) (67% rec).

Two additional batches of ***æ/* ş-Ru-4T** were prepared in order to evaluate the batch-to-batch variability of the enantiomerically resolved complexes, which are grouped as “A”, “B”, or “C” in the photobiological assays in Figure S11 and Table S3–S7. Batch B was prepared following the exact procedure described above. Batch C was resolved using a mobile phase of 50/50 (v/v) CO_2/modifier where the modifier is 100/0.25 (v/v) MeOH/TFA, and was then concentrated under reduced pressure, redissolved in minimal MeOH, and passed through a 12-inch column of HCl-treated Amberlite IRA-420 using MeOH as the eluent.

Cell culture

Following previously described techniques[2,3] resazurin-based assays were used to assess the *in vitro* (photo)cytotoxicity of the compounds in this series against both normoxic and hypoxic male human melanoma cells (SK-MEL-28, ATCC HTB-72).

The nonpigmented male human melanoma cells (SK-MEL-28, ATCC HTB-72) were cultured and maintained using EMEM (BioWhittaker, 12-125Q) media, which was further enriched with 10% FB essence (VWR, 10803-034) and 1% Gluta Grow (L-alanyl-L-glutamine; VWR 45001-086). These cells were incubated in a water-jacketed incubator (ThermoFisher Thermo Scientific 4110), which was set at 37°C. The humidity was maintained at or above 90%, and the CO_2 was kept at a 5% concentration. Split ratios ranging from 1:2 to 1:5 were used to achieve a cellular density between 150,000–400,000 cells·ml^{-1}. These cells were used within

15 passages of their procurement. Photobiological assays were conducted on SK-MEL-28 cells after being dispensed into 384-well plates at a seeding density of 3000 cells per well.

Cellular assays

We evaluated the photobiological potency of each compound by executing dose-response cell viability assays on 384-well plates. We applied a concentration range from 1×10^{-3} to 300 μM for ***rac*/*æ*/ş-Ru-3T** and a range of 1×10^{-12} to 300 μM for ***rac*/*æ*/ş-Ru-4T**. To facilitate rapid thermal interchange, irrespective of the experimental setup, we limited the stacking of well plates in the incubator to only two high. Additional tests on **Ru-3T** and **Ru-4T** were performed to assess the consistency between different assays, as reflected in Figure S10–Figure S11.

Ru(II) compound solutions

Stock solutions for **Ru-3T** and **Ru-4T** were formulated at 21 mM and 25 mM concentrations respectively, using 100% DMSO. The remaining compounds had their stock solutions prepared at a concentration of 5 mM in a mixture of 10% v/v DMSO and water. Dilutions were created using 1x Dulbecco's Phosphate-Buffered Saline (DPBS) devoid of Ca^{2+} or Mg^{2+}, which was obtained by diluting 10x DPBS (Corning 20-031-CV). The highest concentration (300 μM) of the diluted solutions contained less than 1.2% v/v DMSO. Stock solutions were stored in glass vials with PTFE-lined caps and these vials were wrapped in aluminum foil to prevent light exposure. All stock solutions were kept at −20°C, wrapped in foil, when not in use.

Cytotoxicity and photocytotoxicity

Following our recent methodology,[2,3] the compounds were put through (photo)cytotoxicity screening using a resazurin assay in a 384-well plate configuration. We used Greiner Bio-One 384-well plates (781182) for this procedure. Inside the biosafety cabinet, DPBS was dispensed into the outermost two wells (144 wells in total), each receiving a volume of 75 µL, creating a boundary. For the experimental arrangement, we used an electronic multichannel pipettor. All inner wells, encompassing sample wells, positive control wells, and negative control wells, had a total volume of 40 µL per well. The sample wells contained 10 µL of complete media, 20 µL of cell slurry (3000 SK-MEL-28 cells per well), and 10 µL of compound dilutions in DPBS. The positive control wells (12 in total) contained 10 µL of complete media, 20 µL of cell slurry (3000 cells per well), and 10 µL of DPBS. The negative control wells (12 in total) contained 30 µL of complete media and 10 µL of DPBS. Prior to cell seeding, the well plates were preincubated with the dispensed media at 37°C, 5% CO_2, and a relative humidity of at least 90%. Post cell seeding, the plates were gently agitated by tilting in all directions and subsequently placed in the incubator for 2-3 hours to promote cell attachment.

During the incubation stage, we arranged serial dilutions of the compounds in sterile 384-well plates, utilizing DPBS as the solvent. For all compounds, dilutions were arrayed over nine concentrations from 1×10^{-3} to 300 µM. Additionally, for **Ru-4T**, we included an extra nine concentrations spanning from 1×10^{-12} to 1×10^{-3} µM. To safeguard against premature cellular activation and limit exposure to light, we ensured the lights in the biosafety cabinet were switched off while preparing the dilutions. The 384-well plates, along with their lids, underwent a pre-incubation period of 2–3 hours before we dispensed the compound dilutions at a volume of 10 µL per well. Experiments were performed in triplicate, and the sample wells were arranged row-wise, separated by every four rows.

The 384-well plates were subjected to overnight incubation, with a drug-to-light interval (DLI) oscillating between 13 to 20 hours. Post-incubation, the plates received light treatments which involved the delivery of approximately 100 J cm^{-2} of light at an intensity ranging from 18–24 mW cm^{-2}. The spectrum of light encompassed cool white visible light (400–700 nm), blue light (Prizmatix LED, 453 nm), green light (Prizmatix LED, 523 nm), and red light (Prizmatix LED, 633 nm). After light treatments, the plates experienced another day of incubation prior to the execution of final viability measurements. It is significant to highlight that edge effects surfaced on the 384-well plate, influencing the adjustment of the post-photodynamic therapy (PDT) period to one day (20–23 hours) for achieving cell viability equilibration, diverging from the conventional 48-hour period. We introduced prewarmed sterifiltered resazurin in a 0.2 M phosphate buffer (pH = 7.4) with a concentration of 0.3 mM into all wells of the plates, allotting a volume of 10 µL per well. The resazurin-stained plates then underwent a 4-hour incubation before the fluorometric measurements were conducted using a Molecular Devices M2e plate reader. These measurements included a 30-second shaking step, a bottom-read setup, an excitation wavelength of 530 nm, a long-pass filter at 570 nm, and an emission wavelength of 620 nm.

Hypoxia cytotoxicity and photocytotoxicity

Compounds were scrutinized under two distinct oxygen settings: normoxia (~18.5% O_2) and hypoxia (1% O_2). During the hypoxia treatment phase, the cells, after seeding, were allowed a 1–2-hour incubation at 37°C, 5% CO_2, and a minimum relative humidity of 90% under normoxic conditions, ensuring adequate cell adhesion. Following this, the plates made a transition to the specialized environment of a Biospherix Xvivo X3 chamber. Here, they were further incubated for 2–3 hours under settings of 1% O_2, 37°C, 5% CO_2, and ≥90% relative humidity. Post this phase, the compound dilutions were introduced in a biosafety cabinet.

The plates then resumed their residence in the Biospherix chamber for a DLI spanning 17–19 hours. To validate the hypoxic state, an immersive optical probe was deployed to measure the dissolved oxygen content within the chamber, which consistently registered between 5–7 µM. Once this hypoxic environment was confirmed, plates slated for light treatment were hermetically sealed within the Biospherix chamber using qPCR films from VWR (89134-428), notable for their low gas permeability and high transparency. This procedure was imperative for the study of the oxygen reliance of the photosensitizer (PS).

Upon completion of the light treatment, the sealing films were removed under the sterile confines of a biosafety cabinet. All the plates that underwent hypoxia treatment were then migrated to an incubator with normoxic conditions set at 37°C, 5% CO_2, and a relative humidity ≥90%. In a manner akin to their normoxic counterparts, these plates were afforded a further 20–23 hours of incubation ahead of the ultimate viability assessment.

Longitudinal studies

The consistency and reliability of the performance of the ***rac*/æ/ş-Ru-3T** and ***rac*/æ/ş-Ru-4T** complexes were rigorously examined over multiple assays using SK-MEL-28. The data from these repeated tests can be consulted in Figure S10, Figure S11, and Table S2–Table S7.

Each repetition was characterized by a uniquely randomized plate map to negate any unintended influences from stray light. Cells involved in these trials were between 10–15 passages.

Light devices and protocols.

For all biological assays, unless stated otherwise, a consistent fluence of 100 J cm^{-2} and an irradiance ranging between 18–22 mW cm^{-2} were employed. The light treatments utilized three different light sources for visible, green, and red light. These sources included a cool white LED panel from SOLLA-CREE, covering a spectral range of 400–700 nm with a maxima around 450 nm. Additionally, two UHP-LEDs from Prizmatix were used, emitting light at 523 nm (green) and 633 nm (red) respectively. The spectral outputs of these light sources can be referenced in Figure S9.

Data manipulation and statistics

Data from the resazurin cell viability assay were corrected for background by subtracting the signal from wells that contained only media and DPBS (no cells) and normalized relative to untreated cells. Because the absorbance and emission of the metal complexes can interfere with the resazurin fluorescence signal, wells treated with the highest concentrations of metal complex were also observed under a microscope. If no cells were detected, these wells were assigned a value of zero. A more detailed discussion of assay limitations for this class of complexes is provided in our 2019 review.[4]

Data points obtained from resazurin fluorescence were fit to a three-parameter log-logistic (Equation S1) and logistic model (Equation S2) using GraphPad Prism 8.4.0. We use Equation S1 for summary log(EC_{50}) plots (Figure 12a) and in the dose-response curves shown in Figure 13, but we use Equation S2 for data in log(PI) plots (Figure 12b) as well as the tabulated EC_{50} and PI values (Table 1 and Table S2–Table S7).

$$Y = \mathrm{Bottom} + \frac{(Top - Bottom)}{(1 + (10^{Log(EC_{50} - X) \times Hillslope})} \qquad \text{Equation S1}$$

$$Y = \mathrm{Bottom} + \frac{(Top - Bottom)}{\left(1 + (EC_{50}/X)^{Hillslope}\right)}$$

Equation S2

Experiments were completed in triplicate and replicated data points are always plotted with error bars denoting the standard deviation (SD). All EC_{50} values are reported alongside the standard error of the mean (SEM). In cases where the hill slope was too steep to calculate a representative SEM, the SEM was labelled as not determined (n.d.). Phototherapeutic indices (PI) are reported as the ratio of dark to light EC_{50} values and serve as a phototherapeutic efficacy benchmark. Any summary plots showing Log EC_{50} and Log PI values of the entire series of complexes are plotted with SEMs from log-logistic fits.

4.7.2 Synthetic Characterization

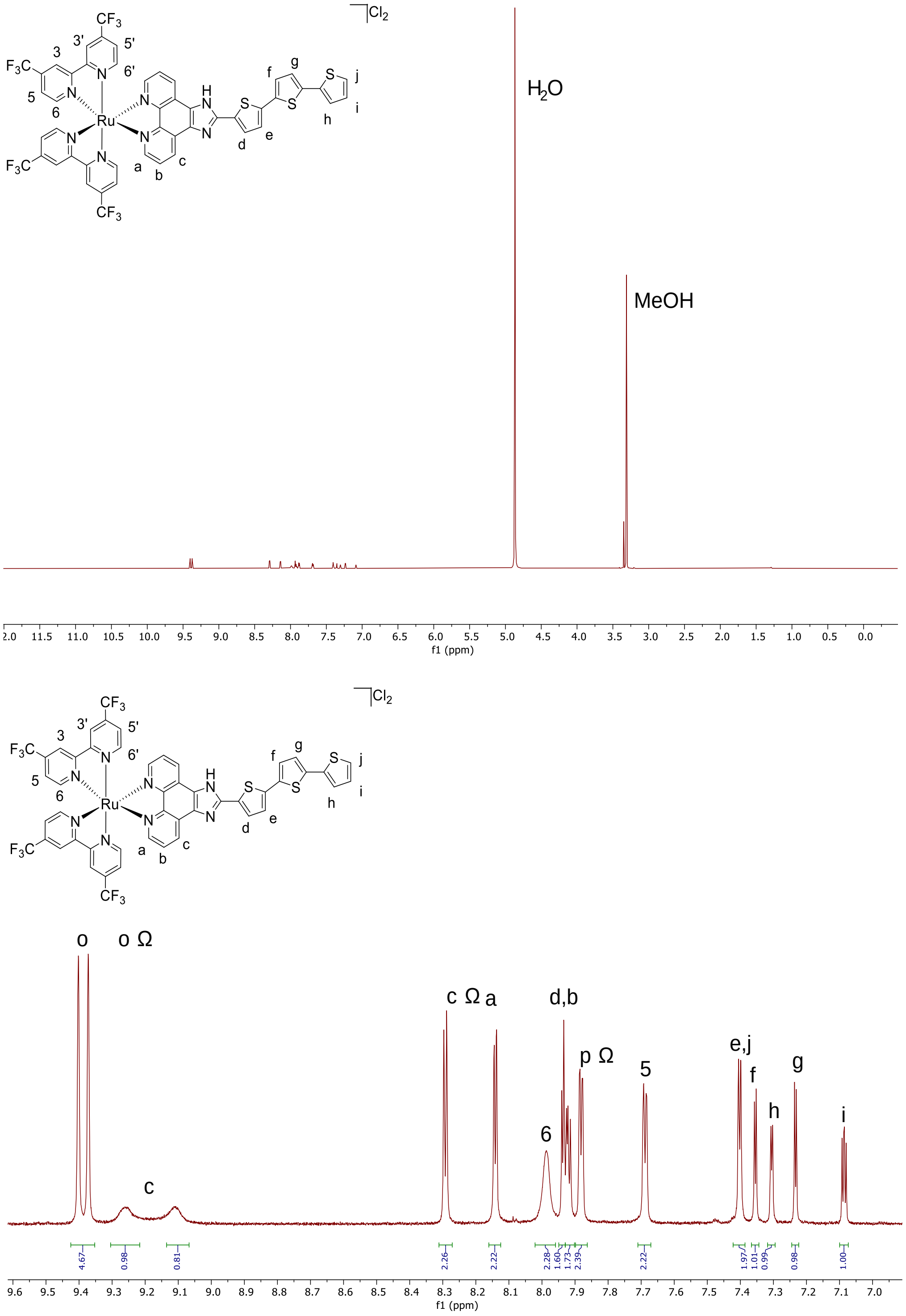

Figure S1. ^{1}H NMR (700 MHz) spectra of ***rac*-Ru-3T** in MeOD-d$_3$ at 298 K with structure labelling and ^{1}H NMR assignments. Top: Full spectrum. Bottom: Zoom of aromatic region from 6.9–9.6 ppm.

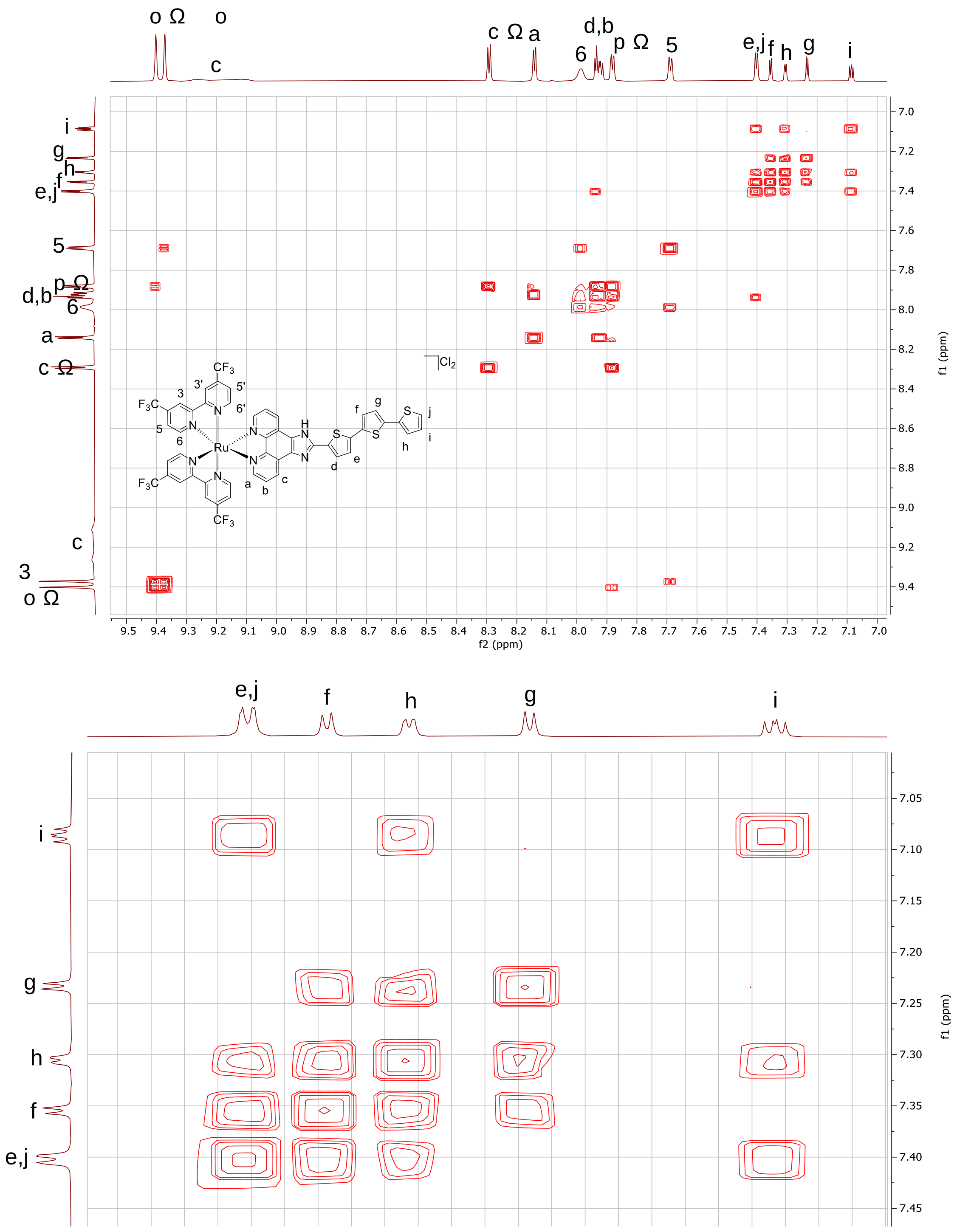

Figure S2. ^1H-^1H COSY (700 MHz) NMR Spectra of ***rac*-Ru-3T** in MeOD-d_3 at 298 K with structure labelling and ^1H NMR assignments. Top: Zoom of aromatic region. Bottom: zoom of aromatic thiophene signals.

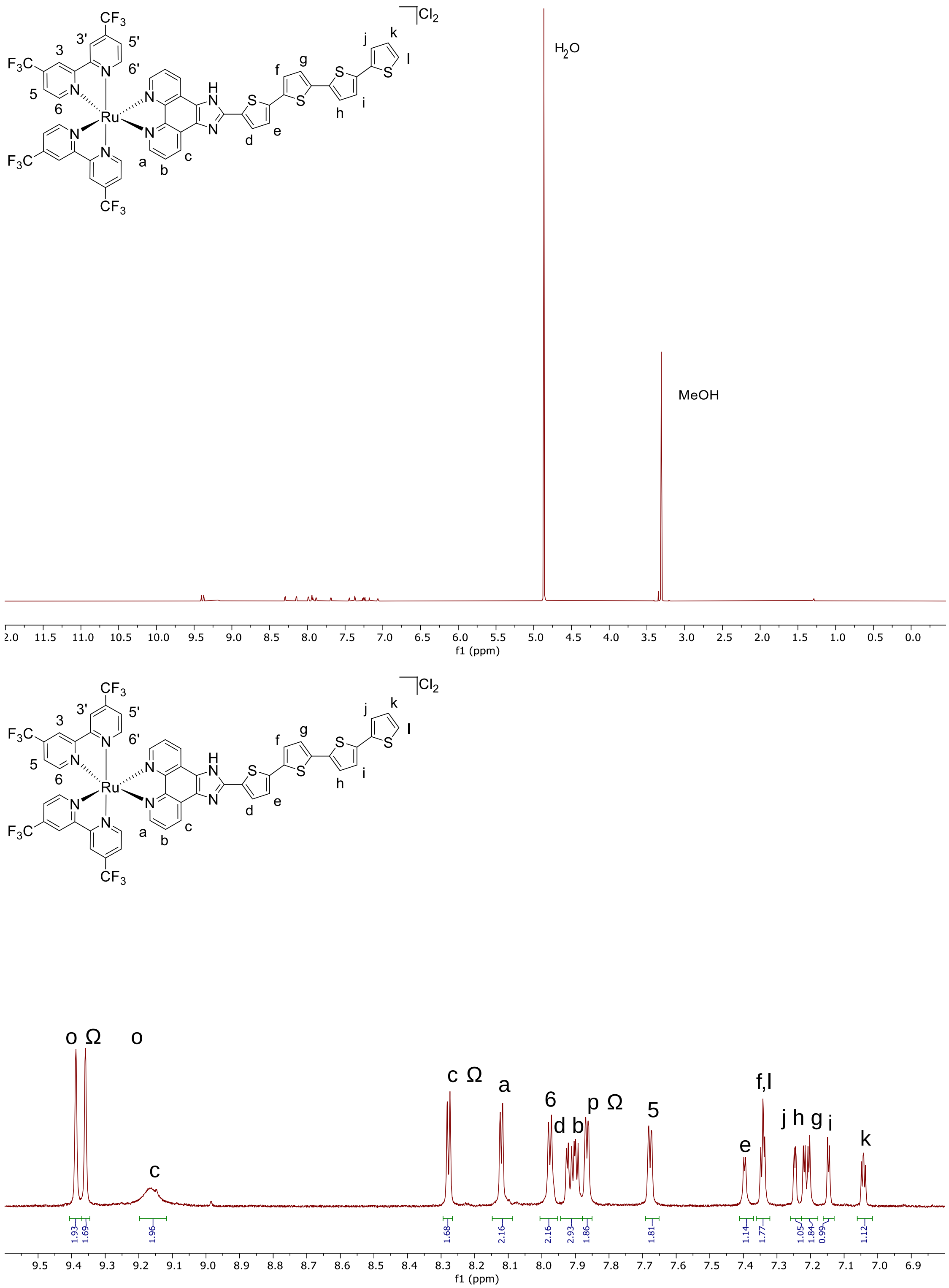

Figure S3. ^{1}H NMR (700 MHz) spectra of ***rac*-Ru-4T** in MeOD-d_3 at 298 K with structure labelling and ^{1}H NMR assignments. Top: Full spectrum. Bottom: Zoom of aromatic region from 6.8—9.6 ppm.

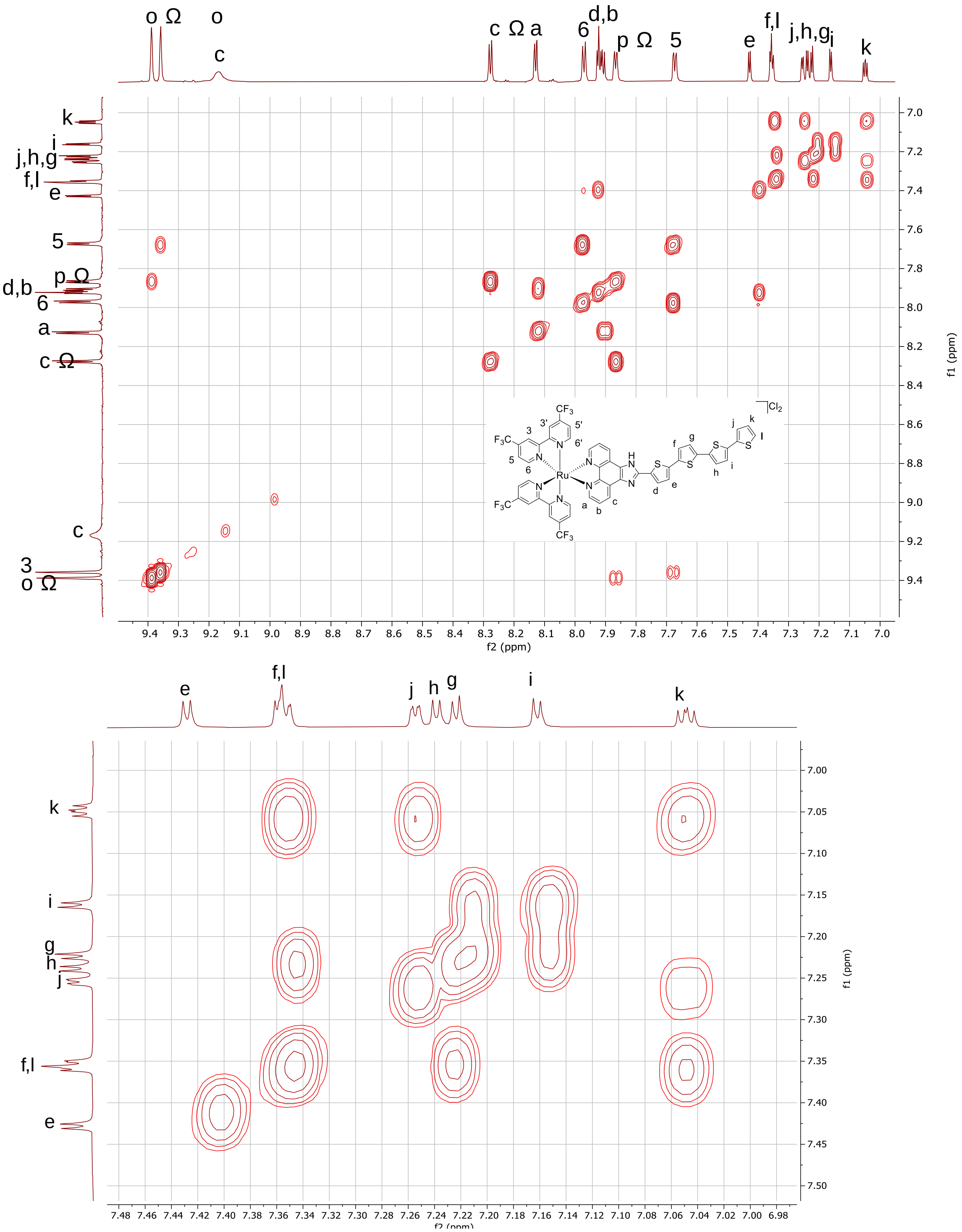

Figure S4. ^1H-^1H COSY NMR (700 MHz) spectra of ***rac*-Ru-4T** in MeOD-d_3 at 298 K with structure labelling and ^1H NMR assignments, aromatic region. Top: Zoom of entire aromatic region. Bottom: Zoom of aromatic region highlighting key thiophene peaks.

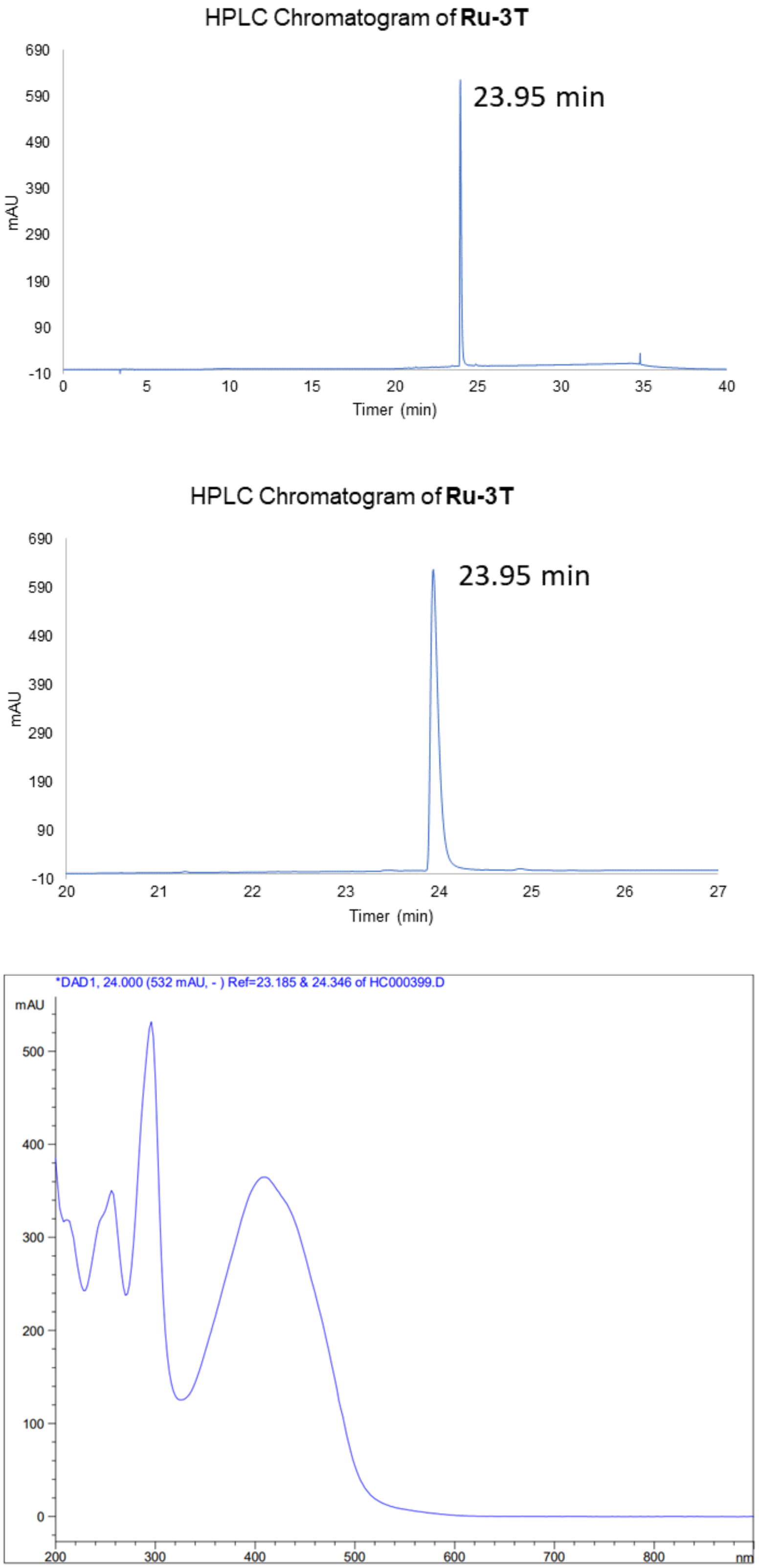

Figure S5. (top) HPLC chromatogram for ***rac*-Ru-3T** collected at the following wavelengths: 285 nm. (middle) Zoom of HPLC chromatogram for ***rac*-Ru-3T** collected at 285 nm. (bottom) Overlay of UV-Vis absorption spectra of HPLC Chromatogram peaks of ***rac*-Ru-3T** at 285 nm.

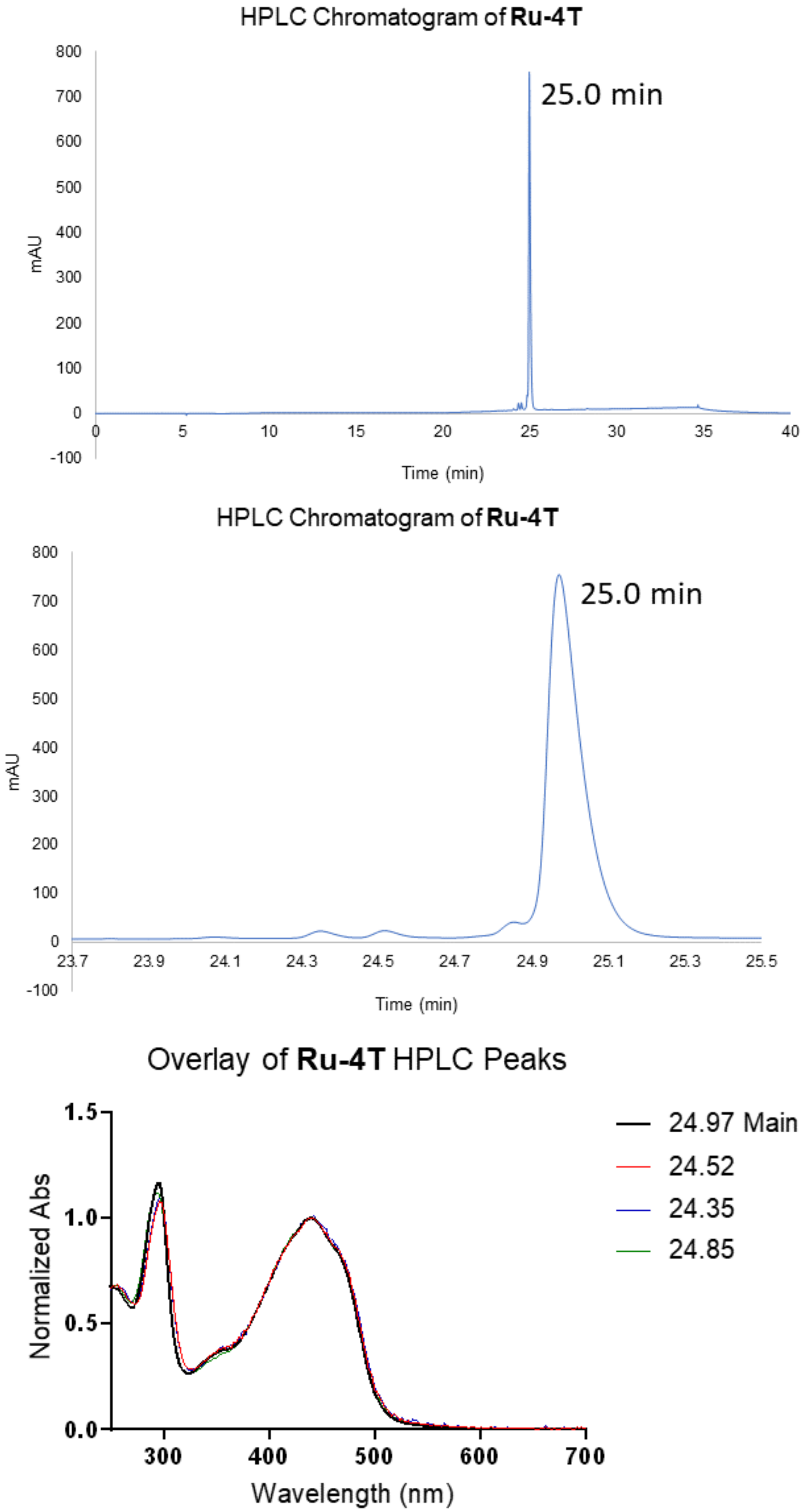

Figure S6. (a) HPLC chromatogram for ***rac*-Ru-4T** collected at the following wavelengths: 285 nm. (b) Zoom of HPLC chromatogram for ***rac*-Ru-4T** collected at the following wavelengths: 285 nm. (c) Overlay of UV-Vis absorption spectra of HPLC Chromatogram peaks of ***rac*-Ru-4T** at 285 nm.

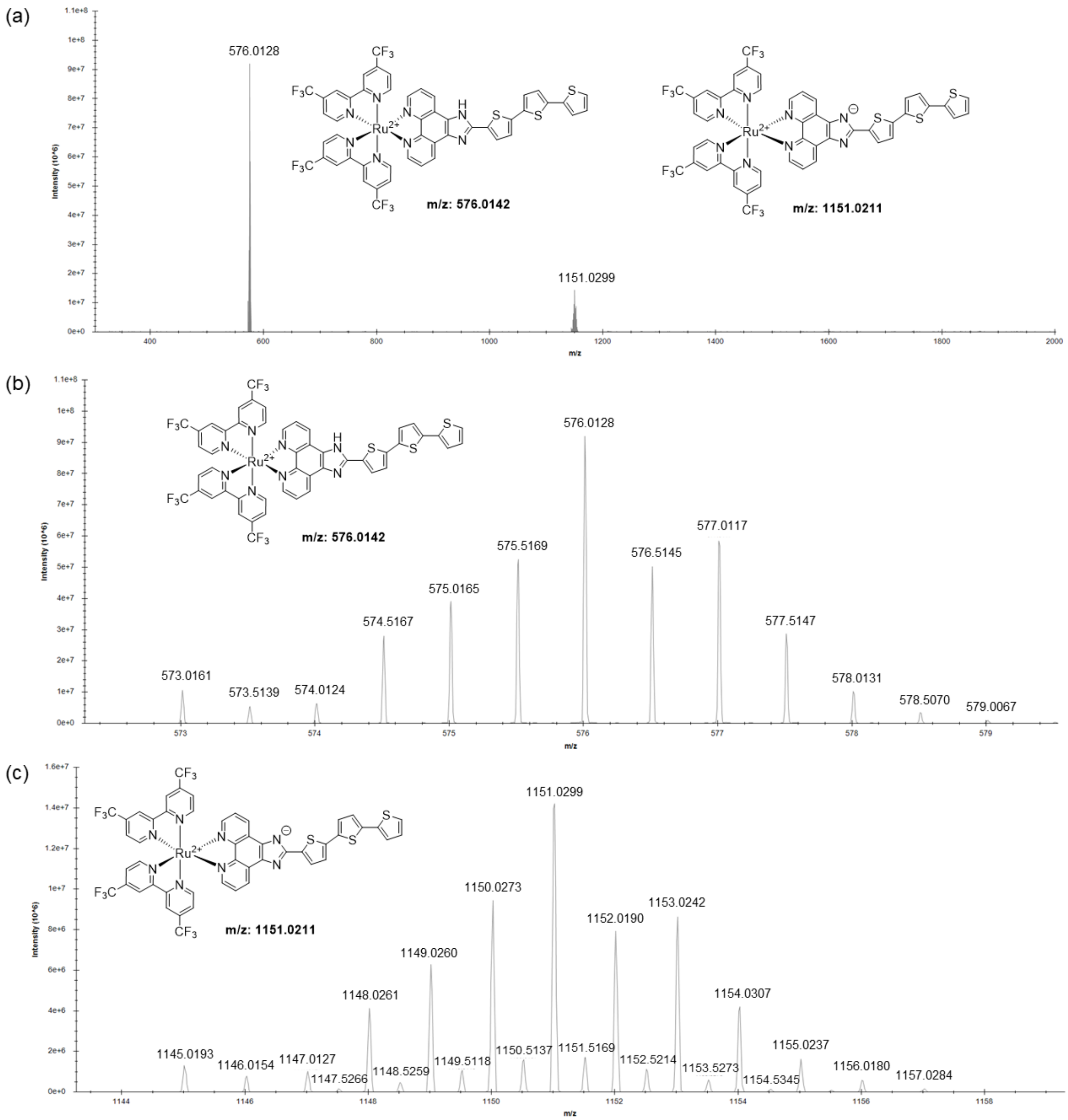

Figure S7. (a) High resolution ESI+-MS spectrum for ***rac*-Ru-3T** (b) Zoom of 576.0128 m/z showing isotopic distribution. (c) Zoom of 1151.0299 m/z showing isotopic distribution.

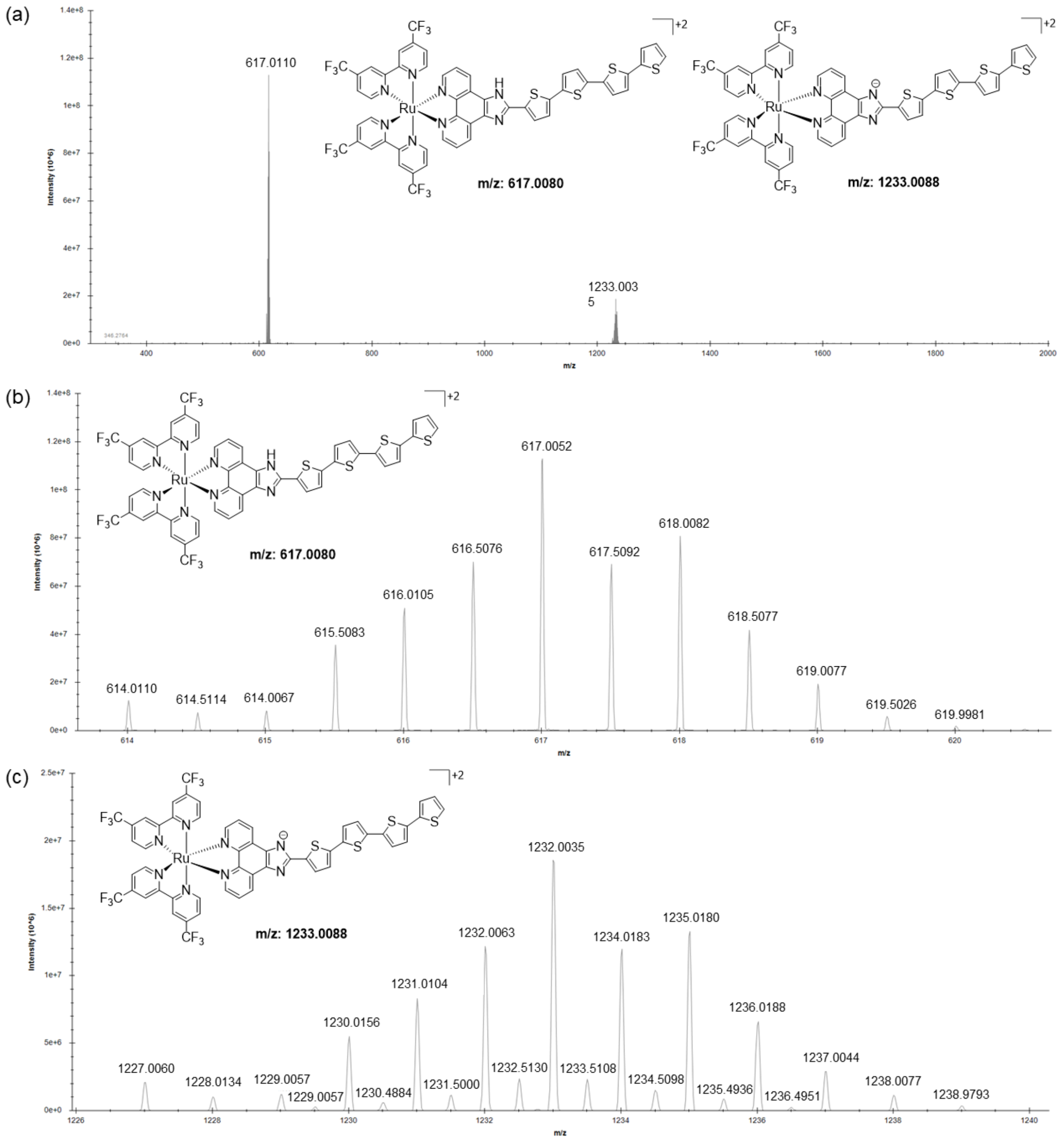

Figure S8. (a) High resolution ESI$^+$-MS spectrum for ***rac*-Ru-4T** (b) Zoom of 617.0052 m/z showing isotopic distribution. (c) Zoom of 1232.0035 m/z showing isotopic distribution.

Table S1. Analytical HPLC method using the Hypersil GOLD C_{18} Column.

	time (min)	%MeCN	%Water
Pre-run	20	2	98
Run	0	2	98
	2	5	95
	5	30	70
	15	30	70
	20	60	40
	30	95	5
	35	2	98
	40	2	98
Post-run	10	2	98
Flow rate (mL min^{-1})	1		

Both eluents contain 0.1% optima grade formic acid with runs involving a 20 µL injection at 50–200 µM of metal complex dissolved in optima grade MeOH.

4.7.3 Photobiological Evaluation

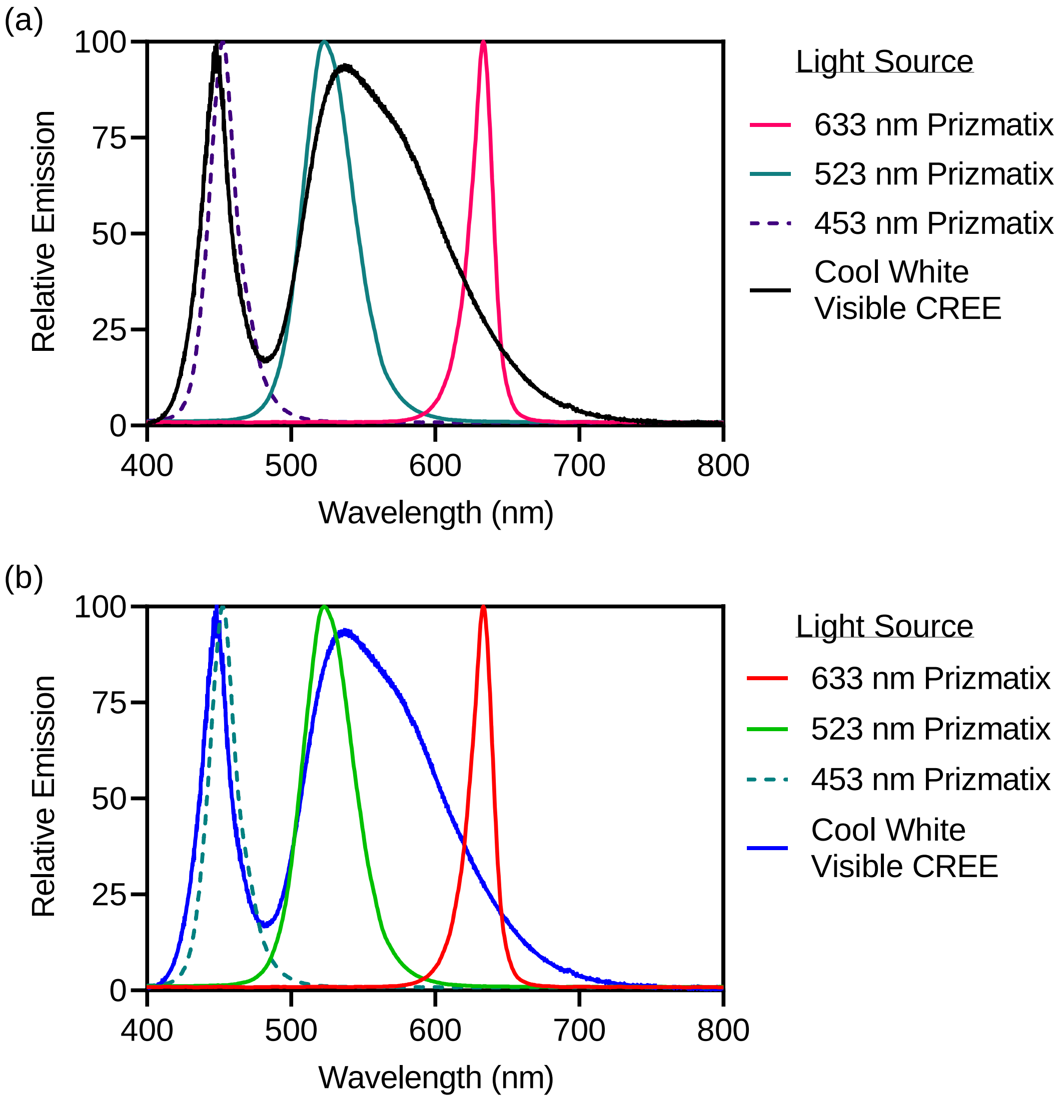

Figure S9. Relative spectral emissions or output of the light sources applied in photobiological studies manufacturer of the LED chip and/or light device is indicated (Prizmatix or CREE). Two color schemes are shown with (a) being colorblind-friendly and (b) matching colors used in reported biological plots (approximately matching apparent colors).

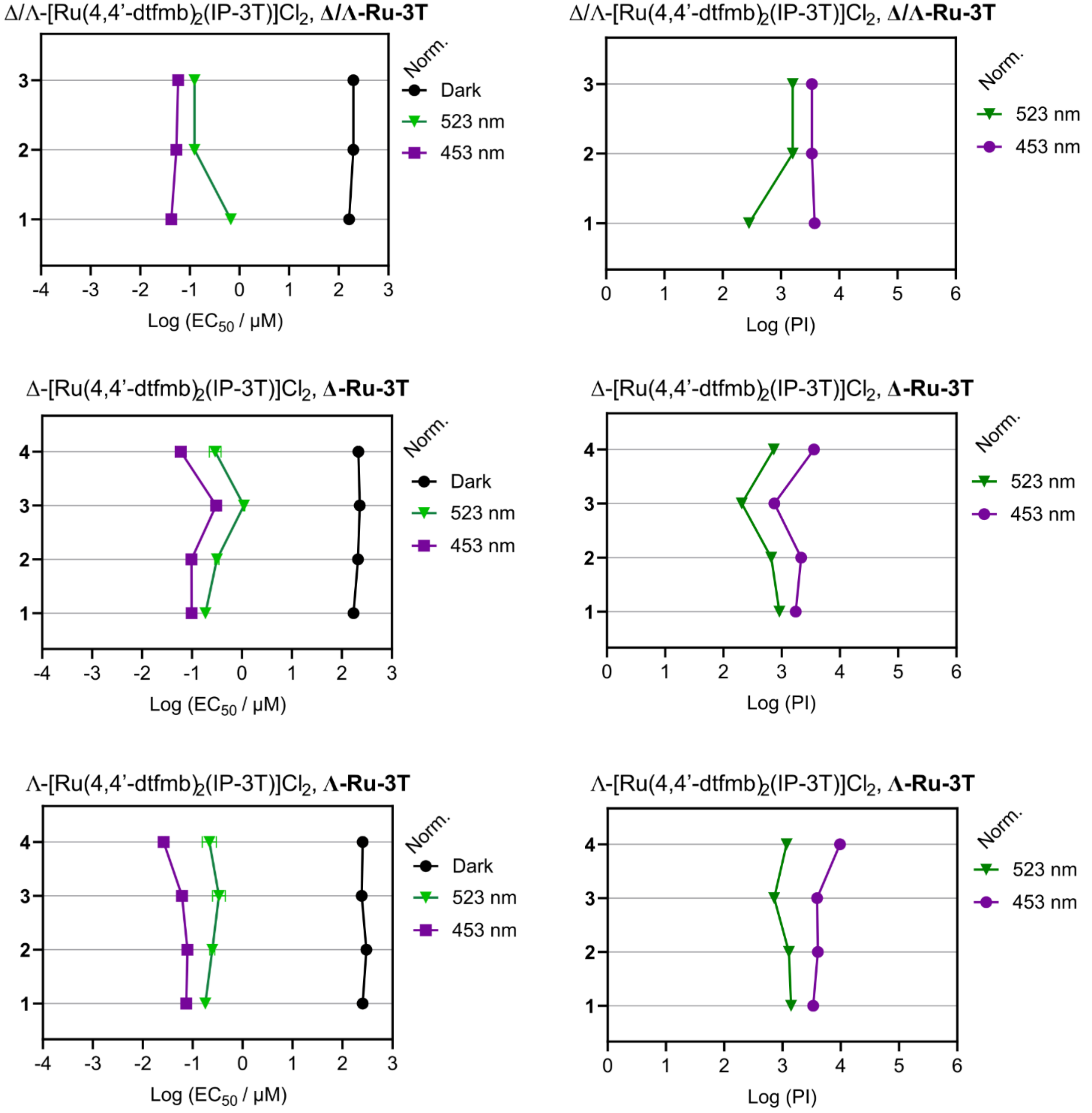

Figure S10. Interassay cytotoxicity and photocytotoxicity of **rac-Ru-3T** (top), **æRu-3T** (middle), and **ş-Ru-3T** (bottom) in normoxic-treated SK-MEL-28 melanoma cells. (EC$_{50}$ ± SEM) values (left) and PI values (right). Treatments included dark (0 J cm^{-2}) and 100 J cm^{-2} doses of 523 nm and 453 nm light.

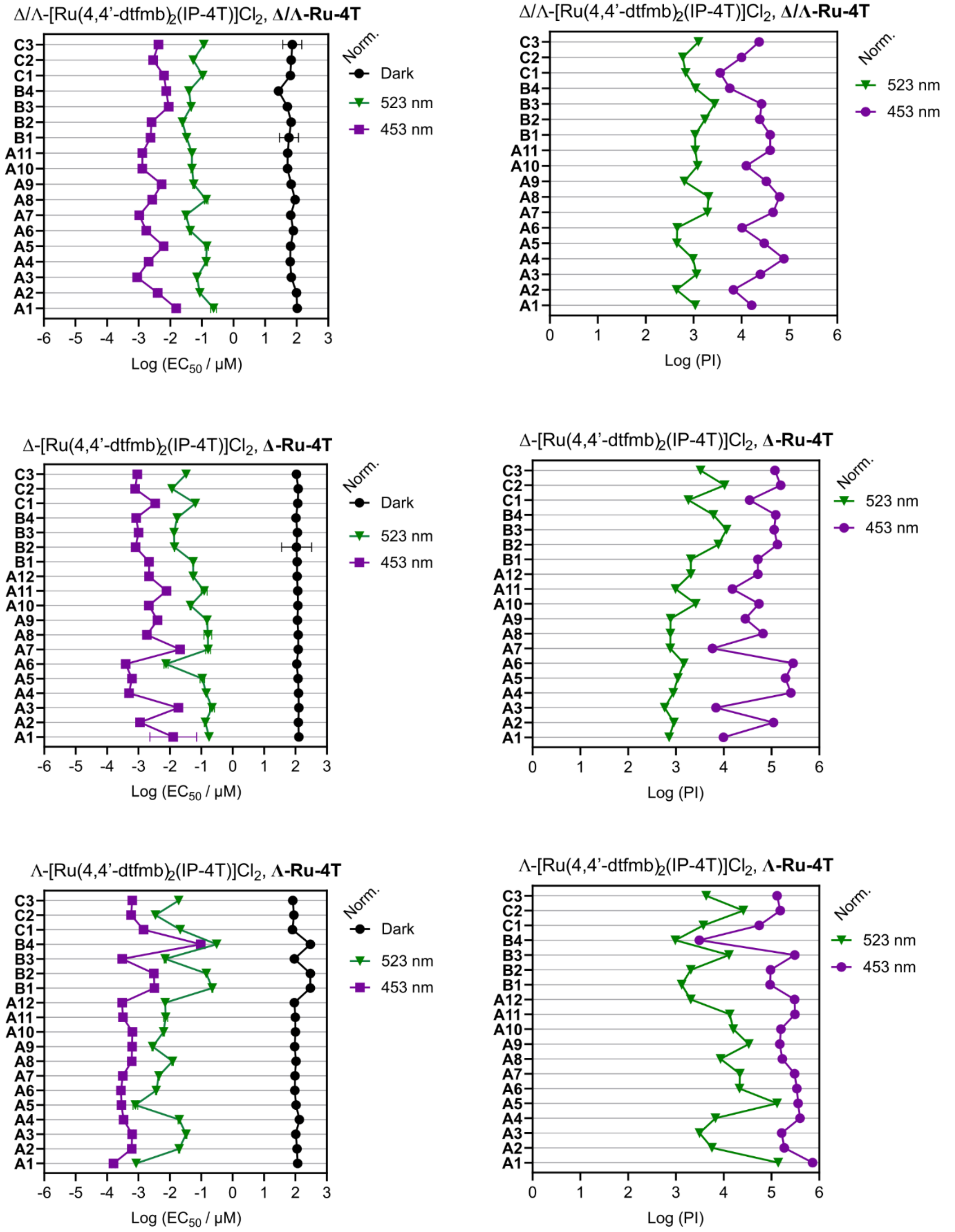

Figure S11. Interassay cytotoxicity and photocytotoxicity of ***rac*-Ru-4T** (top), **æRu-4T** (middle), and **ş-Ru-4T** (bottom) in normoxic-treated SK-MEL-28 melanoma cells. (EC$_{50}$ ± SEM) values (left) and PI values (right). Treatments included dark (0 J cm^{-2}) and 100 J cm^{-2} doses of 523 nm and 453 nm light. The experiment codes are on the y-axis and they indicate the batch of material that was used as well as the total number of runs for each batch. The total number of assays ran is 12.

Table S2. Interassay performance: cytotoxicity and photocytotoxicity of ***rac*-Ru-3T** in normoxic-treated (~18.5% O_2) male SK-MEL-28 melanoma cells.

	Resazurin-Normoxia (~18.5% O_2) *rac*-Ru-3T Repeats					
	EC$_{50}$ ± SEM (μM)			PI[d]		
Repeat	Dark	Blue[a]	Green[b]	Blue[a]	Green[b]	**Assay Batchcode**
1*	192 ± 8	0.22 ± 0.027	0.016 ± n.d.	870	12000	GS9-104
2	160 ± 7	0.043 ± 0.0044	0.57 ± n.d.	3700	280	GS9-108
3	200 ± 14	0.058 ± n.d.	0.12 ± n.d.	3400	1600	GS9-110

Light treatments were approximately 100 J cm^{-2} delivered at 18–22 mW cm^{-2}. [a] blue 453 nm, [b] green 523 nm, [c], [d] PI = phototherapeutic index (dark EC$_{50}$ / light EC$_{50}$), [e] cool white visible light (400-700 nm) used in lieu of blue light *original run in Table 1.

Table S3. Interassay performance: cytotoxicity and photocytotoxicity of **æRu-3T** in normoxic-treated (~18.5% O_2) male SK-MEL-28 melanoma cells.

	Resazurin-Normoxia (~18.5% O_2) æRu-3T Repeats					
	EC_{50} ± SEM (μM)			PI[d]		
Repeat	Dark	Blue[a]	Green[b]	Blue[a]	Green[b]	**Assay Batchcode**
1	170 ± 9	0.098 ± n.d.	0.19 ± n.d.	1745	900	GS9-94
2*	210 ± 7	0.097 ± n.d.	0.32 ± 0.031	2165	656	GS9-104
3	230 ± 8	0.30 ± 0.034	1.1 ± 0.03	760	207	GS9-108
4	210 ± 13	0.059 ± 0.014	0.29 ±0.078	3610	734	GS9-110

Light treatments were approximately 100 J cm^{-2} delivered at 18–22 mW cm^{-2}. [a] blue 453 nm, [b] green 523 nm, [c], [d] PI = phototherapeutic index (dark EC_{50} / light EC_{50}), [e] cool white visible light (400-700 nm) used in lieu of blue light *original run in Table 1.

Table S4. Interassay performance: cytotoxicity and photocytotoxicity of **ş-Ru-3T** in normoxic-treated (~18.5% O_2) male SK-MEL-28 melanoma cells.

	Resazurin-Normoxia (~18.5% O_2) ş-Ru-3T Repeats					
	EC_{50} ± SEM (µM)			PI[d]		
Repeat	Dark	Blue[a]	Green[b]	Blue[a]	Green[b]	**Assay Batchcode**
1	250 ± 17	0.074 ± n.d.	0.18 ± n.d.	3400	1400	GS9-94
2*	>300	0.079 ± n.d.	0.25 ± 0.029	3800	1200	GS9-104
3	240 ± 8	0.061 ± 0.0059	0.34 ± 0.10	4000	710	GS9-108
4	250 ± 15	0.026 ± 0.0021	0.22 ± 0.07	9800	1200	GS9-110

Light treatments were approximately 100 J cm^{-2} delivered at 18–22 mW cm^{-2}. [a] blue 453 nm, [b] green 523 nm, [c], [d] PI = phototherapeutic index (dark EC_{50} / light EC_{50}), [e] cool white visible light (400-700 nm) used in lieu of blue light. *original run in Table 1.

Table S5. Interassay performance: cytotoxicity and photocytotoxicity of ***rac*-Ru-4T** in normoxic-treated (~18.5% O_2) male SK-MEL-28 melanoma cells. The “Run” column indicates the total number of assays on one complex, and the “Experimental Code” indicates which batch was used as well as the total number of assays with that batch.

		Resazurin-Normoxia (~18.5% O_2) *rac*-Ru-4T Repeats				
		EC_{50} ± SEM (μM)			PI[d]	
Run	Experiment Code	Dark	Visible[c]	Green[b]	Visible[c]	Green[b]
1*	**A1**	105 ± 3	(6.4 ± 0.64)*10^{-3} [e]	0.097 ± 0.0058	16000[e]	1100
2	**A2**	104 ± 3	(15.0 ± 2.1)*10^{-3} [e]	0.24 ± 0.049	6900[e]	430
3	**A3**	99 ± 3.8	(4.0 ± 0.27)*10^{-3} [e]	0.086 ± n.d.	25000[e]	1200
4	**A4**	68 ± 1.3	(0.89 ± n.d.)*10^{-3}	0.070 ± 0.0027	77000	970
5	**A5**	63 ± 0.7	(2.1 ± 0.15)*10^{-3}	0.14 ± 0.012	30000	450
6	**A6**	64 ± 1.2	(6.2 ± 0.31)*10^{-3}	0.14 ± 0.019	10000	460
7	**A7**	79 ± 1.5	(1.7 ± 0.13)*10^{-3}	0.043 ± 0.0033	45000	1800
8	**A8**	65 ± 1.5	(1.1 ± n.d.)*10^{-3}	0.032 ± 0.0028	62000	2000
9	**A9**	90 ± 1.1	(2.7 ± 0.35)*10^{-3}	0.14 ± 0.017	33000	640
10	**A10**	67 ± 1.3	(5.3 ± 0.43)*10^{-3}	0.055 ± 0.0037	13000	12000
11	**A11**	52 ± n.d.	(1.3 ± 0.10)*10^{-3}	0.048 ± 0.0037	40000	1000
12	**B1**	57 ± 2.0	(2.4 ± 0.11)*10^{-3}	0.033 ± 0.0021	24000	1700
13	**B2**	67 ± 2.4	(2.6 ± 0.18)*10^{-3}	0.024 ± 0.0075	26000	2700
14	**B3**	51 ± n.d.	(0.89 ± n.d.)*10^{-3}	0.046 ± 0.0034	5700	1100
15	**B4**	27 ± 1.2	(0.74 ± 0.17)*10^{-3}	0.039 ± 0.0035	3600	680
16	**C1**	64 ± 1.3	(6.4 ± 0.55)*10^{-3}	0.11 ± n.d.	10000	600
17	**C2**	67 ± 1.1	(2.9 ± 0.41)*10^{-3}	0.054 ± 0.0804	23000	1200

Light treatments were approximately 100 J cm^{-2} delivered at 18–22 mW cm^{-2} [a]blue 453 nm, [b]green 523 nm, [c]cool white visible (400–700 nm), [d]PI = phototherapeutic index (dark EC_{50} / light EC_{50}),. [e]blue 453 nm used, *original run in repeat 0 from Table 1.

Table S6. Interassay performance: cytotoxicity and photocytotoxicity of **æRu-4T** in normoxic-treated (~18.5% O$_2$) male SK-MEL-28 melanoma cells.

		Resazurin-Normoxia (~18.5% O$_2$) æRu-4T Repeats				
		EC$_{50}$ ± SEM (μM)			PI[d]	
Run	Experiment Code	Dark	Visible[c]	Green[b]	Visible[c]	Green[b]
1*	**A1**	127 ± 5	0.014 ± n.d.	0.18 ± n.d.	9000	706
2	**A2**	123 ± 4	(1.1 ± 0.070)*10^{-3} [e]	0.14 ± 0.010	110000	879
3	**A3**	129 ± 4	(19.0 ± 1.1)*10^{-3} [e]	0.22 ± 0.038	6800	586
4	**A4**	126 ± 7	(0.50 ± 0.037)*10^{-3} [e]	0.14 ± n.d.	252000	900
5	**A5**	121 ± 4	(0.62 ± n.d.)*10^{-3}	0.11 ± 0.017	200000	1100
6	**A6**	110 ± 3	(0.39 ± 0.074)*10^{-3}	(7.55 ± 1.10)*10^{-3}	280000	15000
7	**A7**	122 ± 4	(0.021 ± 0.002)*10^{-3}	0.16 ± 0.030	5800	760
8	**A8**	123 ± 4	(1.9 ± 0.17)*10^{-3}	0.16 ± 0.046	66000	770
9	**A9**	116 ± 3	(4.1 ± 0.31)*10^{-3}	0.15 ± 0.012	28000	770
10	**A10**	120 ± 4	(2.2 ± 0.60)*10^{-3}	0.046 ± 0.0018	55000	2600
11	**A11**	118 ± 3	(7.8 ± 0.63)*10^{-3}	0.12 ± 0.028	15000	1000
12	**A12**	113 ± 3	(2.2 ± 0.30)*10^{-3}	0.055 ± 0.0025	52000	2100
13	**B1**	108 ± 3	(0.8 ± 0.16)*10^{-3}	0.0140 ± 0.0064	134000	7700
14	**B2**	115 ± 5	(1.0 ± n.d.)*10^{-3}	0.013 ± n.d.	114000	8500
15	**B3**	104 ± 3	(0.85 ± n.d.)*10^{-3}	0.017 ± 0.0157	123000	6100
16	**B4**	97 ± 3	(0.84 ± n.d.)*10^{-3}	0.017 ± 0.0112	11500	5700
17	**C1**	118 ± 3	(3.4 ± 0.28)*10^{-3}	0.065 ± n.d.	35000	1800
18	**C2**	122 ± 4	(0.78 ± n.d.)*10^{-3}	0.012 ± 0.0007	160000	10000

Light treatments were approximately 100 J cm^{-2} delivered at 18–22 mW cm^{-2} [a]blue 453 nm, [b] green 523 nm, [c] cool white visible (400–700 nm), [d] PI = phototherapeutic index (dark EC$_{50}$ / light EC$_{50}$),. [e] blue 453 nm used, *original run in repeat 0 from Table 1.

Table S7. Interassay performance: cytotoxicity and photocytotoxicity of **ş-Ru-4T** in normoxic-treated (~18.5% O_2) male SK-MEL-28 melanoma cells.

		Resazurin-Normoxia (~18.5% O_2) ş-Ru-4T Repeats				
		EC$_{50}$ ± SEM (μM)			PI[d]	
Run	Experiment Code	Dark	Visible[c]	Green[b]	Visible[c]	Green[b]
1*	**A1**	117 ± 3	(0.21 ± 0.016)*10^{-3}	(0.85 ± n.d.)*10^{-3}	560000	14000
2	**A2**	113 ± 3	(0.61 ± n.d.)*10^{-3} [e]	(20.0 ± 1.0)*10^{-3}	190000	5700
3	**A3**	103 ± 3	(0.63 ± 0.072)*10^{-3} [e]	(33.0 ± 1.8)*10^{-3}	160000	3100
4	**A4**	134 ± 7	(0.33 ± 0.016)*10^{-3} [e]	(20.0 ± 1.7)*10^{-3}	410000	6700
5	**A5**	105 ± 3	(0.29 ± 0.042)*10^{-3}	(0.80 ± n.d.)*10^{-3}	360000	13000
6	**A6**	96 ± 2.3	(0.28 ± 0.030)*10^{-3}	(3.7 ± 0.19)*10^{-3}	340000	21000
7	**A7**	98 ± 2.6	(0.32 ± 0.034)*10^{-3}	(4.5 ± 0.19)*10^{-3}	300000	22000
8	**A8**	105 ± 3	(0.62 ± n.d.)*10^{-3}	(12.2 ± 0.80)*10^{-3}	170000	8600
9	**A9**	95 ± 2.9	(0.63 ± n.d.)*10^{-3}	(2.8 ± 0.15)*10^{-3}	150000	34000
10	**A10**	101 ± 3	(0.64 ± n.d.)*10^{-3}	(6.3 ± 0.35)*10^{-3}	160000	16000
11	**A11**	99 ± 2.4	(0.32 ± 0.060)*10^{-3}	(7.4 ± 1.10)*10^{-3}	310000	13000
12	**A12**	93 ± 2.7	(0.30 ± 0.054)*10^{-3}	(7.2 ± 0.56)*10^{-3}	310000	130000
13	**B1**	>300	(3.2 ± 0.27)*10^{-3}	0.23 ± 0.016	94000	1300
14	**B2**	>300	(3.1 ± 0.20)*10^{-3}	0.15 ± n.d.	96000	2100
15	**B3**	>300	(97.0 ± n.d.)*10^{-3}	0.31 ± 0.030	3100	970
16	**B4**	>300	(96.0 ± n.d.)*10^{-3}	0.31 ± 0.026	3100	960
17	**C1**	82 ± 1.5	(1.5 ± 0.28)*10^{-3}	0.022 ± 0.0034	56000	3800
18	**C2**	90 ± 1.1	(0.59 ± n.d.)*10^{-3}	(3.49 ± 0.22)*10^{-3}	150000	26000

Light treatments were approximately 100 J cm^{-2} delivered at 18–22 mW cm^{-2} [a]blue 453 nm, [b] green 523 nm, [c] cool white visible (400–700 nm), [d] PI = phototherapeutic index (dark EC$_{50}$ / light EC$_{50}$),. [e] blue 453 nm used, *original run in repeat 0 from Table 1.

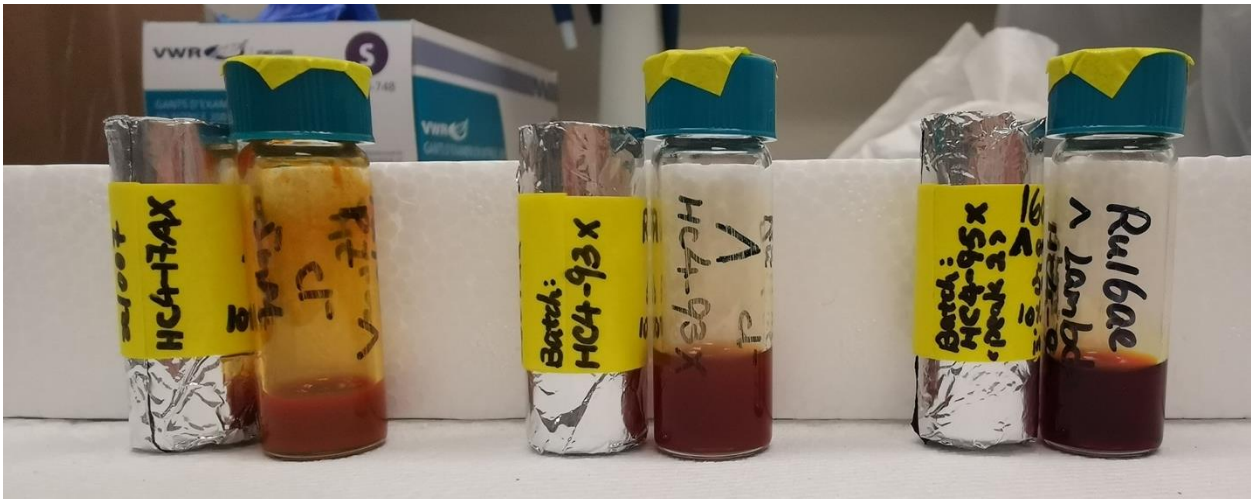

Figure S12. 300 µM stock solutions of **ş-Ru-4T** used in photobiological assays reported in Tables S2 through S7. Left: batch **A**. Center: batch **B**. Right: batch **C**. The stock solution of batch A was prepared several months prior to the other two batches, and so some compound has precipitated on the walls.

CHAPTER 5. CONCLUSIONS AND PERSPECTIVES

We set out to evaluate the various properties that lead to photocytotoxicity in Ru(II) polypyridyl systems bearing the IP-*n*T ligand, where we tested the effects of the coligand (Chapters 2 and 3) as well as the chiral configuration of the photosensitizers (PSs) (Chapter 4). Our investigations in Chapter 2 led to the identification of $[Ru(phen)_2(IP\text{-}4T)](Cl)_2$ as being another "ubertoxin", with phototoxicity occurring at as concentrations as low as ~10 fM and phototherapeutic indices (PIs) (the ratios of dark to light EC_{50} values) reaching over 1 trillion! This extremely high degree of activity has, so far, only been observed in the 2,9-dimethyl phenanthroline analog published previously,[1,2] *but is otherwise unprecedented in the literature*. Alongside this activity is the very high degree of photobiological variability, sometimes spanning 5 or 6 orders of magnitude. In response, we performed extensive biological replication on both complexes and documented our findings. We do not have a clear explanation for this variation, but we suspect that it is related to relatively poor solubility observed in certain IP-4T complexes.

In Chapter 3, we combined our IP-*n*T ligands with two 4,4'-bistrifluoromethyl-2,2'-bipyridine (4,4'-btfmb) coligands to evaluate the effects of fluorination on the photobiological, photophysical and electrochemical properties of our complexes. The complexes were somewhat less active in comparison to our phenanthryl complexes (10 nM vs 0.7 nM), but their activity was extremely consistent, with all EC_{50} values being within one order of magnitude of one another. We speculate this is related to the complexes being much easier to dissolve in aqueous media, but we are uncertain what is specifically causing this behavior. The electrochemical properties of these complexes are also of note. Specifically, the fluorinated 4,4'-btfmb ligands facilitate the acceptance of additional electrons while in the ground state (compared to the standard three reductions in $[Ru(bpy)_3]^{+2}$ type complexes, one for each ligand), with $[Ru(4,4'\text{-btfmb})_2(IP\text{-}4T)](Cl)_2$ being able to tolerate a staggering 8 electrons! This observation is likely contributing to the overall photobiological activity, but the specific mechanisms related to this are still under active investigation.

In Chapter 4, we probe the effects of chirality on the photobiological activity of our complexes. In order to minimize interference from biological variation, we chose to focus on the aforementioned [Ru(4,4'-btfmb)$_2$(IP-*n*T](Cl)$_2$ complexes, and we utilized chiral HPLC to resolve the complexes in collaboration with the Armstrong group. Our photobiological assays did not show any differences in the dark toxicity of any of the complexes. Furthermore, *rac*/Δ/Λ-[Ru(4,4'-btfmb)$_2$(IP-3T](Cl)$_2$ all shared similar light-derived activity. However, the activity of *rac*/Δ/Λ-[Ru(4,4'-btfmb)$_2$(IP-4T](Cl)$_2$ is significantly different when tested alongside one another. Specifically, the lambda enantiomer was the most active, followed by the racemate, with the delta enantiomer being the least active among the three. The difference in activity was roughly one order of magnitude when comparing the lambda enantiomer with either the racemate or delta enantiomer, with Λ-[Ru(4,4'-btfmb)$_2$(IP-4T](Cl)$_2$ leading in terms of activity by up to a factor of 30 (**rac-Ru-4T** visible EC_{50}=6.4 µM, **ş-Ru-4T** EC_{50}=0.21 µM)!

In summary, this dissertation identifies several new and interesting photoactive complexes for photodynamic therapy. These studies add a layer of complexity to our larger initiative of correlating structural variations with photobiological activities across different families of coordination complexes, where we are considering the metal ion, coligands, thienyl-appended ligands, number of thiophenes, counter ions, ionizable groups, protonation states, and coordination number and geometry. In the future, we seek to further expand upon these studies by combining other phenanthroline-based and trifluoromethylated ligands with our IP-*n*T system, and we plan to study the effects of chirality on other IP-*n*T complexes against SKMEL28 as well as other cancer cell lines.

5.1 REFERENCES

(1) Roque III, J. A.; Cole, H. D.; Barrett, P. C.; Lifshits, L. M.; Hodges, R. O.; Kim, S.; Deep, G.; Francés-Monerris, A.; Alberto, M. E.; Cameron, C. G.; McFarland, S. A. Intraligand Excited States Turn a Ruthenium Oligothiophene Complex into a Light-Triggered Ubertoxin with Anticancer Effects in Extreme Hypoxia. *J. Am. Chem. Soc.* **2022**, *144* (18), 8317–8336. https://doi.org/10.1021/jacs.2c02475.

(2) Cole, H. D.; Roque, J. A.; Shi, G.; Lifshits, L. M.; Ramasamy, E.; Barrett, P. C.; Hodges, R. O.; Cameron, C. G.; McFarland, S. A. Anticancer Agent with Inexplicable Potency in Extreme Hypoxia: Characterizing a Light-Triggered Ruthenium Ubertoxin. *J. Am. Chem. Soc.* **2022**, *144* (22), 9543–9547. https://doi.org/10.1021/jacs.1c09010.